BIBLIOTHÈQUE
CÉGEP DE L'ABITIBI-TÉMISCAMINGUE
UNIVERSITÉ DU QUÉBEC EN ABITIBI-TÉMISCAMINGUE

Mise en garde

La bibliothèque du Cégep de l'Abitibi-Témiscamingue et de l'Université du Québec en Abitibi-Témiscamingue (UQAT) a obtenu l'autorisation de la personne autrice de ce document afin de diffuser, dans un but non lucratif, une copie de son œuvre dans Depositum, site d'archives numériques, gratuit et accessible à tous. L'autrice ou l'auteur conserve néanmoins ses droits de propriété intellectuelle, dont son droit d'auteur, sur cette œuvre.

Warning

The library of the Cégep de l'Abitibi-Témiscamingue and the Université du Québec en Abitibi-Témiscamingue (UQAT) obtained the permission of the author to use a copy of this document for nonprofit purposes in order to put it in the open archives Depositum, which is free and accessible to all. The author retains ownership of the copyright on this document.

UNIVERSITÉ DU QUÉBEC EN ABITIBI-TÉMISCAMINGUE

ÉTUDES MÉTALLOGENIQUE, GÉOCHIMIQUE ET GÉOPHYSIQUE : IMPLICATIONS SUR LE PORPHYRE À CU-MO-AU-AG D'IMOURKHSSEN (OUZELLAGH-SIROUA, ANTI-ATLAS CENTRAL, MAROC)

Thèse
présentée
comme exigence partielle
du doctorat sur mesure

PAR

Mariam FERRAQ

MARS 2026

© Mariam Ferraq, 2026

UNIVERSITÉ DU QUÉBEC EN ABITIBI-TÉMISCAMINGUE

METALLOGENIC, GEOCHEMICAL AND GEOPHYSICAL INSIGHTS INTO THE IMOURKHSSEN CU-MO-AU-AG PORPHYRY DEPOSIT (OUZELLAGH-SIROUA SALIENT, CENTRAL ANTI-ATLAS, MOROCCO)

Thesis
presented
in partial fulfillment of the requirements for the tailor-made doctorate degree

BY

Mariam FERRAQ

MARS 2026

© Mariam Ferraq, 2026

ACKNOWLEDGEMENTS

This thesis is the result of many years of dedicated effort, and upon reaching its completion, I am pleased to express my profound gratitude to all those who, directly or indirectly, contributed to its successful accomplishment.

I would like to express my sincere gratitude to my supervisors: **Pr. Saïd Belkacim** and **Pr. Li-Zhen Cheng**, for their invaluable guidance and constant support throughout this research. Beyond, their kindness, patience, invaluable assistance and insightful suggestions, I am deeply grateful for their unwavering efforts in fostering academic and logistical conditions greatly contributed to the success of this co-joint PhD program. Their constant support, motivation and encouragement greatly contributed to the progress and the successful completion of this work.

My appreciation also goes to Committee Members**,** for taking the time and effort to travel from afar to evaluate my research and to share their knowledge and expertise. Their constructive feedback and valuable insights will be immensely helpful to enhance the quality of this research.

My heartfelt thanks go to **Pr. Joshua H. F. L. Davies** and **Pr. Morgann G. Perrot** from the **UQAM** and **McGill** University for their invaluable assistance and expert advice during the geochronological analyses. I extend as well my thanks to the geophysical expert from Eagle Geoscience: **Mr. Alain Théberge** for his astute advices and thoughtful suggestions in the framework of this study.

I am deeply grateful to friends from childhood: **Zineb** and **Fatima-Zahra Atich**, and several colleagues either from UIZ, UQAT or elsewhere**: Amira Merchichi, Amine Aboual, Hamza Ait Moh, Brahim Meskour, Brahim Mali** and **Said El Hachemy,** for the stimulating discussions, the shared knowledge, and for their steadfast support during challenging moments.

I would like to sincerely thank the staff of the UIZ, UQAT and UQAM for their assistance and commitment, as well to the CNRST, CRSNG and J.A DeSève Foundations for their financial support during my PhD program.

Finally, I would like to acknowledge all those who contributed to this work and I dedicate my final words of thanks to my family, with special recognition to my **parents, my brother** and **my sister** for their boundless love, encouragement, belief, prayers and prosperous guidance that has been the source of strength and motivation throughout my journey.

RÉSUMÉ

Le gisement à Cu±Mo±Au±Ag d'Imourkhssen est situé dans le promontoire d'Ouzellagh-Siroua, à la jonction entre l'Anti-Atlas central et le Haut Atlas central. Ce porphyre cuprifère est encaissé par les suites magmatiques fini-édiacariennes (LEMS) du Groupe de Ouarzazate (580-539 Ma) : (i) la Suite d'Assarag incluant la granodiorite d'Askaoun, (ii) la Suite d'Amassine comprenant le granite d'Imourkhssen et (iii) la Suite d'Ougougane représentée par le granite d'Ougougane. La lithogéochimie de ces granitoïdes révèle une affinité calco-alcaline hautement potassique typique des granitoïdes de type I. Les données géochronologiques U-Pb sur les zircons indiquent que le porphyre granitique minéralisé et le granite d'Imourkhssen sont datés à 550 ± 2 Ma et à 558 ± 1 Ma respectivement. Dès lors, le porphyre minéralisé, auparavant interprété comme une simple apophyse du premier, est une intrusion distincte et plus tardive, reconnu comme un corps granitique indépendant, désormais désigné sous le nom de granite d'Imourgane.

Les altérations hydrothermales associées à la minéralisation comprennent : (1) une altération potassique, (2) une altération chlorite–séricite, (3) une altération séricitique et (4) une altération propylitique, le tout généralement accompagnées d'une silicification et d'une pyritisation diffuses. Les événements minéralisateurs comprennent (i) une dissémination primaire de sulfures (molybdénite, pyrite, chalcopyrite, galène, tennantite), résultant de la précipitation magmatique-hydrothermale initiale ; (ii) un stade hydrothermal subséquent, canalisé par un réseau de structures NNE–SSO à N–S, au sein duquel se développent la pyrite, chalcopyrite, bornite, covellite, diagénite, sphalérite, hématite, galène, or et chenguodaite. Le stade supergène est caractérisé par la formation de la malachite, l'azurite, la barytine, l'hématite, l'epsomite et la chrysocolle.

Les données aéromagnétiques de la région d'Assarag ont été traités à l'aide de plusieurs transformations, et ont permis de décrire les caractéristiques structurales de la feuille d'Assarag (1/50 000). La réduction au pôle (RTP), la continuation vers le haut (UC) et centre de ciblage d'exploration (CET) ont permis de cartographier des failles orientées NNE-SSO, NNO-SSE et NE-SO au nord, en plus d'un halo magnétique incurvé dans la partie sud-ouest de la région. Le filtre de la continuation vers le haut (UC) a subdivisé ce secteur en deux morpho-structuraux domaines magnétiques : une région septentrionale faiblement magnétique et une région méridionale fortement magnétique, alors que le filtres de déconvolution d'Euler (ED) supporte les linéaments extraits. Les résultats de l'analyse en composante principale (ACP) et indépendante (ACI) corroborent les linéaments précédemment extraits et mettent en évidence une nouvelle structure orientée ENE-OSO. Les transformations en ondelettes continues bidimensionnelles (2D CWT) nous a permis de conclure que les tendances NNE, NNO et NE sont peu profondes et a mis en évidence des structures profondes orientées NO-SE et ENE-OSO. Nous définissons ici la tendance profonde ENE comme faisant partie de la Faille Sud Atlasique (SAF) qui traverse la région. Par ailleurs, les failles tectoniques peu profondes orientées NE-SO et NNE-SSO peuvent constituer des voies de circulation des fluides hydrothermaux pour la minéralisation à Cu-Mo-Au-Ag d'Imourkhssen.

Ces résultats sont discutés dans le cadre de la province magmatique felsique de Ouarzazate (SLIP). Cette dynamique post-panafricaine associée aux failles majeures dans le terrane de Saghro, ont favorisé une activité hydrothermale diffuse à l'origine d'une province porphyrique-épithermale, dont le gisement d'Imourkhssen constitue une expression remarquable.

Mots clés : Anti-Atlas, Ediacaran ; Panafricain, Imourkhssen ; porphyre cuprifère ; SLIP ; données aéromagnétiques.

ABSTRACT

The Imourkhssen Cu±Mo±Au±Ag deposit is located within the Ouzellagh–Siroua salient, at the junction between the central Anti-Atlas and the central High Atlas. This porphyry-type copper mineralization is hosted by the late Ediacaran magmatic suites (LEMS) of the Ouarzazate Group (580–539 Ma), namely: (i) the Assarag Suite, which includes the Askaoun granodiorite; (ii) the Amassine Suite, comprising the Imourkhssen granite; and (iii) the Ougougane Suite, represented by the Ougougane granite. The whole-rock geochemistry of these granitoids reveals a highly potassic calc-alkaline affinity typical of I-type granitoids. U–Pb zircon geochronological data indicates that the mineralized granitic porphyry and the Imourkhssen granite are dated 550 ± 2 Ma and 558 ± 1 Ma respectively. Therefore, the mineralized porphyry; previously interpreted as a simple apophysis of the latter; is in fact a distinct and younger intrusive body, recognized as an independent granitic intrusion, herein referred to as the Imourgane granite.

The hydrothermal alterations associated with the mineralization include: (1) potassic alteration, (2) chlorite–sericite alteration, (3) sericitic alteration, and (4) propylitic alteration, generally accompanied by pervasive silicification and pyritization. Mineralizing events comprise: (i) a primary dissemination of sulfides (molybdenite, pyrite, chalcopyrite, galena, and tennantite), corresponding to the initial magmatic-hydrothermal precipitation; and (ii) a subsequent hydrothermal stage channeled through a network of NNE–SSW to N–S structures, within which pyrite, chalcopyrite, bornite, covellite, digenite, sphalerite, hematite, galena, gold, and chenguodaite develop. The supergene stage is characterized by the formation of malachite, azurite, barite, hematite, epsomite, and chrysocolla.

Aeromagnetic data from the Assarag area were processed using multiple transformations, allowing the structural features of the Assarag 1:50,000 sheet to be characterized. Reduction to the pole (RTP), Upward Continuation (UC), and Center for Exploration Targeting (CET) filters enabled the mapping of NNE–SSW, NNW–SSE, and NE–SW trending faults in the northern part of the area, as well as a curved magnetic halo in the southwest. Upward continuation filtering divided the area into two magnetic morpho-structural domains: a weakly magnetic northern region and a strongly magnetic southern region, while Euler Deconvolution (ED) supports the extracted lineaments. Principal Component Analysis (PCA) and Independent Component Analysis (ICA) corroborate these structures and reveal an additional ENE–WSW trending feature. Two-dimensional continuous wavelet transforms (2D CWT) indicate that the NNE, NNW, and NE trends correspond to shallow structures, while deep-seated NW–SE and ENE–WSW lineaments are also present. We interpret the deep ENE trend as part of the South Atlas Fault (SAF) that crosscuts the region. In addition, shallow NE–SW and NNE–SSW faults likely acted as conduits for hydrothermal fluids responsible for the Cu–Mo–Au–Ag mineralization at Imourkhssen.

These results are integrated into the broader geodynamic framework of the magmatic–hydrothermal evolution of the Ouarzazate Silicic Large Igneous Province (SLIP). This post-Pan-African magmatic activity, coupled with the structural role of major regional faults, favored diffuse hydrothermal circulation that led to the development of a porphyry–epithermal metallogenic province in the Saghro terrane, of which the Imourkhssen deposit represents a key expression.

Keywords: Anti-Atlas; Ediacaran; Pan-African; Imourkhssen; porphyry copper; SLIP; aeromagnetic data.

TABLE OF CONTENT

ACKNOWLEDGEMENTS iii
RÉSUMÉ iv
ABSTRACT v
TABLE OF CONTENT vi
LIST OF FIGURES viii
LIST OF TABLES xiv
INTRODUCTION GÉNÉRALE 15
Etat de l'art et Problématique 15
Approches 16
Objectifs 18
Organisation du manuscrit de thèse 18
GENERAL INTRODUCTION 20
State of the art and issue: 20
Approaches 21
Aims 22
Organization of the thesis manuscript 23
1. CHAPTER 1: LITERATURE REVIEW 25
1.1 Introduction 25
1.2 Porphyry copper deposit 25
1.2.1 Definition: 25
1.2.2 Geochemistry and tectonic setting: 26
1.2.3 Spatial and temporal distribution: 28
1.2.4 Classification: 30
1.2.5 Hydrothermal alteration and mineralization: 30
1.3 Epithermal deposits: 32
1.3.1 Definition and Classification: 32
1.3.2 Hydrothermal alteration: 34
1.3.3 Genetic model: 35
1.4 Exploration of porphyry and epithermal ore deposits: 36
1.4.1 Porphyry ore deposit exploration 36
1.4.2 Epithermal ore deposits exploration: 42
1.5 Porphyry-Epithermal relationship: 43

2. CHAPTER 2: GEOLOGICAL AND GEODYNAMIC FRAMEWORK 45
2.1 Geological overview 45
2.2 Litho-stratigraphic and geodynamic insights: 47
2.3 Geodynamic framework 50
2.4 The Pan-African Anti-Atlas belt: connections with peri-Gondwanan crustal blocks 54
2.5 Geographical location of the studied area 55
3. CHAPTER 3: NEW GEOCHEMICAL AND GEOCHRONOLOGICAL CONSTRAINTS ON THE GENESIS OF THE IMOURKHSSEN CU±MO±AU±AG PORPHYRY DEPOSIT (OUZELLAGH-SIROUA SALIENT, ANTI-ATLAS, MOROCCO): GEODYNAMIC AND METALLOGENIC IMPLICATIONS 57
3.1 Résumé 58
3.2 Abstract 59
3.3 Introduction 60
3.4 Regional Geology 61
3.4.1 The Anti-Atlas 61
3.4.2 Deposit-scale Geology 63
3.5 Sampling and Analytical Methods 65
3.6 Results 67
3.6.1 Petrography of the Host Rocks 67
3.6.2 Whole rock Geochemistry 70
3.6.3 X-Ray data 73
3.6.4 Hydrothermal alteration and vein system 74
3.6.5 The Imourkhssen porphyry style mineralization 77
3.6.6 LA-ICP-MS U/Pb zircon dating 81
3.7 Discussion 83
3.7.1 Timing of the plutonic magmatism 83
3.7.2 Ore genesis and source in the framework of the geodynamic context of the Anti-Atlas 86
3.7.3 Late Ediacaran Ouarzazate SLIP and implications for Anti-Atlas metallogeny 89
3.7.4 A probable late Ediacaran Porphyry-Epithermal province in the Anti-Atlas 91
3.7.5 Similarities with porphyry and epithermal ore deposits in the world 92
3.7.6 Spatial correlations with the Avalon epithermal ore deposits 94
3.8 Conclusions 96
3.9 References 98

4. CHAPTER 4: AEROMAGNETIC DATA FROM THE ASSARAG AREA: IMPLICATIONS FOR THE IMOURKHSSEN PORPHYRY MINERALIZATION 109
4.1 Résumé 110
4.2 Abstract 111
4.3 Introduction 112
4.4 Geological setting 113
4.5 Geophysical Survey 115
4.6 Aeromagnetic Data Processing 116
4.7 Advanced feature extraction and integration with CWT, PCA and ICA 118
4.8 Results 121
4.9 Discussion 127
4.10 Conclusion: 131
4.11 References 132
CONCLUSIONS GÉNÉRALES 140
GENERAL CONCLUSIONS 142
APPENDIX 144
GENERAL REFERENCES 159

LIST OF FIGURES

Figure 1. A) Échantillonnage des principales unités lithologiques et roches minéralisées de la zone d'Imourkhssen : B) Granite d'Imourkhssen. C) Microgranite d'Ougougane. D) Veine de barytine-hématite. E) Échantillon altéré à chlorite-séricite. F) Veine de quartz-chlorite. G) Veine de barytine. 16

Figure 2. Démarche pluridisciplinaire adoptée pour la réalisation de cette thèse. 17

Figure 1. A) Sampling of the main lithological units and mineralized rocks of the Imourkhssen area: B) Imourkhssen granite. C) Ougougane microgranite. D) Barite-hematite vein. E) Chlorite-sericite altered sample. F) Quartz-chlorite vein. G) Barite vein. 21

Figure 2. Multi-study approaches workflow adopted for the purposes of this thesis. 22

Figure 1.1. Porphyry copper mineralization and associated epithermal, skarn and base metal deposits (from Sinclair, 2007). 26

Figure 1.2. Schematic representation of an ocean-continent subduction zone (continental arc) where Porphyry copper deposits represent shallow level intrusions (2–5km) in the crust (From Lee and Tang, 2020)..... 27

Figure 1.3. Map showing Phanerozoic igneous provinces with porphyry Cu-Mo-Au deposits (from Seedorff et al., 2005). 28

Figure 1.4. Age distribution of porphyry deposits (modified from Sinclair, 2007 and references therein). 29

Figure 1.5. Ages of Precambrian porphyry Cu deposits and prospects (red bars) in relation to atmospheric O2 (Sillitoe, 2025). 29

Figure 1.6. Generalized alteration-mineralization zoning pattern for telescoped porphyry Cu deposits (Sillitoe, 2010)..... 31

Figure 1.7. Schematic hydrothermal alteration patterns of HS and IS epithermal ore deposits (modified from Sillitoe, 2010). HS = high sulfidation, IS = intermediate sulfidation. 33

Figure 1.8. Cross-section of alteration zones characteristic of high-sulfidation deposits as observed at the Summitville Au-Cu deposit, Colorado, US. Diagram left (simplified from Steven and Ratte, 1960) shows schematic outward zonation from a subvertical mineralized body shown at right (modified after Stoffregen, 1987). 35

Figure 1.9. Spatial and genetic relationship between epithermal deposits and underlying porphyry systems (modified after Hedenquist and Lowenstern, 1994) 35

Figure 1.10. RTP magnetic anomaly pattern over the Bajo de la Alumbrera Cu–Au porphyry deposit, Catamarca, Argentina (Clark, 2014)..... 38

Figure 1.11. Radiometric ternary map of a part of the Egyptian central eastern Desert (Elkhateeb and Abdellatif, 2018). 41

Figure 1.12. Representative hydrothermal ore deposits associated with subduction-related magmatism (modified from Hedenquist and Lowenstern, 1994). 44

Figure 2.1. Structural domain of Morocco (modified from Michard et al., 2008). 46

Figure 2.2. Generalized lithostratigraphic column for the Anti-Atlas Pan-African orogen (after Errami et al., 2021) 48

Figure 2.3. Geodynamic model of the Pan-African evolution of the Anti-Atlas belt (Ennih and Liégeois, 2001) 52

Figure 2.4. Geodynamic evolution model illustrating the tectonic development of the Anti-Atlas chain (Walsh et al., 2012, modified after Benziane, 2007)..... 53

Figure 2.5. A) Global Location of Morocco; **B**) Geographic Setting of the Study Area within Morocco. **C**) Position of the Study Area within the Anti-Atlas Belt. 55

Figure 3.1. Global distribution of porphyry deposits (modified from Seedorff et al., 2005).. 60

Figure 3.2. A) Location of the Anti-Atlas domain and its relationship to the West African Craton. B) Location of the studied area modified after (Gasquet et al., 2008). The geology of the studied area is detailed in figure 3. C) Simplified geological map of the Saghro domain showing the location of major porphyry and epithermal ore deposits (Tuduri et al., 2018).... 62

Figure 3.3. Geological map of the studied area (modified from Toummite et al., 2012; Belkacim et al., 2017). 64

Figure 3.4. The Zaghar dykes crosscut the Ougougane granite. 65

Figure 3.5. Selected photomicrographs of the LEMS at XPL (cross polarized light), with the Askaoun granodiorite in A), the Imourkhssen granite in B), the Imourgane granite in C) and the Zaghar mafic dyke in D). Mineral abbreviations: Opq: opaque, Amp: amphibole, Qz: quartz, Chl: chlorite, Bt: biotite, Kln: kaolinite, K-Fsp: K-feldspar, Or: orthoclase, Cpx: clinopyroxene, Sr: sericite, Pl: plagioclase, Zrn: zircon 69

Figure 3.6. Co-mingling texture between the Askaoun granodiorite and Zaghar mafic dyke in Talat nl'bour area. The transition between the two magmatic bodies is progressive, and outlined by the incorporated granodioritic fragments within the mafic dyke. 70

Figure 3.7. Whole rock geochemistry of the Late Ediacaran granites of the TV area. A) Total alkali ($Na_2O + K_2O$) (wt%) versus SiO_2 (wt%) diagram after (Middlemost, 1994). B) A/NK versus A/CNK diagram of (Maniar and Piccoli, 1989). C) SiO_2 vs. K_2O diagram after (Boynton, 1983). D) Tectonic discrimination Rb vs. Y + Nb diagram after (Pearce et al., 1984; Pearce, 1996) syn-COLG: syn-collisional granite, WPG: within plate granite, POG: Post-collisional granite, VAG: volcanic arc granite, ORG: oceanic ridge granite . E) and F) Primitive mantle-normalized trace-element spidergram and chondrite- normalized REE distribution diagrams of the TV magmatic rocks compared to previous trends by (Toummite et al., 2012) shown as grey trends. The MORB values are from (Pearce, 1983), and the chondrite values are from (Boynton, 1983). 71

Figure 3.8. Harker diagrams of selected major oxide and trace elements content of the Late Ediacaran granites of the TV area. The proximal evolutionary trends are highlighted by the grey arrows. 72

Figure 3.9. A) P_2O_5 vs. SiO_2 classification diagram after (Sylvester, 1994). Data for geochemical trend are from this study. B) Sr and Nd isotopic initial ratios (εNd vs ($^{87}Sr/^{86}Sr$)i at 570 Ma for the TV magmatic rocks from (Toummite et al., 2012), I-Type granite values from (Raeisi et al., 2024). 72

Figure 3.10. Mineralogy of the Imourkhssen deposit determined after XRD analysis. Abbreviations: Qz: quartz, Ab: albite, Chl: chlorite, Pl: plagioclase, Ms: muscovite, Or: orthoclase, Py: pyrite, Hm: hematite, Bt: biotite, Esm: epsomite. Mineral abbreviations from (Whitney and Evans, 2010; Warr, 2021). 74

Figure 3.11. Photomicrographs of the hydrothermal alteration mineral assemblages with associated samples. A) Potassic alteration highlighted by brick-red colored K-feldspar and molybdenite (Mol) dissemination within the Imourgane granite. B) Chlorite-sericite alteration with molybdenite dissemination. C) Phyllic or sericitic alteration highlighted by bleached outcrops. D) Propylitic halo within the Imourgane granite along with molybdenite dissemination. Mineral abbreviations: K-Fsp: K-feldspar, Chl: chlorite, Mol: molybdenite. . 75

Figure 3.12. The different hydrothermal vein types observed in the studied area: (A) Aplite mega-lens surrounded by the bleached zone. (B) Quartz stockworks. (C) Quartz-hematite lens. d) Barite-hematite lens out crops in phyllic alteration zone. E) and F) Quartz-Chlorite sulfide lenses. 76

Figure 3.13. A) Cockade texture in a centimetric barite-hematite vein observed within the Imourgane granitic intrusion. B) Hydrothermal breccia affecting the quartz-chlorite-sulfide lens in a gallery of the Talat nl'bour area. Mineral abbreviations: Chl: chlorite, Qz: quartz, Hm: hematite, Brt: barite. 77

Figure 3.14. Inferred paragenetic sequence of the Imourkhssen Cu±Mo±Au±Ag deposit (modified from Belkacim, 2014). 78

Figure 3.15. Reflected light (RL) photomicrographs and scanning electron microscopy (SEM) of: A) Molybdenite (Mol) flake in the Imourgane granite. B) Pyrite (Py) and chalcopyrite (Ccp) dissemination in the Askaoun granodiorite. C) Galena (Gn) inclusion surrounded by chalcopyrite, that is enclosed itself by pyrite. D) Barite (Brt), bornite (Bn) and hematite assemblage within the Zaghar dyke sample. E) Sphalerite (Sp), hematite (Hm) and

pyrite inclusions within the chalcopyrite. E) Hematite displays chenguodaite (Cgu) and galena inclusions. Mineral abbreviations from (Whitney and Evans, 2010; Warr, 2021). 79

Figure 3.16. Quantitative results for molybdenite dissemination (MD) and molybdenite veinlets (MV) powdered samples. 80

Figure 3.17. A) Molybdenite dissemination within the Imourgane granite. B) Molybdenite veinlets within a propylitic halo. 81

Figure 3.18. Cathodoluminiscence images for the dated zircon from J23IM09 and J23IM13 samples. 82

Figure 3.19. U–Pb concordia and The Pb^{206}/U^{238} Weighted mean diagrams showing LA-ICP-MS zircon ages of 550 ± 2 Ma and 558 ± 1 Ma for the J23IM09 and J23IM13 samples, respectively. Error ellipses are given at 2σ level. Ages were calculated using Isoplot R (Vermeesch, 2018) 83

Figure 3.20. The emplacement of the late Ediacaran magmatic suites (LEMS) related to the three magmatic pulses of the Ouarzazate SLIP (Tuduri et al., 2018; Belkacim et al., 2021) and the position of Imourkhssen and many Ore deposits of the Anti-Atlas. 90

Figure 3.21. The emplacement of many ore porphyry and epithermal deposit within Saghro domain creating a late Ediacaran porphyry epithermal province in the Anti-Atlas of Morocco (Tuduri et al., 2018). 92

Figure 3.22. Paleogeography of the Avalonian-Cadomian active margin, peri-Gondwanan terranes and the Saghro domain at ca. 570 Ma. Modified from (Linnemann et al., 2014; Ouabid and Garrido, 2023). 95

Figure 4.1. a) Location of the Anti-Atlas domain within the West African craton. b) Location of the studied area and generalized geological map of the Anti-Atlas, modified after (Gasquet et al. 2008). c) Detailed geological map of the Assarag area modified from (Thomas et al., 2002. Toummite et al., 2012. Belkacim et al., 2017). 114

Figure 4.2. Data processing workflow. 121

Figure 4.3. a) Residual magnetic field (RMF) and b) reduced to pole maps (RTP) of the Assarag area. 122

Figure 4.4. RTP maps are extended upwards to: a) 250m, b) 500m, c) 1000m and d) 2000m. The dashed lines represent the suggested ENE lineament. 123

Figure 4.5. a) Tilt derivative map of the RTP data with the extracted magnetic lineaments (black lines) by the Center for exploration targeting and corresponding Rose Diagram. b) Euler solution map for SI = 0 with the structural fault outlined by the black lines and associated Rose Diagram 124

Figure 4.6. Continuous wavelet transformation (CWT) with the Gaussian mother wavelet by increasing scale map a) to map b). The black dashed lines are the extracted magnetic lineaments with a curved magnetic feature in the southwestern part of the Assarag area. 125

Figure 4.7. a) and b) 1st and 2nd PCA results respectively. c) 3rd k-ICA map. d) 1st n-ICA map highlighting the ENE lineament. 127

Figure 4.8. NNE oriented fractures in the Imourkhssen area. a) Aplitic mega lens. b) Multi-scale-NNE oriented fractures. c) N to NNE ore bearing system. d) Barite-Hematite lens exhibiting dextral kinematic. 130

LIST OF TABLES

Table 1.1. Characteristic mineralogy for oxidation classes of igneous rocks (Champion and Heinemann, 1994). 38

Table 1.2. Characteristic mineral assemblages of the main alteration types in porphyry systems (Clark, 2014). 39

INTRODUCTION GÉNÉRALE

Etat de l'art et Problématique

La géologie du Maroc reflète une histoire tectono-magmatique complexe, façonnée par de multiples événements orogéniques et sédimentaires depuis le Précambrien jusqu'à l'actuel. Dans l'Anti-Atlas, ces événements géologiques ont contribué de manière significative au développement et à l'exposition de plusieurs types de gisements de minéraux dans sa ceinture panafricaine (Gasquet et al., 2005). Au cours des phases finales de l'orogenèse panafricaine, la période édiacarienne tardive (580-539 Ma) a été notamment caractérisée par un régime tectonique transtensif (Thomas et al., 2002; Gasquet et al., 2005) associé à une intense activité magmatique felsique. Cette activité est interprétée comme une large province ignée felsique (Silicic Large Igneous Province), reconnue sous le nom de la SLIP de Ouarzazate (Youbi et al., 2021 ; Belkacim et al., 2021), en référence au Groupe de Ouarzazate (580-538 Ma) auquel est associée cette activité magmatique. Ce cadre géodynamique particulier a favorisé une activité hydrothermale à l'origine d'un processus métallogénique responsable de divers types de gisements minéraux (Gasquet et al., 2005; Tuduri et al., 2018; Belkacim et al., 2021). Parmi ces types de gisements, figurent les porphyres cuprifères. Dans l'Anti-Atlas, de nombreux exemples de gisements semblent présenter certaines caractéristiques indicatives des porphyres cuprifères, comme le gisement de Tiouit (Mouttaqi et al., 2011; Bouabdellah et al., 2016), la partie "Patte d'Oie'' du gisement de Bouskour (Jébrak and Marcoux, 2008; El Azmi et al., 2014) et les minéralisations filoniennes aurifères d'Ismlal (Tuduri et al., 2018) et le gisement de Cu±Mo±Au d'Imourkhssen (Belkacim, 2014). Ce dernier constitue l'objet de cette thèse, dans laquelle sont décrites ci-après les caractéristiques géologiques, géochimique, tectono-structurale et métallogéniques de ce gisement.

Les gisements porphyriques constituent un type essentiel des gisements magmatiques-hydrothermaux, connus par leur important tonnage et leur contribution significative à la production de cuivre, d'or et de molybdène, d'où l'intérêt croissant qu'ils suscitent en matière de recherche et d'exploration (Sillitoe, 2010; Sun et al., 2015). Par ailleurs, les investigations aéromagnétiques ont été largement utilisées pour ces fins économiques (Sassioui et al., 2024; Tobi et al., 2025), en s'appuyant sur l'analyse de la relation spatiale entre les linéaments magnétiques et les structures minéralisées (Aabi et al., 2024 et les références qui y figurent). En outre, les données magnétiques peuvent être compilés et corrélés avec divers types de données provenant d'autres méthodes géophysiques ou géologiques, offrant ainsi une vision

intégrée et multidimensionnelle du contexte tectono-structural et des caractéristiques du substratum.

Approches

Lors d'une étude géologique, l'échantillonnage représentatif et le recours à des techniques analytiques appropriées constituent des étapes fondamentales pour la caractérisation pétrographique et géochimique des roches. Dans le cadre de ce travail, l'échantillonnage a été réalisé dans diverses unités lithologiques de la zone d'Imourkhssen, ainsi que sur les anciennes galeries de Talat n'l'Bour, l'un des secteurs minéralisés majeurs de la région. Plus de soixante-dix échantillons ont été prélevés au cours des missions de terrain afin de couvrir les principales unités lithologiques de la zone étudiée (**Figure 1**).

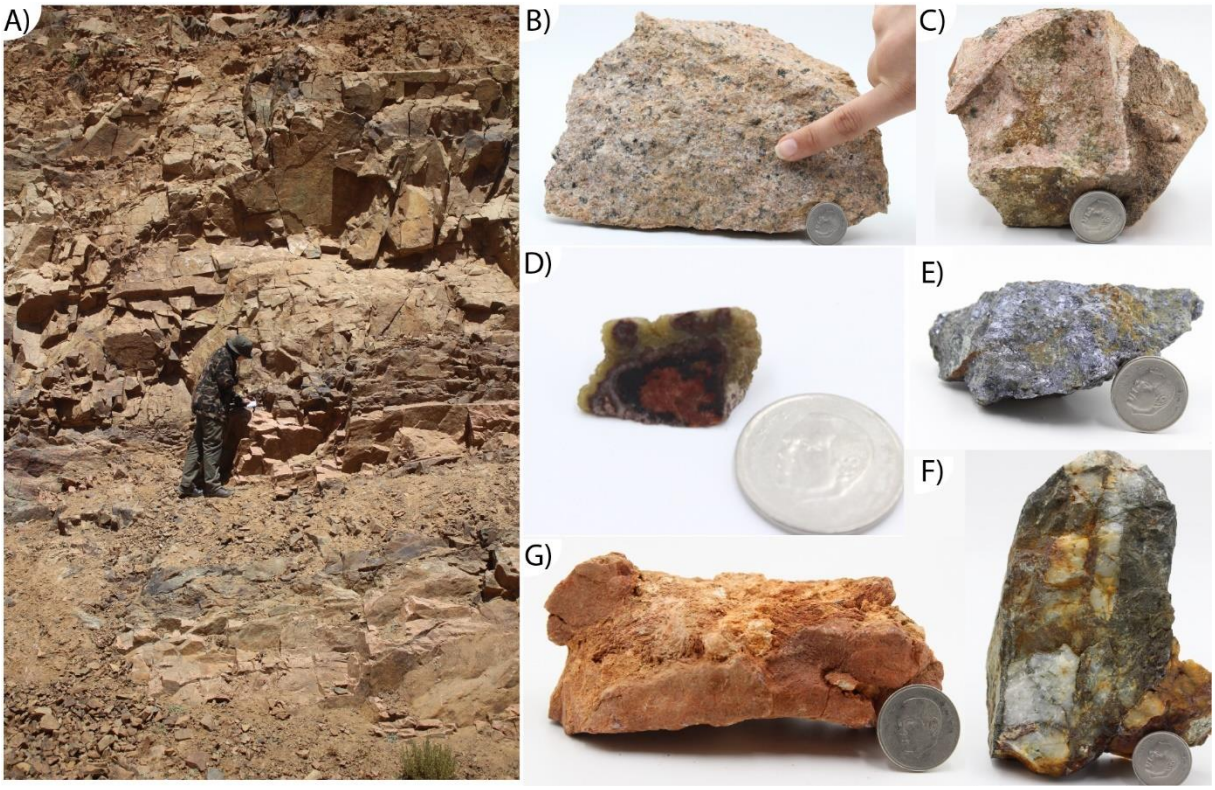

Figure 1
A) Échantillonnage des principales unités lithologiques et roches minéralisées de la zone d'Imourkhssen : B) Granite d'Imourkhssen. C) Microgranite d'Ougougane. D) Veine de barytine-hématite. E) Échantillon altéré à chlorite-séricite. F) Veine de quartz-chlorite. G) Veine de barytine.

Les échantillons représentatifs (**Annexe 1**) ont été sélectionnés en vue d'une approche pluridisciplinaire intégrant des analyses pétrographiques, minéralogiques, géochimiques et géochronologiques. L'ensemble des données acquises permet d'établir une compréhension globale des caractéristiques géologiques et structurales, ainsi que des processus d'altération et

de minéralisation. Les procédures analytiques détaillées et les résultats correspondant à chaque méthode sont présentés dans les sections suivantes, tandis que les données et abréviations minéralogiques utilisées sont synthétisées dans les **Annexes 1 à 6**.

Il convient de souligner que des travaux antérieurs ont porté sur les aspects lithologiques et géochimiques de la région d'Assarag (Thomas et al., 2002 ; Toummite et al., 2012 ; Belkacim et al., 2014 ; Belkacim et al., 2017), ainsi que sur ses caractéristiques métallogéniques (Belkacim et al., 2014). En revanche, le présent travail adopte une approche pluridisciplinaire approfondie (**Figure 2**), intégrant la pétrographie, la géochimie de roches totale, la diffraction des rayons X, des analyses à la microsonde électronique et au microscope électronique à balayage, des datations U–Pb sur zircon, une étude métallogénique de la minéralisation d'Imourkhssen et une caractérisation structurale basée sur le traitement des données aéromagnétiques du feuillet d'Assarag.

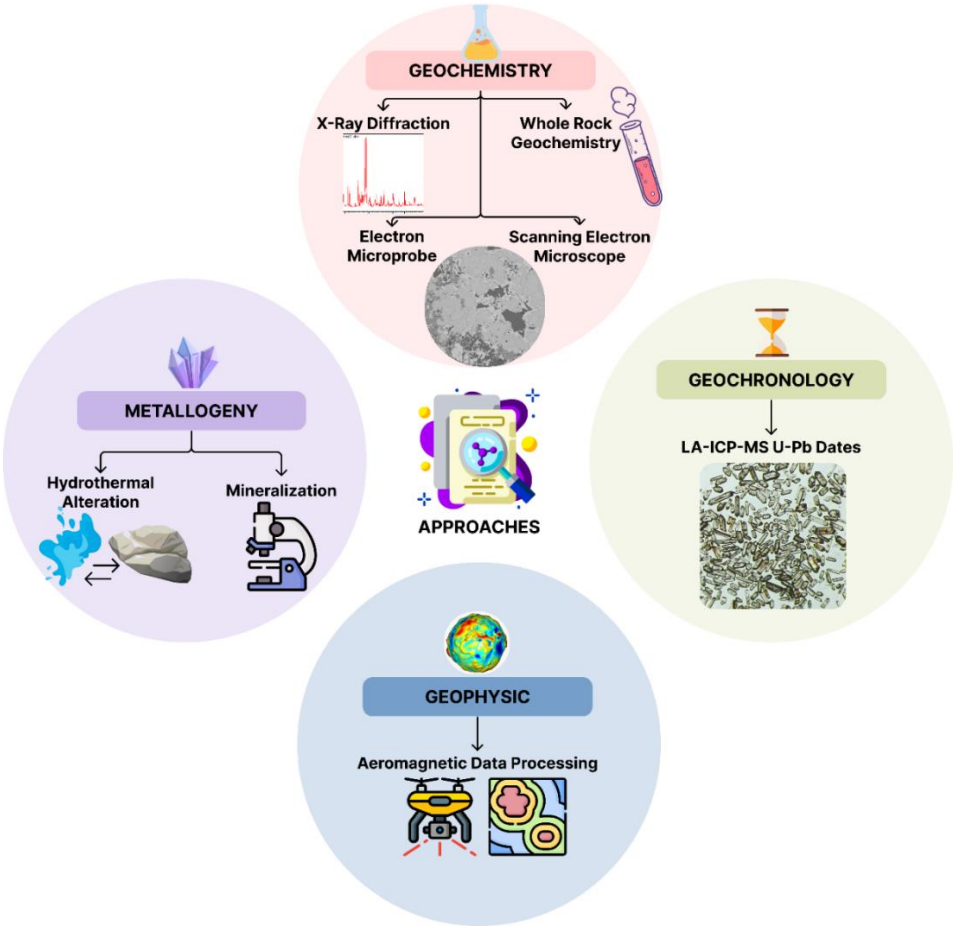

Figure 2
Démarche pluridisciplinaire adoptée pour la réalisation de cette thèse.

Objectifs

L'étude de la genèse des minéralisations à Cu±Mo±Au±Ag d'Imourkhssen, ainsi que des processus magmatiques, hydrothermaux et structuraux ayant conditionné leur mise en place dans l'évolution géodynamique de la chaîne panafricaine de l'Anti-Atlas, a requis une démarche pluridisciplinaire mobilisant des investigations géologiques, pétrographiques, géochimiques, métallogéniques et géophysiques. Ainsi, les objectifs scientifiques visés par ce travail sont de :

- Caractériser la pétrographie et la lithogéochimie des roches encaissantes.
- Dater le porphyre minéralisé et élucider sa relation avec le granite d'Imourkhssen.
- Définir les principales phases minérales du porphyre d'Imourkhssen et décrire les textures et les structures minérales associées afin de déduire la succession paragénétique.
- Décrire les différentes altérations hydrothermales associées à la minéralisation.
- Établir une corrélation intégrée entre les gisements porphyriques et épithermaux d'âge fini-édiacarien du terrane de Saghro et ceux observés dans certains terranes péri-gondwaniens (Avalon), considérés comme des blocs crustaux amalgamés à la marge de la Gondwana.
- Décrire les caractéristiques structurales de la région d'Assarag en se basant sur les traitements des données aéromagnétiques.
- Évaluer le contrôle structural sur la minéralisation d'Imourkhssen.
- Intégrer la genèse du porphyre d'Imourkhssen dans le contexte géodynamique global de l'évolution panafricaine de la chaîne de l'Anti-Atlas.

Organisation du manuscrit de thèse

Outre cette introduction qui présente la philosophie et la problématique de cette étude, les approches et les méthodes mobilisées, ainsi que les principaux objectifs de ce travail, ce manuscrit de thèse s'articule autour de quatre chapitres, soigneusement décrits ci-dessous :

- **Le chapitre I** est intitulé « **Literature Review** ». Il s'agit d'une revue bibliographique consacrée aux principales caractéristiques des gisements porphyriques et épithermaux, mettant en lumière leurs définitions, classifications, contextes géodynamiques, les altérations hydrothermales qui leur sont associées, modèles génétiques, ainsi que les méthodes les plus pertinentes pour leur exploration. Ce chapitre vise à se familiariser

avec la thématique de la problématique étudiée, et situer la présente étude dans son cadre général.

- **Le chapitre II** est intitulé « **Contexte Géologique et Géodynamique Régional** ». Ce chapitre présente une synthèse des grands domaines structuraux du Maroc, avec une description détaillée de la lithostratigraphie et du contexte géodynamique de l'Anti-Atlas pour placer ce travail dans son cadre géologique global. Il introduit par ailleurs la localisation géographique de la zone d'étude, afin de fournir au lecteur un repère spatial clair et de situer la zone étudiée dans son contexte régional.
- **Le chapitre III** figure sous le titre de « **New Geochemical and Geochronogical Constraints on the Genesis of the Imourkhssen Cu±Mo±Au±Ag Porphyry Deposit (Ouzellagh-Siroua Salient, Anti-Atlas, Morocco) : Geodynamic and Metallogenic Implications** ». Il met en lumière une étude pétrographique, géochimique et géochronologique des roches encaissantes, complétées par une caractérisation métallogénique de la minéralisation à Cu±Mo±Au±Ag d'Imourkhssen et des altérations hydrothermales qui lui sont associées.
- **Chapitre V** est désigné par le titre de « **Aeromagnetic Data from the Assarag Area : Implications for the Imourkhssen Porphyry Style Mineralization** ». Il présente une série de traitements géophysiques afin de décrire les caractéristiques structurales majeures du feuillet d'Assarag (1/50 000), et évaluer le contrôle structural sur la minéralisation d'Imourkhssen.

Ce manuscrit s'achève par des **conclusions générales** constituant une synthèse des idées tirées de l'ensemble des approches déployées, offrant une compréhension cohérente de la problématique étudiée et répondant aux objectifs poursuivis.

Remarque : Il convient de noter que le résumé, l'introduction et les conclusions générales ont été rédigés en français et en anglais, conformément aux exigences de soumission des deux universités partenaires (UQAT et UIZ) dans le cadre de ce programme de doctorat en cotutelle.

GENERAL INTRODUCTION

State of the art and issue:

Morocco's geology reflects a complex tectono-magmatic history shaped by multiple orogenic and sedimentary events from the Precambrian to the present. In the Anti-Atlas, these geological events contributed significantly to the development and exposure of several types of mineral deposits in its the Pan-African belt (Gasquet et al., 2005). During the final phases of the Pan-African orogeny, the Late Ediacaran period (580-539 Ma) was notably characterized by a transtensive tectonic regime (Thomas et al., 2002; Gasquet et al., 2005) together with intense felsic magmatic activity, referred to as the Ouarzazate SLIP (Youbi et al., 2021; Belkacim et al., 2021), in reference to the Ouarzazate Group (580–538 Ma) with which this magmatic activity is associated. This particular geodynamic framework promoted hydrothermal activity that triggered a metallogenic process responsible for various types of mineral deposits (Gasquet et al., 2005; Tuduri et al., 2018; Belkacim et al., 2021). Among these deposit types are copper porphyry deposits. In the Anti-Atlas, several examples of deposits appear to exhibit certain characteristics indicative of porphyry copper deposits, such as the Tiouit deposit (Mouttaqi et al., 2011; Bouabdellah et al., 2016), the "Patte d'Oie" part of the Bouskour deposit (Jébrak and Marcoux, 2008; El Azmi et al., 2014) and the gold-bearing vein mineralizations of Ismlal (Tuduri et al., 2018) and the Imourkhssen Cu±Mo±Au porphyry deposit (Belkacim, 2014). The latter constitutes the focus of this thesis, in which we describe the geological, geochemical, tectono-structural, and metallogenetic characteristics of this deposit

Porphyry deposits are an essential type of magmatic-hydrothermal deposit, known for their large tonnage and significant contribution to copper, gold, and molybdenum production, leading to a rising interest in both research and exploration (Sillitoe, 2010; Sun et al., 2015). For these reasons, aeromagnetic data have been widely employed for these purposes (Sassioui et al., 2024; Tobi et al., 2025), by analyzing the spatial correlation between magnetic lineaments and mineralized zones (Aabi et al., 2024 and references therein). In addition, magnetic data can be compiled and correlated with various types of data from other geophysical or geological methods, providing an integrated and multidimensional view of the tectono-structural context and the subsurface features.

Approaches

When conducting geological research, representative sampling and the use of appropriate analytical techniques are crucial for accurately characterizing rocks, minerals, and geochemical features. In this study, sampling encompassed various lithological units and structural settings in the Imourkhssen area as well as in the abandoned Talat nl'bour galleries, which represent one of the most significant mineralized sectors of the region. More than seventy samples were collected during field missions to cover the main lithological units of the studied area (**Figure 1**).

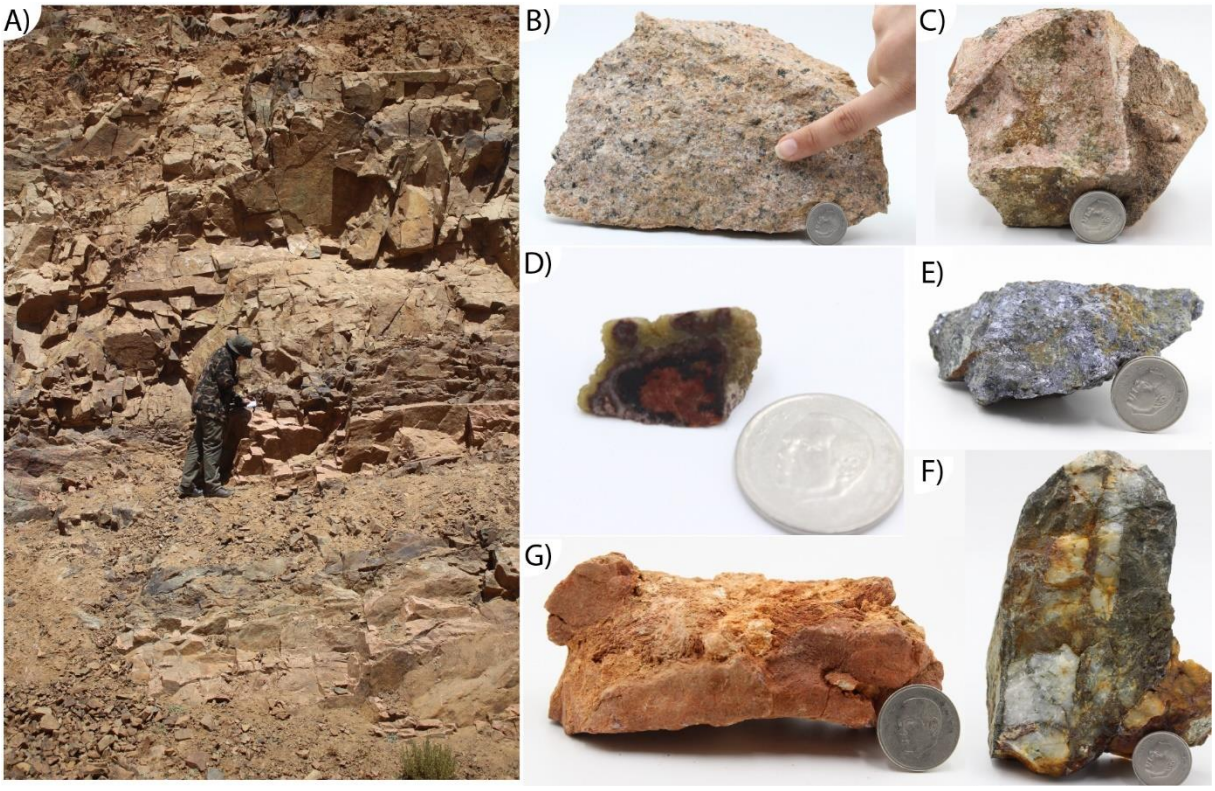

Figure 1
A) Sampling of the main lithological units and mineralized rocks of the Imourkhssen area: B) Imourkhssen granite. C) Ougougane microgranite. D) Barite-hematite vein. E) Chlorite-sericite altered sample. F) Quartz-chlorite vein. G) Barite vein.

The representative samples (**Appendix 1**) were selected for multidisciplinary approach including petrographic, mineralogical, geochemical and geochronological studies. The entire data adopted is used to provide a comprehensive understanding of the geological and structural features along with the alteration and mineralization process. The detailed analytical procedures and results corresponding to each method are presented in the subsequent sections, while the data and mineral abbreviations used is summarized in **Appendixes 1-6**.

It is worth noting that previous investigations have addressed the lithological, geochemical (Thomas et al., 2002; Toummite et al., 2012; Belkacim et al., 2014; Belkacim et al., 2017), and metallogenic aspects (Belkacim et al., 2014) of the Assarag area. Al though, the present work consists of a multi-approach study (**Figure 2**) including petrography, whole rock geochemistry, X-Ray diffraction, microprobe analysis and scanning electron microscopy, U-Pb on zircon dating, metallogenic study of the Imourkhssen mineralization, and structural investigation based on the aeromagnetic data processing of the Assarag map.

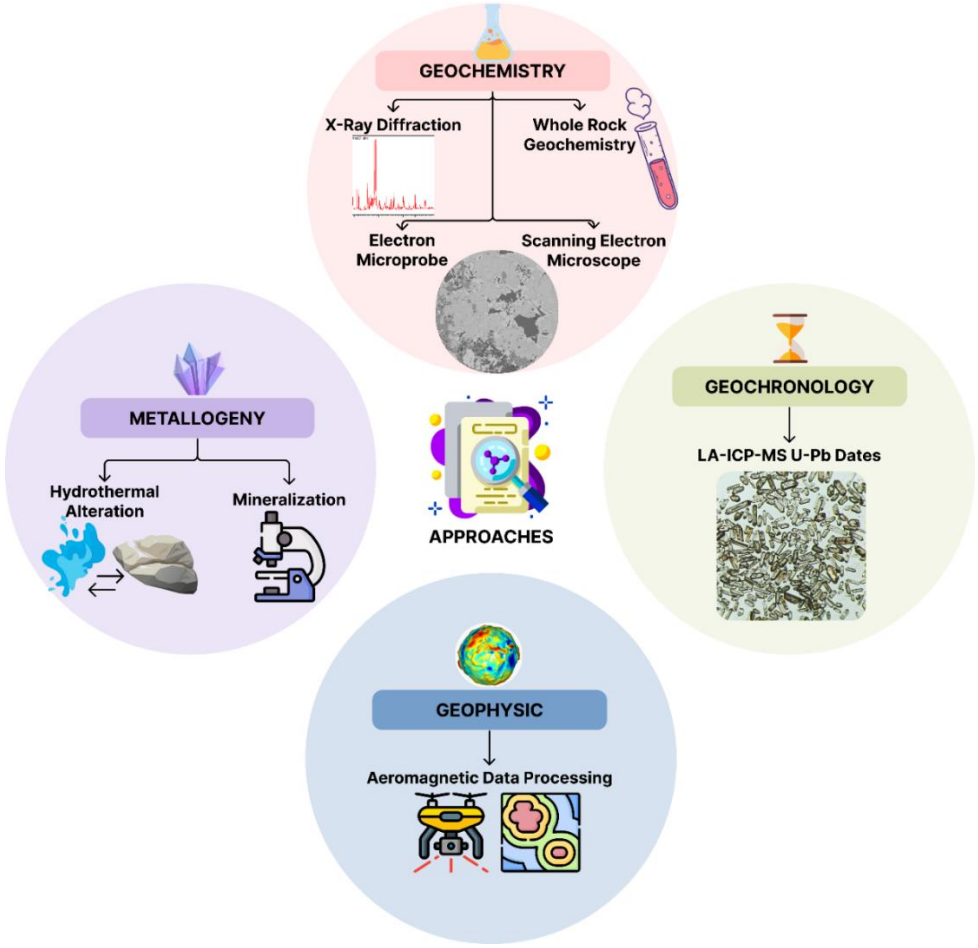

Figure 2
Multi-study approaches workflow adopted for the purposes of this thesis.

Aims

The study of the genesis of the Imourkhssen Cu±Mo±Au±Ag mineralization, as well as the magmatic, hydrothermal, and structural processes that controlled their emplacement and their role in the geodynamic evolution of the Pan-African chain of the Anti-Atlas, requires a multidisciplinary approach involving geological, petrographic, geochemical, metallogenetic,

and geophysical investigations. Accordingly, the main scientific objectives pursued in this work are primarily to:

- Characterize the petrography and lithogeochemistry of the host rocks.
- Date the mineralized porphyry and clarify its relationship with the Imourkhssen granite.
- Define the main mineral phases of the Imourkhssen porphyry and describe the associated mineral textures and structures to deduce the paragenetic sequence.
- Describe the various hydrothermal alterations associated with the mineralization.
- Establish an integrated correlation between the late-Ediacaran porphyry and epithermal deposits of the Saghro terrane (domain) and those observed in certain peri-Gondwanan terranes (Avalon), in order to highlight geological and metallogenetic similarities.
- Describe the structural characteristics of the Assarag region based on aeromagnetic data processing.
- Assess the structural control on the Imourkhssen mineralization.
- Integrate the genesis of the Imourkhssen porphyry within the global geodynamic context of the Pan-African evolution of the Anti-Atlas chain

Organization of the thesis manuscript

Beyond this introduction, which presents the philosophy and the research problem of the study, the approaches and methods employed, as well as the main objectives of this work, this doctoral manuscript is structured around four chapters, which are described in detail below:

- **Chapter I** is entitled "**Literature Review**." It is a bibliographic review devoted to the main characteristics of porphyry and epithermal deposits, highlighting their definitions, classifications, geodynamic contexts, associated hydrothermal alterations, genetic models, and the most relevant methods for their exploration. This chapter aims to familiarize readers with the subject matter under study and to situate the present study in its general context.
- **Chapter II** is entitled "**Regional Geological and Geodynamic Framework**." This chapter provides a summary of the major structural domains of Morocco, with special description of the lithostratigraphic and geodynamic framework of the Anti-Atlas, to place this research within its overall geological context. It also introduces the geographical location of the study area, providing the reader with a clear spatial reference and placing the area within its regional setting.

- **Chapter III** is entitled "**New Geochemical and Geochronological Constraints on the Genesis of the Imourkhssen Cu±Mo±Au±Ag Porphyry Deposit (Ouzellagh-Siroua Salient, Anti-Atlas, Morocco): Geodynamic and Metallogenic Implications**." It highlights a petrographic, geochemical, and geochronological study of the host rocks, supplemented by a metallogenic characterization of the Imourkhssen Cu±Mo±Au±Ag mineralization with the associated hydrothermal alterations.
- **Chapter IV** is entitled "**Aeromagnetic Data from The Assarag Area: Implications for The Imourkhssen Porphyry Style Mineralization**." It presents a series of geophysical treatments to describe the major structural features of the Assarag region and evaluate the structural control on the Imourkhssen mineralization.

The manuscript concludes with **General Conclusions**, which summarize the ideas drawn from all of the approaches used, providing a coherent understanding of the issue studied and achieving the objectives pursued.

Remark: It should be noted that the Abstract, General Introduction and Conclusions have been written in both French and English, in accordance with the submission requirements of the two partner universities (UQAT and UIZ) within the framework of this joint PhD program.

1. CHAPTER 1: LITERATURE REVIEW

1.1 Introduction

Widespread discussions and substantial research and exploration efforts in recent decades have revolved around the porphyry and epithermal deposits. This heightened interest is driven by their crucial significance and substantial impact on the worldwide production of copper, gold, silver, and molybdenum. Indeed, porphyry deposits provide 50 to 60% of world copper production and more than 95% of world molybdenum production (Sinclair, 2007), whilst the epithermal deposits are frequently mined due to their high concentration of gold and silver. Furthermore, numerous porphyry and epithermal deposits exhibit a clear spatial association, which attracted a considerable scientific attention and fueled ongoing debate about their relationship. This discussion often focuses on the link between the deeper porphyry deposits and shallower epithermal systems, fluid evolution and broader tectono-magmatic controls (Pei et al., 2020; Dilles and John, 2021).

In the other hand, copper-bearing porphyry systems are widely recognized and extensively documented across many metallogenic provinces of the world, but their origin and evolution remain poorly understood in many cases due to: (i) the diversity of their geodynamic contexts ranging from continental arcs to post-collisional environments, (ii) the marked variability in the nature of the host rocks, which influences the geochemical interactions between magmas and crustal lithologies; and (iii) the complex zoning patterns commonly observed, both in terms of paragenetic mineral successions and alteration assemblages, which record multi-stage magmatic-hydrothermal processes and can obscure the reconstruction of the system's temporal and spatial evolution (Sinclair, 2007; Sillitoe, 2010).

1.2 Porphyry copper deposit

1.2.1 Definition:

Porphyry copper deposits are defined as a low grade disseminated mineralization related to shallower, polyphase featured magmatic intrusions from 1 to 5 km, often having a porphyric texture (Jébrak and Marcoux, 2008). The concept is a long-standing one, first perceived in Australia in 1848, then developed by (Lindgren, 1933) in Chile and Arizona.

Sillitoe, (2010) described porphyry copper systems as large volumes (10 to 100 km^3) of hydrothermally altered rocks centered on porphyry copper stocks, and usually associated with

skarn, and high- and intermediate-sulfidation epithermal base and precious metal mineralization (**Figure 1.1**).

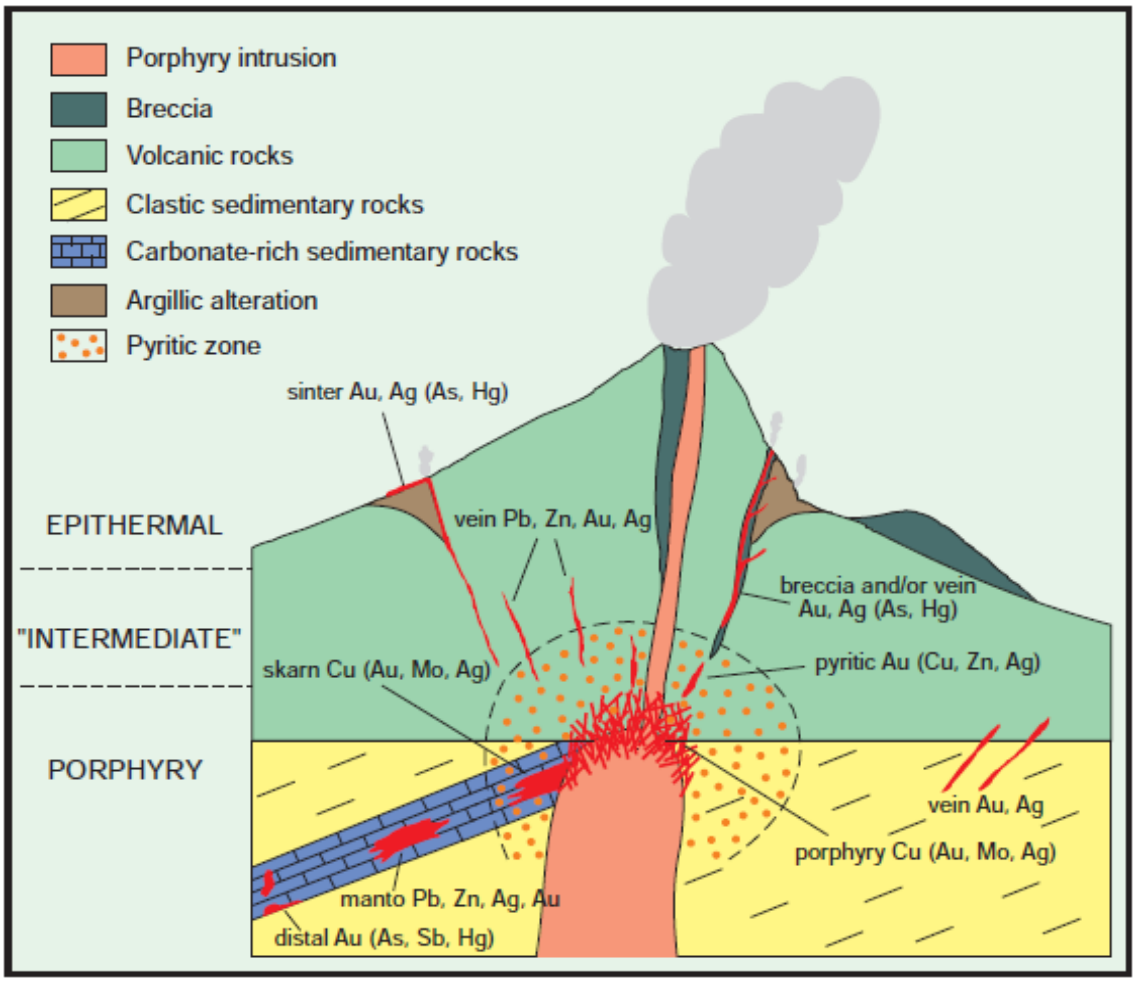

Figure 1.1
Porphyry copper mineralization and associated epithermal, skarn and base metal deposits (from Sinclair, 2007).

1.2.2 Geochemistry and tectonic setting:

The porphyry copper deposits are related to I-type magnetite series magmatism having medium K to high K calc-alkaline, shoshonitic or alkaline affiliation (Sillitoe, 1972; Cooke et al., 2014; Seedorf et al., 2005). This magmatism is generated frequently in magmatic arcs constructed above an active subduction zone at convergent plate margins (**Figure 1.2**; Sillitoe, 1972; Richards, 2003; Jébrak and Marcoux, 2008). Porphyry copper systems tend to occur in linear orogen-parallel belts and extending thousands of kilometers long, as represented by the Andes of western South America (Sillitoe and Perelló, 2005). However, several porphyry copper deposits are recognized in the framework of post-collisional context (Jébrak and Marcoux, 2008; Richards, 2009; Sillitoe, 2010; Cooke et al., 2014), and does not always require a direct

link to oceanic plate subduction. As an illustration, approximately 40% of giant and nearly 65% of intermediate sized porphyry Cu deposits in China are documented within post-collisional tectonic settings (Yang and Cooke, 2019). The Sungun porphyry copper and the Siah Kamar porphyry molybdenum deposits constitute additional representative examples of mineralization in the Qarachilar district, northwestern Iran. These ore systems are associated with I-type magmatism emplaced in the framework of a collisional episode that led to the closure of the Neo-Tethys Ocean between the Central Iranian and Arabian plates (Simmonds et al., 2019 and references therein).

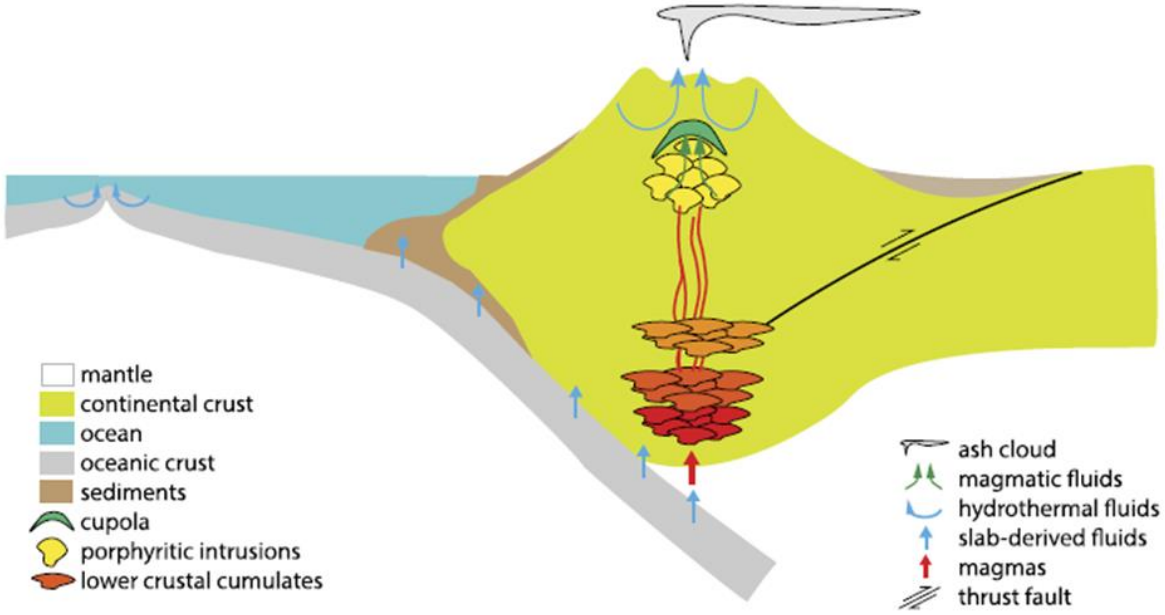

Figure 1.2
Schematic representation of an ocean-continent subduction zone (continental arc) where porphyry copper deposits represent shallow level intrusions (2–5km) in the crust (From Lee and Tang, 2020).

It is well established that magmatic rocks associated with mineralized systems can be classified according to their oxidation state into four main categories: strongly reduced, reduced, oxidized, and strongly oxidized (Champion and Heinemann, 1994). In this context, porphyry copper deposit, particularly those enriched in gold, are typically linked to oxidized magmatic intrusions characterized by abundant magnetite, occurring either as a primary igneous phase or as a secondary product formed during early potassic alteration (Clark, 2014 and references therein).

1.2.3 Spatial and temporal distribution:

A large number of the porphyry copper deposits concentrates in the peri-pacific belt (**Figure 1.3**), particularly in the Andean (Chili, Peru) and North America Cordillera (Colorado belt), where the three largest molybdenum porphyry deposits in the world are located (e.g., Climax, Urad-Henderson and Emmons Mounts; Carten et al., 1993; Sillitoe, 2008). Other porphyry deposits are distributed within Paleozoic orogens, in Central Asia and Eastern North America, and within Precambrian terranes (Sinclair, 2007).

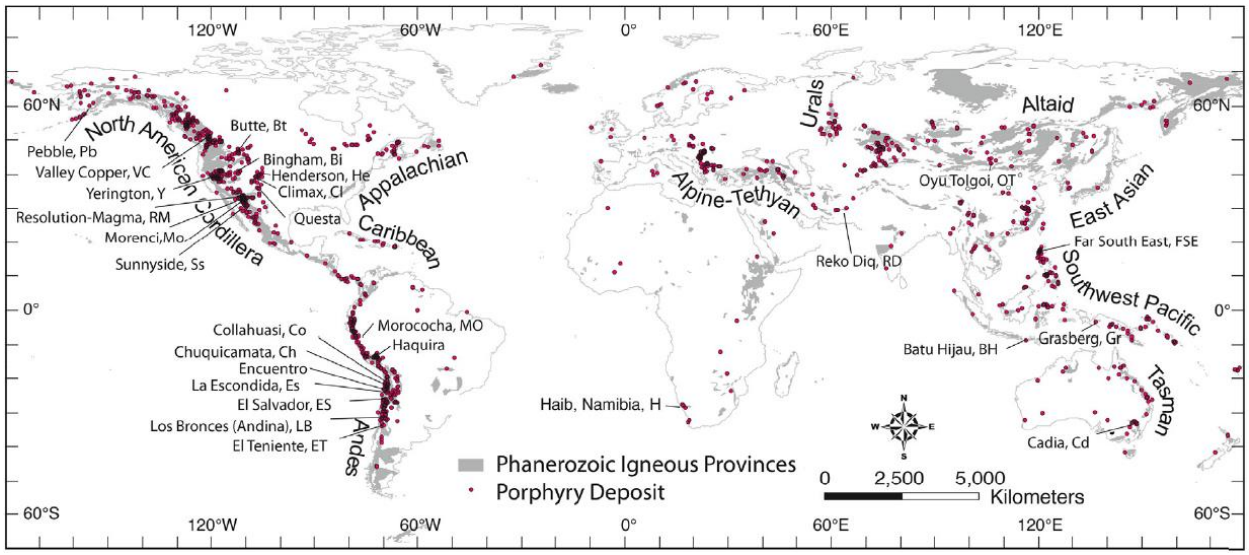

Figure 1.3
Map showing Phanerozoic igneous provinces with porphyry Cu-Mo-Au deposits (from Seedorff et al., 2005).

Porphyry deposits have been documented throughout the geological record, spanning from the Archean to the Holocene (**Figure 1.4**), which highlights their persistence as a fundamental expression of crust–mantle interaction and large-scale magmatic-hydrothermal processes. Despite this long temporal distribution, deposits of Precambrian age remain relatively rare in the geological record. This scarcity is generally attributed to the combined effects of prolonged erosion, tectonic reworking, metamorphism, and crustal recycling, which have either removed or significantly modified older systems, making their recognition more difficult (Sillitoe, 2010).

In contrast, most deposits of significant economic importance are predominantly Jurassic or younger, reflecting both their better preservation and more favorable tectonic and magmatic conditions for mineralization (Seedorff et al., 2005; Sinclair, 2007; Meng et al., 2021).

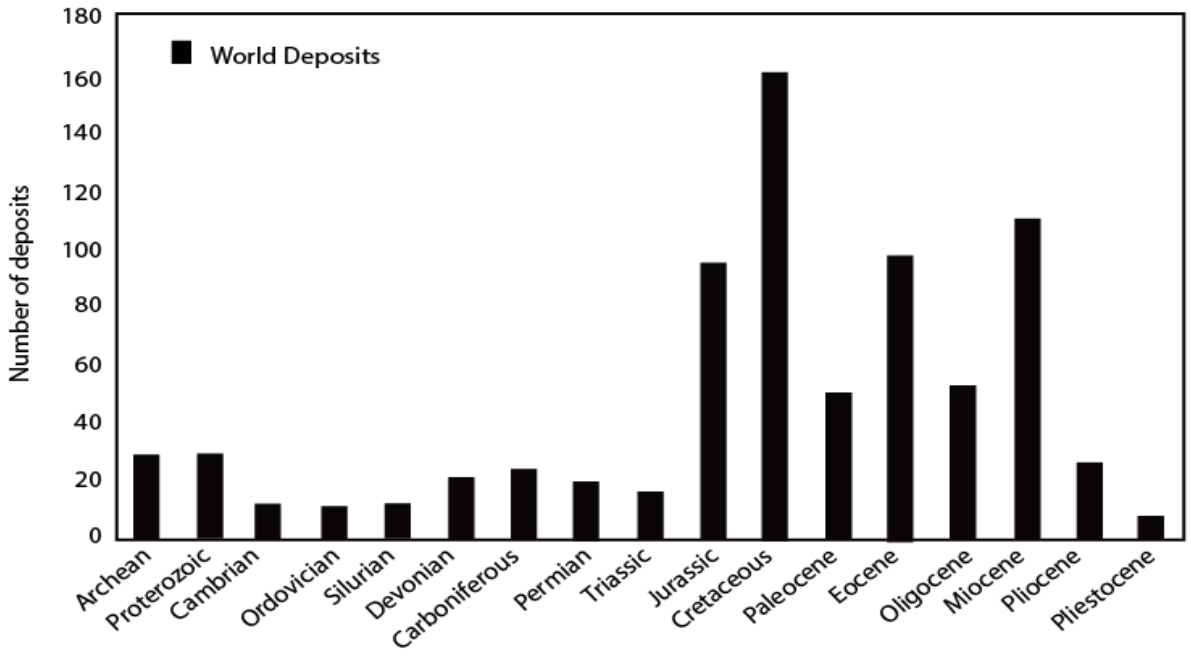

Figure 1.4
Age distribution of porphyry deposits (modified from Sinclair (2007) and references therein).

During Precambrian times, the progressive oxygenation of the atmosphere and oceans played a crucial role in the emergence of porphyry mineralization. The rise in environmental oxygen levels increased the availability of marine sulfate (SO_4^{2-}), which was essential for generating oxidized magmas in subduction settings. This transition favored the production of magmas capable of efficiently mobilizing and concentrating metals such as copper and molybdenum (**Figure 1.5**; Sillitoe, 2025).

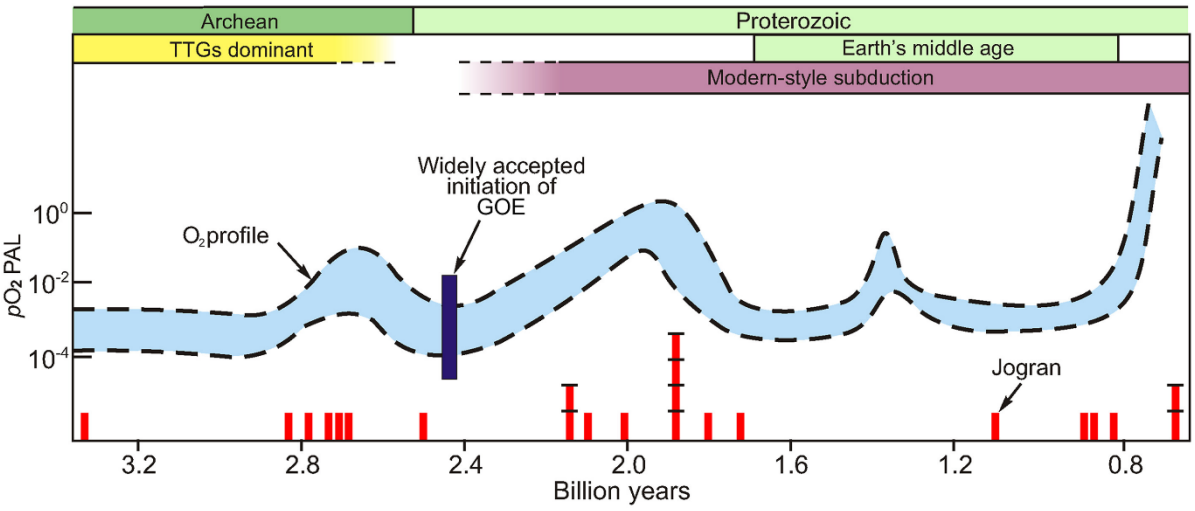

Figure 1.5
Ages of Precambrian porphyry Cu deposits and prospects (red bars) in relation to atmospheric O2 (Sillitoe, 2025).

1.2.4 Classification:

Based on the grade and the tonnage of copper, molybdenum and gold, a simple classification had established by Sinclair, (2007) as following:

Porphyry Cu deposit: Having Cu grades from 0.2% to more than 1%, Mo content from approximately 0.005 to about 0.03%, and Au from 0.004 to 0.35 g/t.

Porphyry Mo deposit: This porphyry type is divided by Sillitoe, (1980) in two sub-types; Climax-type and Endako-type which match with rift-related and subduction-related deposits respectively. Climax-type deposits are large and rich, as exemplified by the Climax deposit with resources of 907 Mt grading 0.24% Mo and the Henderson deposit in Colorado, grading 0.17% Mo. The Endako-type deposits have generally 0.15% Mo or less.

Chen et al, (2017) reported 69 Mo-only or Mo-dominated and 9 Cu-Mo deposits in Northeast China, that are subdivided in two types: Climax and Endako types according to their post-collisional or subduction zone context, respectively.

Porphyry W, Sn, and Ag deposits may also be considered, provided that their grade and tonnage are sufficient (Pearson et al., 1988; Sillitoe et al., 1975; Sinclair, 1995b). A continuum exists between porphyry Cu and porphyry Mo deposits, and also between W-Mo and W deposits, giving rise to a complex deposit style (Sinclair, 2007).

1.2.5 Hydrothermal alteration and mineralization:

The solidification and cooling of an oxidized, saturated sulphur and metal-rich plutonic intrusion led to pervasive circulation of fluids within the country rocks, and trigger different hydrothermal alteration overprints (Sillitoe, 2010). Porphyry Cu deposits display a distinctive, broad-scale alteration and mineralization zoning pattern (**Figure 1.6**), including from the core to the periphery; sodic-calcic, potassic, chlorite-sericite, serecitic, advanced argillic and propylitic alteration assemblages affecting several cubic kilometers of rocks (Lowell and Guilbert, 1970; Sillitoe, 2010 and reference therein).

Sodic-calcic alteration: It is the deeper alteration observed in the immediate wall rocks of many porphyry copper deposits (e.g., Copper Mountain and Ajax, Sinclair, 2007 and references therein). The sodic-calcic alteration zone is typically sulfide-poor and consists of albite, oligoclase, actinolite and magnetite without any economic potential (Sillitoe, 2010).

Potassic alteration: This alteration zone is the innermost alteration grading marginally and irregularly into propylitic alteration (Sillitoe, 2010). It is strongly mineralized and divided into an inner K-feldspar zone and an outer biotite zone. The inner potassic zone consists of quartz, magnetite and K-feldspar veins. The outer potassic zone corresponds to a biotite, K-feldspar, quartz, magnetite assemblage (Clark, 2014; Yang and Cooke, 2019). The mineralization is formed by two-phase fluids, including hypersaline liquid and low-density vapor exsolved from the shallower magmatic intrusion (Sillitoe, 2010 and references therein).

Chlorite-sericite alteration: Considered as the early stage of the phyllic alteration (Yang and Cooke, 2019), the chlorite-sericite alteration overprints the preexisting potassic alteration, especially in Cu-Au porphyry deposits (Sillitoe, 2010).

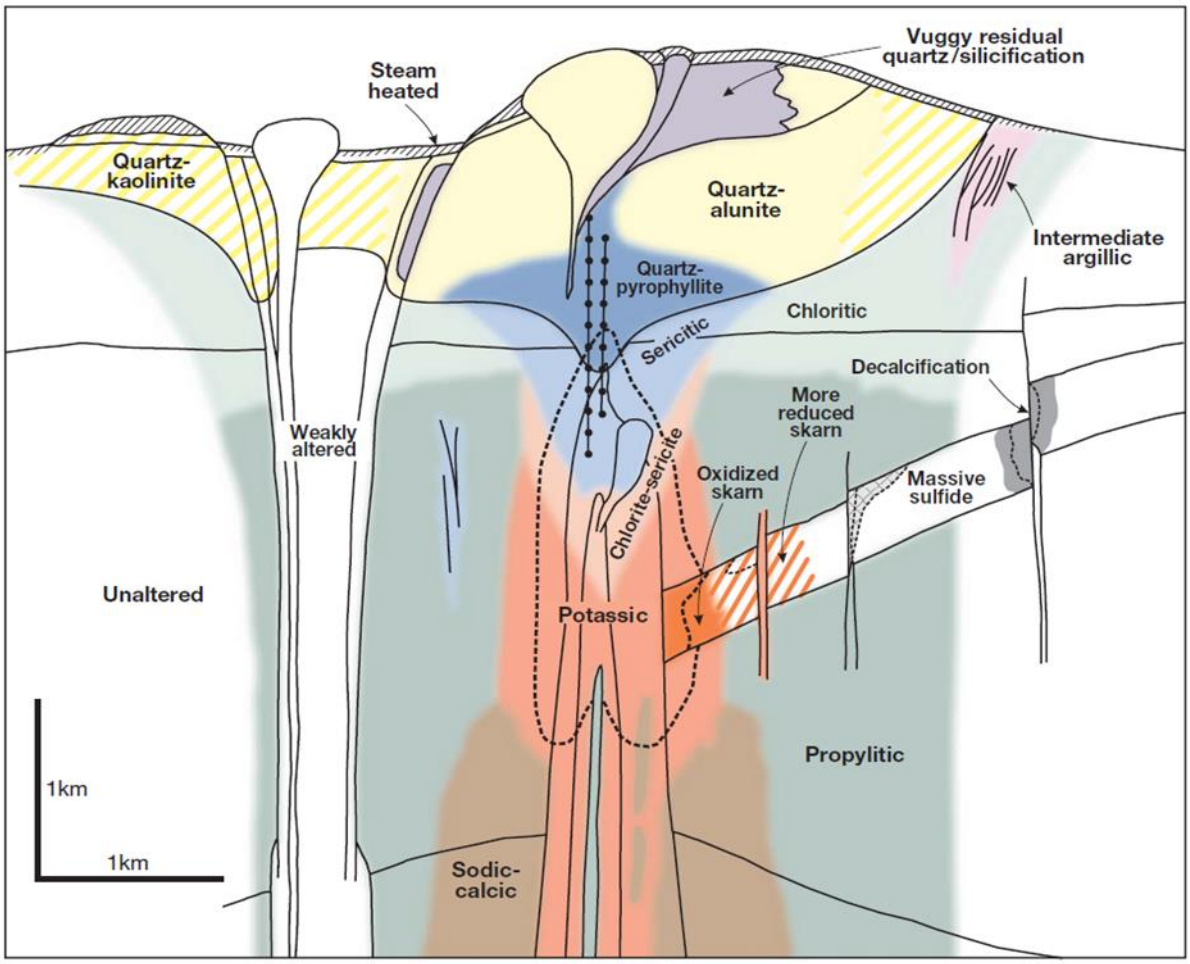

Figure 1.6
Generalized alteration-mineralization zoning pattern for telescoped porphyry Cu deposits (Sillitoe, 2010).

It results from the progressive cooling of the hydrothermal fluids in the form of a single liquid phase at temperatures below 350 °C, which lead to the transformation of mafic minerals to

chlorite, and plagioclase to sericite/illite and hematite (Sillitoe, 2010). This alteration is accompanied by pyrite and chalcopyrite mineralization, which are occasionally hosted within magmatic-hydrothermal breccia bodies (Sillitoe, 2010).

Phyllic or serecitic alteration: It is commonly known as phyllic or serecitic alteration overprinting and totally or partially destroying the potassic and chlorite-sericite assemblage, or generating annular zones separating those alterations from propylitic halos (Sillitoe, 2010). This type of alteration forms a pyrite-dominated shell with quartz and sericite minerals. It is also characterized by the development of chalcopyrite and high sulfidation assemblages including bornite, chalcocite and covellite with higher copper content (Brimhall, 1979; Sillitoe, 2010). In the field, this alteration manifests as bleached zones, as observed in extensive outcrops surrounding the Infiernillo Cu–(Mo) porphyry deposit in Argentina (Tommaso and Rubinstein, 2007).

Advanced argillic alteration: Argillic alteration zones overlay upper parts of porphyry copper deposits, and are generated by pervasive leaching due to pervasive circulation of acidic fluids formed by the mixing of hot magmatic gases with groundwater (e.g., Meyer and Hemley, 1967). Many advanced argillic lithocaps are vertically zoned, from quartz-pyrophyllite at depth to predominant quartz-alunite and residual quartz after extreme base leaching (Stoffregen, 1987), with a vuggy texture revealing the circulation of acidic fluids (Sillitoe, 2010; Hedenquist and Arribas, 2022).

Propylitic alteration: This distal part of alteration zones is formed due to the circulation of the interstitial meteoric water with residual hydrothermal fluids (e.g., Bingham; Bowman et al., 1987). This circulation is enabled by the heat flow generated during the protracted potassic alteration (Meyer and Hemley, 1967). The propylitic alteration consists of chlorite, carbonate, epidote, adularia and albite mineral assemblages (Lowell and Guilbert, 1970; Sillitoe, 2010). This alteration zone coincides with Zn-Pb-Ag ± Mn anomalies, and the presence of the sphalerite and galena (Sillitoe, 2010).

1.3 Epithermal deposits:

1.3.1 Definition and Classification:

Epithermal deposits were first defined as a large range of precious-metal, base-metal, mercury and stibnite deposits formed from aqueous fluids derived from magmatic intrusions at relatively low temperatures (200 °C) and moderate pressures (Lindgren, 1922).

The distinction between epithermal deposits is established regarding their related alteration assemblages. Heald et al., (1987) divided the epithermal deposits into acid-sulphate and adularia-sericite types. Recent studies subdivide epithermal systems into three end members: high-, intermediate-, and low-sulfidation based on their geological environments, the geochemistry of mineralizing fluids, the nature of hydrothermal alterations, and the gangue and ore mineralogy (White, and Hedenquist, 1995; Hedenquist et al., 2000; Sillitoe and Hedenquist, 2003; Dilles and John 2020; **Figure 1.7**).

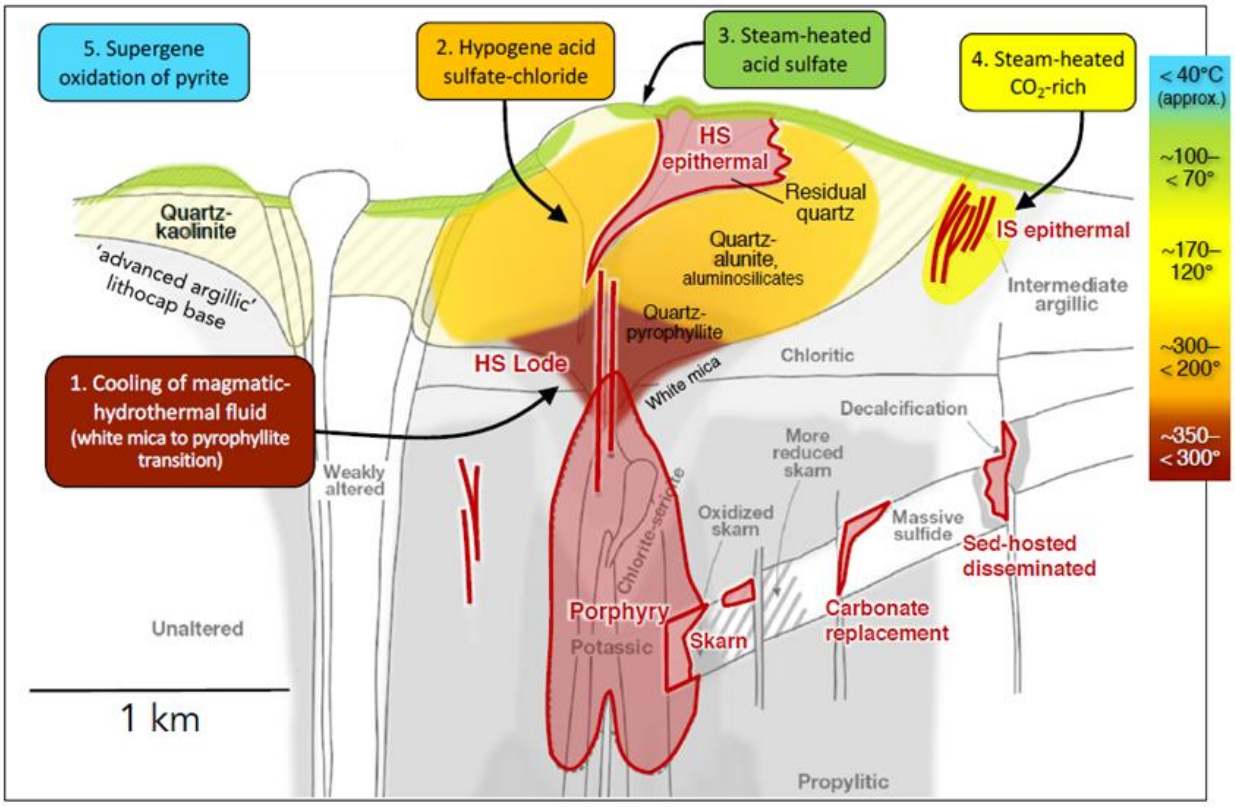

Figure 1.7
Schematic hydrothermal alteration patterns of HS and IS epithermal deposits (modified from Sillitoe, 2010). HS = high sulfidation, IS = intermediate sulfidation.

Low sulfidation epithermal deposits form in hydrothermal environments analogous of geothermal springs, where reduced (H_2S-rich) neutral pH hydrothermal fluids are encountered (White and Hedenquist, 1995; Arribas, 1995). Those deposits are characterized by specific alteration and mineral assemblages, including steam-heated acid-sulfate alteration, along with associations of pyrite, pyrrhotite, arsenopyrite and high Fe sphalerite (Arribas, 1995; Hedenquist et al., 2000). This mineralization is mostly linked with quartz-adularia-calcite/sericite assemblages (Hedenquist et al., 2000). The genesis of high sulfidation (HS) deposits occurs in oxidized high acidic hydrothermal environments characterized by alteration

minerals such as alunite, kaolinite, and pyrophyllite. These environments also feature diagnostic high-sulfidation minerals, including enargite–luzonite, and covellite (**Figure 1.7;** Arribas, 1995; Hedenquist et al., 2000). Those deposits were the object of several evaluations and discussions in order to assess their probable relationship with the underlying or adjacent porphyry deposits (Heald, 1987; Hedenquist et al., 2000).

1.3.2 Hydrothermal alteration:

The genesis of epithermal ore deposits is triggered by the cooling of a shallow intrusion where a hydrothermal system is developed at depths of less than 500m (Hedenquist and Arribas, 2022). The spatial distribution of alteration patterns reflects efficient degassing of oxidized magmatic vapor with limited interaction or dilution with groundwater, a process most commonly associated with fractured volcanic domes, caldera structures or diatreme-related faults (Arribas, 1995). The latter represent a prevalent volcanic characteristic, and are closely linked to epithermal ore formation both spatially and temporally (Sillitoe and Hedenquist, 2003; Dilles and John, 2020).

In high-sulfidation deposits, the separated magmatic vapor, upon reaching shallow depths, is either discharged as fumaroles or absorbed by groundwater, where it condenses by aqueous redox disproportionation of SO_2 to H_2SO_4 and HCl (Arribas, 1995; Hedenquist and Arribas, 2022). The H_2SO_{4-} and HCl-rich solution with very acidic pH conditions (i.e., 1-1.5) allows rock dissolution due to the low solubility of Al and Fe, while SiO_2 remains, resulting in a vuggy texture (**Figure 1.8;** Hedenquist and Arribas, 2022). Rock dissolution increases the acidity of hydrothermal fluids, leading to the formation of quartz-alunite-kaolinite assemblages typical of advanced argillic alteration (Arribas, 1995; Dilles and John,, 2020; Hedenquist and Arribas 2022).

The boiling of the hydrothermal fluid generates vapor containing H2S and CO2, which condenses above the water table conditions to evolve into a steam-heated acid solution (Hedenquist and Arribas, 2022). In this framework, kaolinite and alunite overprints previous mineral assemblages in addition to amorphous quartz (Hedenquist and Arribas, 2022). Below the water table, this steam-heated acidic solution instead forms kaolinite, Fe-Mn carbonates, and clay, drawing an intermediate argillic alteration pattern (Hedenquist and Arribas, 2022).

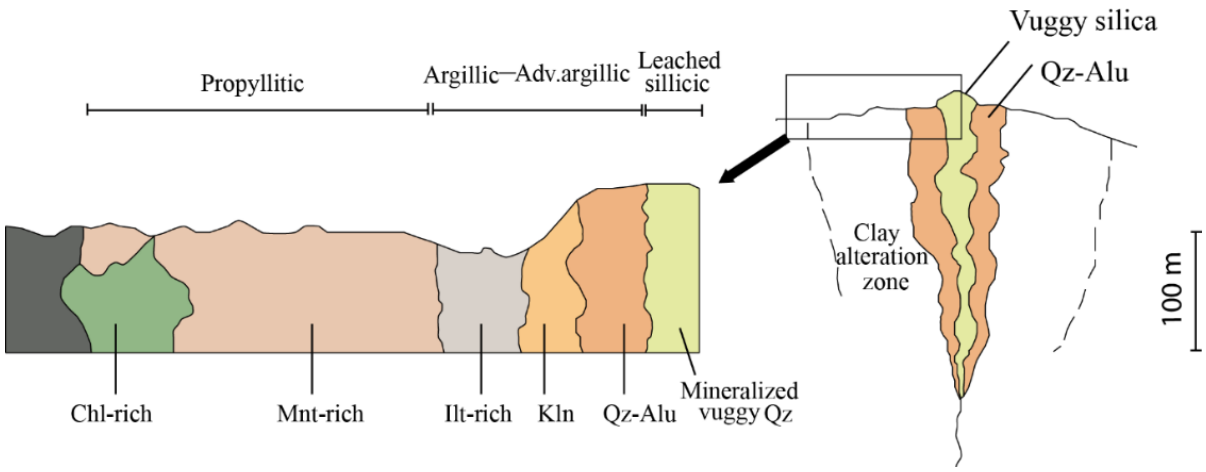

Figure 1.8
Diagram left (simplified from Steven and Ratte, 1960) shows schematic outward zonation from a subvertical mineralized body shown at right (modified after Stoffregen, 1987).

1.3.3 Genetic model:

Knowing that the genesis of high-sulfidation deposits requires the shallower emplacement (a few kilometers) of an oxidized, intermediate calc-alkaline magma (Arribas, 1995; Sillitoe and Hedenquist, 2003; Dilles and John, 2020; Hedenquist and Arribas, 2022), the cooling of such magma leads to the exsolution of a fluid phase that concentrates ore-forming metal (Arribas, 1995). The fluid phase subsequently separates into a low-salinity vapor and hypersaline liquid (**Figure 1.9**; Hedenquist and Lowenstern, 1994).

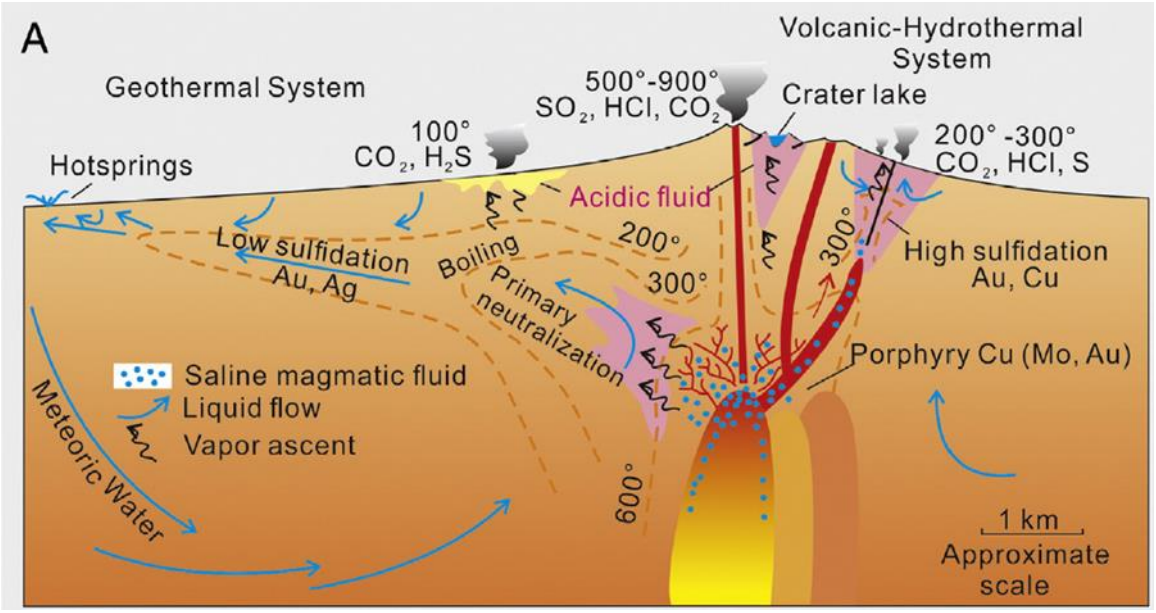

Figure 1.9
Spatial and genetic relationship between epithermal deposits and underlying porphyry systems (modified after Hedenquist and Lowenstern, 1994).

The main effective process involved in the genesis of epithermal deposits is vapor boiling, which limits temperatures to a maximum of 300 °C and typically occurs at depths of about 700m below the water table (Hedenquist et al., 2000). Nevertheless, many epithermal deposits have been shown to form at depths below 1000 m (Hedenquist et al., 2000). Boiling occurs during fluid ascent, causing changes in the geochemical composition of the fluid and promoting the precipitation of bi-sulfide-complexed metals such as gold (Lindgren, 1933; Hedenquist et al., 2000; Dilles and John, 2020). This process, along with the concomitant rapid cooling and sharp depressurization, also contributes to the formation of gangue minerals and triggers the circulation of steam-heated waters. These fluids, in turn, develop characteristic argillic and advanced argillic halo patterns (Hedenquist et al., 2000).

Indeed, fluids from various sources contribute to the genesis of epithermal ore deposits, including variable proportions of magmatic and evolved meteoric waters (Bodnar et al., 2013). The meteoric-magmatic mixing trends are highlighted by oxygen and hydrogen isotopic compositions during three stages of alteration/ mineralization in the Julcani epithermal deposits, Peru (e.g., Magmatic dominated early stage of acid-sulfate alteration, main ore-stage to meteoric-dominated late-stage; Arribas, 1995 and references therein). The precious metal-bearing minerals can be sourced predominately from oxidized magmatic fluids, whilst the base metal sulfide association could be derived from deep leaching of crustal rocks involving a meteoric component (Camprubí et al., 2006).

Intermediate-sulfidation deposits typically exhibit high silver concentrations, with gold contents and Au/Ag ratios, and yield recoverable amounts of lead and zinc (Dilles and John, 2020).

1.4 Exploration of porphyry and epithermal ore deposits:

A variety of geophysical tools are employed to generate reliable models and delineate the main subsurface geological and structural features. These features play a crucial role in mapping the pathways of hydrothermal ore-bearing fluids and therefore contribute significantly in the identification of prospective mineralized zones.

1.4.1 Porphyry ore deposit exploration

Magnetic effects of hydrothermal alteration and implication for magnetic signatures:

Taking into consideration the different alteration patterns described above, each alteration type exerts a specific influence on magnetite, either promoting its formation or causing its destruction. Clark, (2014) reviewed the effects of hydrothermal alteration on the magnetic properties and geophysical signatures of porphyry copper deposits. Since these magnetic anomalies reflect lithology, metamorphic and alteration zones, and tectonic structures that control ore deposits, they can provide valuable insights into specific types of mineralized systems, such as porphyry deposits, especially Au-rich porphyry deposits (Clark, 2014).

Therefore, developing predictive magnetic anomaly models requires an understanding of magnetic petrology, which is itself influenced by several geological factors, including tectonic setting, magma type, lithology and geometry of host rocks, depth of emplacement and subsequent erosion level, post-emplacement faulting and tilting and remanence effects (Clark, 2014). Furthermore, redox or acid-base reactions can produce large changes in magnetic proprieties, particularly through the transformation of magnetite and hematite via Fe metasomatism or Fe-leaching alteration, as illustrated below: (Clark, 2014 and references therein).

$$Fe_2O_3 + H_2O + Fe^{2+} \longleftrightarrow Fe_3O + 2H^+$$

Clark (2014) also assessed the impact of host-rock composition on magnetic anomalies through the relative contrast in magnetic proprieties. The contrast increases as the host rocks are weakly magnetic, hence a high reduce to the pole (RTP). Conversely, strongly magnetic host rocks generate low reduced to the pole.

Before discussing the general magnetic features of porphyry copper deposit, it is very important to identify the probable effect of magnetic remanence. The latter could reflect a multicomponent attribute by overprinting normal and reverse segments during the magmatic-hydrothermal evolution of a mineralized porphyry systems (Clark, 2014) spanning from~100,000 to several million years (Sillitoe, 2010). The reported magnetic remanence is mainly influenced by magnetite or hematite (Robert et al., 2017 and references therein).

For porphyry copper deposits, alteration products affect the magnetic signal, yielding positive anomalies where magnetite is produced (magnetite-constructive alteration) and weak to negative anomalies where magnetite is destroyed (magnetite-destructive alteration). The resulting response is also influenced by the composition of the protolith. (Clark, 2014). The

mineralogical characteristics of each class are shown in **Table 1.1** (from Champion and Heinemann, 1994).

Table 1.1
Characteristic mineralogy for oxidation classes of igneous rocks (Champion and Heinemann, 1994).

Oxidation state category	*Mineralogy*
Strongly oxidised	Magnetite + primary sphene ± hematite
Oxidised	Magnetite ± ilmenite (high Fe3+ or Mn)
Reduced	Ilmenite without magnetite
Strongly reduced	Ilmenite (low Fe3+ and Mn) + pyrrhotite; magnetite absent

Therefore, Clark, (2014) summarized the magnetic effects of porphyry copper–associated alteration patterns, as presented in **Table 1.2**. Overall, potassic alteration is the only hydrothermal process that produces magnetite, particularly within mafic to intermediate rocks. Meanwhile, all the remaining alterations are either partially or totally magnetite- destructive.

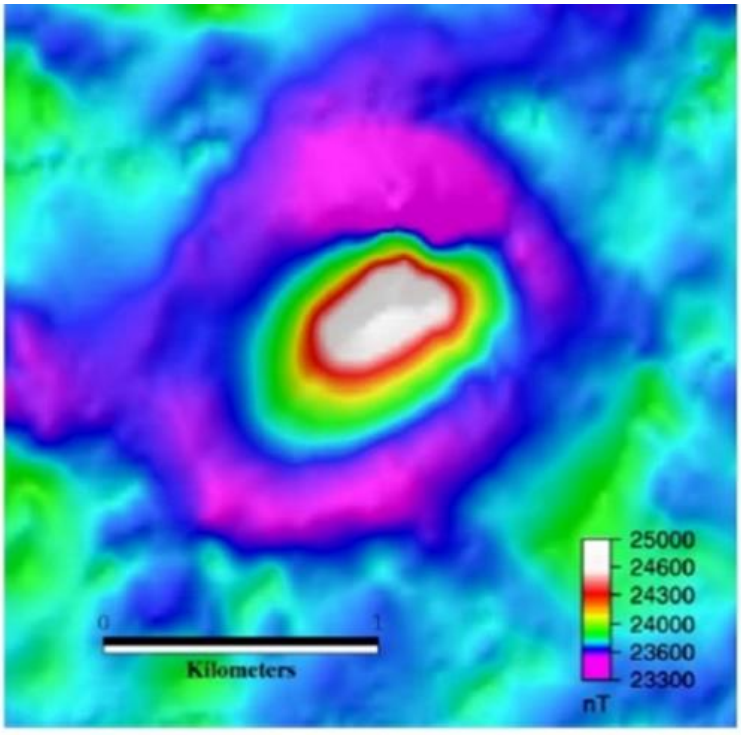

Figure 1.10
RTP magnetic anomaly pattern over the Bajo de la Alumbrera Cu–Au porphyry deposit, Catamarca, Argentina (Clark, 2014).

Table 1.2
Characteristic mineral assemblages of the main alteration types in porphyry systems (Clark, 2014).

Alteration type	*Characteristic assemblage [magnetic effects]*
Potassic (K-silicate)	K-feldspar and/or biotite, plus one or more of: sericite, chlorite and quartz (e.g., in the interior zone of porphyry copper deposits) [Usually magnetite-producing (e.g., gold-rich porphyry copper deposits); minor magnetite addition in felsic rocks; often associated with early quartz–magnetite–(amphibole) veins. Sometimes magnetite-destructive in high sulphidation systems.]
Phyllic (Serecitic)	Quartz–sericite–pyrite–chlorite (e.g., in large halos around porphyry copper deposits) [Magnetite-destructive (pyrite + hematite produced); decreased k]
Intermediate Argillic	Smectite and kaolinite, commonly replacing plagioclase (e.g., variably developed zone outside serecitic zone in some porphyry coppers) [magnetite-destructive; decreased k]
Propylitic	Albite (or K-feldspar in potassic rocks), chlorite and epidote group minerals; with only minor change in bulk composition (e.g., outermost alteration zone of porphyry copper deposits) [strong: Partially to totally magnetite destructive (Fe in pyrite, hematite, epidote, chlorite, actinolite), decreased k] [weak: magnetite stable, k unchanged]
Albitic	Na-rich plagioclase + epidote and other propylitic minerals; with substantial addition of Na [magnetite-destructive, decreased k]
Sodic–calcic	Sodic feldspar and epidote ± actinolite ± chlorite (e.g., adjacent to intrusion at depth, beneath certain porphyry copper deposits) [magnetite-destructive, decreased k]
Advanced Argillic	Quartz plus one or more of: kaolinite, dickite, pyrophyllite, diaspore, pyrite, alunite, zunyite, topaz (e.g., in epithermal systems that may overlie porphyry systems) [magnetite-destructive, decreased k]

The potassic alteration is particularly significant due to its strong mineralization, especially in Au-rich (≥0.4 g/t) porphyry copper systems (Sillitoe, 2010 and references therein). It is typically characterized by concentric, near-circular zones exhibiting a positive magnetic anomaly (Holden et al., 2011).

For example, the Bajo de la Alumbrera Cu–Au deposit in Argentina is hosted in a relatively homogeneous rock mass, without significant tilting or faulting (Hoschke, 2011). As a result, its reduced-to-pole (RTP) magnetic pattern displays a central high that coincides with the potassic

alteration, encircled by an annular magnetic low corresponding to areas where magnetite has been destroyed by subsequent alteration processes (**Figure 1.10**; Clark, 2014).

Macnae, (1995) assumes that the intrusion itself and the inner alteration (potassic alteration) are usually associated with positive anomalies, while the outer alteration zones are much less magnetic. Nevertheless, some authors argue that potassic alteration could exhibit either high or low magnetic susceptibility, depending on whether secondary magnetite is formed during alteration, or primary magnetite is destroyed (Seedorff et al., 2005).

Further studies by Byrne et al. (2019) explored the relationship between variation in magnetic susceptibility and weathered rocks associated with the porphyry system of the Highland Valley Copper district (HVC). The information derived from modeling of outcrop magnetic susceptibility data assumes geometric mean magnetic susceptibility and the coefficient of variation. This coefficient defined as a geometric factor to describe the dispersion of lognormal data (Kirkwood, 1979) and to explore its correlation of the vein frequency and altered rocks. Typically, mapped veins and halos generally overlaps with the large coefficient of variation anomaly surrounding the porphyry centers. Indeed, this coefficient of variation has a positive correlation with altered rocks, and negative correlation with the mean magnetic susceptibility (Byrne et al., 2019). In addition, Byrne et al., (2016) described large footprints of hydrothermally altered rocks around Cu-Fe-sulfide mineralization, to be huge volumes of rocks exhibiting high coefficient of variation (>0.3) and a magnetic susceptibility low. This magnetic susceptibility led to map rocky weathered outcrops related with mineralized systems (Byrne et al., 2019).

Aeromagnetic investigations coupled with radiometric data: For the purpose of mapping structures, lithology and hydrothermal alteration zones, aeromagnetic and radiometric investigation are launched not only to enhance the understanding of subsurface structures, but also to provide valuable insights into the potential presence of underlying porphyry-related mineralization, thereby contributing to more targeted exploration strategies. In this framework, Elkhateeb and Abdellatif (2018) examined the potential of gold mineralization in the central eastern part of the Egyptian desert. Those investigations are carried out using some enhancement techniques for data processing and lineaments mapping, such as the first vertical derivative and the center for exploration targeting filters. In addition, the radiometric data treatment allowed the assessment of potassium, thorium and uranium distributions, as well as the calculation of K/eTh ratios. The entire components lead to delineate altered outcrops

characterized by low magnetic intensity, high potassium content and high K/eTh ratios, highlighted on the map as white areas (**Figure 1.11**).

Therefore, aeromagnetic and radiometric methods are valuable tools for exploring mineralization and are widely applied in gold-bearing systems (Menezes et al., 2022). Shives et al. (1997) underline the value of gamma-ray spectrometry in porphyry exploration, reporting several Canadian deposits (e.g., Casino Cu–Au–Mo), in which mineralized potassic alteration is marked by anomalous potassium and low eTh/K ratios. The resulting ratios reflect the remaining thorium, which does not accompany potassium during alteration process (Shives et al., 1995).

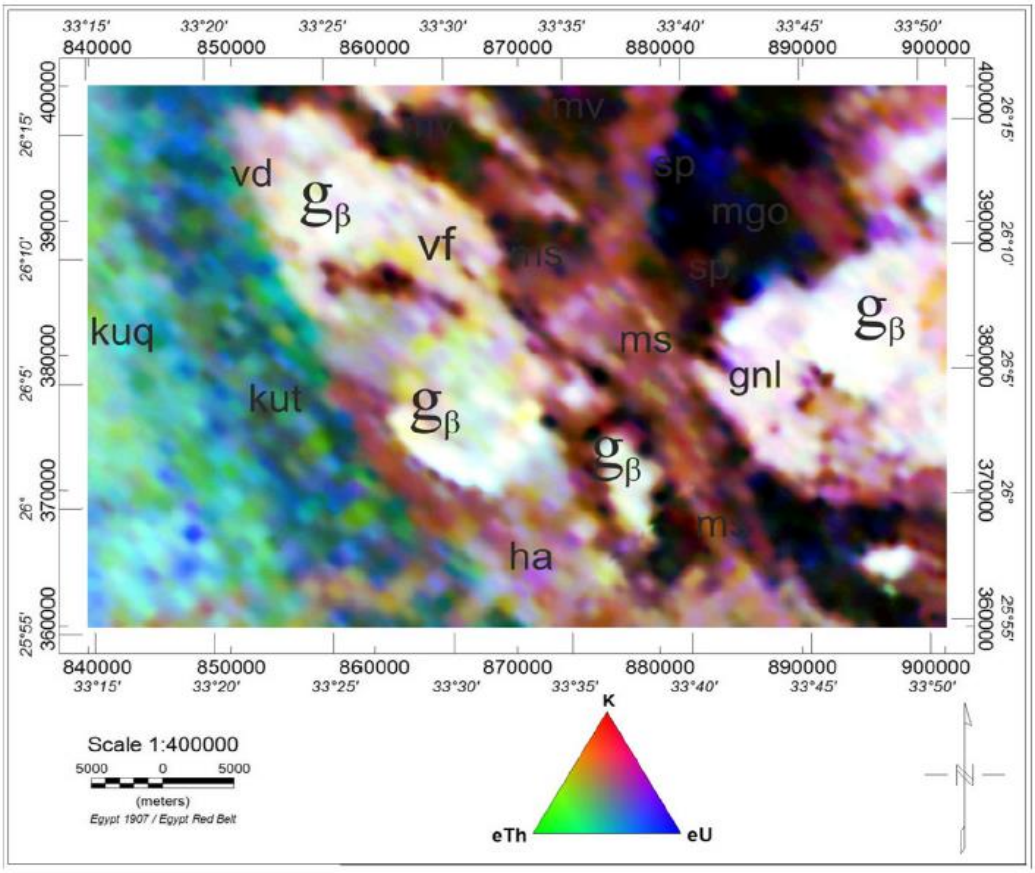

Figure 1.11
Radiometric ternary map of a part of the Egyptian central eastern Desert (Elkhateeb and Abdellatif, 2018).

In the case of weak physical proprieties contrast, the traditional geophysical studies remain inadequate for producing meaningful physical models (Montsion et al., 2021). For example, the signal of magnetic susceptibility can be masked by nearby strongly magnetic units (e.g., Fe-rich units like magnetite-bearing dikes or banded iron formations), or are attenuated by the

overburden (e.g., Vallée et al., 2019). Thus, high pass filtering techniques are required to mitigate those effect, namely the Phase Preserving Dynamic Range Compression (PPDRC) from the Grid Analysis tool in the Oasis MontajTM software (Holden et al., 2012)

Application of ASTER data for exploring porphyry copper deposit: Satellite imagery is a powerful tool for identifying hydrothermal alteration zones, especially in porphyry copper and epithermal gold systems. The Advanced Spaceborne Thermal Emission and Reflection "ASTER" sensor offers advanced remote-sensing capabilities for exploration (Pour and Hashim 2012), with reliable geological models relying on optimized image-processing techniques.

The ASTER SWIR spectral bands allow to the identification of hydrothermal alteration zones associated with porphyry copper deposit, discriminated by different virtue of their spectral absorption features. Alimohammadi et al. (2015) reviewed the important role of logical operator algorithms for detecting particular mineral assemblages in hydrothermal alteration zone in the Cu ± Mo ± Au Urumieh–Dokhtar magmatic belt of Iran. They emphasized very convincingly the performance of ASTER imagery for the distribution of hypogene alteration zones (i.e., phyllic, argillic, propylitic and silicic) associated with porphyry Cu ± Mo ± Au deposit in the regional and district scale. Yousefi et al., (2021) suggest a sequence of modeling operators for the detection of hydrothermal alteration in Zefreh porphyry copper, Iran. Their work demonstrates the applicability of machine learning algorithms to ASTER data and pointed out their usefulness for exploration worldwide.

1.4.2 Epithermal ore deposits exploration:

Several authors suggest advanced argillic alteration as a key exploration target for epithermal ore deposits (Arribas, 1995; Hedenquist et al., 2000; Hedenquist and Arribas, 2022). Consequently, Uncovering the concealed footprints of alteration is crucial for successful epithermal prospecting.

Geophysic investigations: Given that high-grade epithermal deposits, whether low- or high-sulfidations, are frequently fracture controlled (Hedenquist et al., 2000), magnetic methods are particularly valuable as they delineate geological boundaries and tectonic structures. Consequently, they serve as an effective tool in the exploration of epithermal systems. In addition, airborne magnetic surveys not only detect magnetic responses associated with magnetite-bearing minerals in porphyry deposits (Clark, 2014), but reveal as well the subdued magnetic signatures produced by hydrothermal alteration, as commonly observed during the

development of epithermal systems (Clark, 2014; Hedenquist et al., 2000). Moreover, epithermal ore deposits may also exhibit weak magnetic signatures due to magnetic destructive alterations (i.e., advanced argillic alteration; Clark, 2014).

Electric approaches are also used. The vuggy quartz is electrical resistant in dry conditions, conversely to conductive clays in argillic and advanced argillic halos. Both of the features could be detected by resistivity and induced polarization methods (Hedenquist et al., 2000).

Synergy between geophysics and satellite imagery: The synergy between geophysics and satellite imagery provides a powerful framework for mineral exploration, as each method offers complementary insights into subsurface and surface features. Recent studies by Abbassi et al., (2022) proposed new geophysical processing and machine learning targeting through the spectral feature subset selection (SFSS) algorithm. Those investigations were treated through the synergy between the independent component analysis (ICA) and continuous wavelet transformation (CWT), and allowed to learn and make predictions of the lithotype and Au grade of the Au-Ag epithermal system in British Columbia, Canada.

In the present study, this integrated approach is applied to the Imourkhssen Cu-Mo-Au-Ag Porphyry deposit to improve the understanding of the structural architecture of the study area. The complimentary datasets highlight the main structural features controlling the investigated system, thereby strengthening the geological interpretation and the potential of exploration (see aeromagnetic data section).

1.5 Porphyry-Epithermal relationship:

Discussing the probable genetic connection between porphyry and epithermal deposits require a well understanding of the metallogenic process of their formation, including metals sources and sulfide conditions genesis (Ransome, 1907). The latter proceeds through a progressive evolution of the magmatic–hydrothermal system.

Indeed, hydrothermal systems are fueled by magmatic intrusions leading to the convection paths of a large proportion of Earth's heat to the surface. In the meantime, fluids, derived from different sources, scavenge metals producing specific hydrothermal alteration and mineralization styles, such as porphyry, epithermal, skarn, and others types of ore deposits (**Figure 1.12;** Hedenquist and Lowenstern, 1994).

At high temperature conditions, the hydrothermal fluids consist of low to moderate salinity liquids. During their ascent, these liquids undergo phase separation into hypersaline liquid and vapor phase, generating potassic alteration along with low sulfidation-state porphyry Cu ± Au mineralization. Whilst, the low-pressure vapor escape upward to produce generally advanced argillic alteration (Sillitoe, 2010) and different alteration patterns described for epithermal ore deposits. As a consequence, the porphyry-epithermal style mineralization was widely debated (e.g., Heald, 1987), and several examples of epithermal deposits are suggested to be associated with porphyry buried ones, (i.e., the hope Brook high sulfidation epithermal gold deposit; Dubé et al., 1998).

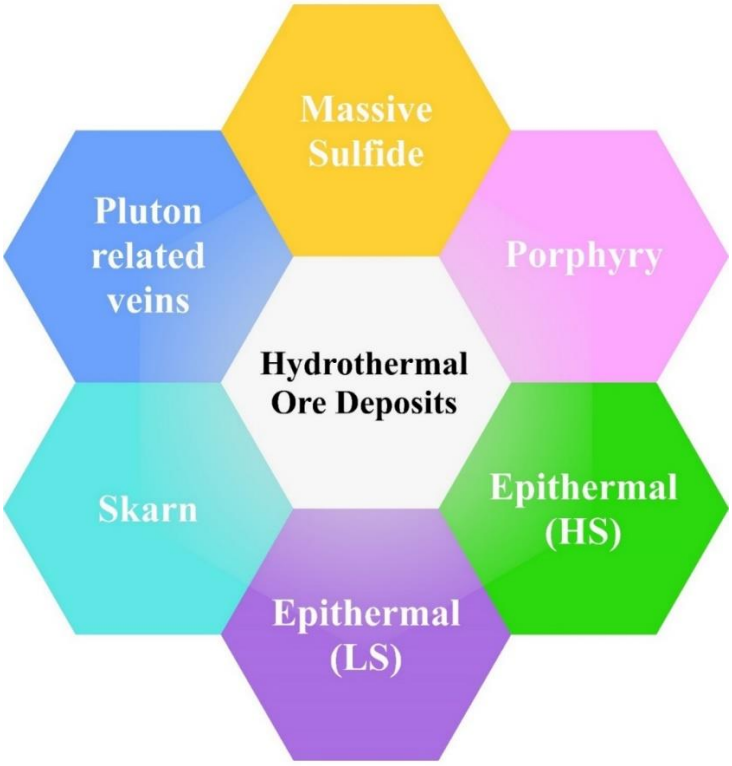

Figure 1.12
Representative hydrothermal ore deposits associated with subduction-related magmatism (modified from Hedenquist and Lowenstern, 1994).

In the discussion section, particular emphasis is placed on examining the relationships between several well-documented ore deposits worldwide and those occurring within the Saghro terrane (domain) as defined by Schulte et al. (2022). This comparative approach not only highlights similarities and differences in their geological settings, but also provides insights into the geodynamic context that governed their formation.

2. CHAPTER 2: GEOLOGICAL AND GEODYNAMIC FRAMEWORK

2.1 Geological overview

Morocco is a mountainous country located in the northwesternmost part of Africa. The country possesses coastlines along both the Mediterranean Sea in the north and the Atlantic Ocean in the west. Geologically, Morocco is subdivided into five main structural domains (**Figure 2.1**): ***(i) The Rif domain,*** the youngest orogenic system which belongs to the Alpine cycle and is, subdivided into three major domains: the Internal Domain, the Flysch Domain, and the External Domain (Frizon de Lamotte et al., 2008). This belt is characterized by a well-defined arcuate belt (Lonergan and White, 1997) developed between the colliding African and Eurasian plates during the closure of Tethys Ocean (Platt et al., 2013 and references therein). Therefore, the Rifan Domain embodies a key segment of the collisional system between Africa and Eurasia recording a complex tectonic process, including crustal shortening, deformation, and rotation during the Miocene epoch (Lonergan and White, 1997).

(ii) The Atlas system, comprising the High and Middle Atlas, is likewise associated with the Alpine orogenic cycle. However, unlike typical collisional belts, the Atlas Mountains represent an intracontinental orogenic chain that developed upon a continental crust (Frizon de Lamotte et al., 2008). The Atlas system comprises the NE-trending Middle Atlas and the E–ENE-oriented High Atlas chain, which is bounded to the south by a major structural feature known as the South Atlas Fault (SAF) (Frizon de Lamotte et al., 2008; Alvaro et al., 2014b). Nevertheless, the High Atlas incorporates segments of the Late Ediacaran-Cambrian basement, which are exposed in the Ouzellagh–Siroua salient (Michard et al., 2023).

(iii) The Meseta chain and the Ouled Dlim massif belt, are formed during the Variscan (Hercynian) orogeny that developed during the Late Paleozoic times (Michard et al., 2008). Comprising the Eastern Meseta, the Western Meseta, and the Coastal Block, the Meseta chain was formed through the convergence and final collision of Gondwana with Laurussia, giving rise to widespread deformation, metamorphism, and magmatism (Simancas et al., 2009). These belts represent the suture zones where fragments of Gondwanan and Laurussian crust were welded together, preserving evidence of late Paleozoic plate tectonic processes (Michard et al., 2010).

(iv) The Anti-Atlas exposes a complex mosaic of variably shaped and sized inliers, formed by the Precambrian Eburnean basement, and overlain by a Neoproterozoic to Paleozoic cover (Gasquet et al., 2008).

To the south, *(v) the Saharian domain* is represented by the Oulad Dlim Massif and the Reguibat Shield, which together constitute a critical segment of the northern West African Craton (WAC), and provide insights into both Precambrian continental evolution and the tectono-stratigraphic framework of North Africa (Ennih and Liégeois et al., 2001).

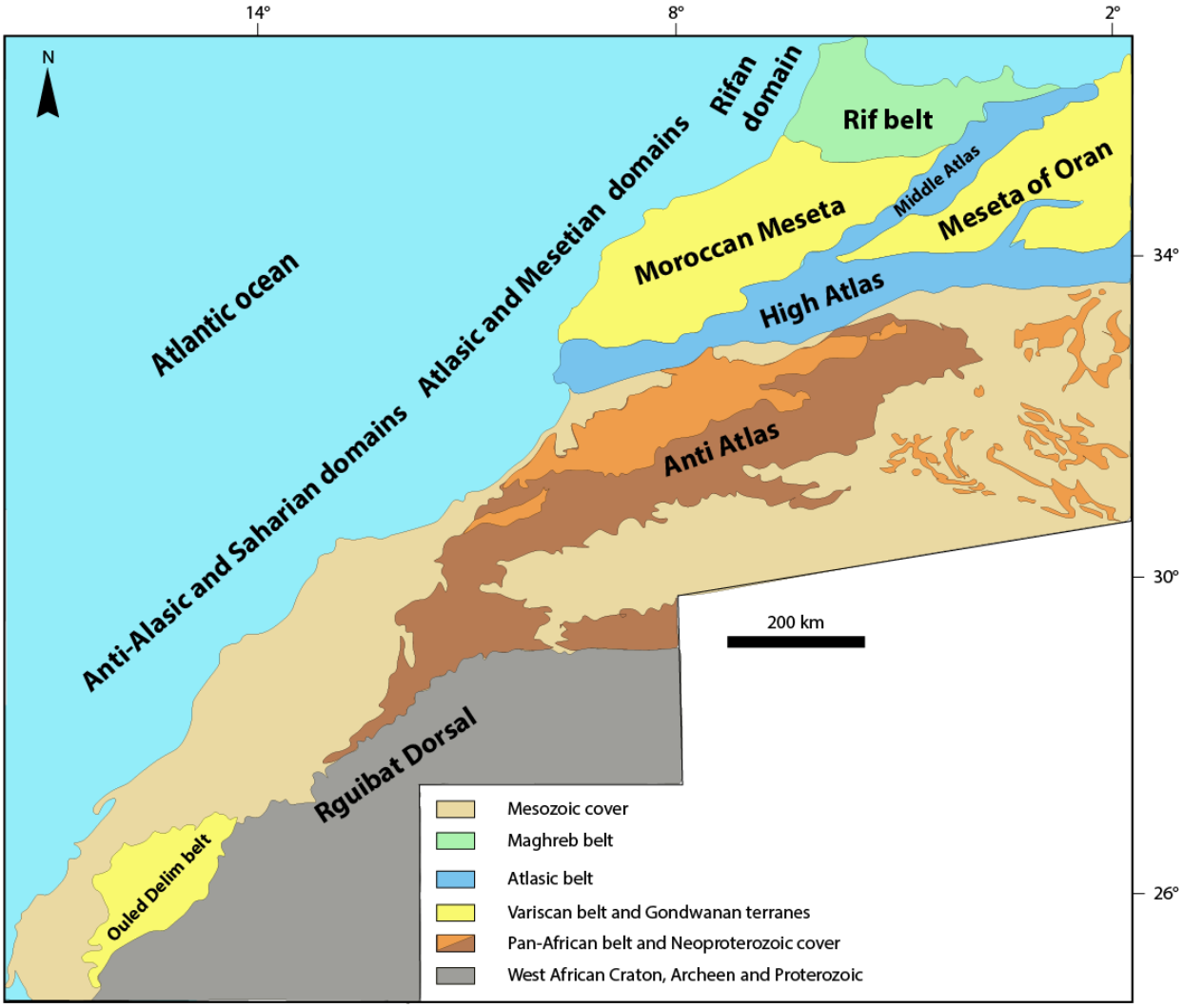

Figure 2.1
Structural domain of Morocco (modified from Michard et al., 2008).

Morocco provides an exceptional geological record, ranging from the earliest Precambrian events, through the Paleozoic and Mesozoic evolutionary episodes, and extending up to the most recent Alpine orogenic events that shaped its present-day structural framework. The succession of these major geological events has fostered the formation of an exceptional

diversity of mineral deposits throughout Morocco. In the Anti-Atlas domain, the prolonged evolution of the Pan-African belt system, especially during its final stages, created a complex of structural, magmatic, and sedimentary environments highly favorable to ore formation. As a result, the Anti-Atlas hosts numerous precious-metal deposits (notably Au and Ag), extensive base-metal porphyry and epithermal systems, and a variety of sedimentary-exhalative (SEDEX) occurrences (Gasquet et al., 2005). This geological complexity places the Anti-Atlas domain among the most metallogenically endowed regions of North Africa.

2.2 Litho-stratigraphic and geodynamic insights:

The Anti-Atlas Mountains trend east-northeast to west-southwest, extending over 700 kilometers in length and about 150 kilometers in width from the Atlantic Ocean in the west to the Tafilalt basin in the east (**Figure 2.1**). This belt is bordered to the north by the High Atlas Mountain along the South Atlas Fault (SAF); southwards, it transitions to the deserts of the Saharian domain.

The Anti-Atlas exhibits a well-preserved lithostratigraphic record, encompassing a mosaic of Precambrian basement inliers (i.e., Bas Drâa, Ifni, Kerdous, Tagragra of Akka, Tagragra of Tata, Igherm, Siroua, Zenaga, Bou Azzer, Saghro, and Ougnat) and overlying formations. These inliers are distributed across two distinct domains that are delineated by the Anti-Atlas Major Fault (AAMF) (i.e., the western cratonic and the eastern mobile domains; Choubert, 1963). The mobile domain, bounded to the north by the SAF, comprises Siroua-Bou Azzer-Saghro and Ougnat inliers, and was recently identified as a single terrane referred to as the Saghro domain (Schulte et al., 2022).

Paleoproterozoic rocks corresponding to the Eburnean basement (e.g., Complex of Zenaga and Kerdous) are exposed exclusively south of the AAMF (i.e., cratonic domain; Choubert, 1963; Gasquet et al., 2005; Kouyaté et al., 2013). However, geochemical evidence shows that Neoproterozoic magmatism in the mobile domain incorporated the Paleoproterozoic cratonic material, indicating the presence of a deeply buried Eburnean basement beneath the whole Anti-Atlas (Ennih and Liégeois, 2001; Gasquet et al., 2005; Soulaimani et al., 2006; Errami et al., 2009). This Eburnean basement consists of schists, micaschists, gneisses, dolerite and migmatites, intruded by granitic and granodioritic plutons, with U–Pb zircon ages consistently around 2000 Ma (Hassenforder, 1987; Walsh et al., 2002; Thomas et al., 2004; Gasquet et al., 2005; Pereira et al., 2015). In the Anti-Atlas, this crystalline basement is overlain by a sequence of shallow water formations formed by quartzite and limestones of the Lkest (Kerdous inlier)

and Taghdout (Zenaga inlier) groups, highlighting a major unconformity, that is well preserved in the Tizi n Taghatine area (Gasquet et al., 2005).

The Mesoproterozoic, previously considered as a gap in the geological history, is locally recorded by doleritic dykes in the Baa Draâ inlier, where they crosscut the Taghdout Group, and U–Pb dating of baddeleyite has yielded ages of 1380 Ma and 1640 Ma (El Bahat et al., 2013; Kouyaté et al., 2013; Söderlund et al., 2013; Youbi et al., 2013). Similar mafic dykes in the Jbel Lkest have yielded ages around 1650 Ma, suggesting a late Proterozoic age range (Kouyaté et al., 2013; Youbi et al., 2019). These findings prompted a revision of the age of the entire sequence assigned to the Taghdout Group, and call into question the previously reported ages of ca. 1706 Ma (Ikenne et al., 2017) and ca. 1639 Ma (Ait Lahna et al., 2016) for mafic sills in the Ighrem and Zenaga inliers, respectively.

The Neoproterozoic succession corresponds to the Pan-African orogeny, and reveals the different stages of the Wilson cycle; **Figure 2.2:**

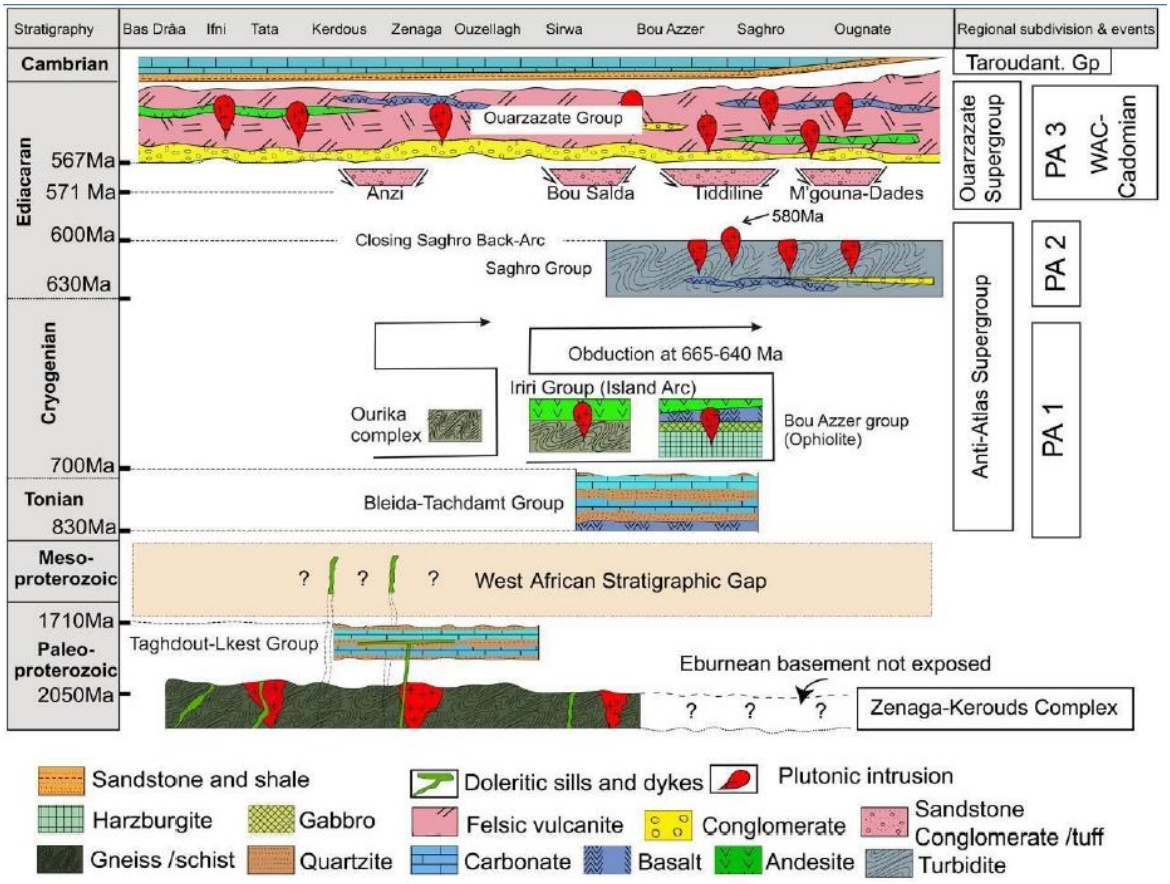

Figure 2.2
Generalized lithostratigraphic column for the Anti-Atlas Pan-African orogen (after Errami et al., 2021).

(i) Rifting and fragmentation of an unidentified continent incorporating the West African Craton (WAC), and development of passive margin (Tachdamt Group; Thomas et al., 2004; Bouougri et al., 2020) with an associated magmatic activity (Alvaro et al., 2014b).

(ii) Development of an ocean and island arcs (770-650 Ma), with the deposition of sediments in back-arc basins (Bleida Group; Samson et al., 2005; Blein et al., 2014a; Triantafyllou et al., 2016, 2020; Bouougri et al., 2020).

(iii) Ocean closure (650-640 Ma), highlighted by a polyphase accretion of oceanic rocks, as a diverse amphibolite to greenschist facies metamorphosed assemblage of ophiolitic complexes (Iriri and Bou Azzer Groups;Triantafyllou et al., 2016; D'Lemos et al., 2006).

(iv) Post-collisional period (630-539 Ma), characterized by high potassic calc-alkaline to shoshonitic volcano-plutonic rocks, accompanied by sedimentary successions deposited into pull-apart basins (Ennih and Liégeois, 2001; Thomas et al., 2002; Gasquet et al., 2008; Belkacim et al., 2017). This stage consists of:

- The Ediacaran turbiditic deposits of the Saghro Group (630-600 Ma; Fekkak et al., 1999; Errami et al., 2009; El Kabouri et al., 2023).
- The Anzi (Tata-Kerdous), Bou Salda (Siroua), Tiddiline (Zenaga-Bou Azzer) and M'gouna-Dadès (Saghro-Ougnat) Groups between 600 and 580 Ma (Thomas et al., 2002; Gasquet et al., 2008).
- The widespread Ouarzazate Group (580–539 Ma) comprising high potassic calc-alkaline volcanic, volcanoclastic and plutonic rocks (Toummite et al., 2012; Belkacim et al., 2017; Linnemann et al., 2019; Youbi et al., 2020; Schulte et al., 2022). This intense felsique magmatic activity is affiliated to a continental silicic large igneous province (SLIP) (Tuduri et al., 2018; Belkacim et al., 2021; Schulte et al., 2022; Ferraq et al., 2024).

During this final stage of the Pan-African activity, the transtensional regime together with the huge magmatic activity of the Ouarzazate SLIP are widely regarded as a key driver of the extensive metallogenic activity in the central and eastern Anti-Atlas (Gasquet et al., 2005; Belkacim et al., 2017; Tuduri et al., 2018).

Following the collapse of the Pan-African orogen, the Ouarzazate Group was succeeded by thick post-orogenic sedimentary deposits (Taroudant and Tata Groups) in an extensional setting

related to the opening of the Rheic Ocean (Gasquet et al., 2005, 2008; Alvaro et al., 2014a; Soulaimani et al., 2014). The Anti-Atlas was dissected into intracontinental basins that accommodated the entire Paleozoic succession, along with associated tholeiitic and alkaline volcanic episodes (Piqué, 2001; Alvaro et al., 2014a; Pouclet et al., 2018).

It should be noted that Precambrian rocks are not confined to the Anti-Atlas domain, as they are also exposed in the eastern block of the High Atlas Paleozoic massif (The Ouzellagh promontory), in the Western High-Atlas and in the Western and Eastern Mesetas (Pereira et al., 2015; Ouabid and Garrido, 2023). Moreover, both the Anti-Atlas and Atlas-Meseta belts are covered by a Lower Cambrian carbonate platform and share Ordovician glacial sediments, suggesting that they were probably adjacent at least during the late Ediacaran-Cambrian period (Le Heron, 2007; El Kabouri et al., 2023, 2025).

2.3 Geodynamic framework

The Anti-Atlas experienced a complex succession of protracted tectono-magmatic events, the impacts of which are heterogeneously distributed across the mountain belt, but have played a decisive role in shaping its litho-tectonic organization. Among the most significant geological events is the Pan-African orogeny, which not only governed the lithostratigraphic evolution of the Anti-Atlas, but also provides essential insights into the broader geodynamic evolution of Gondwana's peri-cratonic domains.

Initially acting as basins for the deposition of quartz-carbonate successions during an extensional regime associated with a passive margin (Lkest-Taghdout groups) and back-arc setting (Tachdamt-Bleida groups), the Anti-Atlas subsequently underwent a compressional phase that culminated in subduction, obduction (Bou Azzer-Iriri groups), and ultimately leading to the collision of the arc with the northern margin of the West African Craton (Gasquet et al., 2005). Besides, several geodynamic models have been proposed for the spatio-temporal evolution of the Anti-Atlas during the Pan-African orogenic cycle. The models discuss the vergence of the subduction zone to be the south and toward the West African Craton (WAC) (Leblanc, 1975; Leblanc et Lancelot, 1980), or to the north toward the unknown continent (Saquaque et al.,1989). The polarity of this subduction is important, as it provides critical insights into the structural evolution and the magmatic activity, helps constrain the broader geodynamic processes that shaped the WAC's assembly, and discuss the suture of the WAC. In this geodynamic framework, the suture zone is classically interpreted as the Anti-Atlas Major Fault (AAMF) (Leblanc, 1975). Yet, Ennih and Liégeois, (2001) challenged this view,

interpreting the Saghro Group as allochthonous units between WAC and Avalonia, which makes the (SAF) is more accurately to be the suture zone (**Figure 2.3**). Whereas, Geochemical and geochronologic evidence of deep buried Eburnean basement to the north of the AAMF, in addition to magnetic modeling of the Bou Azzer ophiolite led Gasquet et al., (2008) to suggest that the suture zone should occurred north to the SAF itself.

Subsequent studies by Walsh et al., (2012) have constrained the geodynamic evolution of the Anti-Atlas based on the model proposed by Benziane et al. (2007) and several geochronological dates in the central and eastern Anti-Atlas. Overall, the tectonic evolution is summarized in three major Pan-African periods (**Figure 2.4**):

(i) **The early orogenic activity (PA1)**, corresponds to the rifting of the West African Craton (WAC), and the development of a passive margin during the Tonian period. This stage was followed by northward-dipping subduction, arcs development, and obduction of the ophiolitic units.

(ii) **The major phase of the Pan-African orogeny (PA2)**, includes the slab break-off and lithospheric delamination, which allowed the emplacement of calc-alkaline intrusions beneath molassic deposits (e.g., Tiddiline, Dadès groups). They were deformed during this tectonic phase.

(iii) **The late stage (PA3)**, is characterized by the Ediacaran magmatism interpreted as occurring in a post-collisional setting. These plutonic and volcanic activities imply the reworking of the West African Craton margin or to the establishment of a continental volcanic arc above a short-lived, southward-dipping subduction zone.

However; Gasquet et al., (2008) argue for a metacratonic evolution started from PA2 to PA3 of the norther edge of the WAC, during which the ultimate magmatic activity of the Ouarzazate Group was accompanied by the formation of large-scale precious metal deposits, base-metal porphyry and SEDEX-type occurrences (Gasquet et al., 2005). The discussion section of chapter 3 provides more insights into this geodynamic framework of the Anti-Atlas and its relationship with the metallogenic activity during the Late Ediacaran times.

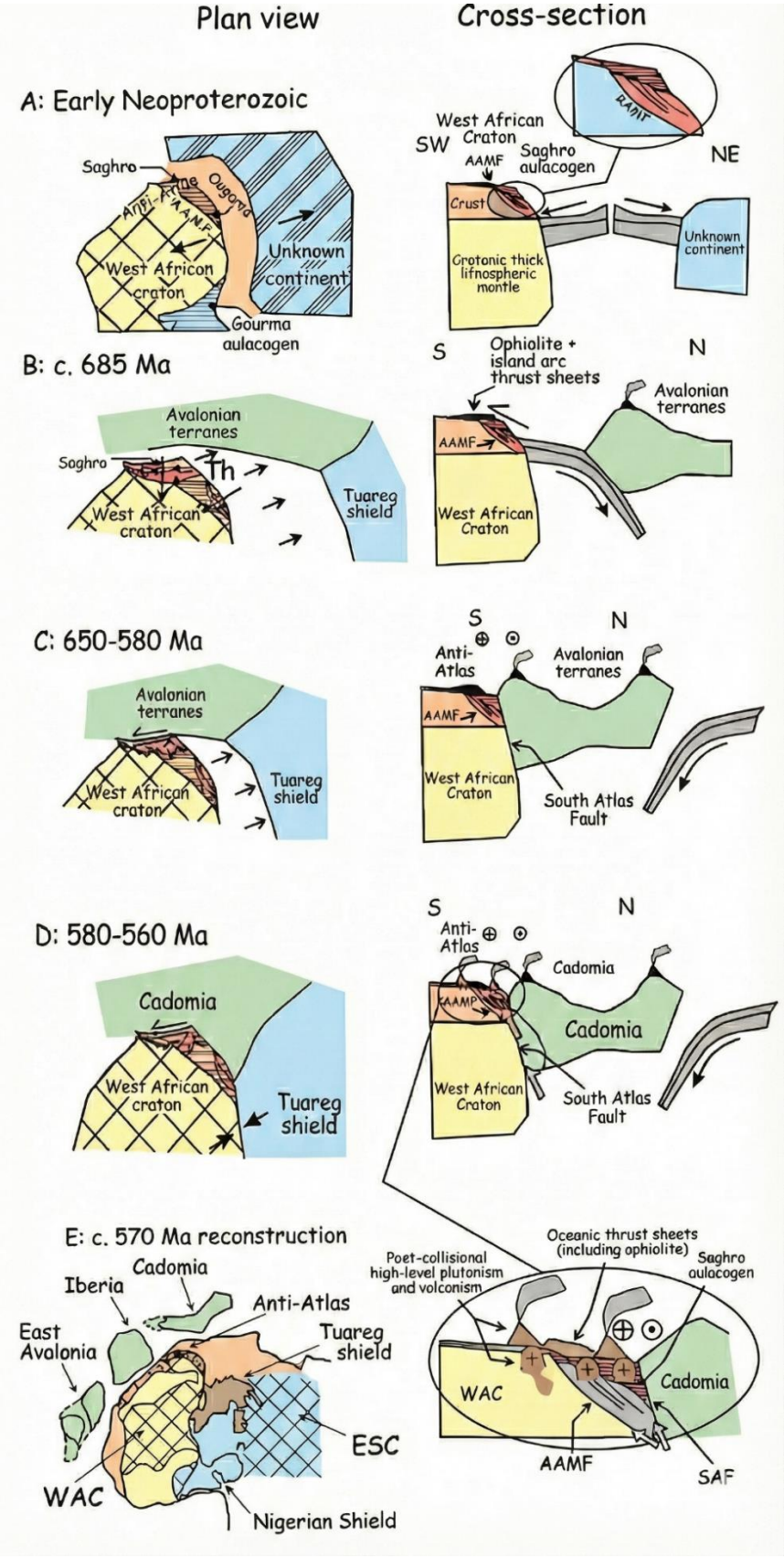

Figure 2.3
Geodynamic model of the Pan-African evolution of the Anti-Atlas belt (Ennih and Liégeois, 2001).

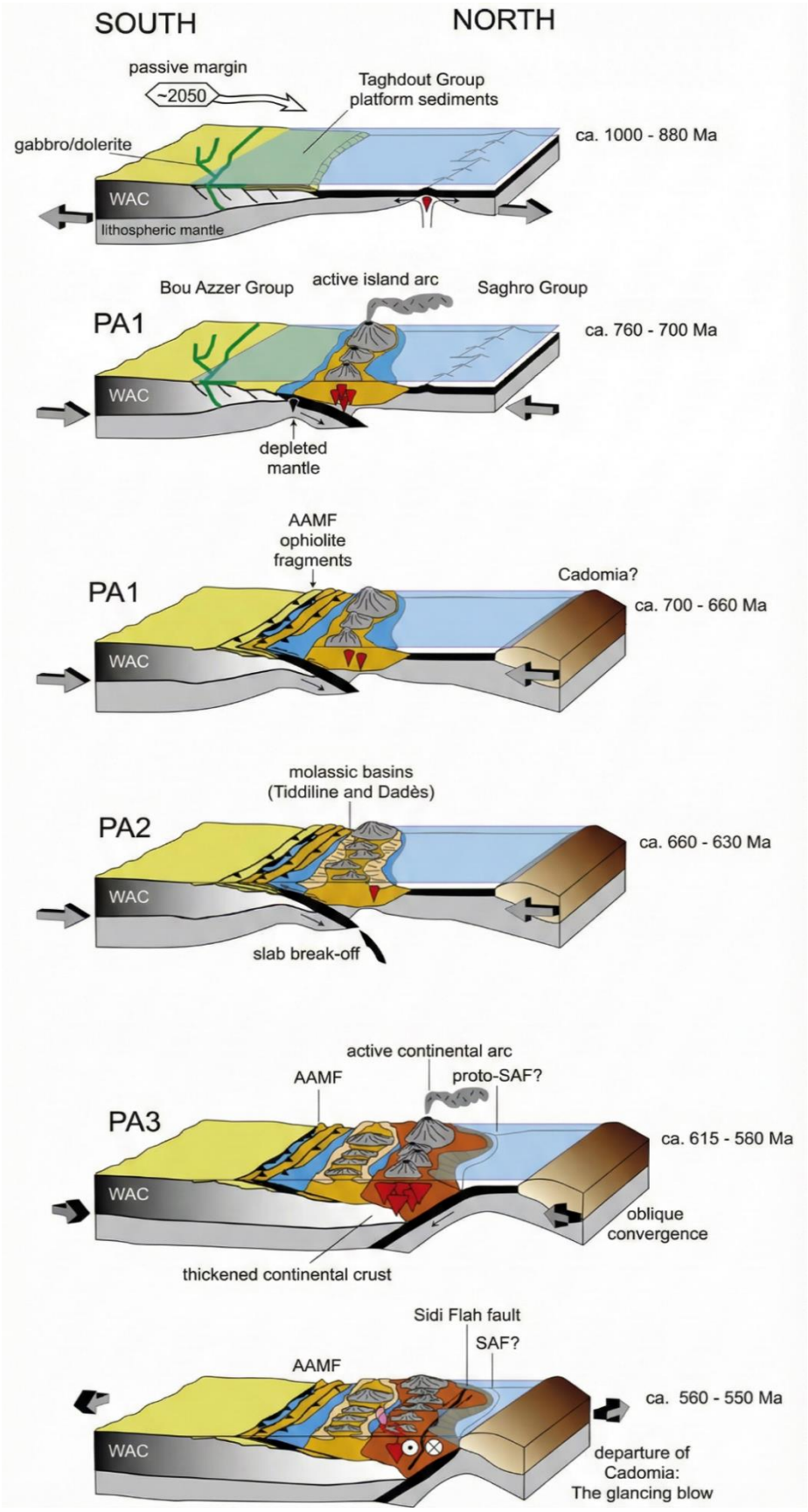

Figure 2.4
Geodynamic evolution model illustrating the tectonic development of the Anti-Atlas chain (Walsh et al., 2012, modified after Benziane, 2007).

2.4 The Pan-African Anti-Atlas belt: connections with peri-Gondwanan crustal blocks

During the Ediacaran period (635-538 Ma), the closure of the Pan-African Ocean led to the formation of the Gondwana supercontinent as a result of large-scale amalgamation of continents and microcontinents located within East and West Gondwana (Murphy and Nance, 1989). Within the framework of this amalgamation, the West African craton (WAC) being in the position of a passive margin, was surrounded by Pan-African terranes including island arcs or continental active margins (Ennih and Liégeois, 2008 and references therein). From the northwestern margin of Gondwana, peri-Gondwanan terranes split off during Paleozoic time leading to the opening of the Rheic Ocean (Linnemann et al., 2012; Nance et al., 2012; Herbosch and Liégeois, 2016), as a continuation of Neoproterozoic orogenic activity. Therefore, certain peri-Gondwanan terranes show marked similarities in age, tectonic history, and facies development relative to the Pan-African belts of the West African Craton (Nance et al., 2012).

The position of the Anti-Atlas belt of Morocco during the Neoproterozoic makes this region a key in understanding the interactions among crustal blocks that are now in the Appalachians and the Pan-African orogen. The original position of these blocks is still debated, and it is uncertain whether they belong to a hypothetical North Moroccan continent (Villeneuve and Cornée, 1994), to Avalonian terranes (Ennih and Liégeois, 2001, Keppie et al., 2003), or to Iberian terrane (Piqué, 2003). In a tectonic model proposed by Hefferan et al., (2000), the Anti-Atlas Major Fault (AAMF) considered as a large area of ophiolitic suture encompassing to the north the Siroua-Saghro arc on which the Avalonia-Cadomia blocks would have been accreted. More recently, the compilation of geochronological and tectonic data on the Neoproterozoic series of the Anti-Atlas led Hefferan et al., (2014) to split the Pan-African Orogeny into three orogenic pulses: Iriri-Tichibanine orogeny (760–700 Ma), Bou Azzer orogeny (680–640 Ma), the WA Cadomian orogeny (620–555 Ma), and time-equivalent events that are also recognized in the Appalachian orogen, especially in the terranes grouped together as Avalonia (Van Staal et al., 2021).

In the following chapter, the correlations between the Imourkhssen and several epithermal deposits of comparable age within the Avalonian terrane, will be examined with the aim of highlighting similarities in their geological setting, metallogenic characteristics, and geodynamic context.

2.5 Geographical location of the studied area

The investigated area is situated within the Ouzellagh–Siroua Salient (**Figure 2.5**), an inlier that represents a significant uplifted segment of the Anti-Atlas basement, which itself protrudes into the southern margin of the High Atlas belt (Toummite et al., 2012; Belkacim, 2014).

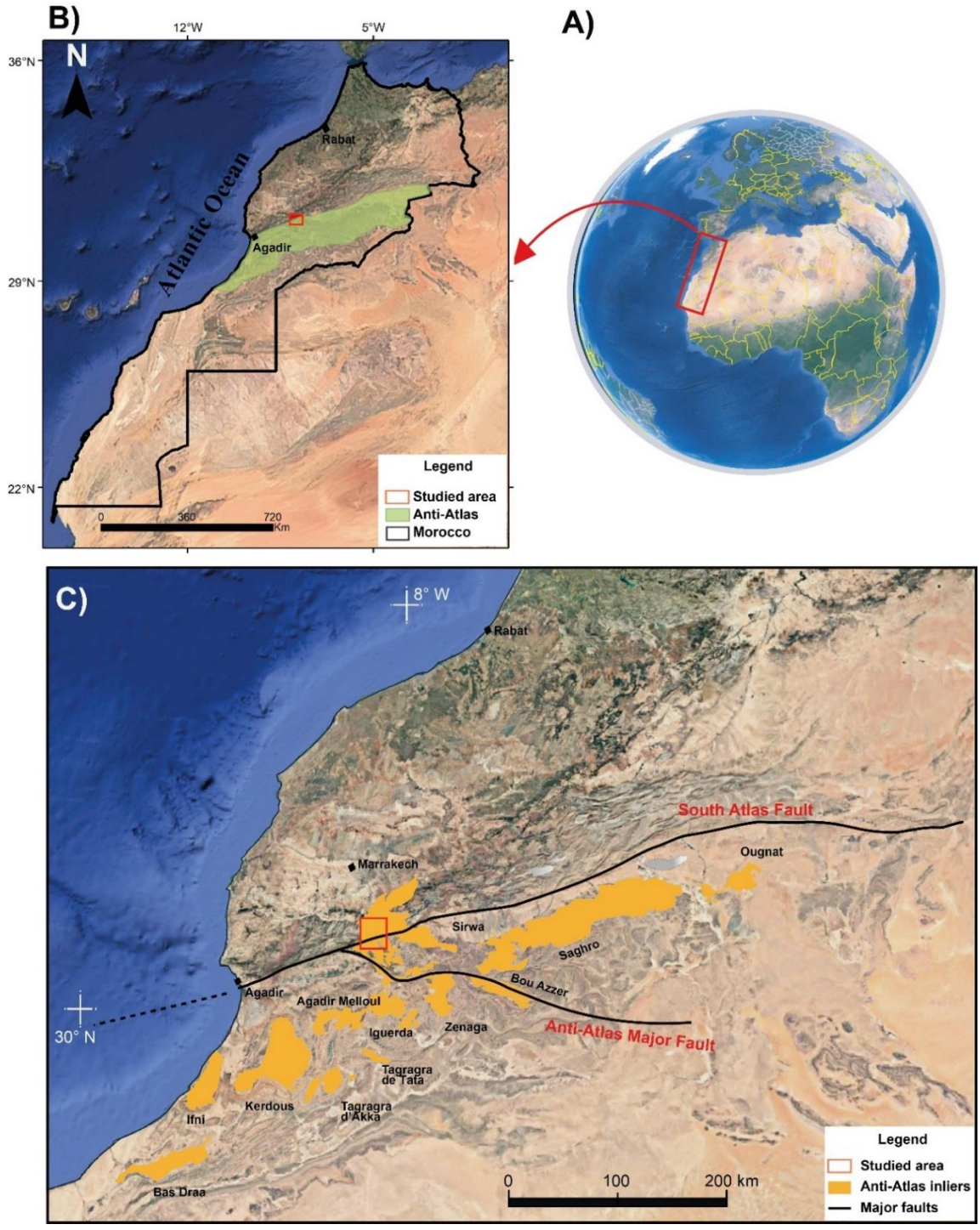

Figure 2.5
A) Global location of Morocco; B) Geographic setting of the study area within Morocco. C) Position of the study area within the Anti-Atlas Belt.

Geographically, this area is located approximately 140 km northeast of the city of Taroudant. Access to the area is relatively straightforward: it can be reached through the secondary road R110, which winds along the picturesque Tifnoute valley, connecting the village of Aoulouz to that of Amsouzert.

From a cartographic perspective, the area falls within the limits of the Assarag topographic sheet, at 1:50,000 scale, which provides detailed morphological and structural information for the region. This setting, at the crossroads of the Anti-Atlas and High Atlas domains, makes it particularly interesting for geological investigations, as it offers both structural and stratigraphic insights into the evolution of these major tectonic domains. The boundary between these structural provinces, as well as the detailed geology of the study area are addressed and critically considered in the subsequent sections.

3. CHAPTER 3: NEW GEOCHEMICAL AND GEOCHRONOLOGICAL CONSTRAINTS ON THE GENESIS OF THE IMOURKHSSEN CU±MO±AU±AG PORPHYRY DEPOSIT (OUZELLAGH-SIROUA SALIENT, ANTI-ATLAS, MOROCCO): GEODYNAMIC AND METALLOGENIC IMPLICATIONS

Mariam Ferraq [1,2]*, Saïd Belkacim [1,2], Li Zhen Cheng [2], Joshua H.F.L. Davies [3], Morgann G. Perrot [3], Abdelhay Ben Tami [1] and Mohammed Bouabdellah [4,5]

1 Department of Earth Sciences, Faculty of Sciences, Ibn Zohr University, Agadir, Morocco; mariam.ferraq@edu.uiz.ac.ma; s.belkacim@uiz.ac.ma; abdelhayben-tami@gmail.com

2 Mining and Environmental Research Institute, University of Quebec in Abitibi-Timiskaming, Rouyn-Noranda, Canada; lizhen.cheng@uqat.ca

3 Department of Earth and Atmosphere Sciences, University of Quebec in Montreal, Montreal, Canada; davies.joshua@uqam.ca; perrot.morgann@uqam.ca

4 Department of Earth Sciences, Faculty of Sciences, Mohammed Premier University, Oujda, Morocco; mbouabdellah2002@yahoo.fr

5 Geology and Sustainable Mining Institute, Mohammed VI Polytechnic University, Benguerir, Morocco; mbouabdellah2002@yahoo.fr

* Correspondence: mariam.ferraq@edu.uiz.ac.ma

Article published in the journal Minerals, Vol 14(832). August, 2024

3.1 Résumé

Le gisement porphyrique de cuivre, molybdène, or et argent d'Imourkhssen est situé dans le saillant d'Ouzellagh-Siroua (OSS), à cheval entre l'Anti-Atlas central et le Haut Atlas central. Il se caractérise par un style de minéralisation porphyrique typique. Géologiquement, il est constitué de roches volcaniques du Groupe du Saghro (630-600 Ma), qui sont envahies par de nombreuses roches magmatiques du Groupe de Ouarzazate (580-539 Ma), appelées les suites magmatiques de l'Édiacarien tardif (LEMS). Parmi celles-ci, les granites d'Askaoun, d'Imourkhssen et d'Imourgane sont les plus importants, car ils sont liés à la minéralisation porphyrique. L'ensemble est envahi par les essaims de dykes mafiques de Zaghar. Les datations U-Pb sur zircon du granite d'Imourkhssen et du porphyre granitique minéralisé montrent que ces roches intrusives se sont mises en place respectivement à 558 ± 1 et 550 ± 2 Ma. De plus, la géochimie des éléments majeurs et traces de la roche totale révèle une composition calco-alcaline hautement potassique de type I, compatible avec une mise en place dans un contexte post-collisionnel sous un régime tectonique transtensif.

La minéralisation est encaissée par la granodiorite d'Askaoun et le granite d'Imourgane. La minéralisation se présente sous forme de disséminations à grains fins et de remplissages de veines et de filons hydrothermaux altérés orientés NNE-SSO à N-S. Les altérations hydrothermales associées à la minéralisation comprennent : une altération potassique, une association à chlorite–séricite, une altération séricitique et une altération propylitique, généralement accompagnées d'une silicification et d'une pyritisation diffuses. Les périodes minéralisées comprennent des périodes supergènes et magmatiques-hydrothermales. Ces dernières comprennent deux stades (i) de dissémination primaire et (ii) de système minéralisé secondaire orienté NNE-SSW à N-S. La molybdénite est confinée aux zones d'altération potassique et à chlorite-séricite du granite minéralisé sous forme de disséminations fines, aussi bien qu'elle est présente sous forme de remplissages de veinules dans les halos propylitiques. Les occurrences de molybdénite, ainsi que la dissémination de pyrite, chalcopyrite, galène et de tennantite, sont attribuées à la phase minéralisée primaire, tandis que le système minéralisé NNE-SSO à N-S est lié à la phase de minéralisation secondaire. Il se compose de pyrite, chalcopyrite, bornite, covellite, diagénite, sphalérite, hématite, galène, or et de chenguodaite. The predominance of cockade and crack-and-seal textures suggest multiple episodes of ore-forming fluid circulations under epithermal conditions. Le stade supergène est atteint par la malachite, azurite, barytine, hématite, epsomite et la chrysocolle. D'après les descriptions ci-dessus, nous affirmons que la minéralisation Imourkhssen Cu±Mo±Au±Ag partage de

nombreuses caractéristiques minéralogiques et paragénétiques des gisements de cuivre porphyrique.

Mots clés : Ediacaran ; Imourkhssen ; porphyre-cuivre.

3.2 Abstract

The Imourkhssen porphyry Cu±Mo±Au±Ag deposit is located at the Ouzellagh-Siroua Salient (OSS) straddling the boundary between the central Anti-Atlas and the central High Atlas. It is characterized by a typical porphyry mineralization style. The volcanic rocks are intruded by numerous magmatic rocks of the Ouarzazate Group (580-539 Ma), referred to as the late Ediacaran magmatic suites (LEMS). Of these, the Askaoun, Imourkhssen and Imourgane granites are the most significant as they are related to the porphyry mineralization. The entire set is intruded by the Zaghar mafic dyke swarms. Zircon U-Pb dating of the Imourkhssen granite and the ore-bearing granite porphyry shows that these intrusive rocks were emplaced at 558 ± 1 and 550 ± 2 Ma, respectively. Moreover, whole-rock major and trace element geochemistry reveal a high-K calc-alkaline I-type composition, consistent with an emplacement in a post-collisional setting under a trans-tensional tectonic regime.

Ore bodies are hosted by the Askaoun granodiorite and the Imourgane granite as well. The mineralization occurs as fine-grained dissemination and infills of hydrothermally altered NNE-SSW to N-S trending veins and veinlets. Ore-related hydrothermal alteration consists of potassic, chlorite-sericite, serecitic and propylitic mineral assemblages along with pervasive silicification and pyritization, providing a porphyry style alteration pattern. The ore periods comprise supergene and magmatic-hydrothermal periods. The latter includes primary dissemination and secondary NNE-SSW to N-S ore bearing system stages. The occurrence of molybdenite is either restricted to the potassic and chlorite-sericite alteration zones of the ore-bearing granite as fine disseminations, or alternatively as veinlets infills within the propylitic halos. The molybdenite occurrences along with pyrite and chalcopyrite, galena and tennantite dissemination are assigned to the primary ore stage, while the NNE-SSW to N-S ore bearing system is related to the secondary ore stage. It consists of pyrite, chalcopyrite, bornite, covellite, diagenite, sphalerite, hematite, galena, gold and chenguodaite. The predominance of cockade and crack-and-seal textures suggest multiple episodes of ore-forming fluid circulations under epithermal conditions. The supergene stage is achieved by subordinate malachite, azurite, barite, hematite, epsomite and chrysocolla. From the descriptions above, we argue that the

Imourkhssen Cu±Mo±Au±Ag mineralization shares many mineralogical and paragenetic attributes of porphyry-copper deposits.

Keywords: Ediacaran; Imourkhssen; porphyry-copper.

3.3 Introduction

Porphyry deposits are a critical type of magmatic-hydrothermal ore deposit, known for their large tonnage and significant contribution to the production of copper, gold, and molybdenum, encouraging research and exploration (Sillitoe, 2010; Sun et al., 2025). These deposit types are widely documented but their origin and evolution are in many cases still poorly constrained due to: (i) the diversity of geodynamic setting in which they form, (ii) the variability of the host rocks and (iii) the zoning in both paragenetic succession and alteration assemblage (Sillitoe, 2010; Sinclair, 2007). Indeed, porphyry copper deposits are commonly associated with medium to high potassic calc-alkaline (shoshonitic) or alkaline I-type magnetite series (Cooke et al., 2005). This type of magmatism is frequently associated with subduction zones in continental arc settings (Lee and Tang., 2020), as well as with orogenic collapse zones linked to post-collisional events (Jébrak and Marcoux, 2008).

Porphyry Copper deposits range in age from Archean to Holocene, although the most productive are Jurassic or younger (Sinclair, 2007). A large number of these deposits occur along the peri-pacific belt (**Figure 3.1**), particularly in the Andean (Chili, Peru) and North America Cordillera (Colorado belt), where the three largest molybdenum porphyry deposits occur (e.g., Climax, Urad-Henderson and Emmons Mounts (Sillitoe, 2008).

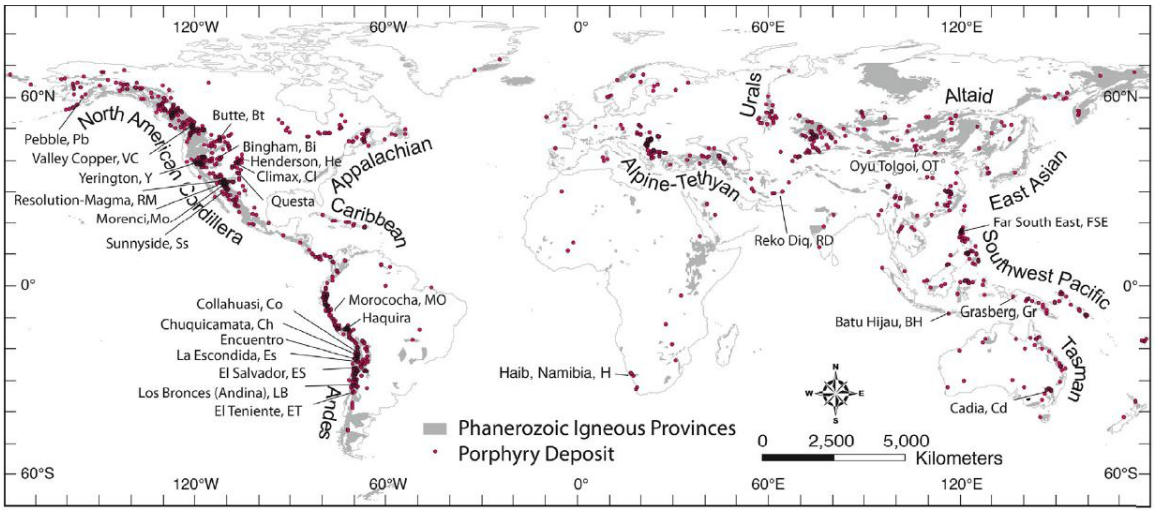

Figure 3.1
Global distribution of porphyry deposits (modified from Seedorff et al., 2005).

Porphyry ore deposits display a distinctive, broad-scale alteration-mineralization zoning pattern, that includes from the core to the periphery, sodic-calcic, potassic, chlorite-sericite, serecitic, advanced argillic and propylitic mineral assemblages (Sillitoe 2008, 2010). Potassic alteration is usually the innermost alteration which grades irregularly and laterally into propylitic alteration patterns (Zhiming and Cooke, 2019). The chlorite-sericite zone is considered as the early stage of the phyllic alteration overprinting the previous potassic mineral assemblage (Zhiming and Cooke, 2019). Phyllic (or serecitic) alteration is observed in the field by bleached outcrops (Di Tommaso and Rubinstein, 2007). It is a pyrite dominated shell, and contains also quartz and sericite minerals (Sillitoe, 2010). The most distal part of the alteration zone is the propylitic alteration, which consists of: chlorite, carbonate, epidote, adularia and albite (Di Tommaso and Rubinstein 2007; Sillitoe 2010). These widespread and distinctive hydrothermal zones provide a useful footprint for porphyry copper exploration (Cooke et al., 2005).

In the Anti-Atlas belt of Morocco, many examples of deposits seem to exhibit some of the characteristics which are indicative of porphyry copper systems such as Tiouit (Mouttaqi et al., 2011; Bouabdellah et al., 2016), ‘’Patte d’Oie’’ part of Bouskour (Jébrak and Marcoux, 2008; El Azmi et al., 2024) and Ismlal Au stockwork deposits (Tuduri et al., 2018). Here we describe the geological features of the Imourkhssen deposit, which is thought to be the first example of a Neoproterozoic porphyry Cu±Mo±Au deposit in Morocco (Belkacim et al., 2014). This study provides new geological, geochemical, geochronological data and mineralogical descriptions for the Imourkhssen Cu±Mo±Au±Ag porphyry deposit. The timing of the ore emplacement is discussed in the framework of a multi-pulsed Ouarzazate Silicic Large Igneous Province (SLIP) (Belkacim et al., 2021), during the concluding stages of the Pan-African orogeny, within the context of an extensional regime along the northern border of the West African Craton (WAC).

3.4 Regional Geology

3.4.1 The Anti-Atlas

The Anti- Atlas Mountains of Morocco are a WSW-ENE oriented belt, formed by Precambrian basement unconformably overlain by slightly folded Paleozoic sedimentary formations (**Figure 3.2, B**). The orogen records the effects of two main periods of tectono-magmatic activity linked to the Paleoproterozoic Eburnean (2.07–2.20 Ga) and Neoproterozoic Pan-African (885–539 Ma) orogenies (Ennih and Liégeois, 2001; Karaoui et al., 2015).

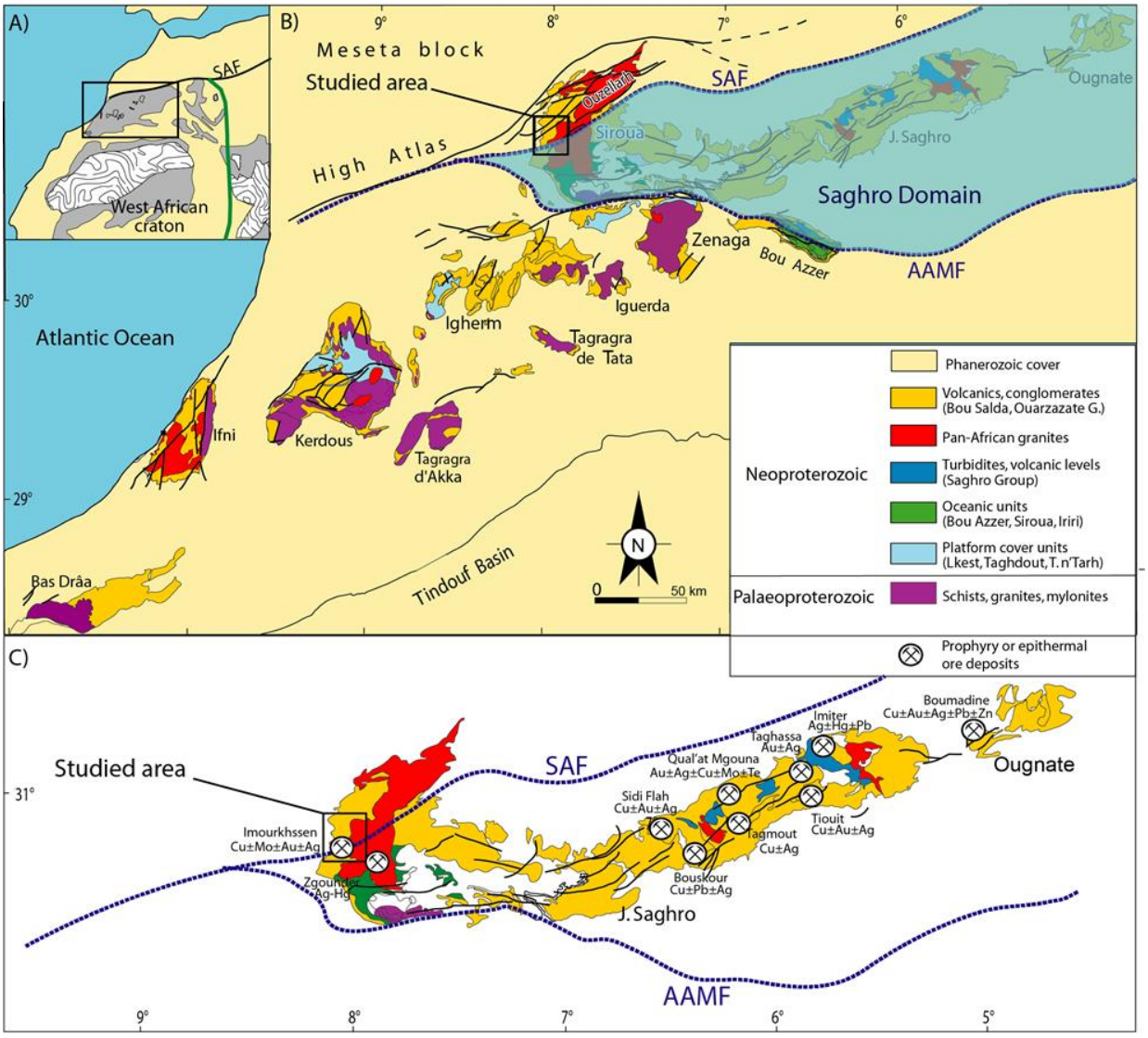

Figure 3.2
A) Location of the Anti-Atlas domain and its relationship to the West African Craton. B) Location of the studied area modified after (Gasquet et al., 2008). The geology of the studied area is detailed in figure 3. C) Simplified geological map of the Saghro domain showing the location of major porphyry and epithermal ore deposits (Tuduri et al., 2018).

The Eburnean terranes form the crystalline basement on which some Neoproterozoic Pan-African successions were deposited, and subsequently deformed in four stages, which likely correspond to a Wilson cycle: (1) rifting and break-up (>800 Ma) of an unknown continent to which belonged the WAC, accompanied by rift-related magmatism activity (Álvaro et al., 2014); (2) formation of island arcs at 770- 650 Ma and associated back-arc sedimentary basin of Bleida Group (Samson et al., 2004; Blein et al., 2014a; Triantafyllou et al., 2016, 2020; Bouougri et al., 2020); (3) ocean closure (650-640 Ma), highlighted by the obduction of ophiolitic complexes (Samson et al., 2004; D'Lemos et al., 2006; Triantafyllou et al., 2016,

2020); (4) post-collisional (630-539 Ma) transpressive to transtensive tectonics, and emplacement of huge high-K calc-alkaline to shoshonitic volcano-plutonic rocks, accompanied by sedimentary successions deposited into pull-apart basins (Ennih and Liégeois, 2001; Thomas et al., 2002; Gasquet et al., 2008; Belkacim et al., 2017). This final stage is associated with the deposition of:

(i) the Saghro Group (620–600 Ma), consists of andesite-basaltic and andesitic to trachytic volcanic and volcaniclastic rocks, with rare sedimentary intercalations (630-600 Ma; Fekkak et al., 1999; Gasquet et al., 2008; Errami et al., 2009; El Kabouri et al., 2023);

(ii) The Bou Salda Group (600–580 Ma) is characterized clastic sedimentary rocks and abundant high-K calc-alkaline volcanic and intrusive rocks (Gasquet et al., 2005; Álvaro et al., 2014);

(iii) The Ouarzazate Group (580–539 Ma) is composed by high-K calc-alkaline volcanic, volcanoclastic and plutonic rocks, which are widespread throughout the Anti-Atlas (Toummite et al., 2012; Belkacim et al., 2017; Linnemann et al., 2019; Youbi et al., 2020). This Late Neoproterozoic magmatism is also widespread to in the High-Atlas and Meseta (Karaoui et al., 2015; Schulte et al., 2022).

In the Anti-Atlas, the late Ediacaran magmatic activity coupled with extensional trans-tensional tectonic structures, are invoked to explain the pervasive hydrothermal activity at the origin of the genesis of some of the world-class precious metal deposits, base–metal and SEDEX-type deposits that have been documented throughout the central and eastern parts of the Anti-Atlas (Gasquet et al., 2005; Belkacim et al., 2017; Tuduri et al., 2018), and have recently been defined as the Saghro Domain (**Figure 3.2 B,C**; Schulte et al., 2022).

3.4.2 Deposit-scale Geology

The Cu±Mo±Au±Ag Imourkhssen deposit is hosted by granitic intrusions (**Figure 3.3**), stratigraphically assigned to the Ouarzazate (580-539 Ma) Group and , within the Ouzellagh-Siroua Salient (Hollard et al., 1985). These intrusions intrude the rocks of the Saghro Group (630-610 Ma; (Thomas et al., 2002), and comprise a wide spectrum of igneous rocks spanning from sub-volcanic to plutonic bodies. These rocks belong to the Late Ediacaran magmatic Suites (LEMS), comprising the Assarag, Amassine and Ougougane suites.

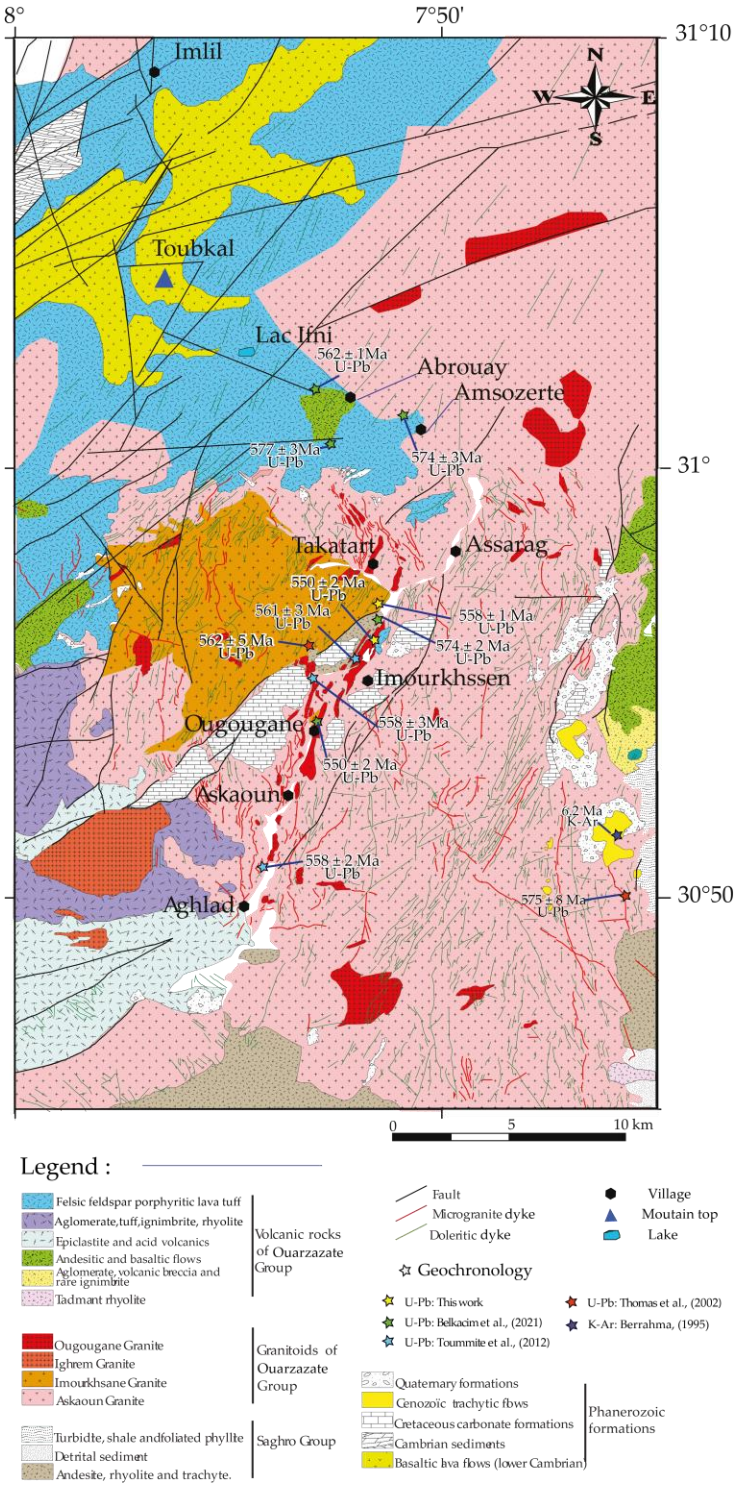

Figure 3.3
Geological map of the studied area (modified from Toummite et al., 2012; Belkacim et al., 2017).

In the Imourkhssen area, the Assarag Suite includes the large Askaoun batholith which consists of the Askaoun granodiorite and quartz diorite. This batholith covers 800 km2 in the NW part of the OSS (Thomas et al., 2002). The Amassine Suite is represented by the star-shaped Imourkhssen granite. This Suite was previously interpreted to encompass an ore-bearing granite

porphyry. In this study, the latter lithotype is referred to as “the Imourgane granite”, since it is actually related the Ougougane Suite (see geochronology section). This porphyritic intrusion consists of a succession of rhyolite, microgranite and granite, all of which are crosscut by the Zaghar mafic dyke swarms (**Figure 3.4**).

The emplacement of the LEMS is related to the development of many base and precious metal deposits in the OSS, including the Ag-Hg Zgounder ore deposit (Pelleter et al., 2016), and the Cu-Co-Mo Inki mineralization (Thomas et al., 2002). Nonetheless, the Imourkhssen deposit has been identified as a Cu ± Mo ± Au porphyry mineralization associated with Imourkhssen and Askaoun granitoids (Belkacim, 2014).

Figure 3.4
The Zaghar dykes crosscut the Ougougane granite.

3.5 Sampling and Analytical Methods

Sampling was carried out on both fresh and altered rocks from the Imourkhssen area, including the abandoned Talat nl’bour galleries. More than seventy samples were collected. The representative samples were selected for petrographic, mineralogical, geochemical and geochronological studies (**Appendix 1**).

Polished thin-sections representing different alteration assemblages and mineralized veins were examined using plane-polarized and reflected-light microscopy. For phase identification, and for the semi-quantitative mineralogical determination, nine thin sections were analyzed at the research center of the Faculty of Sciences of Agadir, Université Ibnou Zohr using a JEOL JSM IT-100 scanning electron microscope. The resolution was at most 100 nm, when both back scattered electrons and energy-dispersive spectroscopy were used.

Six samples were also analyzed for mineral composition using a D8 ADVANCE Twin X-ray diffractometer (XRD). The diffractometer has a two-theta geometry with a copper sealed tube x-ray source, producing Cu Kα1 radiation at a wave-length of 1.5406 Å. The x-rays are issued from a generator operating at 40 kV and 25 mA and it's operating energy is 100W. XRD data were collected from 5 to 100° ± 0.05θ. The diffraction patterns obtained were used for mineral identification and semi-quantitative assessment of mineral content, and indexed using the X'Pert HighScore Plus v. 3. Software

For whole-rock geochemistry, major and trace elements of seventeen samples were analyzed by ICP-OES /ICP-MS (Fusion-Inductively coupled plasma optical emission spectrometers and inductively coupled plasma mass spectrometer) methods at Actlabs laboratory, Canada (**Appendix 2**). Moreover, two polished sections of molybdenite samples from Imourgane granite were analyzed at the Robert M. MacKay electron microprobe laboratory, located in the Department of the Earth Sciences, Dalhousie University, Halifax. The analyses were carried out in a JXA-8200 electron microprobe, using the internal standards for quality control (**Appendix 3**).

For geochronological purposes, two granite samples were dated by LA-ICP-MS U-Pb on zircon at the Geotop research center of the Université du Québec à Montréal (UQAM). Each sample was crushed and sieved to obtain a uniform grain size fraction of 50-250 μm. The resulting fraction was then introduced over a Wilfley table to separate the smaller and denser minerals. The fine dense fraction was collected and then processed with heavy liquids (methylene diodide) and a Franz isodynamic separator using a current up to 1 ampere to concentrate zircon grains.

Hundreds of clear, well-formed zircon grains were hand-picked from each sample under a binocular microscope, avoiding inclusions and fractures. Selected grains were then annealed in a muffle furnace at 1000 degrees for 48 hours. Before being mounted in epoxy resin on a

standard 1-inch round mount, polished and imaged on a Hitachi S-3400 variable pressure scanning electron microscope at an accelerating voltage of 20 kV using a Centaurus Cathodoluminescence (CL) detector to outline the growth zoning, rims, and inherited cores within individual grains and guide the spot selection for the in-situ laser ablation analysis. The U-Pb analyses were performed using the Nu Atom single collector mass spectrometer coupled with a Photon Machines G2 193nm excimer laser following a modified procedure reported in (Perrot et al., 2017), adding 3 ml/min N2 before the torch to reduce oxide formation in the plasma. Sensitivity of the mass spectrometer was optimized using U from a NIST610 glass, and gas flow was adjusted to ensure a U/Th of 1 and a Th/ThO of 1.10^{-3} for the NIST glass. We used a laser energy of 4.54 J/cm^2, a repetition rate of 6 Htz, and a 30 µm ablation spot. Measurements were conducted using a sample-reference material bracketing approach, with sets of 15 unknown samples bracketed by two primary reference analyses and at least one secondary reference grain analysis for quality control purposes.

The 91500 (1065 Ma, (Wiedenbeck, 1995) and Plešovice (Sláma et al., 2008) and were used respectively as primary and secondary reference material. The two samples were analyzed over one analytical session. The individual analyses were processed and corrected for down-hole fractionation using Iolite v4 software with the U-Pb geochronology data reduction scheme (DRS) (Wiedenbeck et al., 1995). Analyses with detectable ^{204}Pb were excluded prior to data reduction, and no general Pb correction was applied. The repeated analyses of Plešovice produced a weighted mean ^{206}Pb/^{238}U age of 337 ± 1 Ma in agreement within error with its known age (Sláma et al., 2008; see **Appendixes 4** and **5**). After processing the raw data and generating U-Pb ratios, Isoplot R (Vermeesch, 2018) was used to generate U-Pb ages, draw Concordia diagrams and calculate discordance distance, and ^{206}Pb/^{238}U weighted mean ages. All error bars and reported errors in the text are at the 2σ level.

3.6 Results

3.6.1 Petrography of the Host Rocks

The host rocks comprise the Late Ediacaran magmatic suites of the Ouarzazate Group (580-539 Ma), which intrude the volcanic and volcanoclastic rocks of the Saghro Group (620-600 Ma) (Thomas et al., 2004; Toummite et al., 2012; Belkacim et al., 2014). Considering their absolute ages, the LEMS in the Imourkhssen area comprise the Assarag, Amassine and Ougougane suites:

The Assarag magmatic Suite: The Assarag Suite is represented by the Askaoun quartz diorite and amphibole-biotite granodiorite. The granodiorite is pink colored and medium-grained rock. The primary mineral paragenesis consists of variable proportions of euhedral plagioclase, quartz and K-feldspar locally developing mermekitic and graphic textures, while biotite and amphibole occur as anhedral megacrysts (**Figure 3.5 A**). Accessory minerals consist of apatite, zircon, titanite and magnetite. Secondary minerals consist of sericite, chlorite, epidote, and kaolinite. The quartz diorite is dark-grey colored and medium to coarse-grained and heavily altered. Its mineral paragenesis consists of millimetric sized sericitized plagioclase, epidotized amphibole, chloritized biotite and abundant quartz and opaque minerals.

The Amassine magmatic Suite: This Suite is represented by the large Imourkhssen granite which occurs as a star-shaped barren batholith intruded into the granodiorite of the Assarag Suite. The Imourkhssen granite is pinkish and coarse-grained rock. The primary mineral paragenesis comprises perthitic K-feldspar (≃30%), albite-oligoclase (≃30%), along with quartz (≃35%) and chloritized biotite (<5%) (**Figure 3.5 B**). Accessory minerals contain magnetite, apatite and zircon, while the secondary mineral assemblage consists of sericite, chlorite and kaolinite.

The Ougougane magmatic Suite: This Suite consists of a series of rhyolitic, microgranitic and granitic intrusions cutting across both the Amassine and the Assarag suites. The rhyolite exhibits a characteristic hyaline spherulitic texture, as well as radiant fibers of orthoclase surrounding quartz nucleus. Accessory minerals include of zircon, rare apatite and Fe-oxides, while sericite and chlorite are the secondary minerals.

The microgranite occurs as pink-colored and fine-grained dykes. It consists of a significant proportion of interstitial quartz, perthitic K-feldspar, and albite-oligoclase displaying locally a well-developed mermekitic texture. Biotite and opaque minerals are observed as accessory minerals within the microgranite.

The granite of the Ougougane Suite, including the nearby Imourgane intrusion, occurs as a pinkish and coarse-grained to porphyritic granite (**Figure 3.5 C**). The mineral paragenesis consists of quartz and K-feldspar displaying a graphic texture. The feldspars are commonly

hydrothermally altered to sericite and/or kaolinite. Muscovite is rarely observed, whereas biotite is ubiquitous. The latter is commonly altered to chlorite and exhibits numerous inclusions of apatite, zircon, and opaque minerals.

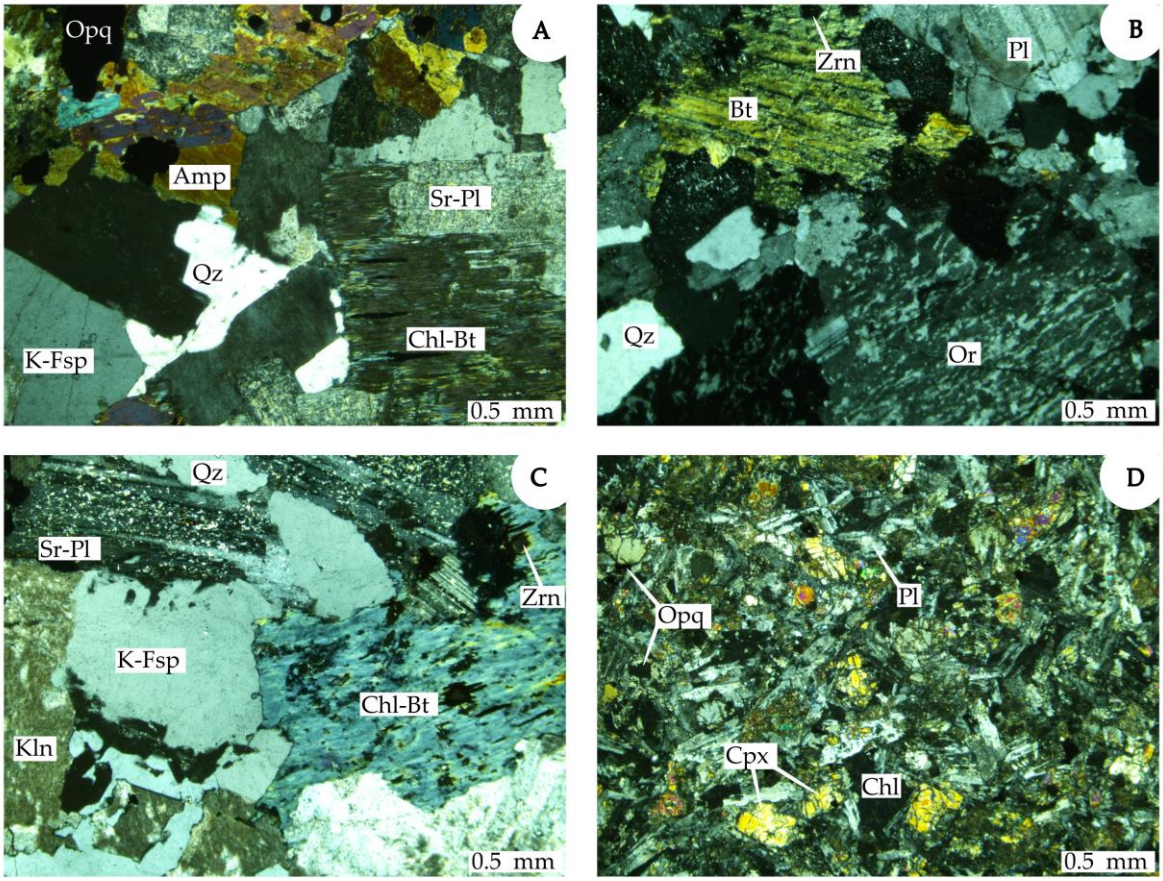

Figure 3.5
Selected photomicrographs of the LEMS at XPL (cross polarized light), with the Askaoun granodiorite in A), the Imourkhssen granite in B), the Imourgane granite in C) and the Zaghar mafic dyke in D). Mineral abbreviations: Opq: opaque, Amp: amphibole, Qz: quartz, Chl: chlorite, Bt: biotite, Kln: kaolinite, K-Fsp: K-feldspar, Or: orthoclase, Cpx: clinopyroxene, Sr: sericite, Pl: plagioclase, Zrn: zircon.

The Zaghar Mafic Dykes: The Zaghar mafic dykes consist of a swarm of doleritic dykes (2 to 15 m thick) that intrude the LEMS. These dykes are fine to medium-grained, olive green in color, and have intersertal ophitic textures. The primary mineralogy of some dykes consists of plagioclase laths, while the Fe-Mg minerals are often transformed to chlorite and epidote (**Figure 3.5 D**). Some dykes contain clinopyroxene glomerocrysts.

Locally, the Zaghar dyke swarm shows co-mingling magmatic textures at the contact with the Askaoun granodiorite of the Assarag Suite (**Figure 3.6**), suggesting their simultaneous emplacement. Similar textures have also been documented in the Zaghar mafic dyke swarms located in Douar Eç-çour, north of the studied area (El Moume et al., 2020). Geochronological dates have not been reported in the Imourkhssen area. However, a zircon/apatite/rutile U-Pb age of 554 ± 6 Ma had been documented from a dolerite dyke in the Douar Eç-çour (El Moume et al., 2020).

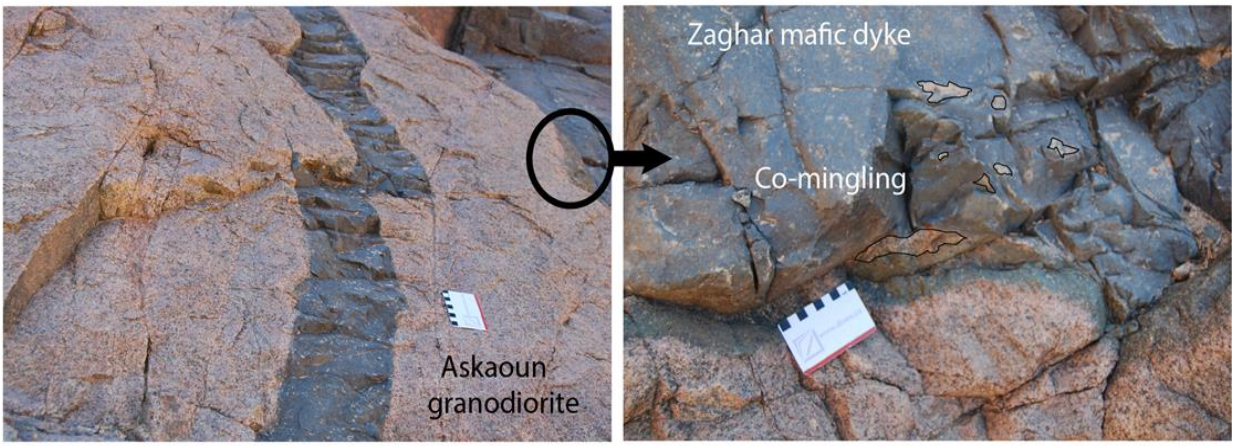

Figure 3.6
Co-mingling texture between the Askaoun granodiorite and Zaghar mafic dyke in Talat nl'bour area. The transition between the two magmatic bodies is progressive, and outlined by the incorporated granodioritic fragments within the mafic dyke.

3.6.2 Whole rock Geochemistry

Seventeen representative samples of the LEMS have been analyzed for major and trace elements represented in the **Appendix 2**. The rocks of the Ougougane Suite including the Imourgane granite exhibit high SiO_2 content (72.39-77.02 wt%) and medium total alkali content (K_2O+Na_2O) contents are predominantly around 8.27 wt%. They fall into granite field on the total alkalis versus SiO_2 diagram (**Figure 3.7 A**). The A/CNK values [Al_2O_3/ ($CaO + Na_2O + K_2O$)] of these samples are of 1.34 to 1.67, whereas the A/NK values [Al_2O_3/ ($Na_2O + K_2O$)] range from 1.38 to 1.72 indicating a peraluminous composition (**Figure 3.7 B**). The A/CNK and A/NK ratios are expressed as molar ratios.

The spidergrams (**Figure 3.7 E**) of these rocks are generally parallel and typical of calc-alkaline series with enrichments in LILE (Large Ion Lithophile Element, K to Th) in addition to strong Sr, Ba, P and Ti negative anomalies. These anomalies can be explained by feldspar (Sr and Ba) and accessory mineral fractionation and accumulation in the source as apatite (P) and titanite (Ti), whilst the Nb anomaly is likely to be characteristic of the melt source (See discussion section). Their chondrite-normalized REE (Rare Earth Element) patterns (**Figure 3.7 F)** are also typical of calc-alkaline rocks, with fractionated LREE and flat HREE patterns, minor Ce and Pr negative anomalies in some of the samples, in addition to a notable negative Eu anomaly.

The Askaoun batholith of the Assarag Suite are distinctive due to their high Fe_2O_3(T) contents oscillating between 7.76–9.01 wt%, and 4.1–5.57 wt% for the quartz diorite and the granodiorite, respectively. The silica contents vary from 57.4 to 66.54 wt%. The A/CNK ratios

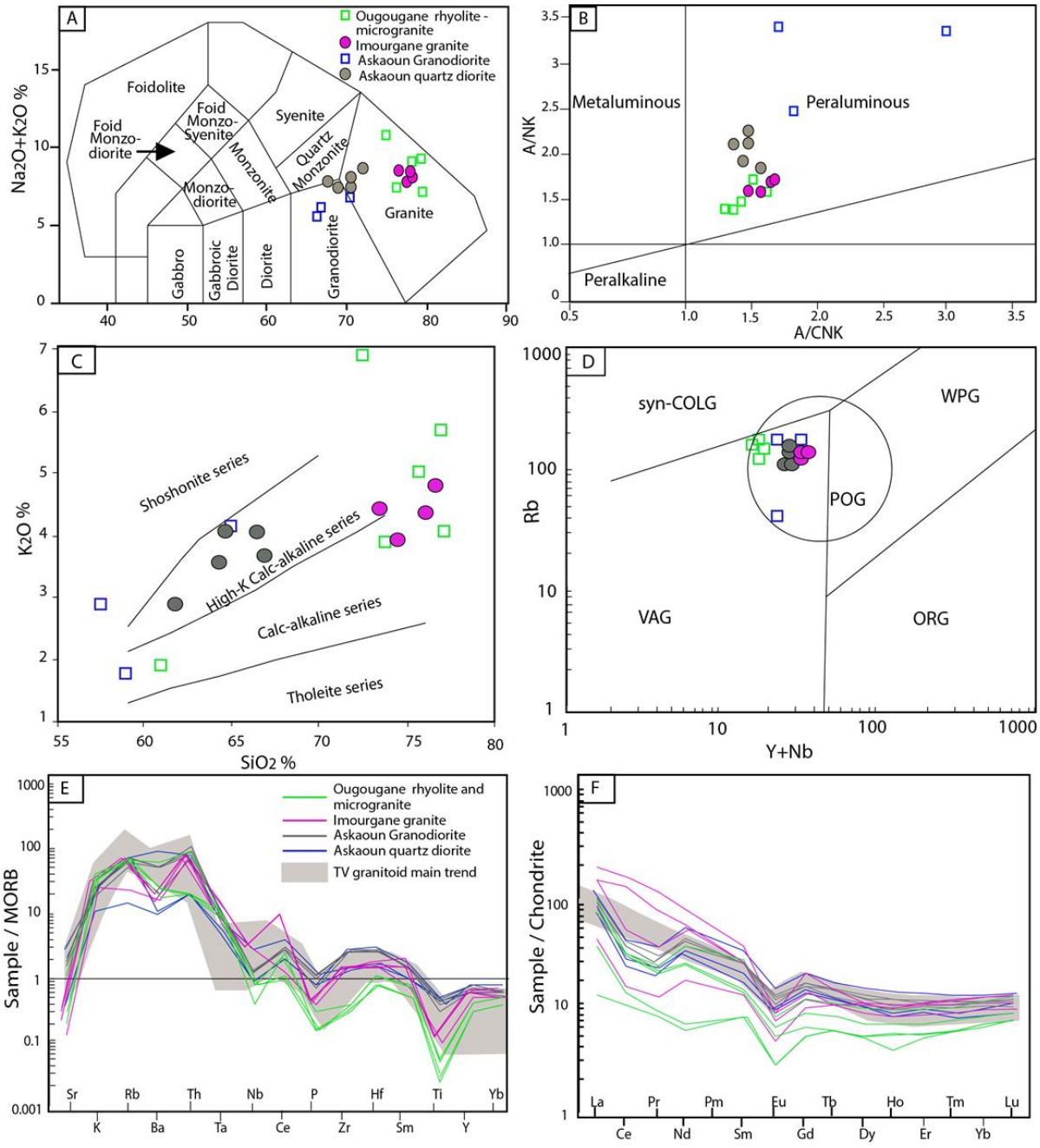

Figure 3.7
Whole rock geochemistry of the Late Ediacaran granites of the Imourkhssen area. A) Total alkali ($Na_2O + K_2O$) (wt%) versus SiO_2 (wt%) diagram after Middlemost (1994). B) A/NK versus A/CNK diagram of Maniar and Piccoli (1989). C) SiO_2 vs. K_2O diagram after Boynton (1983). D) Tectonic discrimination Rb vs. Y + Nb diagram after Pearce et al. (1984); Pearce (1996) syn-COLG: syn-collisional granite, WPG: within plate granite, POG: Post-collisional granite, VAG: volcanic arc granite, ORG: oceanic ridge granite . E) and F) Primitive mantle-normalized trace-element spidergram and chondrite- normalized REE distribution diagrams of the LEMS compared to data of Toummite et al. (2012) shown in grey.(Toummite et al., 2012) shown as grey trends. The MORB values are from Pearce (1983), and the chondrite values are from Boynton (1983).

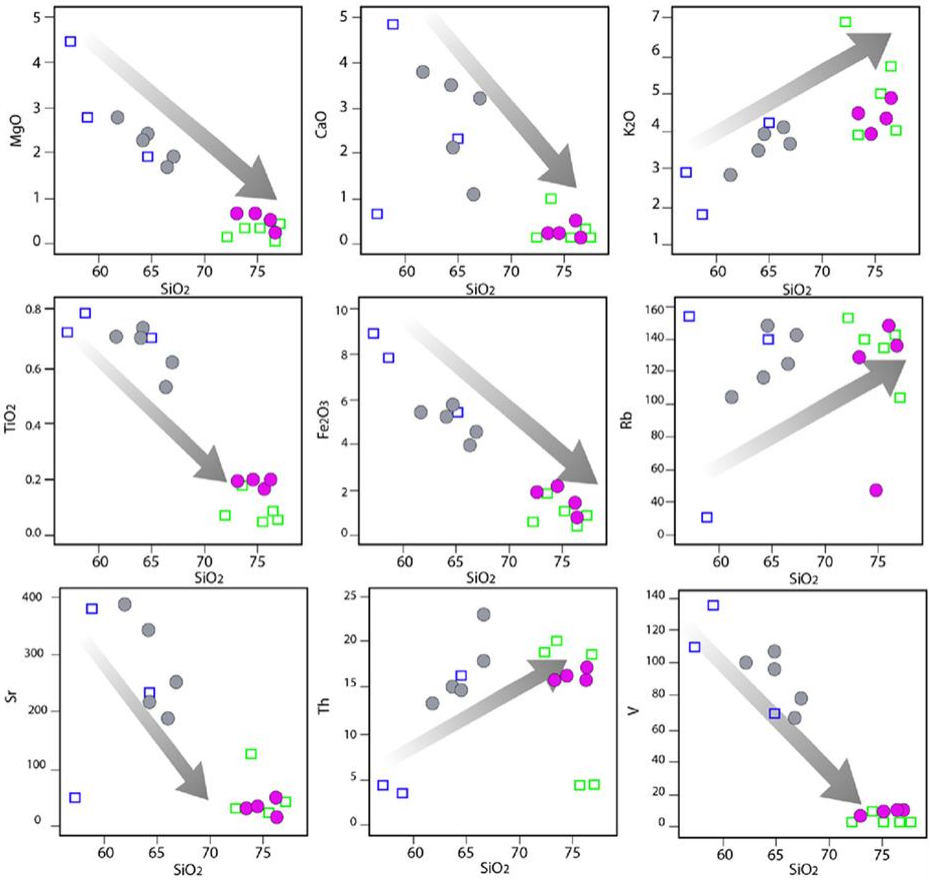

Figure 3.8
Harker diagrams of selected major oxide and trace elements content of the Late Ediacaran granites of the TV area. The proximal evolutionary trends are highlighted by the grey arrows.

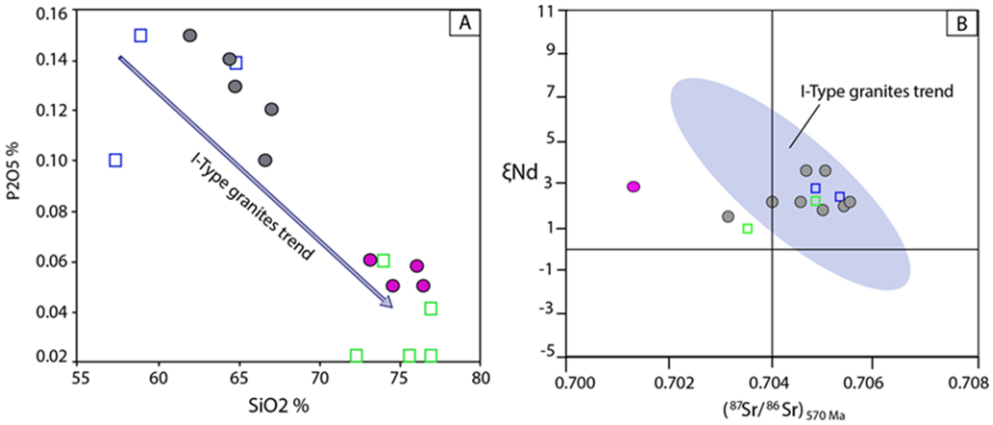

Figure 3.9
A) P_2O_5 vs. SiO_2 classification diagram after Sylvester (1994). Data for geochemical trend are from this study. B) Sr and Nd isotopic initial ratios (εNd vs ($^{87}Sr/^{86}Sr$)i at 570 Ma for the TV magmatic rocks from Toummite et al. (2012), I-Type granite values from Raeisi et al. (2024).

of 1.37–2.90 indicate a peraluminous composition (**Figure 3.7 B**). Their spidergrams and REE patterns are close to those of the Ougougane Suites, but with less pronounced Sr, Ba, P, Nb, Ti and Eu negative anomalies.

Though their Nb-Ta arc signature, the LEMS samples straddle the post-orogenic field in the Rb versus (Y + Nb) tectonic discrimination diagram (**Figure 3.7 D**). Their Harker diagrams show a negative correlation of SiO_2 with MgO, FeO, CaO, TiO_2, Sr and V, and a positive correlation with K_2O, Rb and Th (**Figure 3.8**). Such compositional variations could be produced by increasing crystal fractionation with increasing SiO2 concentration (Dabiri et al., 2018).

The LEMS of the Imourkhssen area plot in the high-K calc-alkaline series in the K_2O versus SiO_2 diagram (**Figure 3.7 C**), as already mentioned by (Toummite et al., 2012). They exhibit a peraluminous composition and lack Al-rich minerals (e.g., muscovite, cordierite, and garnet). This geochemical feature is consistent with an I-type affinity (Chappell, 1999), that is portrayed as well by Nd and Sr isotopes values (εNd-560Ma between + 0.8 and + 3.5, and initial $^{87}Sr/^{86}Sr$ between 0.7034 and 0.7065; Toummite et al., 2012) (**Figure 3.9 B**) pointing to a mainly juvenile source (mantle or young lower crust) (Toummite et al., 2012).

The negative correlation of SiO_2 versus P_2O_5 (**Figure 3.9 A**) for the LEMS also suggests an I-type granite trend (Chappell and White, 2001; Yang et al., 2016; Wang et al., 2021) for the LEMS. The entire geochemical characteristics of the LEMS is typical to post-collisional magmas (Liégeois et al., 1998). Those magmas have been emplaced in the framework of the Late Ediacaran collapse of the Pan-African orogen (Thomas et al., 2002; Gasquet et al., 2005).

3.6.3 X-Ray data

The XRD analyses were carried out for the identification of various primary and secondary mineral assemblages in several samples, especially those related to alteration zones (**Figure 3.10**). The serecitic mineral assemblages (i.e., 22im05) is composed mainly of quartz and sericitized feldspars. The Imourgane granite (i.e., 22im02) is composed of quartz, feldspar, biotite and muscovite. Furthermore, X-Ray analysis delineate the quartz-chlorite-sulfide assemblages (i.e., 22im17; 22im 13C), which form the ore-bearing structures (see mineralization section). The pervasive silica enrichment within the Imourgane granite is also outlined (i.e., 22im20). It impacts the outcrops near the galleries, where epsomite ($MgSO_4 \cdot 7H_2O$) encrustations can be found (i.e., T1). This mineral was recently discovered to be useful for geochemical classification (Ferdous and Podder, 1970).

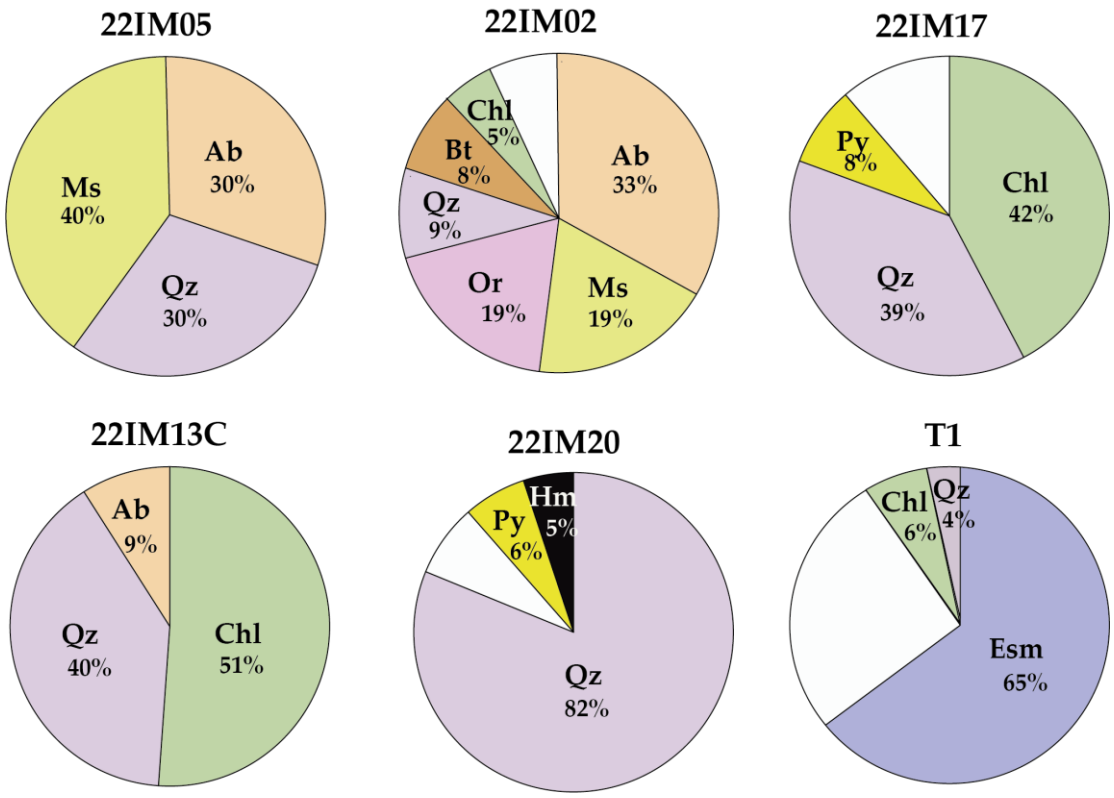

Figure 3.10
Mineralogy of the Imourkhssen deposit determined after XRD analysis. Abbreviations: Qz: quartz, Ab: albite, Chl: chlorite, Pl: plagioclase, Ms: muscovite, Or: orthoclase, Py: pyrite, Hm: hematite, Bt: biotite, Esm: epsomite. Mineral abbreviations from Whitney and Evans (2010); Warr (2021).

3.6.4 Hydrothermal alteration and vein system

Hydrothermal alteration: Field observations and petrographic examinations have allowed to identify several hydrothermal alteration assemblages including: (i) potassic, (ii) chlorite-sericite, (iii) serecitic and (iv) propylitic alteration (**Figure 3.11**).

(i) The potassic alteration affects the Imourgane granite, and exhibits disseminated molybdenite and molybdenite veinlets (**Figure 3.11 A**). This alteration is highlighted by the characteristic brick-red color of secondary K-feldspars, locally crossed by stockworks of chlorite. The altered feldspar to clay minerals (kaolinite), along with quartz, chlorite and altered biotite make up the potassic alteration mineral assemblage.

(iii) The serecitic or phyllic alteration overprints a large area of the Imourgane granite as evidenced by the large bleached zones (**Figure 3.11 C**) extending over tens of square meters. It consists of quartz and sericite along with pervasive pyritization and silicification.

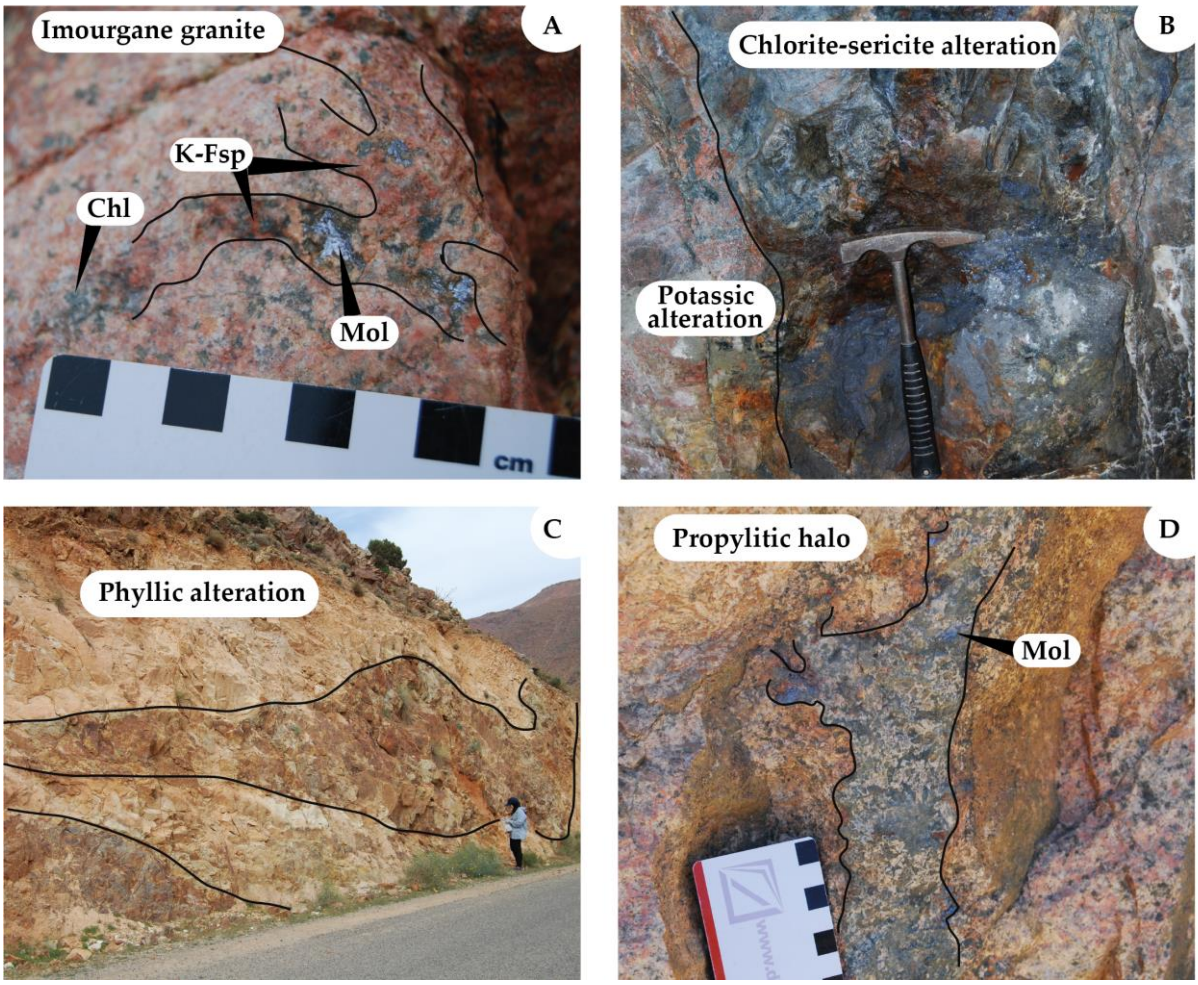

Figure 3.11
Hydrothermal alteration in the Imourkhssen area. A) Potassic alteration highlighted by brick-red colored K-feldspar and molybdenite (Mol) dissemination within the Imourgane granite. B) Chlorite-sericite alteration with molybdenite dissemination. C) Phyllic or sericitic alteration highlighted by bleached outcrops. D) Propylitic halo within the Imourgane granite along with molybdenite veinlets. Mineral abbreviations: K-Fsp: K-feldspar, Chl: chlorite, Mol: molybdenite.

(ii) The chlorite-sericite alteration surrounds the potassic alteration zone. It occurs as grey dark halos surrounding disseminated molybdenite (**Figure 3.11 B**). This alteration consists of chloritized biotite crystals along with quartz and sericitized plagioclase.

(iv) The propylitic alteration consists of chlorite alteration halos along with epidote and local calcite (**Figure 3.11 D**).

Vein System: The predominant strike orientation of veins and their controlling faults are of NNE-SSW to N-S directions. In the studied area, several vein types are recognized and can be categorized into four types: (i) aplitic mega lenses, (ii) stockwork-type quartz veins, (iii) quartz-hematite-barite veins and (iv) quartz-chlorite-sulfide lenses (**Figure 3.12**).

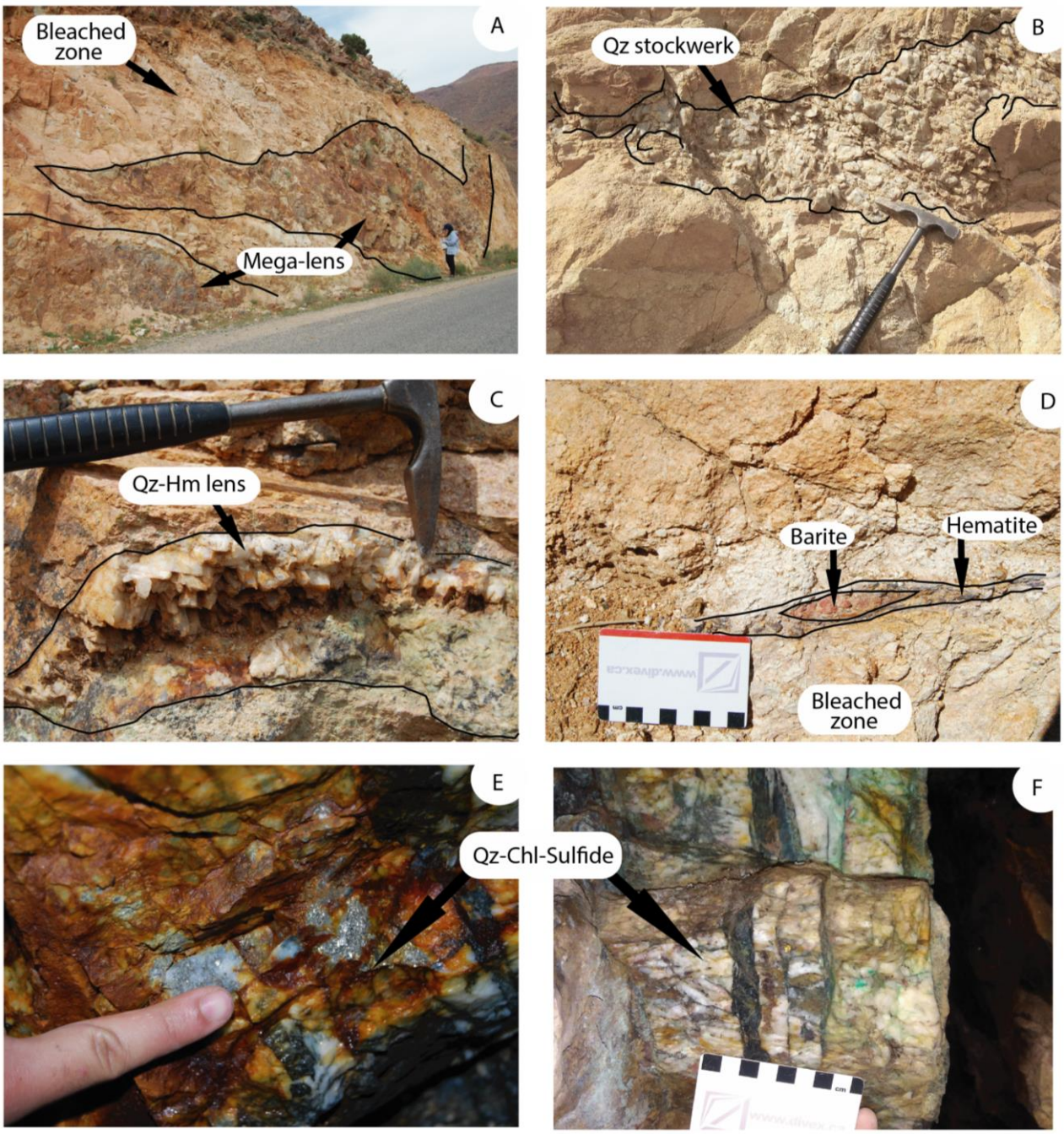

Figure 3.12
Field photographs of hydrothermal vein types in the studied area: (A) Aplite mega-lens surrounded by the bleached zone. (B) Quartz stockworks. (C) Quartz-hematite lens. d) Barite-hematite lens out crops in phyllic alteration zone. E) and F) Quartz-Chlorite sulfide lenses.

(i) The aplitic mega lenses occur as N-S oriented structures within the Imourgane granite (**Figure 3.12 A**). These structures consist mainly of quartz, sericitized K-feldspars and plagioclase with minor disseminated pyrite. The aplitic lenses extend for several meters, especially in the sericitized areas.

(ii) Stockwork-type quartz veins are shown in (**Figure 3.12 B**) and characterized by anastomosing quartz networks affecting the Imourgane granite. These veins occur more frequently within the altered potassic and serecitic bleached zones.

(iii) Quartz-hematite veins manifest are decimetric (**Figure 3.12 C**), they evolve to barite-hematite veins, and are exclusively developed in the Imourgane granite (**Figure 3.12 D**). The evolution from the quartz-hematite to baryte-hematite assemblages could be the result of quartz transformation to baryte during cooling of the hydrothermal solutions, if the fluid's composition and the physical conditions (T, P) allow it (see Burisch et al., 2017). The barite-hematite veins zonation is observed at the small scale, creating a centimetric cockade texture. Thus, an active pulsating process during the mineralization is suspected (Jébrak et al., 1998).

(iv) Quartz-chlorite-sulfide veins occur as NNE-SSW to N-S trending mineralized structures (**Figure 3.12 E, F**) affecting mainly the Askaoun granodiorite and the Imourgane granite. These structures exhibit crack-and-seal and cockade textures (**Figure 3.13 A**) along with hydrothermal breccia (**Figure 3.13 B**) highlighting multiple episodes of fluid circulation (Jébrak and Marcoux, 2008).

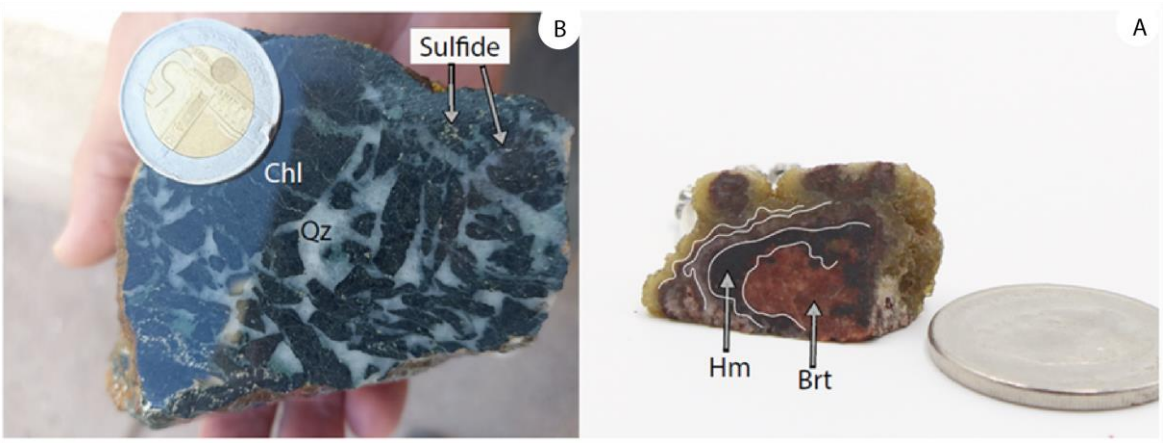

Figure 3.13
A) Cockade texture in a centimetric barite-hematite vein observed within the Imourgane granitic intrusion. B) Hydrothermal breccia affecting the quartz-chlorite-sulfide lens in a gallery of the Talat nl'bour area. Mineral abbreviations: Chl: chlorite, Qz: quartz, Hm: hematite, Brt: barite.

3.6.5 The Imourkhssen porphyry style mineralization

The mineralization of the Imourkhssen Cu±Mo±Au±Ag deposit can be divided into a supergene period and a magmatic-hydrothermal period, which includes primary dissemination and secondary NNE-SSW to N-S bearing system stages (**Figure 3.14**).

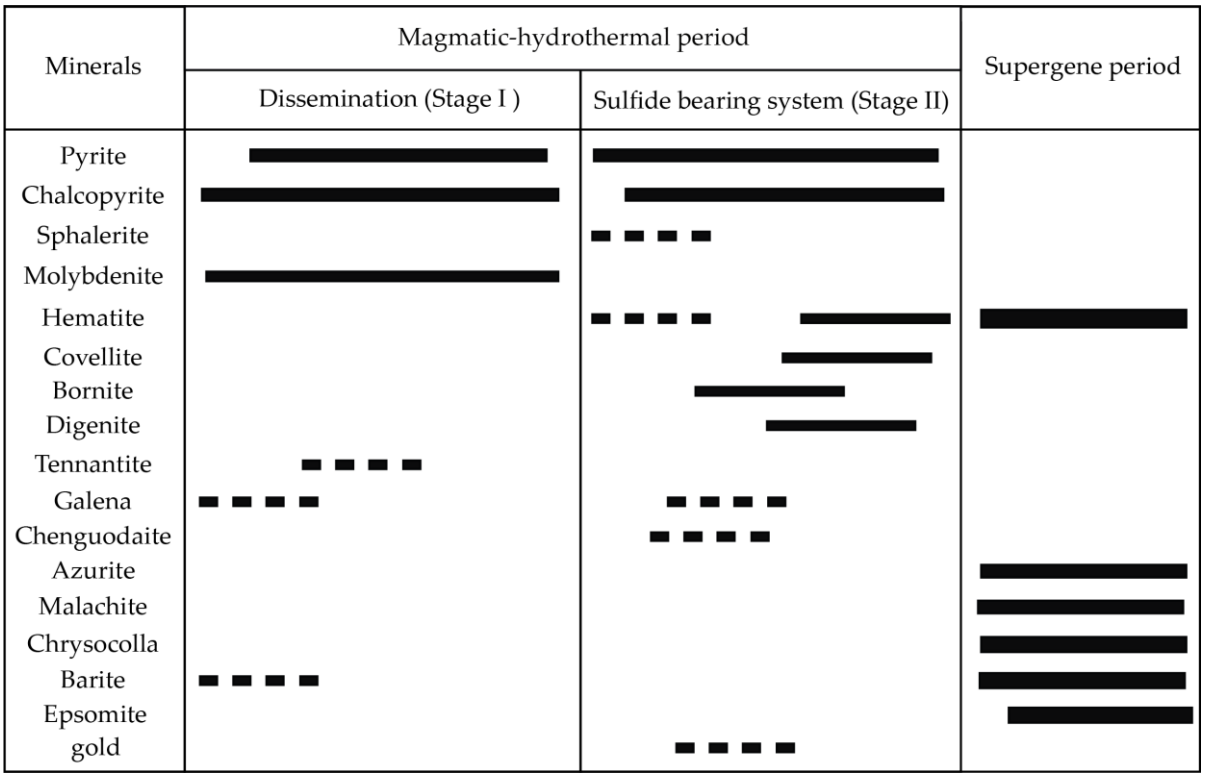

Figure 3.14
Inferred paragenetic sequence of the Imourkhssen Cu±Mo±Au±Ag deposit (modified from Belkacim, 2014).

The molybdenite occurrences and Fe-Cu disseminated sulfides belong to the primary ore stage, while the NNE-SSW to N-S quartz-chlorite-sulfides bearing system is assigned to the secondary ore stage (**Figure 3.14**):

(i) The molybdenite is exclusively enclosed by the small elongated Imourgane granite. It occurs as fine-grained disseminations or fine flake aggregates in the potassic and the chlorite-sericite alteration zones (**Figure 3.15 A** and **3.16 A**), and as centimetric veinlets within the propylitic halos (**Figure 3.16 B**). The microprobe analysis of the two molybdenite types show different geochemical compositions (**Figure 3.17, Appendix 3**), suggesting that the molybdenite was remobilized during multiple fluid circulation events.

(ii) Fe-Cu sulfide disseminations occur as patchy pyrite, chalcopyrite, galena and tennantite mineralization in the Askaoun granodiorite (**Figure 3.15 B**) and the Imourgane granite. Pyrite contains composite inclusions of chalcopyrite and galena (**Figure 3.15 C**). Tennantite is enclosed in calcite veins, while scarce barite and bornite crystals locally occur within a Zaghar doleritic dyke sample (**Figure 3.15 D**).

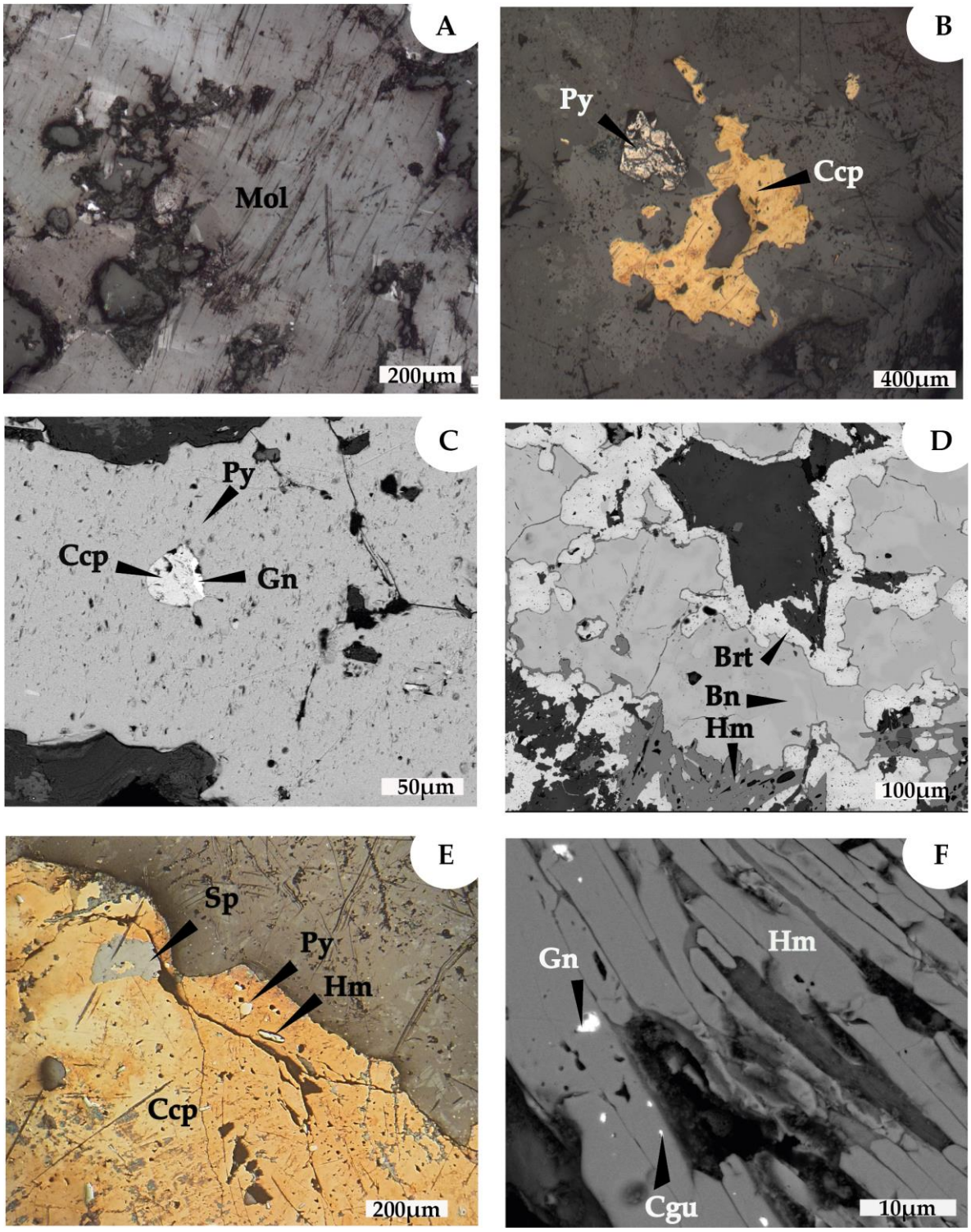

Figure 3.15
Reflected light (RL) photomicrographs and scanning electron microscopy (SEM) of: A) Molybdenite (Mol) flake in the Imourgane granite. B) Pyrite (Py) and chalcopyrite (Ccp) dissemination in the Askaoun granodiorite. C) Galena (Gn) inclusion surrounded by chalcopyrite, that is enclosed itself by pyrite. D) Barite (Brt), bornite (Bn) and hematite assemblage within the Zaghar dyke sample. E) Sphalerite (Sp), hematite (Hm) and pyrite inclusions within the chalcopyrite. E) Hematite displays chenguodaite (Cgu) and galena inclusions. Mineral abbreviations from Whitney and Evans (2010); Warr (2021).

(iii) NNE-SSW to N-S quartz-chlorite-sulfides veins are well developed in the Talat nl'bour area, where they are hosted mainly by the Askaoun granodiorite, as well as the Imourgane granite, in which traces of chenguodaite, a silver telluro-sulfide, have been identified (**Figure 3.15 F**).

Overall, the post mineral assemblage is formed by secondary chalcopyrite exhibiting sphalerite and pyrite inclusions (**Figure 3.15 E**). Bornite, digenite and covellite occur as replacement phased as small veinlets, mantle the primary hypogene ore minerals, whereas traces of gold have been previously documented (Belkacim, 2014). These mineralized veins display crack-and-seal, cockade textures and a hydrothermal breccia along NNE-SSW to N-S trends, suggesting multiple episodes of fluid circulation (see veining system section). The supergene stage achieved by the mineral assemblage composed by hematite, azurite, malachite, barite, chrysocolla and epsomite.

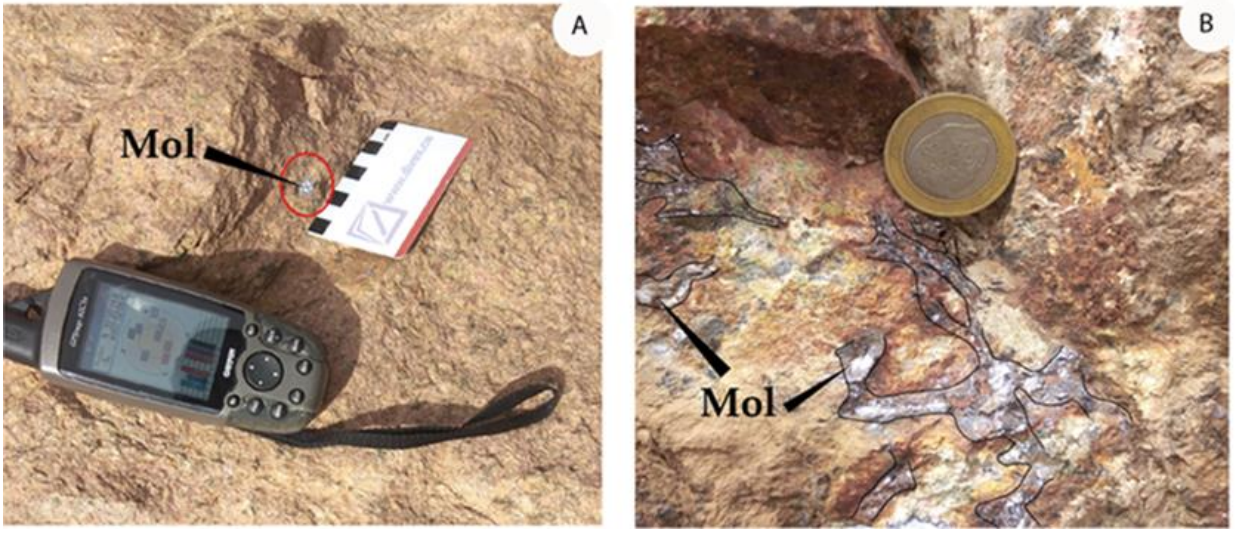

Figure 3.16
A) Molybdenite dissemination within the Imourgane granite. B) Molybdenite veinlets within a propylitic halo.

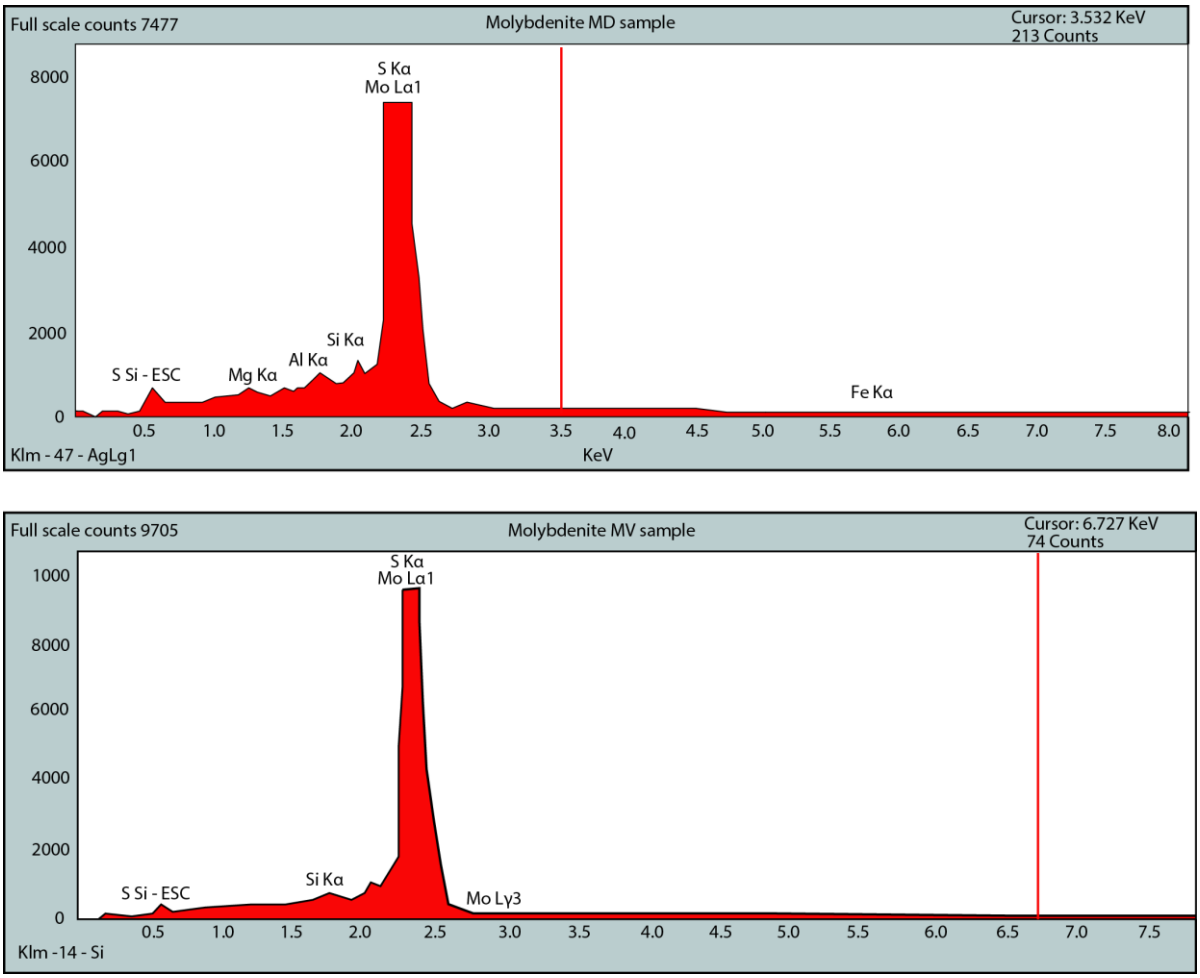

Figure 3.17
Quantitative results for molybdenite dissemination (MD) and molybdenite veinlets (MV) powdered samples.

3.6.6 LA-ICP-MS U/Pb zircon dating

The ore-bearing Imourgane granite was previously thought to be part of the star-shaped barren Imourkhssen granite. To clarify the ages and the timing of the associated porphyry mineralization, U-Pb geochronology was conducted on both granites. Sample J23IM09 represents the Imourgane granite, while sample J23IM13 has been collected from the star-shaped barren granitic intrusion of the Imourkhssen granite. One hundred and two zircon grains were collected for LA-ICP-MS (Laser ablation inductively coupled plasma mass spectrometry) U-Pb dating. Most of the zircons were euhedral and prismatic, with rare elliptic ones. CL images show mostly homogeneous texture with some oscillatory zoning (**Figure 3.18**). Many zircon grains exhibit titanite inclusions and sharp edges.

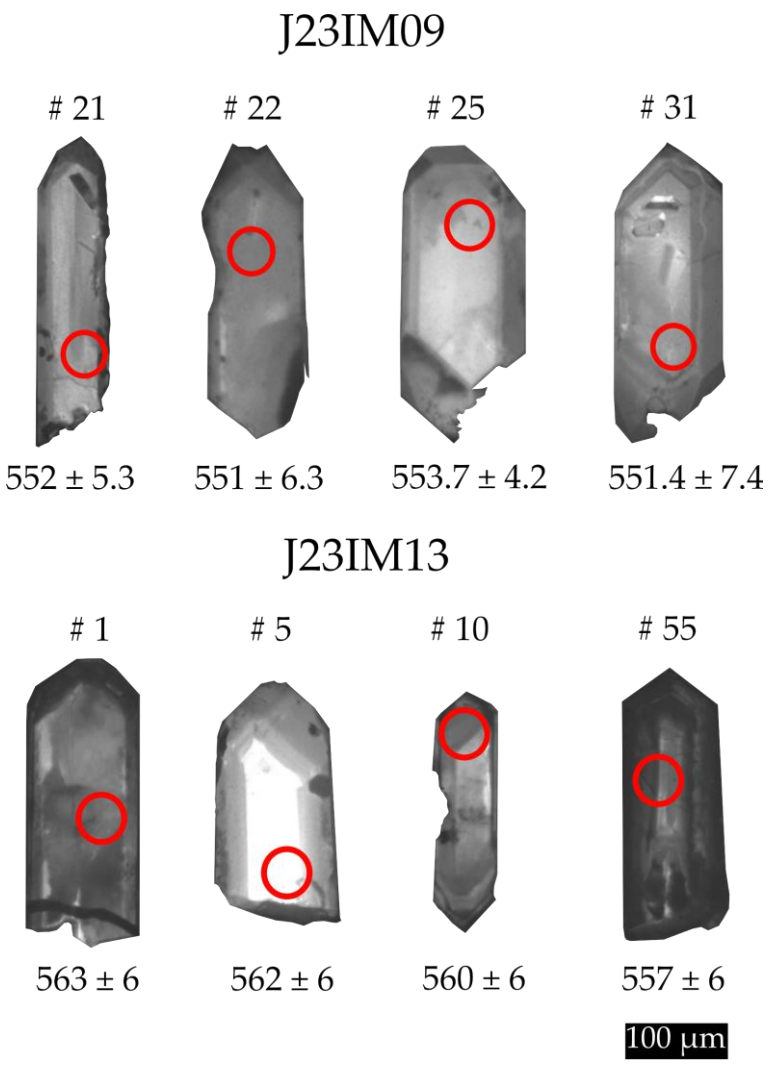

Figure 3.18
Cathodoluminiscence images for the dated zircon from J23IM09 and J23IM13 samples.

The age interpretations and calculations were performed using all the zircons that are concordant within error (**Appendix 4**; **Figure 3.19**). The ages of the Imourkhssen and the Imourgane granites show a homogeneous distribution, and can be subdivided into three classes. The first consists of an older generation with ages over ca. 580 Ma. These ages are considered to be inherited from the Saghro Group and older formations. The second class is made up of a younger generation yielding scattered ages less than 550 Ma, which we interpret as resulting from Pb loss and likely due to the hydrothermal alteration recognized in the Imourkhssen area. The remaining concordant analyses are used for the concordia and weighted mean $^{206}Pb/^{238}U$ age calculations. Nineteen zircons for the Imourgane granite (J23IM09) yielded an age of 550 ± 2 Ma, while thirty-nine zircons from the Imourkhssen granite (J23IM13) yielded and 558 ± 1 Ma.

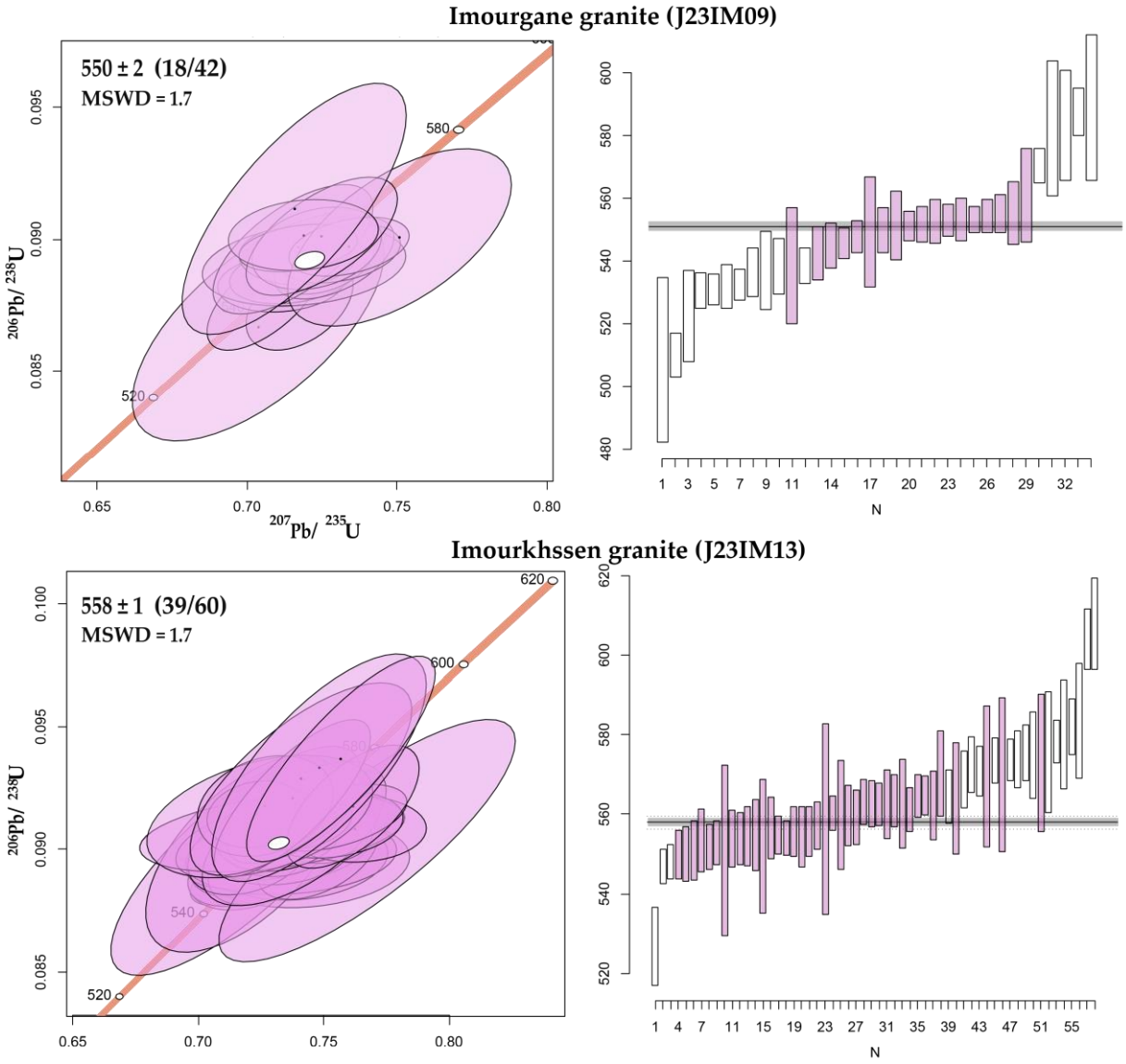

Figure 3.19
U–Pb concordia and Pb^{206}/U^{238} weighted mean diagrams showing LA-ICP-MS zircon ages of 550 ± 2 Ma and 558 ± 1 Ma for the J23IM09 and J23IM13 samples, respectively. Error ellipses are given at 2σ level. Ages were calculated using Isoplot R (Vermeesch, 2018).

3.7 Discussion

3.7.1 Timing of the plutonic magmatism

The previous geochronological data reveal the existence of, at least three granitoid intrusions corresponding to three magmatic pulses during the Late Ediacaran, one of which contains the Cu±Mo±Au±Ag Imourkhssen deposit (Thomas et al., 2004; Toummite et al., 2012; Belkacim et al., 2021). The time sequence of this magmatism is described below:

The Askaoun granodiorite: It is dated at 575 ± 8 Ma (SHRIMP method) (Thomas et al., 2002) with a similar age of 575 ± 2 Ma reported by Belkacim et al. (2021). LA–ICP–MS zircon U-Pb dating by Toummite et al. (2012) yield younger ages of 558 ± 2 Ma and 558 ± 6 Ma. On the other hand, an additional SHRIMP U-Pb zircon study provided both an older age of 579 ± 7 Ma for the same granodiorite outcropping in the douar Eç-çour area (El Moume et al., 2020) (the northeastern part of the studied area). These ages provide evidence of the multi-stage feature of the Askaoun granodiorite.

Based on a geochronological compilation of ages published throughout the Saghro domain as defined by (Schulte et al., 2022), the Ouarzazate Group (OG) seems to have been emplaced over three pulses (Belkacim et al., 2021). In this paper, we propose that the initial magmatic pulse (1st flare-up) of the Ouarzazate Group took place around ca. 575 Ma. This age announces the beginning of the deposition of the Ouarzazate Group (Thomas et al., 2004; Belkacim et al., 2021). In the Imourkhssen area, Belkacim et al., (2021) documented same age within error for a rhyodacitic ignimbrite (577 ± 3), and a rhyolitic flow (574 ± 3 Ma) at the bottom of the volcanic series. A similar U-Pb age within error has been measured from the Bas Drâs inlier for the Taourgha granite (575± 2 Ma; Aït Malek et al., 1998). In the Saghro massif, this age was reported for a rhyolitic tuff and for the Wizergane granodiorite (574± 7 Ma and 577± 6 Ma, respectively; Walsh et al., 2012), and for the Igoudrane granodiorite (575± 10 Ma; Baidada et al., 2019) and Bou Teglimt granite (576± 4 Ma; Errami et al., 2009) as well. In the Siroua massif, similar age is reported by Pelleter et al., (2016) for a rhyolitic plug (578 ± 4 Ma) and by Thomas et al., (2002) for the Tourcht Diorite (579 ± 7 Ma), a rhyolite from the Tikhfist Formation (571 ± 8 Ma), the Aguins member (577 ± 8 Ma), and the Tilsakht Granite (579 ± 7 Ma). In the Zenaga inlier, a rhyolitic ignimbrite and the Tilsakht granite have been dated at 575 ± 3 Ma and 579 ± 7 Ma by Letsch et al. (2018) and Thomas et al. (2002), respectively. In the Sidi Ifni Inlier, it has been considered that the earliest magmatic event occurred at c. 590 Ma (Schulte et al., 2022). This was evidenced by the emplacement of the Taoulecht and Tirhite intrusions.

The Imourkhssen granite: A SHRIMP U-Pb zircon study of the Imourkhssen granite produced an age of 562 ± 5 Ma (Thomas et al., 2002), whereas an age of 561 ± 3 Ma has been obtained using LA–ICP–MS U-Pb dating of zircon (Toummite et al., 2012). The LA-ICP-MS U-Pb zircon dates conducted from this study yield an age of 558 ± 1 Ma for the Imourkhssen granitic intrusion of the TV area.

This age of approximately 560 Ma could correspond to the 2nd pulse of the Ouarzazate Group magmatism that is also reported in many inliers of the Anti-Atlas belt. In the Sirwa inlier, an andesitic tuff is dated at c. 562 ± 1 Ma (Belkacim et al., 2021). This tuff contains inherited zircons, the age of which overlaps with that of the Saghro the Saghro Group (<610 Ma), as is the case with the Imourkhssen granite. The ignimbrite of Sirwa has also been dated by Mifdal and Peucat (1985) at 563 ± 5 Ma. The ages of 558 ± 2 Ma and 558 ± 6 Ma obtained for the Askaoun by Toummite et al. (2012) could be assigned to the second pulse of the Ouarzazate Group. A similar age of 560 ± 2 Ma was for the Tarçouate gabbro-norite from the Bas Draâ inlier (Aït Malek et al., 1998). In the Ighrem inlier, the Ighrem tuff, Minount rhyodacite and Houssi El Gah rhyolitic are dated at 564.6 ± 3.2 Ma, 562.89 ± 0.49 Ma and 560.0 ± 2.1 Ma, respectively (Maloof et al., 2005). A rhyolitic ignimbrite in Tagragra of Tata yielded a comparable age (565 ± 7 Ma; Walsh et al., 2002). Similar ages are reported in the Agadir-Melloul inlier, many rhyolitic domes yield ages bracketed between 567 Ma and 564 Ma (Blein et al., 2014). In the Saghro inlier, the age of 560 ± 5 Ma was reported for a mineralized halo of the Imiter deposit (Levresse, 2001). whereas the Isk-n-Alla granite yielded ages of 566 ± 20 Ma O'Connor (2010) and 559 ± 5 Ma (Walsh et al., 2012). An age of 564 ± 6 Ma was recorded from the Ikniwn pluton (Tuduri et al., 2018). Similar ages are reported by Schulte et al., (2022) for the volcanic and plutonic rocks in the Ifni inlier (e.g., .the Mesti monzogranite at 567 ± 4 Ma and Ifni syeno-granite at 566 ± 4 Ma).

The Ougougane granite: It yielded a LA–ICP–MS zircon U-Pb age of 550 ± 1.5 Ma (Belkacim et al., 2021). In this study, geochronological dating has been performed on the ore-bearing granite, that has been formerly assigned to the Amassine Suite. LA-ICP-MS U-Pb dates on zircon yielded an age of 550 ± 2 Ma for the mineralized granite, leading to constrain its affiliation among the Ougougane Suite, and to renamed it as the Imourgane granite.

Similar ages are documented in many inliers of the Anti-Atlas (c.a 550 Ma) and could correspond to the 3rd pulse of the Ouarzazate Group. In the Ougnat inlier, the Bou Madine rhyolite has been dated at 552 ± 5 Ma by Gasquet et al. (2005), and at 553 ± 16 Ma (Levresse, 2001). In the Saghro inlier, the Takhatert and Tachkakacht rhyolites have been dated at 550 ± 3 Ma and 547 ± 8 Ma respectively (Levresse, 2001). This period of magmatism could be correlated to regional events, that occurred throughout the whole Anti-Atlas, mainly the transition from a transpressive to transtensive tectonic regime by the orogenic collapse (Levresse, 2001).

3.7.2 Ore genesis and source in the framework of the geodynamic context of the Anti-Atlas

To reconstruct the magmatic-hydrothermal processes responsible for the formation of the Imourkhssen Cu±Mo±Au±Ag deposit, the regional geodynamic context has to be considered. As clearly reported by Belkacim, (2014), the ore genesis of the Imourkhssen deposit is linked to the emplacement of the LEMS. This period is clearly correlated to the huge metallogenic activity associated with the highly silicic magmatism of the Ouarzazate Group. During this epoch, a large volume of juvenile material, precious metals and chalcophile elements was added to the continental crust all over the Pan-African Anti-Atlas belt system (Cheilletz et al., 2002; Levresse et al., 2004; Gasquet et al., 2005). Therefore, numerous deposits in the Moroccan Anti-Atlas, particularly in the Saghro domain as defined by Schulte et al., (2022), seem to be affected by this magmatic event. This magmatic manifestation triggered pervasive hydrothermal activity and gave rise to world-class epithermal mineralization and base metal porphyry deposits (e.g., Imiter and Zgounder (Ag-Hg), Bou-Azzer (Co-Ni-As-Ag-Au), Iourirn (Au), and Bou Ma-dine (Cu-Pb-Zn-Au-Ag); Gasquet et al., 2005; Belkacim et al., 2021).

In the Ouzellagh-Siroua Salient, the LEMS show a high-K calc-alkaline I-type granite affinity, with enrichment in LILE, relative depletion in HFSE and a pronounced Nb-Ta anomaly. These geochemical features are akin to rocks derived from subduction-related sources (Green, 1995). Nevertheless, this signature is considered as an inherited signature, transferred to the igneous rocks during the remelting of subduction-related lithosphere (Morris et al., 2000). Therefore, the emplacement of the LEMS invokes the contribution of a recycled subduction-related component (Toummite et al., 2012; Belkacim et al., 2017). This component could be involved in the mineralization as indicated by several studies especially for Mo and Au mineralization (Chen et al., 2017). Its significant role is due to the H_2O, CO_2 and Cl provided from the subducted material, which ultimately contributes to the enhancement of associated hydrothermal systems (Sillitoe, 2010).

In general, the metal source for porphyry copper deposits is still debated. However, a crustal component is widely invoked for the genesis of fertile sulfide rich magmas. Feteha et al., (2022) suggest that the Gattar fertile magmas originated from an underplated crustal source that was fertilized by metasomatized underplating mantle derived melts. This magmatism was responsible for the molybdenite bearing granitic intrusions in the northern Eastern Desert of Egypt. Wang and Ji (2024) assume that the mineralization of the fertile Yulong porphyry copper deposit (Eastern Tibet) originated from an eclogitized sulfide-rich juvenile lower crust melt.

These melts are fueled by the injection of an ultrapotassic subduction-related metasomatized subcontinental lithospheric mantle derived melt. Mao et al. (2011) presume the melting of the lower crust for the Mo enrichment, whilst the copper is suggested to be sourced from mantle melts, including subducted slab. Nevertheless, Crusius et al. (1996) assumes that Mo is more enriched in reduced sediment. In this regard, Delibaş et al. (2017) associated the Mo enrichment of the porphyry Mo–Cu Pınarbaşı system (Western Turkey) with the melting of terrigenous sediment, or at least the melting of the lower crust and metasomatized mantle by subducted sediment derived-fluids.

Analogous with the observations made by Delibaş et al. (2017), the Imourkhssen porphyry mineralization seems to contains a terrigenous component. The chondritic Zr/Hf ratios of the Assarag Suite are scattered within the range of crustal material (32-37), while the rocks of the Ougougane Suite show low Zr/Hf ratios (26-32). This feature highlights its fractionated nature (Claiborne et al., 2006) . Chondritic values of Zr/Hf are from (Claiborne et al., 2006). Moreover, the ages of many inherited zircons (c.a 720-630 Ma) of the Imourkhssen and Imourgane granites correspond to the subduction episode occurred in the Anti-Atlas during the Pan-African orogeny. Therefore, the LEMS could have originated from melts that include recycled subducted sediments.

The emplacement of the LEMS is contemporaneous with the widespread Ouarzazate Group and its subsequent intense hydrothermal activity. This thermo-magmatic event occurred in a trans-tensional tectonic regime corresponding to the post-collisional stage of the Pan-African orogeny that evolved towards extension during the Cambrian (Gasquet et al., 2005). In this context, the uprising of the asthenospheric mantle close to the Moho generated a high regional heat flow which fueled the melting of the lithospheric or even the asthenospheric mantle itself (Toummite et al., 2012), in addition to the lower crust with the incorporated recycled juvenile sulfide rich subduction components.

The involvement of mafic components may have played a significant role in supplying sulphur and chalcophile metals to the parental magma, thereby promoting metal enrichment (Sillitoe, 2010 and references therein). We can assess the likely involvement of the Zaghar mafic dykes on the Imourkhssen ore genesis using the following observations: (i) many porphyry ore deposits record the associations of rhyolites of bimodal basalt-rhyolite suites (Carten et al., 1993); (ii) the Zaghar mafic dykes of the Imourkhssen deposit area are a coeval with the Late Ediacaran granitoids, as suggested by mingling structures; and (iii) disseminated mineralization

is observed within the Zaghar dykes in the Imourkhssen area. Those observations lead us to assume the possible contribution of this mafic component in the evolution of the Cu±Mo±Au±Ag Imourkhssen porphyry mineralization.

The multi-pulse character of the Askaoun pluton evidenced by older and younger ages, and by new geophysical data interpretations (Ferraq et al., 2023), and the proximity of the samples dated by Toummite et al., (2012) to the studied area, lead us to constraint the age of the mineralized granodioritic rocks of Askaoun pluton at c.a 558 Ma. Consequently, the Imourkhssen Cu±Mo±Au±Ag porphyry style mineralization is considered to be associated with the emplacement of the Askaoun granodiorite (c.a 558 Ma) and the Imourgane granite (c.a 550 Ma) that are coeval with the 2nd and 3rd magmatic pulses of the Ouarzazate SLIP (See next section). Field observations and detailed analysis of the Imourkhssen mineralization led us take into account the following issues:

- All the late Ediacaran granitoids follow the same trend as mentioned in the geochemistry section. Thus, these rocks belong to a single parental magma that evolved progressively and gave rise to multiple pulses more and became more fractionated and differentiated over time (i.e., Ougougane Suite)

- Secondly, the Cu sulfide mineralization occurs mainly within the Askaoun granodiorite. This pluton locally contains elevated Cu and Au values up to 0.30 wt% and 22 g/t on selected samples, respectively (Mining Research and Participation Office, 1976). In this framework, the probable contribution of the Zaghar mafic dykes for Cu and Au mineralization could be envisaged because of their co-magmatic feature with the Askaoun pluton.

- The molybdenite occurrences are restricted to the more felsic Imourgane granite, which is widely known for porphyry mineralization (e.g., similar to Mamut, East Malaysia) (Kósaka and Wakita, 1978). These observations imply not only a late molybdenite precipitation, but also a spatial shift from the Cu-Au bulk (Sillitoe, 2010). This feature is portrayed by the Imourgane granite Mo occurrences and the Askaoun Cu-Au mineralization. The described shift between Mo and Cu-Au could be related to increasing Mo/Cu ratio in the residual parental melt similarly proposed by (Candela and Holland, 1986).

- The importance of scarce silver is mitigated due to the lack of information. More insights could be drawn from Pb-S-O-C isotopic analysis, Re content in molybdenite as well as

from the gaseous and aqueous compositions of fluid inclusions in quartz, these analyses would be very helpful to understand the low silver concentrations here.

3.7.3 Late Ediacaran Ouarzazate SLIP and implications for Anti-Atlas metallogeny

Large igneous provinces (LIPs) include large volumes (> 0.1 million km^3) of mafic rocks with their plumbing systems, and are emplaced within an intraplate setting in a single pulse of short duration (< 5 Ma) (Ernst et al., 2021). Nonetheless, the LIPs may contain several pulses of magmatism extending over a period of less than 50 Ma (Ernst et al., 2013). In continental margins, LIPs can also be associated with silicic magmatism and in these cases, they are referred to as silicic large igneous provinces (SLIPs) (Bryan and Ferrari, 2013).

During the late Ediacaran, huge silicic magmatic activity took place in the Anti-Alas belt of Morocco (Gasquet et al., 2005). This magmatism has been more recently bracketed between 575–540 Ma and included in a lithostratigraphic unit referred to as the Upper Complex by Tuduri et al., (2018). Those authors assume that throughout this timeframe (575-540 Ma) the whole Anti-Atlas belt witnessed a long-lived tectono-magmatic event evolving from high-K calc-alkaline (575-550 Ma) to alkaline (550-540 Ma) affinity, which is also reported by Abia et al., (2003) and Zahour et al., (2022) in the Saghro inlier. This magmatism is thought to belong to a continental silicic large igneous province, defined by Schulte et al., (2022) as the Ouarzazate SLIP, and emplaced over multiple pulses at c.a 575 Ma, at c.a 560 Ma and at c.a 550 Ma (Belkacim et al., 2021)(**Figure 3.20**).

Several studies have outlined the significant role of LIPs for several metallogenic systems. LIPs are commonly related to a wide variety of metal deposits (Ernst et al., 2013), and can represent the source of metals and energy for hydrothermal systems (Ernst et al., 2021). The emplacement of LIPs can provide copper and other metals for several ore deposit types, including iron-oxide-copper-gold (IOCG) and volcanogenic massive sulfide (VMS), potentially gold containing (Ernst et al., 2013). Nevertheless, the epithermal Au and Carlin type deposits appear to be preferentially related to SLIPs (Bryan et al., 2008).

In this regard, Gasquet et al. (2005) suggested that the long-lived silicic magmatic activity of the Ouarzazate SLIP was accompanied by a pervasive hydrothermal and metallogenic manifestations. Additionally, Tuduri et al. (2018) suggested a possible relationship between hydrothermal mineral deposits and magmatic flare-ups in the Anti-Atlas. These deposits include those of the Qal'at MGouna district Au–Ag (Cu, Mo, Bi, Te), including the Ismlal Au(–

Cu–Mo) porphyry, Zone des Dykes Au(–Ag–Cu–Zn–Pb–Bi) deposit, Thaghassa Au-Ag, Imiter Ag(-Hg-Pb-Zn), Bouskour Ag(-Cu–Pb–Zn) metal, Tiouit Au-Ag-Cu, Sidi Flah Cu-Au-Ag, Tagmout Cu-Ag and Bou Madine Au-Ag(-Pb-Zn-Cu) deposits (**Figure 3.21**).

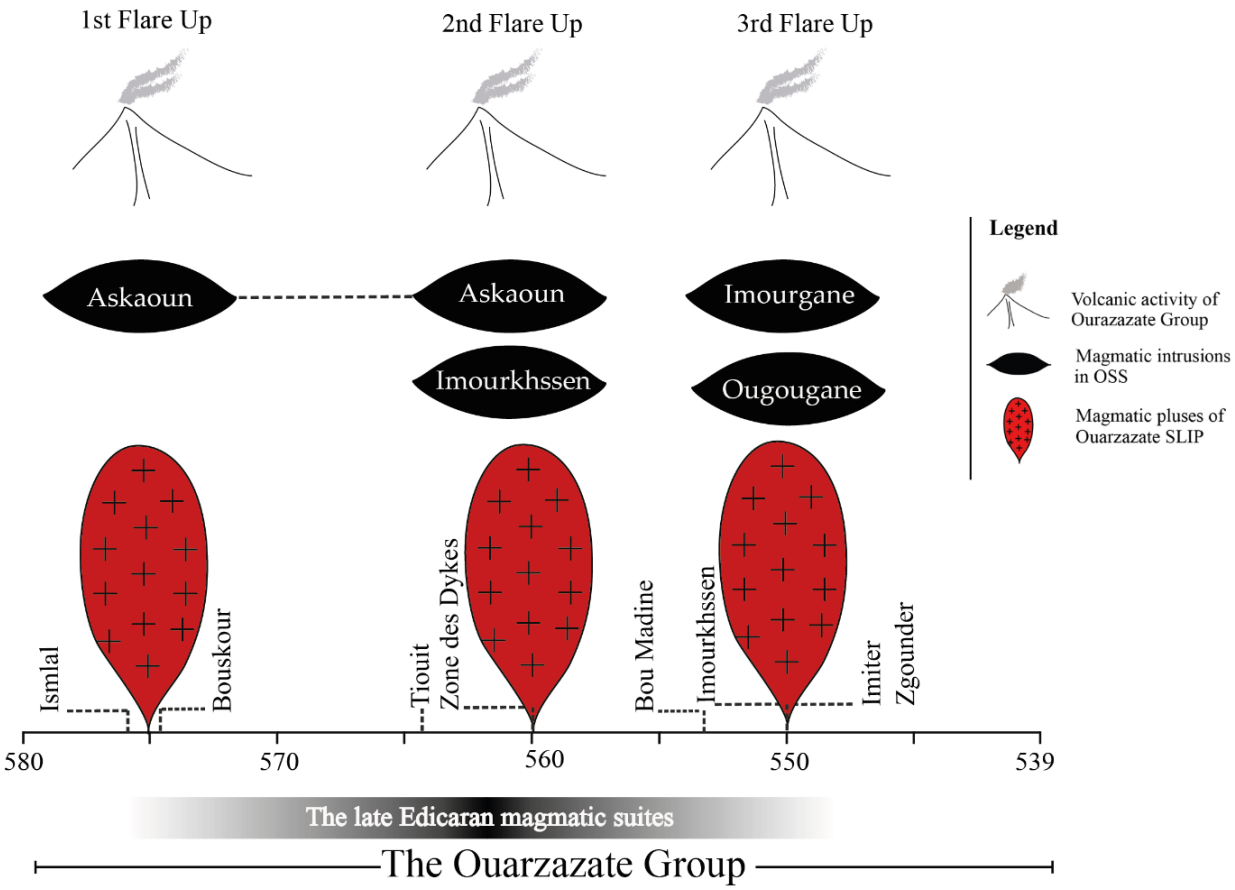

Figure 3.20
The emplacement of the late Ediacaran magmatic suites (LEMS) related to the three magmatic pulses of the Ouarzazate SLIP (Tuduri et al., 2018; Belkacim et al., 2021) and the position of Imourkhssen and many other mineral deposits of the Anti-Atlas.

In the studied area, we suggest an earlier emplacement of the first magmatic pulse generating the Askaoun granodiorite at 575 Ma (**Figure 3.20**). The age obtained by Toummite et al., (2012) (c.a 558 Ma) for this pluton outlines its emplacement during both the first and second magmatic pulses (c.a 560 Ma), during which the barren Imourkhssen intrusion was as well formed. The third magmatic pulse is considered as the last manifestation of the Ouarzazate magmatic activity (Belkacim et al., 2021). It occurred around 550 Ma, and corresponds to the emplacement of the Ougougane Suite including the mineralized Imourgane granite, which developed a spherulitic texture, highlighting fast cooling in low temperature conditions (Bard, 1980).

The Imourkhssen Cu±Mo±Au±Ag porphyry style deposit is considered to be associated with the emplacement of the Askaoun granodiorite (c.a 558 Ma) and the Imourgane granite (c.a 551

Ma) that are coeval respectively with the 2nd and 3rd flares-ups reported by Tuduri et al., (2018). These two flares-up correspond to the 2nd and 3rd magmatic pulses of the Ouarzazate SLIP (560 Ma and 550 Ma) (Belkacim et al., 2021). The 3rd magmatic pulse could be also responsible for the Zgounder Ag-Hg epithermal ore deposit occurring in the southwestern part of the studied area. In this regard, the potential relationship between the Imourkhssen porphyry and the Zgounder epithermal mineralization could be discussed.

Overall, this period could be correlated to reginal events highlighted by the transition from a transpressive to transtensive tectonic regime, and the orogenic collapse (Levresse, 2001). In the context of this extensional setting, leached hydrothermal fluids likely migrated along fault zones, enabling metal transport and deposition of porphyry and epithermal mineralization (Tuduri et al., 2018).

Consequently, the Ouarzazate SLIP could be potentially invoked for the metal source and hydrothermal energy that fueled the late Ediacaran porphyry and epithermal hydrothermal and metallogenic activities in the Central and Eastern Anti-Atlas, namely the Saghro domain of Morocco (see next section).

3.7.4 A probable late Ediacaran Porphyry-Epithermal province in the Anti-Atlas

The post-collisional period in the Pan-African Anti-Atlas belt system involved the transition to a passive continental margin with strong extensional tectonic and subsequent orogenic collapse (Thomas et al., 2002; Gasquet et al., 2005). In the framework of this extensional regime, intense metallogenic activity occurred giving rise to numerous world-class precious metal epithermal deposits (Imiter and Zgounder), base metal porphyry and SEDEX-type occurrences (Bou Madine; Gasquet et al., 2005) associated with silicic magmatism of the Ouarzazate SLIP (Gasquet et al., 2005; Schulte et al., 2022).

The consistency of the geological, geochemical and metallogenic features of several precious and base metal occurrences occurring in the Central and the Eastern part of the Anti-Atlas are remarkable. This part of the Anti-Atlas chain delimited by the Southern High-Atlas fault (SAF) and the Anti-Atlas major fault (AAMF), was recently considered as a single terrane, and referred to as Saghro domain (Schulte et al., 2022). Moreover, numerous ore deposits show a spatial and probably a temporal link with Late Ediacaran silicic magmatism of the Ouarzazate SLIP within the Saghro domain.

In the framework of the extensional tectonic regime and the long-lived magmatic activity of the Ouarzazate SLIP (Tuduri et al., 2018; Belkacim et al., 2021). Tuduri et al., (2018) proposed that Jbel Saghro constitutes a large mineralized province associated with widespread hydrothermal activity. In this paper, we propose that the Saghro domain should be considered as a Late Ediacaran porphyry-epithermal province englobing the entirety of porphyry and epithermal deposits linked to the post orogenic collapse episode of the Pan-African orogen (**Figure 3.21**).

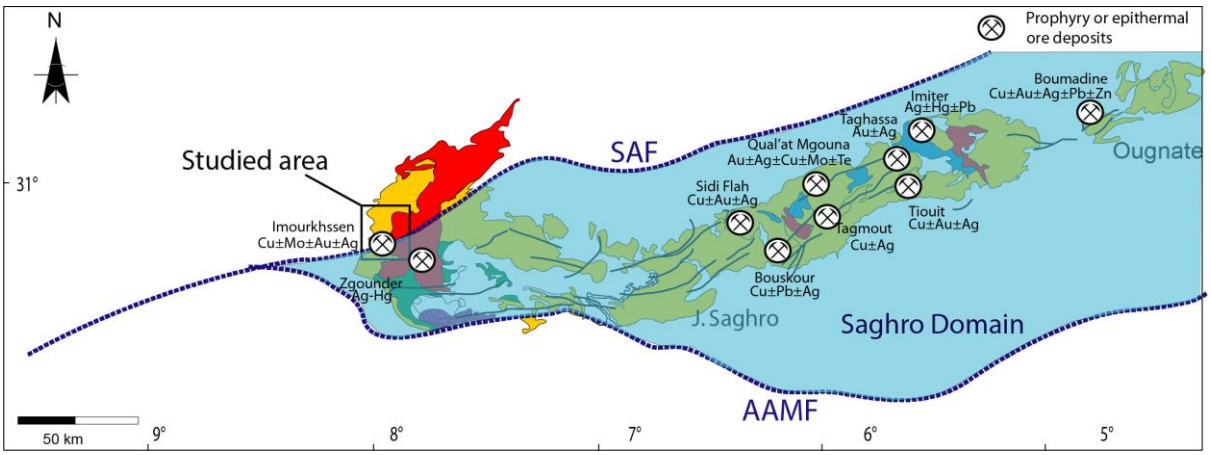

Figure 3.21
Simplified geological map of the Saghro domain showing the location of the major mineral deposits (modified from Tuduri et al. (2018)). The legend is analogous to the one presented in Figure 3.2

This system is powered by the injection of silicic magmatic pulses of the Ouarzazate SLIP. Over three epochs, the incorporation of a juvenile, sulfide-rich subduction-related component into the magma facilitated the emplacement of fertile intrusions. These intrusions develop porphyry and epithermal mineralization under a single porphyry-epithermal system. This system with the associated SLIP magmatism occurred during the post-collisional stage of the Pan-Africain orogeny, corresponding to the metacratonic evolution of the northern edge of the west african craton (WAC) (Linnemann et al., 2014).

3.7.5 Similarities with porphyry and epithermal ore deposits in the world

The mineralization style of the porphyry and epithermal ore deposits and related magmatic activity that occurred in the Saghro domain is widely recognized in several ore deposits around the world.

The multi-pulse character is widely recognized in the development of several deposits, such as the Cu-Pb-Zn polymetallic deposit in the Jiangxi Province (Cao et al., 2021). The latter is considered to be tied to three main magmatic-hydrothermal events (c.a Middle-Late Triassic, Late Jurassic and Early Cretaceous), that are responsible for the metallogenic activity in the north Wuyi area of China (Cao et al., 2021). Still in the Jiangxi province, the porphyry Cu–Au–Mo and the Ag–Pb–Zn epithermal occurrences are related to five magmatic phases recognized in the Dexing area (Mao et al., 2011). Based on geochronogical and geochemical features of both mineralization styles, a link was established between the Dexing Cu–Au–Mo porphyry and Ag–Pb–Zn epithermal deposits in the Jiangxi province.

The connection between porphyry and epithermal deposits envisaged in the Saghro Domain is observed in several deposits worldwide. Indeed, numerous epithermal ore deposits are underlain by porphyry-type mineralization, often rooted in their advanced argillic alteration lithocaps (Sillitoe, 2010; Voudouris et al., 2019). In China, several porphyry and epithermal deposits are suggested to be genetically related. Namely, the Yinshan Ag–Pb–Zn epithermal and the Cu–Au porphyry ore deposits (Simmons et al., 2005).

Moreover, the epithermal deposits can also be grounded within the sericitic alteration zone (e.g., of Cu-Au porphyry deposits, such as in Far Southeast-Lepanto (Philippines) (Hedenquist and Arribas, 1998). In this example, fluid inclusions studies, and δO and δD compositions suggest that gradational alteration patterns from advanced argillic alteration, through phyllic and K-silicate alterations, can be used to outline the spatial evolution of a single hydrothermal fluid (Hedenquist and Arribas, 1998).

On the other hand, discussing the relationship between porphyry and epithermal ore deposits involves understanding the metal source (Sillitoe, 2010). Hedenquist and Arribas, (1998) have suggested a common magmatic metal source for the entire porphyry-epithermal mineralization stages based on similar metal associations. Therefore, the identical magmatic fluid sources for both porphyry and epithermal systems is the best evidence for their genetic connection.

In the Baguio mineral district, Philippines, two porphyry vein stages are superimposed by four paragenetic stages of the Acupan epithermal mineralizations (Figueroa et al., 2022). Fluid inclusion studies reveal that the porphyry vein stages are sourced from hot and hypersaline magmatic fluids exsolved during the crystallization of the subvolcanic porphyry dacite, while the co-existing magmatic vapor generated gold and silver epithermal mineralization with the

development of gangue minerals and alteration halos. This mineralization style was also controlled by structures associated with the emplacement of the Balatoc diatreme (Figueroa et al., 2022).

A further example in Apuseni Mountains, Romania is reported by Cardon et al., (2004). Those authors demonstrate using 3D modeling that there is a spatial link between Bolcana Cu-porphyry and three epithermal deposits (e.g., Troita, Trestia et Magura). This study was based on 3D modeling to study the spatial distribution of metal contents around the Bolcana Cu-porphyry revealing a specific distribution which cannot result from a telescoped system. Thus, a strong relationship between porphyry copper and epithermal ore deposits occurs within the Apuseni Mountains.

3.7.6 Spatial correlations with the Avalon epithermal ore deposits

During the late Ediacaran period, as Gondwana was nearing its final amalgamation, the West African craton (WAC) was surrounded by Pan-African terranes (**Figure 3.22**), which included island arcs or continental active margins. In this context, the WAC assumed the role of a passive margin amidst these geological features (Ennih and Liégeois, 2008 and references therein). During the Paleozoic era, terranes adjacent to the northwestern edge of Gondwana separated, resulting in the formation of the Rheic Ocean (Nance et al., 2012). Hence, specific Peri-Gondwanan terranes exhibit significant similarities in age, tectonic evolution, metallogenic history and facies progression to the Pan-African belts found in the West African Craton, including the Anti-Atlas. Here, we mainly focus on the metallogenic aspect as a tool for global correlation.

One of the peri-Gondwanan terranes proposed for correlation is the Avalon Zone, where most epithermal alteration and associated mineralization occurred between 590 and 550 Ma, and which may also host buried porphyry deposits (Sparkes and Dunning, 2014). In this regard, the late Neoproterozoic epithermal mineralization of the Saghro porphyry-epithermal province portray a link with the west Avalon zone's epithermal deposits.

Indeed, the Hickey's Pond, Big Easy, Long Harbour, Hope Brook, Heritage epithermal deposits occur in the Newfoundland area of the west Avalon zone. The Hickey's Pond high-sulfidation deposits (Arbiol et al., 2021), have an age of 586 ± 3 Ma (Sparkes et al., 2016). A reinterpretation of the age from the host rocks provides a younger age of 572.5 ± 1.5 Ma (Ferguson, 2017).

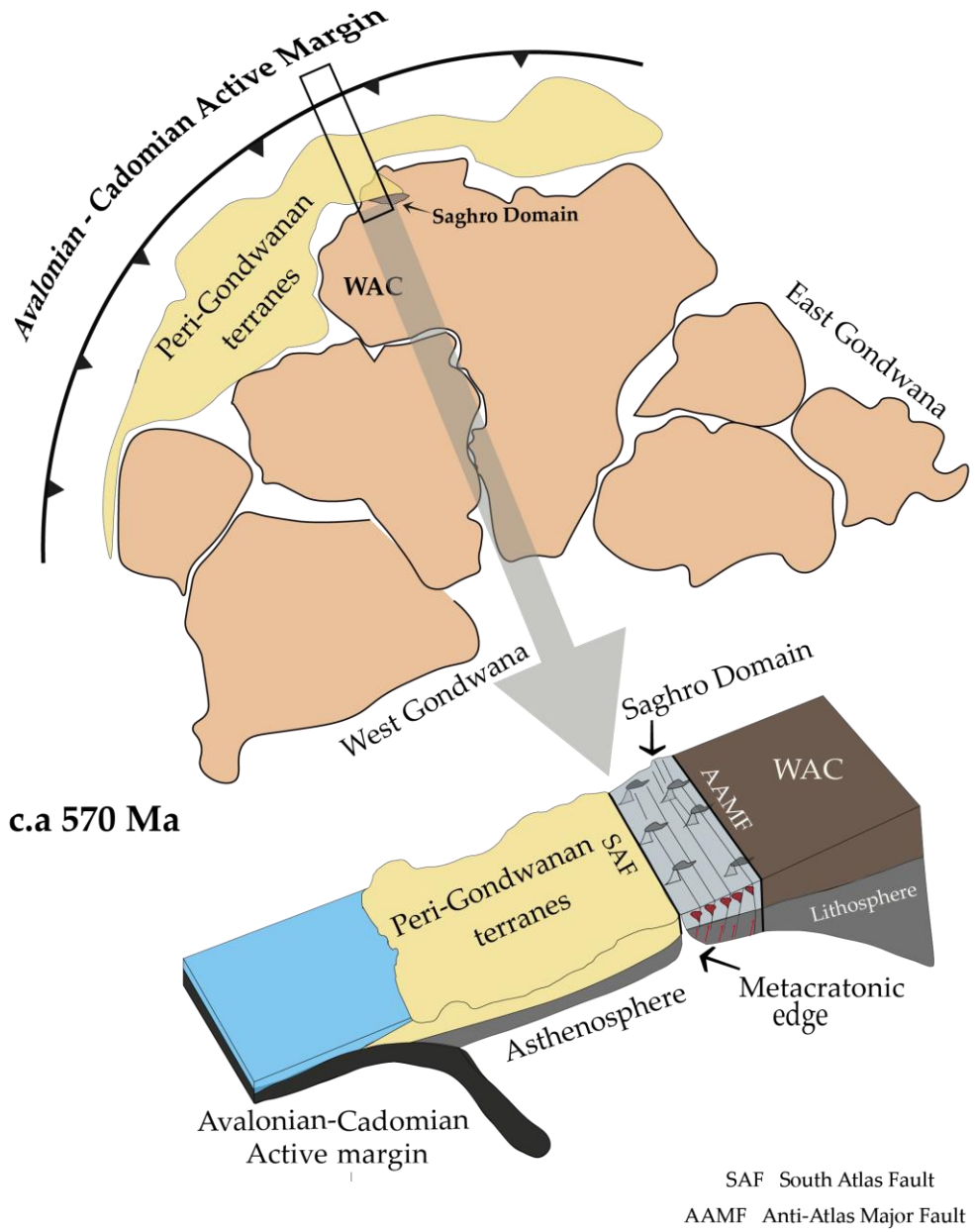

Figure 3.22
Paleogeography of the Avalonian-Cadomian active margin, peri-Gondwanan terranes and the Saghro domain at ca. 570 Ma. Modified from (Linnemann et al., 2014; Ouabid and Garrido, 2023).

Further studies of the Hope Brook high sulfidation deposits have bracketed the age of the alteration and the mineralization between 578 and 574 Ma (Dubé et al., 1998). The Big Easy epithermal deposit has a Late Neoproterozoic age (ca. 573 Ma; Ferguson, 2017), while in the Long Harbour prospect, a mineralized rhyolite constrains the age of this low epithermal deposit

at 566.5 ± 1.9 Ma and has been used to indicate its alkaline affinity and potential relationship with late arc-extension (Ferguson, 2017).

In the other hand, the correlation between the WAC margin and the boundary of North America is currently debated. Based on geochemical and geochronological data, Schulte et al., (2022) had proposed potential correlations between magmatic rocks of the Ouarzazate Group outcropping in the Ifni inlier and the magmatic rocks of the west Avalonia, including the Newfoundland area. El Haibi et al. (2020) interpret the late Ediacaran magmatism in El Jadida region as an example of a Moroccan peri Gondwanan (Avalonian?) remnant, while El Kabouri (2023) described many fossils found in the Anti-Atlas of Morocco (e.g., Aspidella), that is are ubiquitous in the Avalon zone. These fossils points to the Ediacaran period and underscore a similar deposit style.

Here, we suggest a spatial link between the northern boundary of the WAC, namely the Saghro domain and the west Avalon zone during the late Ediacaran times.

3.8 Conclusions

This study allows us to draw several conclusions which we summarize below:

(1) We support the hypothesis of porphyry type mineralization for the Imourkhssen deposit (Central Anti-Atlas, Morocco), that was previously suggested by Belkacim, (2014). We argue this based on the following points: (i) The geochemical nature of the host rocks and multi-phase magmatic (Assarag, Amassine and Ougougane suites) and hydrothermal activity, (ii) the style and the zonation of hydrothermal alteration and mineralization, (iii) the mineral assemblage and paragenetic sequence and (iv) the post-collisional geodynamic setting of the host rocks.

(2) The model envisaged in this study for the Imourkhssen Cu±Mo±Au±Ag deposit could be related to the 2nd and the 3rd flares-up reported by Tuduri et al., (2018), which are coeval with the 2nd and the 3rd magmatic pulses of the Ouarzazate SLIP evidenced by Belkacim et al., (2021).

(3) The ore genesis potentially involves the Zaghar mafic dykes during the magma evolution, which is corroborated by their co-mingling textures.

(4) The Concordia and $^{206}Pb/^{238}U$ ages and averages of the barren Imourkhssen and the mineralized granite from area allow us to constraint the age of the Imourkhssen intrusion at 558 ± 1 Ma.

(5) The ore-bearing granite is newly identified as the "Imourgane granite". The concordia age of 550 ± 2 Ma indicates that it belongs to the Ougougane Suite, and this allows us to constrain the age of the porphyry-epithermal system in the Ouzellagh-Siroua Salient beneath the 2nd and 3rd magmatic pulses of the Ouarzazate SLIP.

(6) Several mineral deposits in the whole Anti-Atlas seem to belong to a late Ediacaran porphyry-epithermal system linked to the emplacement of a multi-pulses continental silicic large igneous province namely the Ouarzazate SLIP (580-539 Ma). This SLIP was generated during the post-collisional period of the Pan-African orogen.

(7) The ages of the epithermal deposits of the west Avalon zone and the porphyry-epithermal province suggest a potential spatial link during the Late Neoproterozoic times, corresponding to the metacratonic evolution of the northern boundary of the West African craton.

Author Contributions: Conceptualization, Mariam Ferraq and Saïd Belkacim; Data curation, Mariam Ferraq, Joshua H.F.L Davies, Morgann.G Perrot and Abdelhay Ben Tami; Investigation, Mariam Ferraq, Li-Zhen Cheng, Joshua H.F.L Davies, Morgann.G Perrot and Mohammed Bouabdellah; Methodology, Mariam Ferraq; Resources, Li-Zhen Cheng; Software, Mariam Ferraq, Saïd Belkacim, Joshua H.F.L Davies, Morgann.G Perrot and Abdelhay Ben Tami; Supervision, Saïd Belkacim and Li-Zhen Cheng; Validation, Saïd Belkacim, Li-Zhen Cheng and Mohammed Bouabdellah; Visualization, Mariam Ferraq, Joshua H.F.L Davies, Morgann.G Perrot, Abdelhay Ben Tami and Mohammed Bouabdellah; Writing – original draft, Mariam Ferraq and Saïd Belkacim; Writing – review & editing, Mariam Ferraq, Saïd Belkacim, Li-Zhen Cheng, Joshua H.F.L Davies, Morgann.G Perrot and Mohammed Bouabdellah; All authors have read and agreed to the published version of the manuscript.

Data Availability Statement: The data used for the research were presented in the article.

Acknowledgments: Most of this work was carried out in the Faculty of Sciences of Agadir, Université Ibnou Zohr and in the Université de Québec en Abitibi-Témiscamingue, Canada. Grateful acknowledgment to the technical staff of the laboratory of the Applied Geosciences and Geo-Environment (LAGAGE), the research center of the Faculty of Sciences of Agadir, as

well as those of the research center of geochronology and isotopic geochemistry (GEOTOP) of the Université de Québec à Montréal, who contributed in this work. We also appreciate the support provided by the National Centre for Scientific and Technological Re-search (CNRST) and their encouragement to succeed in this work. We further thank to journal's anonymous referees for their constructive reviews and edits, as well as to the entire editorial staff of Minerals journal for their handling of the manuscript, which significantly enhanced this work.

Conflicts of Interest: The authors declare no conflict of interest.

3.9 References

Abia, E.H., Nachit, H., Marignac, C., Ibhi, A., Ait Saadi, S., 2003. The Polymetallic Au-Ag-Bearing Veins of Bou Madine (Jbel Ougnat, Eastern Anti-Atlas, Morocco): Tectonic Control and Evolution of a Neoproterozoic Epithermal Deposit. Journal of African Earth Sciences, 36 (4): 251–71. https://doi.org/10.1016/S0899-5362(03)00051-4.

Aït Malek, H., Gasquet, D., Bertrand, J.M., Leterrier, J., 1998. Géochronologie U–Pb Sur Zircon de Granitoïdes Éburnéens et Panafricains Dans Les Boutonnières pro-Térozoïques d'Igherm, Du Kerdous et Du Bas Drâa (Anti-Atlas Occidental, Maroc). R.C Sciences.

Álvaro, J. J., Benziane, F., Thomas, R., Walsh, G. J., Yazidi, A., 2014b. Neoproterozoic–Cambrian stratigraphic framework of the Anti-Atlas and Ouzellagh promontory (High Atlas), Morocco. Journal of African Earth Sciences, 98, 19-33.

Arbiol, C., Layne, G., Zanoni, G., Šegvić, B., 2021. Characteristics and Genesis of Phyllosilicate Hydrothermal Assemblages from Neoproterozoic Epithermal Au-Ag Mineralization of the Avalon Zone of Newfoundland, Canada. Applied Clay Science, 202 . https://doi.org/10.1016/j.clay.2020.105960.

Arribas, A., 1995. Characteristics of High-Sulfidation Epithermal Deposits, and Their Relation to Magmatic Fluid. Mineralogical Association of Canada Short Course Series, 23: 419–54.

Baidada, B., Ikenne, M., Barbey, P., Soulaimani, A., Cousens, B., Haissen, F., Ilmen, S., Alansari., A., 2019. SHRIMP U–Pb Zircon Geochronology of the Granitoids of the Imiter Inlier: Constraints on the Pan-African Events in the Saghro Massif, Anti-Atlas (Morocco). Journal of African Earth Sciences, 150 : 799–810. https://doi.org/10.1016/j.jafrearsci.2018.10.008.

Bard, J.P., 1980. Microtexture Des Roches Magmatique et Métamorphiques.

Belkacim, S., Perrot, M.G., Davies, J.H.F.L., Liégeois, J-P., Ikenne, M., 2021. The Ediacaran Ouarzazate Group, a Metacratonic Silicic Large Igneous Province (SLIP) : New U-Pb Zircon Ages from Ouzellarh-Siroua Salient (Tifnoute Valley, Morocco). In Geological Society of America Northeastern Section (NEGSA), 1/1. T17. Pre-Atlantic Geological Connections among Northwest Africa, Southern Europe, and Eastern North America

Belkacim, S., Gasquet, D., Liégeois, J.P., Arai, S., Gahlan, H.A., Ahmed, H., Ishida, Y., Ikenne, M., 2017. The Ediacaran Volcanic Rocks and Associated Mafic Dykes of the

Ouarzazate Group (Anti-Atlas, Morocco): Clinopyroxene Composition, Whole-Rock Geochemistry and Sr-Nd Isotopes Constraints from the Ouzellarh-Siroua Salient (Tifnoute Valley). Journal of African Earth Sciences, 127: 113–35. https://doi.org/10.1016/j.jafrearsci.2016.08.002.

Belkacim, S., Ikenne, M., Souhassou, M., Elbasbas, A., Toummite, A., 2014. The Cu-Mo±Au Mineralizations Associated to the High-K Calc- Alkaline Granitoids from Tifnoute Valley (Siroua Massif, Anti- Atlas, Morocco): An Arc-Type Porphyry in the Late Neoproterozoic Series. Journal of Environment and Earth Science, 4 (14): 90–106.

Belkacim, S., 2014. Pétrographie, Géochimie et Isotopes (Sr-Nd) Du Volcanisme Édiacarien et Des Dykes Doléritiques de La Vallée de Tifnoute et Caractérisation Des Indices de Cu-Mo±Au d'Imourkhssan (Siroua, Anti-Atlas Central, Maroc). Doctoral dissertation, Ibn Zohr University, 237p.

Blein, O., Baudin, T., Soulaimani, A., Cocherie, A., Chevremont, P., Admou, H., Roger, J., 2014. New geochemical, geochronological and structural constraints on the Ediacaran evolution of the south Sirwa, Agadir-Melloul and Iguerda inliers, Anti-Atlas, Morocco. Journal of African Earth Sciences, 98, 47-71.

Bouabdellah, M., Chekroun, F., Alansari, A., Margoum, D., 2016. The Granitoid-Related Tiouit Gold Deposit, Saghro Inlier, Eastern Anti-Atlas (Morocco): Neoproterozoic Mineralization by a Polyphase Late-Magmatic to Hydrothermal System, 405–14. https://doi.org/10.1007/978-3-319-31733-5_16.

Bouabdellah, M., and Slack, J.F., 2016. Geologic and Metallogenic Framework of North Africa. https://doi.org/10.1007/978-3-319-31733-5_1.

Boynton, W. V., 1983. Cosmochemistry of the Rare Earth Elements: Meteorite Studies. Rare Earth Element Geochemistry, 63–114. https://doi.org/10.1016/b978-0-444-42148-7.50008-3.

Bryan, S.E., and Ferrari, L., 2013. Large Igneous Provinces and Silicic Large Igneous Provinces: Progress in Our Understanding over the Last 25 Years. Bulletin of the Geological Society of America, 125 (7–8): 1053–78. https://doi.org/10.1130/B30820.1.

Bryan, S., Ferrari, E., Reiners, P.W., Allen, C.M., Petrone, C.M., Ramos-rosique, A., H. Campbell, I., 2008. New Insights into Crustal Contributions to Large-Volume Rhyolite Generation in the Mid-Tertiary Sierra Madre Occidental Province, Mexico, Revealed by U-Pb Geochronology. Journal of Petrology, 49 (1): 47–77. https://doi.org/10.1093/petrology/egm070.

Burisch, M., Walter, B.F., Markl, G., 2017. Silicification of Hydrothermal Gangue Minerals in Pb-Zn-Cu-Fluoritequartz-Baryte Veins. Canadian Mineralogist, 55 (3): 501–14. https://doi.org/10.3749/canmin.1700005.

Byrne, K., Lesage, G., Gleeson, S.A., Lee, R.G., 2016. Large-Scale Sodic-Calcic Alteration around Porphyry Cu Systems: Examples from the Highland Valley Copper District, Guichon Batholith, South-Central British Columbia.

Candela, P. A., and H. D. Holland., 1986. A Mass Transfer Model for Copper and Molybdenum in Magmatic Hydrothermal Systems: The Origin of Porphyry-Type Ore Deposits. Economic Geology, 81 (1): 1–19. https://doi.org/10.2113/gsecongeo.81.1.1.

Cao, M.Y., Jiang, S.Y., Su, H.M., Liu, T., 2021. Indosinian Magmatic–Hydrothermal

Metallogenic Event in the North Wuyi Area, Southeastern China: An Example from the Chenfang Skarn Deposit in Jiangxi Province. Ore Geology Reviews, 138 : 104386. https://doi.org/10.1016/j.oregeorev.2021.104386.

Cardon, O., André-Mayer, A.S., Sausse, J., Milu, V., Chauvet, A., Leroy, J.L., Lespinasse, M., Udubasa, S., 2004. The Link between Porphyry Copper and Low-Sulfidation Epithermal Deposit: Structural Study and 3D Representation of the Sector of Bolcana, Apuseni Mountains, Romania. Comptes Rendus - Geoscience, 337 (9): 824–31. https://doi.org/10.1016/j.crte.2005.03.014.

Carten, R.B., White, W.H., Stein., H.J., 1993. High-Grade-Granite Related Molybdenium Systems: Classification and Origin. Geological Association of Canada, no. Special paper: 521–44.

Chappell, B. W., 1999. Aluminium Saturation in I- and S-Type Granites and the Characterization of Fractionated Haplogranites. Lithos, 46 (3): 535–51. https://doi.org/10.1016/S0024-4937(98)00086-3.

Chappell, B. W., and White, A. J.R.., 2001. Two Contrasting Granite Types: 25 Years Later. Australian Journal of Earth Sciences, 48 (4): 489–99. https://doi.org/10.1046/j.1440-0952.2001.00882.x.

Cheilletz, A., Levresse, G., Gasquet, G., Azizi-Samir, M., Zyadi, R., Archibald, D.A., Farrar, E., 2002. The Giant Imiter Silver Deposit: Neoproterozoic Epithermal Mineralization in the Anti-Atlas, Morocco. Mineralium Deposita, 37 (8): 772–81. https://doi.org/10.1007/s00126-002-0317-0.

Chen, Y.J., Zhang, C., Wang, P., Pirajno, F., Li, N., 2017. The Mo Deposits of Northeast China: A Powerful Indicator of Tectonic Settings and Associated Evolutionary Trends. Ore Geology Reviews, 81: 602–40. https://doi.org/10.1016/j.oregeorev.2016.04.017.

Claiborne, L. L., Miller, C. F., Walker, B. A., Wooden, J. L., Mazdab, F. K., Bea, F. Tracking Magmatic Processes through Zr/Hf Ratios in Rocks and Hf and Ti Zoning in Zircons: An Example from the Spirit Mountain Batholith, Nevada. Mineralogical Magazine, 70 (5): 517–43. https://doi.org/10.1180/0026461067050348.

Cooke, D.R., Hollings, P.,.Walshe, J.L., 2005. Giant Porphyry Deposits: Characteristics, Distribution, and Tectonic Controls. Turkish Journal of Fisheries and Aquatic Sciences, 18: 539–46.

Cooke, D. R., P. Hollings, J. J. Wilkinson, and R. M. Tosdal., 2014. Geochemistry of Porphyry Deposits. Treatise on Geochemistry: Second Edition. 2nd ed. Vol. 13. Elsevier Ltd. https://doi.org/10.1016/B978-0-08-095975-7.01116-5.

Core, D., Buckingham, A., Belfield, S., 2009. Detailed Structural Analysis of Magnetic Data-Done Quickly and Objectively.SGEG News,

Crusius, J., Calve, S., Pedersen, T., Sage, D., 1996. Rhenium and Molybdenum Enrichments in Sediments as Indicators of Oxic, Suboxic and Sulfidic Conditions of Deposition. Earth and Planetary Science, Letters, no. 96: 65–78.

D'Lemos, R.S., Inglis, J.D., Samson, S.D., 2006. Newly Discovered Orogenic Event in Morocco: Neoproterozic Ages for Supposed Eburnean Basement of the Bou Azzer Inlier, Anti-Atlas Mountains. Precambrian Research, 147: 65–78.

Dabiri, R., Akbari-Mogaddam, M., Ghaffari, M., 2018. Geochemical Evolution and

Petrogenesis of the Eocene Kashmar Granitoid Rocks, NE Iran: Implications for Fractional Crystallization and Crustal Contamination Processes. Iranian Journal of Earth Sciences, 10 (1): 68–77.

Delibaş, O., Moritz, R., Chiaradia, M., Selby, D., Ulianov, A., Revan, M.K., 2017. Post-Collisional Magmatism and Ore-Forming Systems in the Menderes Massif: New Constraints from the Miocene Porphyry Mo–Cu Pınarbaşı System, Gediz–Kütahya, Western Turkey. Mineralium Deposita, 52 (8): 1157–78. https://doi.org/10.1007/s00126-016-0711-7.

Di Tommaso, I and Rubinstein, N., 2007. Hydrothermal alteration mapping using ASTER data in the Infiernillo porphyry deposit, Argentina. Ore Geology Reviews, 32(1-2), 275-290.

Dilles, J.H., and John., D.A., 2020. Porphyry and Epithermal Mineral Deposits. Encyclopedia of Geology, (1-6), Second Edition 5: 847–66. https://doi.org/10.1016/B978-0-08-102908-4.00005-9.

Dubé, B., Dunning, G., Lauzière, K., 1998. Geology of the Hope Brook Mine, Newfoundland, Canada: A Preserved Late Proterozoic High-Sulfidation Epithermal Gold Deposit and Its Implications for Exploration. Economic Geology, 93 (4): 405–36. https://doi.org/10.2113/gsecongeo.93.4.405.

Errami, E., Bonin, B., Laduron, D., Lasri, L., 2009. Petrology and Geodynamic Significance of the Post-Collisional Pan-African Magmatism in the Eastern Saghro Area (Anti-Atlas, Morocco). Journal of African Earth Sciences, 55: 105–124.

El Azmi, D., Aissa, M., Ouguir, H., Mahdoudi, M. L., El Azmi, M., Ouadjo, A., Zouhair, M., 2014. Magmatic Context of Bou Skour Copper Deposit (Eastern Anti-Atlas, Morocco): Petrogrography, Geochemistry and Alterations. Journal of African Earth Sciences, 97: 40–55. https://doi.org/10.1016/j.jafrearsci.2014.04.020.

El Kabouri, J., Errami, E., Bowyer, F. T., Becker-Kerber, B., Belkacim, S., 2025. Ediacaran-Cambrian Boundary in the Anti-Atlas belt (Morocco): A review of biostratigraphy, chemostratigraphy and geochronology. Earth-Science Reviews, 261, 105010.

El Kabouri, J., Errami, E., Becker-Kerber, B., Ennih, N., Youbi, N., 2023. Microbially induced sedimentary structures from the Ediacaran of Anti-Atlas, Morocco. Precambrian Research, 395, 107135.

El Kabouri, J., 2023. Geobiology and Lithostratigraphy of the Ediacaran Successions of the Eastern Anti-Atlas (Morocco): Implications for the Geobiological and Geodynamic Evolution of the Northern Margin of the West African Craton (Doctoral dissertation, Departement of Geology, University of Chouaib Doukkali)

El Moume, W., Youbi, N., Marzoli, A., Bertrand, H., Ikenne, L., Boumehdi, M A., Ernst, R., El Hachimi, H., Bensalah, M K., Mata, J., Madeira, J., Bento dos Santos, T.M., Martins, S.,. 2020. Geochemistry of Mafic Dyke Swarms of Douar Eç-Çour (High Atlas, Morocco): The Farthest Record of the Central Iapetus Magmatic Province (CIMP) into West African Craton. In The Farthest Record of the Central Iapetus Magmatic Province (CIMP) into West African Craton, Geólogos, 33 (1-2): 95–124.

Ennih, N., Liégeois, J P., 2001. The Moroccan Anti-Atlas: The West African Craton Passive Margin with Limited Pan-African Activity. Implications for the Northern Limit of the Craton. Precambrian Research, 112 (3–4): 289–302. https://doi.org/10.1016/S0301-9268(01)00195-4.

Ennih, N., Liégeois, J P., 2008. The Boundaries of the West African Craton, with Special Reference to the Basement of the Moroccan Metacratonic Anti-Atlas Belt. Geological Society Special Publication, 297: 1–17. https://doi.org/10.1144/SP297.1.

Ernst, R.E., Jowitt, M., Thompson, J. F. H., 2013. Large Igneous Provinces (LIPs) and Metallogeny. Tectonics, Metallogeny, and Discovery, no. C: 17–51. https://doi.org/10.5382/sp.17.02.

Ernst, R. E., Bond, D. P., Zhang, S. H., Buchan, K. L., Grasby, S. E., Youbi, N., El Bilali, H., Bekker, A., Doucet, L. S., 2021. Large igneous province record through time and implications for secular environmental changes and geological time-scale boundaries. Large igneous provinces: A driver of global environmental and biotic changes, American Geophysical Union, 1–26. https://doi.org/10.1002/9781119507444.ch1.

Fekkak, A., Pouclet, A., Ouguir, H., Badra, L., Gasquet, D., 1999. Le groupe du Neoproterozoique inferieur de Kelaat Mgouna (Saghro, Anti-Atlas, Maroc); temoin d'un stade precoce de l'extension pre-panafricaine. Bulletin de la Societe Geologique de France, 170(6), 789-797.

Ferdous, S, and J Podder. 1970. Growth and Characterization of Epsomite Single Crystals Doped with KCl from Low Temperature Aqueous Solutions. Journal of Bangladesh Academy of Sciences, 33 (1): 47–54. https://doi.org/10.3329/jbas.v33i1.2949.

Ferguson, S A., 2017. Late Neoproterozoic Epithermal-Style Au Mineralization of the Burin Peninsula, Newfoundland: U-Pb Geochronology and Deposit Characteristics. Memorial University of Newfoundland October.

Ferraq, M., Belkacim, S., Cheng, L.Z., Alansari, A., 2023. Le Porphyre-Épithermal à Cu-Mo-Au-Ag d'Imourkhssen, Anti-Atlas Central, Maroc : Aperçu Des Données Métallogéniques, Géochimiques et Aéromagnétiques et Implications Pour l'exploration Minière." Québec Mines et Energie. Québec.

Feteha, B.F., Lentz, D.R., El Bouseily, A.M., Khalil, K.I., Khamis, H.A., Moghazi, A.K., 2022. Petrogenesis of Neoproterozoic Mo-Bearing A-Type Granites in the Gattar Area, Northern Eastern Desert, Egypt: Implications for Magmatic Evolution and Mineralization Processes. Ore Geology Reviews ,148 . https://doi.org/10.1016/j.oregeorev.2022.105007.

Figueroa, A. J. T., Gabo-Ratio, J. A. S., Manalo, P. C., Takahashi, R., Sato, H., Ramos, A. Bs., 2022. Breccia and Vein Mineralization of the Balatoc Diatreme, Acupan Gold Deposit, Baguio Mineral District: An Example of a Diatreme-Hosted Epithermal Deposit in the Philippines. Ore Geology Reviews, 144: 104826. https://doi.org/10.1016/j.oregeorev.2022.104826.

Gasquet, D., Ennih, N., Liégeois, J P., Soulaimani, A., Michard, A., 2008. The Pan-African Belt. Lecture Notes in Earth Sciences, 116: 33–64. https://doi.org/10.1007/978-3-540-77076-3_2.

Gasquet, D., Levresse, G., Cheilletz, Azizi-Samir, M R., Mouttaqi, A., 2005. Contribution to a Geodynamic Reconstruction of the Anti-Atlas (Morocco) during Pan-African Times with the Emphasis on Inversion Tectonics and Metallogenic Activity at the Precambrian-Cambrian Transition. Precambrian Research, 140 (3–4): 157–82. https://doi.org/10.1016/j.precamres.2005.06.009.

Haibi, H. E., Hadi, H. E., Tahiri, A., Poyatos, D. M., Gasquet, D., Pérez-Cáceres, I., Lodeiro,

F.G., Mehdioui, S., 2020. Geochronology and Isotopic Geochemistry of Ediacaran High-K Calc-Alkaline Felsic Volcanism: An Example of a Moroccan Perigondwanan (Avalonian?) Remnant in the El Jadida Horst (Mazagonia). Journal of African Earth Sciences, 163. https://doi.org/10.1016/j.jafrearsci.2019.103669.

Hassenforder, B., 1987. La Tectonique Panafricaine et Varisque de l'Anti-Atlas dans le massif du Kerdous (Maroc). Doctoral dissertation, Université Louis Pasteur, Strasbourg, (1971-2008).

Hedenquist, J., and Antonio, A., 1998. Evolution of an Intrusion-Centered Hydrothermal System: Far Southeast-Lepanto Porphyry and Epithermal Cu-Au Deposits, Philippine. Economic Geology, 93: 373–404.

Holden, E.-J., Wong, J.C., Kovesi, P., Wedge, D., Dentith, M., Bagas, L. 2012. Identifying Structural Complexity in Aeromagnetic Data: An Image Analysis Approach to Greenfields Gold Exploration. Ore Geology Reviews, 46: 47–59.

Hollard, H., Suter, G., Didon, J., Guardia, P., Dresnay, R., Medioni, R., Choubert, G., Faure-Muret, A., 1985. Carte Géologique Du Maroc Au 1/1 000 000. Notes et Mémoires Du Service Géologique Du Maroc, Feuille Nord, 260 (2): 1–96.

Jébrak, M., and Marcoux, Eric., 2008. Géologie Des Ressources Minérales. Vol. 33.

Jébrak, M., Marcoux, É., Nasloubi, M., Zaharaoui, M., 1998. From Sandstone- to Carbonate-Hosted Strata Bound Deposits: An Isotope Study of Galena in the Upper-Moulouya District (Morocco). Mineralium Deposita, 33 (4): 406–15. https://doi.org/10.1007/s001260050158.

Karaoui, B., Breitkreuz, C., Mahmoudi, A., Youbi, N., Hofmann, M., Gärtner, A., Linnemann, U., 2015. U-Pb Zircon Ages from Volcanic and Sedimentary Rocks of the Ediacaran Bas Draâ Inlier (Anti-Atlas Morocco): Chronostratigraphic and Provenance Implications. Precambrian Research, 263: 43–58. https://doi.org/10.1016/j.precamres.2015.03.003.

Kósaka, H., and Wakita, K., 1978. Some Geologic Features of the Mmnut Porphyry Copper Deposit, Sabah, Malaysia. Economic Geology, 73: 618–27.

Lee, C-T. A., and Tang., M. 2020. How to Make Porphyry Copper Deposits. Earth and Planetary Science Letters, 529 (115868).

Letsch, D., Large, S., Buechi, M.W., Winkler, W., Quadt., A.V., 2018. Ediacaran Glaciations of the West African Craton – Evidence from Morocco. Precambrian Research, 310: 17–18.

Levresse, G., 2001. Contribution to the Establishment of a Genetic Model of the Imiter (Ag-Hg), Bou Madine (Pb-Zn-Cu-Ag-Au), Bou Azzer (Co-Ni-As-Au-Ag) Deposits in the Moroccan Anti-Atlas. Doctoral dissertation, PhD Thesis.

Levresse, G., Cheilletz, A., Gasquet, D., Reisberg, L., Deloule, E., Marty, B., Kyser, K., 2004. Osmium, Sulphur, and Helium Isotopic Results from the Giant Neoproterozoic Epithermal Imiter Silver Deposit, Morocco: Evidence for a Mantle Source. Chemical Geology, 207 (1–2): 59–79. https://doi.org/10.1016/j.chemgeo.2004.02.004.

Liégeois, J. P., Navez, J., Hertogen, J., Black, R., 1998. Contrasting Origin of Post-Collisional High-K Calc-Alkaline and Shoshonitic versus Alkaline and Peralkaline Granitoids. The Use of Sliding Normalization. Lithos, 45 (1–4): 1–28. https://doi.org/10.1016/S0024-

4937(98)00023-1.

Linnemann, U., Ovtcharova, M., Schaltegger, U., Gärtner, A., Hautmann, M., Geyer, G., Vickers-Rich, P., Rich, T., Plessen, B., Hofmann, M., Zieger, J., Krause, R., Kriesfeld, L., and Smith, J., 2019, New high-resolution age data from the Ediacaran-Cambrian boundary indicate rapid, ecologically driven onset of the Cambrian explosion: Terra Nova, v. 31, no. 1, p. 49–58, https://doi.org/10.1111/ter.12368.

Linnemann, U., Gerdes, A., Hofmann, M., Marko, L., 2014. The Cadomian Orogen: Neoproterozoic to Early Cambrian Crustal Growth and Orogenic Zoning along the Periphery of the West African Craton-Constraints from U-Pb Zircon Ages and Hf Isotopes (Schwarzburg Antiform, Germany). Precambrian Research, 244 (1): 236–78. https://doi.org/10.1016/j.precamres.2013.08.007.

Lowell, J.D., Guilbert, J.M. 1970. Lateral and Vertical Alteration-Mineralization Zoning in Porphyry Ore Deposit. Economic geology, 65(4), 373-408.

Maloof, A.C., Schrag, D.P., Crowley, J.L., Bowring, S.A. 2005. An Expanded Record of Early Cambrian Carbon Cycling from the Anti-Atlas Margin, Morocco. Journal of Earth Sciences, 42: 2195–2216.

Maniar, P.D., and Piccoli, P.M., 1989. Tectonic Discrimination of Granitoids. Geological Society of America Bulletin, 101 (5): 635–43.

Mao, J., Zhang, J., Pirajno, F., Ishiyama, D., Su, H., Guo, C., & Chen, Y., 2011. Porphyry Cu-Au-Mo-Epithermal Ag-Pb-Zn-Distal Hydrothermal Au Deposits in the Dexing Area, Jiangxi Province, East China-A Linked Ore System. Ore Geology Reviews, 43 (1): 203–16. https://doi.org/10.1016/j.oregeorev.2011.08.005.

Middlemost, E.A.K., 1994. Naming Materials in the Magma/Igneous Rock System. Earth Science Reviews, 37 (3–4): 215–24. https://doi.org/10.1016/0012-8252(94)90029-9.

Mifdal, A., and Peucat, J.J., 1985. Datation U/Pb et Rb/Sr Du Volcanisme Acide de l'Anti-Atlas Marocain et Du Socle Sous-Jacent Dans La Région de Ouarzazate; Apport Au Problème de La Limite Précambrien-Cambrien. Sci. Géol, no. Strasbourg 38,: 185–200.

Miller, H.G, and V Singh., 1994. Potential Field Tilt—A New Concept for Location of Potential Field Sources. Journal of Applied Geophysics, 32: 213–17.

Morris, G. A., Larson, P. B., Hooper, P. R., 2000. Subduction Style Magmatism in a Non-Subduction Setting: The Colville Igneous Complex, NE Washington State, USA. Journal of Petrology, 41 (1): 43–67. https://doi.org/10.1093/petrology/41.1.43.

Mouttaqi, A, Rjimati, E.C., Maacha, L., Michard, A., Soulaimani, A., Ibouh, H., 2011. Main Mines of Morocco. New Geological and Mining Guidebooks of Morocco 9: 3–376.

Nance , R.D., Guti errez-Alonso, G., Keppie, J. D., R., Linnemann, U., Murphy, J. B., Quesada, C., Strachan, A., Woodcock, N H., 2012. A Brief History of the Rheic Ocean. Geoscience Frontiers, 3 (2): 125–35.

O'Connor, E. A., 2010. Geology of the Drâa, Kerdous, and Boumalne Districts, Anti-Atlas, Morocco. British Geological Survey, Keyworth, Nottingham, 310.

Ouabid, M., and Garrido, J.C., 2023. Widespread Cadomian–Pan-African Ediacaran Magmatism across the Moroccan Meseta: Implication for the Geodynamic Evolution of the NW Gondwana Margin. Precambrian Research, 387 , 106992.

https://doi.org/10.1016/j.precamres.2023.106992.

Pearce, J.A., 1996. Petrogenetic Implications of Ti, Zr, Y, and Nb Variations in Volcanic Rocks. Contributions to Mineralogy and Petrology, 69: 33–47.

Pearce, J. A., Harris, N. B., Tindle, A. G., 1984. Trace Element Discrimination Diagrams for the Tectonic Interpretation of Granitic Rocks. Journal of Petrology, 25 (4): 956–83. https://doi.org/10.1093/petrology/25.4.956.

Pearce, J.A., 1983. Role of the Sub-Continental Lithosphere in Magma Genesis at Active Continental Margins. In Continental Basalts and Mantle Xenoliths, 230-249.

Pei, N. I., Zhe, C. H. I., Junyi, P. A. N., 2020. An integrated investigation of ore-forming fluid evolution in porphyry and epithermal deposits and their implication on exploration. Earth Science Frontiers, 27(2), 60.

Pelleter, E., Cheilletz, A., Gasquet, D., Mouttaqi, A., Annich, M., Camus, Q., Deloule, E., Ouazzani, L., Bounjama, H., Ouchtouban, L., 2016. U/Pb Ages of Magmatism in the Zgounder Epithermal Ag–Hg Deposit, Sirwa Window, Anti-Atlas, Morocco. In Mineral Deposits of North Africa (pp. 143-165). Cham: Springer International Publishing.

Perrot, M., Tremblay, A., David, J., 2017. Detrital Zircon U-Pb Geochronology of the Magog Group, Southern Quebec - Stratigraphic and Tectonic Implications for the Quebec Appalachians. American Journal of Science, 317 (10): 1049–94. https://doi.org/10.2475/10.2017.01.

Zahour, R., Zahour, G., HADI, H. E., Zerhouni, Y., Baroudi, Z., Khoukhouchi, M., 2022. Petrology, Geochemistry, and Geodynamic Implications of the Ediacaran Volcanism of the Southwestern Edge of the Saghro Massif (Eastern Anti-Atlas, Morocco). Turkish Journal of Earth Science, 339–58.

Raeisi, D., Babazadeh, S., Long, L. E., Zhao, M., Cottle, J. M., Nayebi, N., Modabberi, S., 2024. Geochemical and Isotopic Signatures, and Zircon U-Pb Ages of the Oldest Known Intrusive Rocks Associated with Porphyry Cu Deposits in the Central Urumieh–Dokhtar Magmatic Arc, Iran. Journal of Geochemical Exploration, 256: 107366. https://doi.org/10.1016/j.gexplo.2023.107366.

Samson, S. D., Inglis, J. D., D'lemos, R. S., Admou, H., Blichert-Toft, J., Hefferan, K., 2004. Geochronological, geochemical, and Nd–Hf isotopic constraints on the origin of Neoproterozoic plagiogranites in the Tasriwine ophiolite, Anti-Atlas orogen, Morocco. Precambrian Research, 135(1-2), 133-147

Schulte, B., Boger, S.D., Benziane, F., Yazidi, A., Fanning, C. M., 2022. The Ouarzazate Supergroup and Its Plutonic Keel: The Relicts of an Ediacaran Silicic Large Igneous Province in North Africa.Journal of the Geological Society, 179 (5). https://doi.org/10.1144/jgs2021-114.

Seedorf, E., Dilles, J.D., Proffett, J.M., Einaudi, Jr., Zurcher, M.T., Stavast, M.D., Johnson, W.J.A., Barton, D.A., 2005. Porphyry Deposits: Characteristics and Origin of Hypogene Features. In Economic Geology, 251–98.

Shives, R.B.K., Ford, K.L., Charbonneau, B.W., 1995. Applications of Gamma- Ray Spectrometric/Magnetic/VLF-EM Surveys—Workshop Manual; Geological Survey of Canada, Open File 3061.

Sillitoe, R.H., 2010. Porphyry Copper Systems. Economic Geology ,105 (1): 3–41.

https://doi.org/10.2113/gsecongeo.105.1.3.

Sillitoe, R.H, 2008. Major Gold Deposits and Belts of the North and South American Cordillera: Distribution, Tectonomagmatic Settings, and Metallogenic Considerations. Economic Geology, 103 (4): 663–87. https://doi.org/10.2113/gsecongeo.103.4.663.

Simmons, S. F., White, N. C., John, D. A., 2005. Geological Characteristics of Epithermal Precious and Base Metal Deposits. Economic Geology, no. 1: 485–522. https://doi.org/10.5382/av100.16.

Sinclair, W.D., 2007. Porphyry Deposits. In Understanding Mineral Deposits, 353–413. https://doi.org/10.1007/978-94-011-3925-0_8.

Sláma, J., Košler, J., Condon, D. J., Crowley, J. L., Gerdes, A., Hanchar, J. M., Horstwood, MS.A., Morris, G.A., Nasdala, L., Norberg, N., Schaltegger, U., Schoene, B., Tubrett, N.M., Whitehouse, M. J., 2008. Plešovice Zircon - A New Natural Reference Material for U-Pb and Hf Isotopic Microanalysis. Chemical Geology, 249 (1–2): 1–35. https://doi.org/10.1016/j.chemgeo.2007.11.005.

Sparkes, G W, and G R Dunning., 2014. Late Neoproterozoic Epithermal Alteration and Mineralization in the Western Avalon Zone: A Summary of Mineralogical Investigations and New U/Pb Geochronological Results. Current Research, 99–128.

Sparkes, G. W., Ferguson, S. A., Layne, G. D., Dunning, G. R., O'Brien, S. J., Langille, A., 2016. The Nature and Timing of Neoproterozoic High-Sulphidation Gold Mineralization from the Newfoundland Avalon Zone : Insights from New u – Pb Ages , Ore Petrography and Spectral Data from the Hickey's Pond Prospect. Newfoundland and Labrador Department of Natural Resources Geological Report 16- 1(Geological Survey): 91–116.

Sun, W., Huang, R. F., Li, H., Hu, Y. B., Zhang, C. C., Sun, S. J., Zhang, L.P., Ding, X., Li, C-Y., Zartman, R.E., Ling, M.X., 2015. Porphyry Deposits and Oxidized Magmas. Ore Geology Reviews, 65 (P1): 97–131. https://doi.org/10.1016/j.oregeorev.2014.09.004.

Sylvester, P.J. 1994. Archean Granite Plutons. Developments in Precambrian Geology, 11 (C): 261–314. https://doi.org/10.1016/S0166-2635(08)70225-1.

Thomas, R. J., Fekkak, A., Ennih, N., Errami, E., Loughlin, S. C., Gresse, P. G., Chevallier, L. P., Liégeois, J. P., 2004. A New Lithostratigraphic Framework for the Anti-Atlas Orogen, Morocco. Journal of African Earth Sciences, 39 (3–5): 217–26. https://doi.org/10.1016/j.jafrearsci.2004.07.046.

Thomas, R.J., Chevallier, L.P., Gresse, P.G.., Harmer, R.E., Eglington, B.M., Armstrong, R.A., De Beer, C.H., Martini., J.E.J., de Kock, G.S., Macey, P.H., Ingram, B.A., 2002. Precambrian Evolution of the Sirwa Window, Anti-Atlas Orogen, Morocco. Precambrian Research, 118 (1–2): 1–57. https://doi.org/10.1016/S0301-9268(02)00075-X

Toummite, A., Liegeois, J.P., Gasquet, D., Bruguier, O., Beraaouz, E.H., Ikenne, M., 2012. Field, Geochemistry and Sr-Nd Isotopes of the Pan-African Granitoids from the Tifnoute Valley (Sirwa, Anti-Atlas, Morocco): A Post-Collisional Event in a Metacratonic Setting. Mineralogy and Petrology, 107 (5): 739–63. https://doi.org/10.1007/s00710-012-0245-3.

Triantafyllou, A., Berger, J., Baele, J.M., Mattielli, N., Ducea, M.N., Sterckx, S., Samson, S., Hodel, F., Ennih, N., 2020. Episodic Magmatism during the Growth of a Neoproterozoic

Oceanic Arc (Anti-Atlas, Morocco). Precambrian Research, 339, 105610.

Triantafyllou, A., Berger, J., Baele, J. M., Diot, H., Ennih, N., Plissart, G., Monnier, C., Watlet, A., Bruguier, O., Spagna, P., Vandycke, S.,2016. The Tachakoucht-Iriri-Tourtit Arc Complex (Moroccan Anti-Atlas): Neoproterozoic Records of Polyphased Subduction-Accretion Dynamics during the Pan-African Orogeny. Journal of Geodynamics, 96: 81–103. https://doi.org/10.1016/j.jog.2015.07.004.

Tuduri, J., Chauvet, A., Barbanson, L., Bourdier, J.L., Labriki, M., Ennaciri, A., Badra, L., duboit, M., Ennaciri-Leloix, C., Sizaret, S., Maacha, L., 2018b. The Jbel Saghro Au(–Ag, Cu) and Ag–Hg Metallogenetic Province: Product of a Long-Lived Ediacaran Tectono-Magmatic Evolution in the Moroccan Anti-Atlas. Minerals, 8 (12). https://doi.org/10.3390/min8120592

Tuduri, J., Chauvet, A., Barbanson, L., Labriki, M., Dubois, M., Trapy, P.-H., Lahfid, A., Poujol, M. Melleton, J., Badra, L., 2018a. Structural Control, Magmatic-Hydrothermal Evolution and Formation of Hornfels-Hosted, Intrusion-Related Gold Deposits: Insight from the Thaghassa Deposit in Eastern Anti-Atlas, Morocco. Ore Geology. 97: 171–198.

Vermeesch, P., 2018. IsoplotR: A Free and Open Toolbox for Geochronology. Geoscience Frontiers, 9 (5): 1479–93. https://doi.org/10.1016/j.gsf.2018.04.001.

Voudouris, P., Mavrogonatos, C., Spry, P. G., Baker, T., Melfos, V., Klemd, R., Haase, K., Repstock, A, Djiba, A., Bismayer, U., Trantola, A., Scheffer, C., Moritz, R., Kouzmanov, K., Alfiferis, A., Papvasiliou, K., Schaarschmidt, A., Glanopoulos, E., Galanos, E., Kolodziejczyk, J., 2019. Porphyry and Epithermal Deposits in Greece: An Overview, New Discoveries, and Mineralogical Constraints on Their Genesis. Ore Geology Reviews, 107: 654–91. https://doi.org/10.1016/j.oregeorev.2019.03.019.

Walsh, G. J., Benziane, F., Aleinikoff, J. N., Harrison, R. W., Yazidi, A., Burton, W. C., Quick, J.E., Saadane, A., 2012. Neoproterozoic Tectonic Evolution of the Jebel Saghro and Bou Azzer-El Graara Inliers, Eastern and Central Anti-Atlas, Morocco. Precambrian Research, 216–219: 23–62. https://doi.org/10.1016/j.precamres.2012.06.010.

Walsh, G.J., Aleiniko, J.N., Benziane, F., Yazidi, A., Armstrong, T.R., 2002. U–Pb Zircon Geochronology of the Palaeoproterozoic Tagragra de Tata Inlier and Its Neoproterzoic Cover, Western Anti-Atlas, Morocco. Precambrian Research, 117: 11–20.

Wang, X. Q., and Ji, F. B., 2024. Petrogenesis and Metallogenic Implications of Eocene–Oligocene Magmatism in the Yulong Porphyry Copper Belt, Eastern Tibet: A Review and Analysis of Geochronological, Geochemical, and Sr–Nd–Pb–Hf Isotopic Data. Canadian Journal of Earth Sciences, 61 (3): 270–85. https://doi.org/10.1139/cjes-2023-0087.

Warr, L.N., 2021. IMA–CNMNC Approved Mineral Symbols. Mineralogical Magazine, *85* (3), 291-320

Whitney, D. L., and Evans, B. W., 2010., Abbreviations for Names of Rock-Forming Minerals. American Mineralogist, 95 (1): 185–87. https://doi.org/10.2138/am.2010.3371.

Wiedenbeck, M., Allé, P., Corfu, F., Griffin, W.L., Meier, M., Oberli, F., Von quadt, A., Roddick, J.C., Spiegel, W., 1995. Three Natural Zircon Standards for U-Th-Pb, LU-HF, Trace Element and REE Analyses."Geostandards Geostandards newsletter, 19(1), 1-23

Yang, Z., and Cooke, D, R., 2019. Chapter 5 Porphyry Copper Deposits in China. In Mineral

Deposits of China . Society of Economic Geologists, (pp. 133-187).

Youbi, N., Ernst, R. E., Söderlund, U., Boumehdi, M. A., Ait Lahna, A., Tassinari, C. C. G., El Moume, W., Bensalah, M. K., 2020. The Central Iapetus magmatic province: An updated review and link with the ca. 580 Ma Gaskiers glaciation.

4. CHAPTER 4: AEROMAGNETIC DATA FROM THE ASSARAG AREA: IMPLICATIONS FOR THE IMOURKHSSEN PORPHYRY MINERALIZATION

Mariam Ferraq [1,2], Saïd Belkacim [1,2], Bahman Abbassi [2], Li-Zhen Cheng [2]

1 Laboratory of Applied Geology and Geo-Environment (LAGAGE), Department of Earth Sciences, Faculty of Sciences, Ibn Zohr University, Agadir 80000, Morocco.

2 Research Institute on Mines and Environment, University of Quebec in Abitibi-Timiskaming, Rouyn-Noranda, QC J9X 5E4, Canada.

* Correspondence: mariam.ferraq@edu.uiz.ac.ma

Article Published in the Journal of Africain Earth Sciences, Vol 234. November, 2025

4.1 Résumé

La région d'Assarag est située dans la partie nord du saillant d'Ouzellagh-Siroua, qui est un segment du socle central de l'Anti-Atlas s'élevant dans la ceinture du Haut-Atlas au Maroc. Elle se compose principalement des suites magmatiques de l'Édiacarien supérieur (LEMS) du groupe de Ouarzazate (580-539 Ma). Les LEMS comprennent des granitoïdes calco-alcalines hautement potassiques de type I, qui abritent la minéralisation porphyrique à Cu-Mo-Au-Ag d'Imourkhssen. Les données aéromagnétiques de la région d'Assarag ont permis de décrire les caractéristiques structurales du LEMS sur la base de leurs empreintes magnétiques. Les ensembles de données aéromagnétiques ont été traités à l'aide de plusieurs transformations, notamment la réduction au pôle (RTP), la continuation vers le haut (UC), la dérivée d'inclinaison (TD), le centre de ciblage d'exploration (CET) et les filtres de déconvolution d'Euler (ED). Les transformations RTP, TD et CET ont permis de cartographier des failles orientées NNE-SSO, NNO-SSE et NE-SO dans le nord, en plus d'un halo magnétique incurvé dans la partie sud-ouest de la région d'Assarag. Le filtre UC a subdivisé la région d'Assarag en deux morpho-structuraux domaines magnétiques : une région septentrionale présentant des signatures magnétiques faibles et une région méridionale présentant des propriétés magnétiques élevées avec des structures positives incurvés. Les résultats ED correspondent et supportent les linéaments extraits. Les données aéromagnétiques ont été également traitées à l'aide d'un outil d'extraction et de sélection de caractéristiques spatio-spectrales (SFES2D) utilisant des transformations en ondelettes continues bidimensionnelles (2D CWT), une analyse en composantes principales (ACP) et une analyse en composantes indépendantes par les méthodes de kurtosis et de néguentropie (k-ICA et n-ICA). Les résultats de l'ACP corroborent les linéaments précédemment extraits et mettent en évidence une nouvelle structure orientée ENE-OSO. Parallèlement, la CWT nous a permis de conclure que les tendances NNE, NNO et NE sont peu profondes et a mis en évidence des structures profondes NO-SE et ENE-OSO dans la partie sud de la région d'Assarag. L'ICA met en évidence le linéament ENE et correspond aux résultats précédents. Nous définissons ici la tendance ENE plus profonde comme faisant partie de la Faille Sud Atlasique (SAF), qui recoupe le LEMS dans la zone d'étude. Par ailleurs, les caractéristiques tectoniques peu profondes NE-SO et NNE-SSO ont probablement servi de conduits pour les fluides minéralisés, conduisant à la minéralisation Cu±Mo±Au±Ag d'Imourkhssen. Par conséquent, ces directions constituent une approche précieuse pour guider l'exploration minière dans le saillant d'Ouzellagh-Siroua, de l'échelle prospective à l'échelle régionale.

Mots clés : Ediacaran ; Données aéromagnétiques, minéralisation porphyrique, caractéristiques structurelles, Ouzellagh-Siroua.

4.2 Abstract

The Assarag region is located in the northern part of the Ouzellagh-Siroua salient, being a segment of the central Anti-Atlas basement bulging within the High-Atlas Belt of Morocco. It consists mainly of the Late Ediacaran Magmatic Suites (LEMS) of the Ouarzazate Group (580-539 Ma). The LEMS comprise high potassic calc-alkalic I-type granitoids that host the Imourkhssen Cu-Mo-Au-Ag porphyry mineralization. The aeromagnetic data from the Assarag region led to describe structural features in the LEMS based on their magnetic footprints. aeromagnetic datasets were processed using several transformations including the reduction to pole (RTP), Upward continuation (UC), Tilt derivative (TD), Center for Exploration Targeting (CET) and Euler deconvolution (ED) filters. RTP, TD and CET transformations allowed to map NNE-SSW, NNW-SSE and NE-SW trending faults in the north, in addition to a curved magnetic halo in the southwestern part of the Assarag area. The UC filter subdivided the Assarag area into two magnetic morpho-structural domains: a northern region with low-magnetic features, and a southern high-magnetic region with positive curved trending patterns. The ED results match and support the extracted lineaments. The aeromagnetic data were also processed by a 2D Spatio-Spectral Feature Extraction and Selection tool (SFES2D) using two-dimensional continuous wavelet transformations (2D CWT), principal component analysis (PCA) and independent component analysis by kurtosis and negentropy methods (k-ICA and n-ICA). The PCA results corroborate previously extracted lineaments and highlight a new ENE-WSW oriented structure. Meanwhile, the CWT allowed us to conclude that NNE, NNW and NE trends are shallow and emphasized deep NW-SE and ENE-WSW structures in the southern part of the Assarag area. ICA emphasizes the ENE lineament and matches the previous results. We herein define the deeper ENE trend as a part of the South Atlas Fault (SAF), which crosscuts the LEMS in the study area. Meanwhile, the shallow NE-SW and NNE-SSW tectonic features likely served as conduits for the ore-bearing fluids, leading to the Imourkhssen Cu-Mo-Au-Ag mineralization. Consequently, these directions present a valuable approach for guiding mineral exploration in the Ouzellagh-Siroua salient, from prospect to regional scales.

Keywords: Aeromagnetic data, porphyry mineralization, structural features, Ouzellagh-Siroua.

4.3 Introduction

The diverse geological events spanning from the Eburnean to the Alpine orogenies have significantly contributed to the development and the exposure of several ore deposit types in the Pan-Africain Anti-Atlas (Gasquet et al., 2005) belt of Morocco. These deposits related to regional thermo-tectonic events, were commonly gathered into regional metallogenic provinces (Gasquet et al., 2005; Bouabdellah and Slack, 2016; Tuduri et al., 2018). During the terminal phases of the Pan-African Orogeny, the Late Ediacaran episode (580-539 Ma) was notably characterized by a huge silicic magmatic activity, referred to as the Ouarzazate SLIP (Youbi et al., 2021; Belkacim et al., 2021; Ferraq et al., 2024), within a transtensive tectonic regime that evolved to extension after the post-orogenic collapse (Thomas et al., 2002; Gasquet et al., 2005; O'Connor, 2010; Soulaimani et al., 2014). In this context, major structures mainly correspond to local reactivations of Eburnean fractures along major shear zones (Hassenforder, 1987; Soulaimani et al., 2014). Moreover, N- to NE-trending faults controlled the western part of Anti-Atlas, unlike a transtensive opening regime that characterized its central and eastern parts (Soulaimani et al., 2014). This period was perfectly in favor of hydrothermal activity that was intensified through faults and regional structures, leading to the development of various types of ore deposits (Gasquet et al., 2005; Tuduri et al., 2018; Belkacim et al., 2021).

Aeromagnetic survey has been extensively used in structural mapping (Bouzekraoui et al., 2024b) and mineral exploration (Sassioui et al., 2024; Tobi et al., 2025), because the magnetic assessment is considered to be a very effective tool promoting the identification of deep contacts and regional structures (Domzalski, 1966; Holden et al., 2016). These tectonic structures could be potentially associated with ore deposits in different contexts (Nabighian et al., 2005). Accordingly, the spatial relationship between magnetic lineaments and ore-bearing structures has been widely analyzed to advance the exploration of economic mineral resources (Aabi et al., 2024 and references therein). Meanwhile, magnetic data can be coupled with electrical and/or radiometric methods when investigating petrophysical variations surrounding epithermal ore deposits (Mamouch et al., 2022, 2023), and potential rooted porphyry mineralization (Abbassi et al., 2018, 2022).

In the High Atlas and Anti-Atlas of Morocco, aeromagnetic geophysical studies assessing the spatial and genetic relationships between mineralization and tectonic structures have predominantly targeted: the High Atlas massif (Dadi et al., 2024; Tobi et al., 2025), Saghro

inlier (Miftah et al., 2021b; Mamouch et al., 2023; Achkouch et al., 2023; Aabi et al., 2024), Bou Azzer inlier (Soulaimani et al., 2022), Siroua inlier (Tazi et al., 2022), Ougnat inlier (Sassioui et al., 2024) and Ighrem inlier (Ouchchen et al., 2021; Echogdali et al., 2022).

The present work consists of a series of aeromagnetic data processing aimed at extracting the main structural features of the Assarag region and their implications on the Cu-Mo-Au-Ag porphyry mineralization of Imourkhssen, particularly deep structures. This study has highlighted the continuation of the South Atlas Fault (SAF) that crosses the Assarag region.

4.4 Geological setting

The Anti-Atlas (AA) of Morocco lies along the northern boundary of the West African Craton (WAC), recording the major Eburnean, Pan-Africain and Variscan orogenies (Fig. 1a; Ennih and Liégeois, 2001; Karaoui et al., 2015). The AA belt exhibits a Precambrian crystalline basement beneath a slightly folded Late Ediacaran and Early Paleozoic volcanic and sedimentary sequences (**Figure 4.1 b**; Choubert, 1963; Gasquet et al., 2008), that were slightly reworked during the Variscan and Alpine orogenies (Kouyaté et al., 2013). The Proterozoic basement crops out through erosion of its cover in several inliers (Bas Drâa, Ifni, Kerdous, Tagragra of Akka, Tagragra of Tata, Igherm, Siroua, Zenaga, Bou Azzer, Saghro, and Ougnat). These inliers are distributed across two distinct domains that are delineated by the Anti-Atlas Major Fault (AAMF) (i.e., the western cratonic and the eastern mobile domain; Choubert, 1963). The latter, including, Siroua, Bou Azzer, Saghro and Ougnat inliers is bracketed to the north by the South Atlas Fault (SAF), and was recently identified as a single terrane pointed as the Saghro domain (Schulte et al., 2022). Further geochronological studies had proved the contribution of inherited magmatic zircons from the cratonic material during the Ediacaran magmatism, suggesting a buried cratonic basement beneath the whole Anti-Atlas (Ennih and Liégeois, 2001; Soulaimani et al., 2006; Errami et al., 2009).

Overall, the study area (**Figure 4.1 b, c**) is located in Ouzellagh-Siroua Salient or "promontory" (Choubert, 1963), which is a pivotal zone and distinct paleogeographic area that records the effects of major orogenic events occurred in the Anti-Atlas (Álvaro et al., 2014a). It is one of the largest and best-exposed inliers where the Late Ediacaran rocks represent a key target area for porphyry and epithermal deposit types.

The Precambrian rocks consist of the Late Ediacaran magmatic suites (LEMS) of the Ouarzazate Group (580–539 Ma) (Hollard et al., 1985; Youbi et al., 2011; Linnemann et al.,

2019), intruded within the volcano-sedimentary formations of the Saghro Group (630–600 Ma; Liégeois et al., 2006; Errami et al., 2020). The LEMS consists of high-K calc-alkaline I-type granitoids (Toummite et al., 2012; Belkacim et al., 2014; Ferraq et al., 2024), comprising

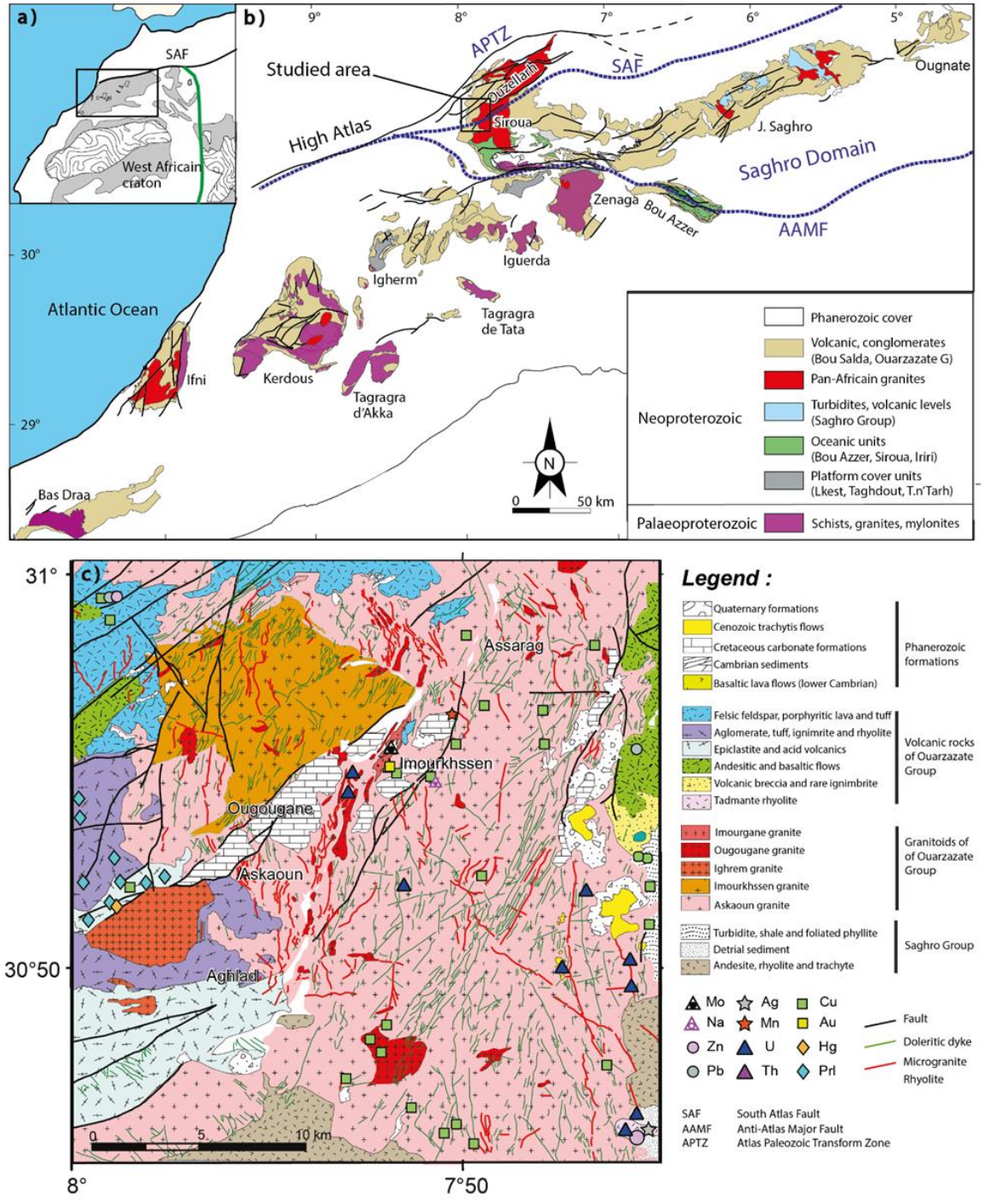

Figure 4.1.

a) Location of the Anti-Atlas domain within the West African craton. b) Location of the studied area and generalized geological map of the Anti-Atlas, modified after (Gasquet et al. 2008). c) Detailed geological map of the Assarag area modified from (Thomas et al., 2002. Toummite et al., 2012. Belkacim et al., 2017).

(i) the Assarag Suite, that includes the Askaoun quartz diorite and granodiorite batholiths. The latter yielded U-Pb zircon ages around 575 Ma (Thomas et al., 2002; Belkacim et al., 2021), and around 558 Ma (Toummite et al., 2012); (ii) the Amassine Suite consists of the star-shaped Imourkhssen granite intruded into the Assarag Suite. This granite has been dated by U-Pb on zircon ages at 562 ± 5 Ma (Thomas et al., 2002), 561 ± 3 Ma (Toummite et al., 2012) and 558 ± 1 Ma (Ferraq et al., 2024); (iii) the Ougougane Suite is intruded into the Assarag and Amassine suites and comprises a wide range from volcanic to plutonic felsic rocks, such as the Ougougane rhyolite dated at 550 ± 1.5 Ma (Belkacim et al., 2021), and the Imourgane granite dated at 550 ± 2 Ma (Ferraq et al., 2024). The entire sequence is transected by the Zaghar mafic dyke swarms, dated at 554 ± 6 Ma in the northeastern part of the studied area (El Moume et al., 2020).

The Assarag area hosts several copper, gold, molybdenum, uranium, manganese and pyrophyllite occurrences (Fig. 1c). The Imourkhssen Cu-Mo-Au-Ag porphyry and the Zgounder Ag-Hg epithermal deposit are the most important of these occurrences (Marcoux and Wadjinny, 2005; Pelleter et al., 2016; Belkacim et al., 2014; Ferraq et al., 2024) in the Ouzellagh-Siroua Salient.

4.5 Geophysical Survey

Aeromagnetic survey provides direct informations on subsurface lithological and structural features that are not detectable at the surface. This geophysical approach is particularly effective in delineating concealed faults, buried intrusive bodies, and structural trends beneath the surface, making them particularly suitable for geological and mineral exploration purposes. Furthermore, aeromagnetic data are readily integrated with other data sets enabling comprehensive and large-scale geological interpretations.

Aeromagnetic data were acquired between November 1998 and May 1999 using Eurocopter AS350B2 and AS350B3 helicopters, by the Geophysics Service of the Ministry of Energy Transition and Sustainable Development of Morocco. The flight lines were oriented at 315 °, 30 °, 10 ° and spaced by 500 m apart. A cesium magnetometer with a sensitivity of 0.01 nT was conducted to collect data at an average ground clearance of 30 m. The initial data underwent corrections including denoising, errors closure and removal of diurnal variations. The resulting data allowed to produce a map of the residual magnetic field, which is digitized and subsequently post-processed (filters and transformations) (**Figure 4.2**).

4.6 Aeromagnetic Data Processing

In order to emphasize geological boundaries, to characterize magnetic anomalies and to outline the main structural features in the Assarag region, several filters were applied to the residual magnetic field map using Oasis Montaj Educational software.

4.6.1 Reduction to pole (RTP)

This filter is an operator applied in the frequency (wavenumber) domain that allows the transformation of the data to the signal that is expected to be recorded at the magnetic poles. RTP leads to eliminate the distortion of the anomalies and to move them straight over their real geological causative sources (Baranov, 1957). The transform formula is given by the following equation (Baranov, 1957; Blakely, 1995):

$$L(\Theta) = \frac{1}{(\sin(I_a) - i\cos(I)\cos(D - \Theta))^2}$$

L(Θ) is the RTP operator in the frequency domain.

I is the geomagnetic inclination.

I_a is the inclination for amplitude correction (never less than I).

D is the geomagnetic declination.

Θ is the azimuth of the wavenumber.

i is the imaginary unit $\sqrt{-1}$.

4.6.2 Upward continuation (UC)

This transformation minimizes the high-frequency near surface magnetic anomalies related to superficial magnetic sources, and emphasizes low-frequency anomalies resulted from deeper origins (Jacobsen, 1987). Consequently, it is used to discriminate between shallower and deeper magnetic sources (Ivan, 1986). The expression of the UC operation is described as follows (Sailhac, 1999):

$$U(x, y, z_0 - \Delta z) = \frac{\Delta z}{2\pi}\iint_{-\infty}^{\infty} \frac{U(x', y', z_0)}{(x - x')^2 + (y - y')^2 + \Delta z^2)^{\frac{3}{2}}} dx'y'$$

Where: Δz: > 0 and Z_0 is the aircraft's elevation and Δz the reference plane.

4.6.3 Tilt derivative (TD)

TD is considered as arctangent of the ratio of the vertical derivative and the total horizontal derivative. It highlights major magnetic lineaments and enhance the detection of the edges of the magnetic sources and estimating their depths (Miller and Singh, 1994; Verduzco, 2004; Salem et al., 2007). The Tilt angle value is bracket between [-π/2 and π/2] (radian), while its amplitude is positive above the magnetic sources, negative outside the magnetic sources and null above the edges (Miller and Singh, 1994).

The TD equation is given by Blakely et al., (2016) and reference therein:

$$\theta = \tan^{-1} \frac{\partial A/\partial z}{\sqrt{(\partial A/\partial x)^2 + (\partial A/\partial y)^2}}$$

Where: ∂A⁄∂x, ∂A⁄∂y, ∂A⁄∂z: derivatives of the magnetic field M in the x, y and z directions.

4.6.4 Center for exploration targeting (CET)

It is performed not only to locate the magnetic lineaments, but also to target potential areas for mineral exploration (Core et al., 2009). It emerges from a combination of several grid analyses and multi-directional detection of magnetics lineaments, that are considered as a prospective zones of ore accumulation (Holden et al., 2012).

The CET is used in this study for lineament and structural complexity mapping using the CET algorithm in five processing stages (Osinowo et al., 2020). The treatment steps comprises: texture analysis, phase symmetry (or congruency), amplitude thresholding, skeletonization and skeleton to vector conversion (Lam and Lee, 1992; Kovesi, 1997; Holden et al., 2010). The texture analysis estimates the location of local variation of magnetic anomalies, while phase symmetry detects the complex structures. The artefacts are processed though the amplitude thresholding, and the linear features are extracted by the skeletonization, and converted thereafter to vector during the last step (i.e., skeleton to vector).

4.6.5 Euler deconvolution (ED)

The ED is used in order to outline the magnetic sources, highlight the magnetic lineaments and provide accurate estimations of their depths (Reid et al., 1990). Important parameters should be well defined for meaningful results, such as: the structural index that leads to detect contacts and lineaments, as well as the size of the window which handles the depth of the magnetic

sources (Reid et al., 1990). In this study the structural index = 0, the window size = 7 and the tolerance is about 4 %. The ED relationship is given as follows (Reid et al., 1990):

$$\frac{(x-x_0)\delta M}{\delta x}+\frac{(y-y_0)\delta M}{\delta y}+\frac{(z-z_0)\delta M}{\delta z}=N(B-M)$$

Where:

x_0; y_0; z_0: Coordinates of anomaly source.

M: Value of the total field (x, y, z).

N: Structural Index.

B: Value of the regional value of total magnetic field.

4.7 Advanced feature extraction and integration with CWT, PCA and ICA

To enhance structural interpretation, aeromagnetic data were combined with satellite imagery and processed using the SFES2D tool (Abbassi and Cheng, 2021; Abbassi et al., 2022; Abbassi and Cheng, 2025). Three complementary methods were applied: the Two-Dimensional Continuous Wavelet Transform (2D CWT), Principal Component Analysis (PCA) and Independent Component Analysis by kurtosis and negentropy methods (k-ICA and n-ICA).

4.7.1 Principal Component Analysis (PCA)

PCA is primarily used to reduce the dimensionality of multivariate geophysical data while retaining the most significant patterns. The dataset is arranged as matrix X, where each row represents a spatial location and each column a variable or measurement channel. The principal component transformation is performed by projecting the data onto the eigenvectors of the covariance matrix:

$$\mathrm{Y} = \mathrm{XW}$$

Where:

- X is the centered data matrix.
- W contains the eigenvectors (principal axes).
- Y is the transformed matrix of principal components.

PCA algorithm efficiently minimizes high redundancy of multi-channel or multi-source geophysical datasets (e.g., magnetic, gravity, and remote sensing images), capturing the principal directions of variance that often correspond to principal component features. This

global feature extraction helps to emphasize dominant geological trends, large-scale structures and suppresses random noise and data redundancy.

4.7.2 Two-Dimensional Continuous Wavelet Transform (2D CWT)

The 2D CWT was applied using the first-order partial derivative of the 2D Gaussian function with respect to x-direction as the mother wavelet, denoted by $\psi_{1,0}(x, \mathrm{y})$:

$$\psi_{1,0}(x, \mathrm{y}) = -\frac{x}{2\pi\sigma^4} e^{-\left(\frac{x^2+y^2}{2\sigma^2}\right)}$$

Where:

- x and y are spatial coordinates.
- $\psi_{1,0}(x, \mathrm{y})$ is the 2D Gaussian derivative wavelet. The subscript (1,0) indicates the order of partial derivatives: first-order derivative in x-direction (n = 1) and zero-order in y-direction (m = 0). This specific choice of this low order of partial derivative (n = 1 and m = 0) creates a wavelet highly effective at edge detection, geological structures and lineament as it is sensitive to gradients along a specific direction. Whereas w high order derivatives (i.e., m or n > 1) allow detection of sharper, high-frequency features, but they inherently carry the risk of amplifying noise (Abbassi et al., 2025).
- and σ is the standard deviation controlling the spatial scale of the wavelet.

The 2D CWT of an image $f(x, \mathrm{y})$ at scale *a* and position $\mathrm{b} = (b_x, b_y)$ is computed as:

$$W_f(a, \mathrm{b}) = \iint_{-\infty}^{\infty} f(x, y) \frac{1}{a^2} \psi_{1,0}\left(\frac{x - b_x}{a}, \frac{y - b_y}{a}\right) dxdy$$

Where:

- $W_f(a, \mathrm{b})$ is the wavelet coefficient at scale *a* and position *b*.
- *a* is the scale (dilation) parameter, controlling the width of the wavelet and thus the size of features analyzed, and $\mathrm{b} = (b_x, b_y)$ is the translation (position) parameter, determining where the wavelet is centered in the image.
- $\frac{1}{a^2}$ is a normalization factor to maintain constant energy across scales.
- the arguments $\left(\frac{x-b_x}{a}, \frac{y-b_y}{a}\right)$ ensure the wavelet is properly scaled and centered at *b*.

The use of $\psi_{1,0}(x, \mathrm{y})$ emphasizes horizontal gradients (changes along the x-direction), making it particularly effective for detecting horizontal edges, lineaments, and structural discontinuities in geophysical data.

2D CWT provides localized and multi-scale analysis, enhancing structural discontinuities such as edges, faults, and lineaments. By tuning the scale parameter, the CWT can discriminate

between shallow and deep features and highlight subtle structural variations that may not be visible in global analyses.

4.7.3 Independent Component Analysis (k-ICA and n-ICA)

The kurtosis and negentropy maximizations represent effective unmixing methods that are widely used independent component analysis algorithms. Unlike PCA, these methods are used for the extraction of features exhibiting a non-Gaussian variation. Kurtosis measures the non-gaussianity by searching a rotation matrix R during the multiplication by principal components Y_{PC} that produce the least Gaussian outputs L (Hyvärinen and Kano, 2001; Abbassi, 2018; Hyvärinen, 2022):

$$L = R^T Y_{PC}$$

Therefore, the kurtosis can be computed as follows (Abbassi, 2018):

$$Kurt\ (L) = E(R^T Y_{PC})^4 - 3\{E((R^T Y_{PC})^2)\}^2$$

Where:

E(.) is the expected value.

Despite its efficiency, kurtosis can be affected by geological noise and artifacts. For this reason, the negentropy methods are used to assess non-Gaussian variations in a different way. Negentropy is based on the information-theoretic quantity of entropy. The entropy (H) of a signal (P) with probability density of p(P) is defined as (Hyvärinen and Oja, 2000):

$$H(P) = -\int p(P)\log\left(p(P)\right)dP$$

Gaussian distributions maximize entropy; by contrast, decrease the negentropy (Abbassi, 2018).

Combining 2D CWT, PCA and ICA leverages both global and local information:

- 2D CWT with the first-order Gaussian derivative wavelet enhances localized scale-dependent features—especially horizontal transitions.
- PCA condenses the dominant spatial patterns and reduces data redundancy.
- ICA handles fluctuations driven by non-Gaussian variations.

This integrated approach capitalizes on the global summarization of PCA and the local, scale-sensitive detection of 2D CWT and ICA, leading to a more comprehensive and reliable mapping of tectonic and structural features in the Assarag region.

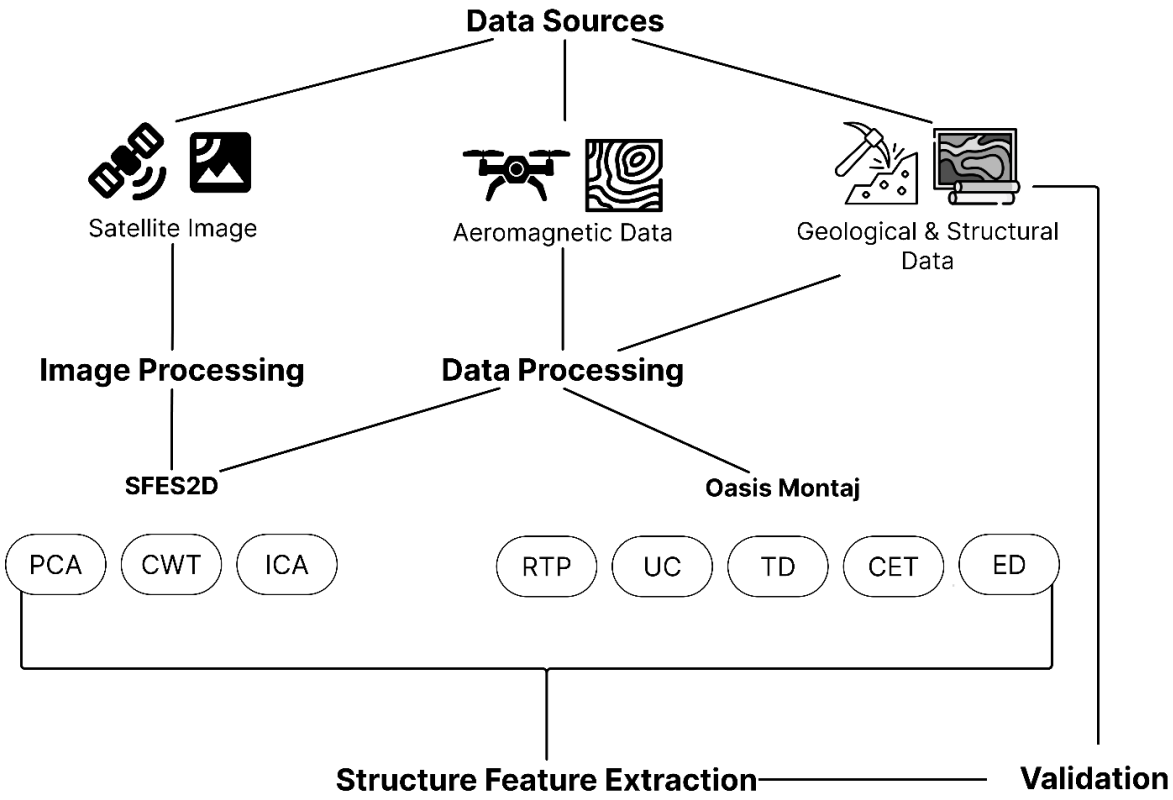

Figure 4.2
Data processing workflow.

4.8 Results

4.8.1 Residual magnetic field (RMF) and Reduction to pole (RTP) maps

The residual magnetic field map (RMF) of the Assarag area shows several anomaly types regarding their shapes, directions and intensity ranging from – 261 to + 302 nT (**Figure 4.3 a**).

Indeed, the magnetic anomalies consist generally of positive and negative types having asymmetric shapes, and directly impacted by the oblique inclination of Earth's magnetic field. To remove this effect, the RMF map of the Assarag region was reduced to pole using a magnetic inclination of 41.9◦ and declination of - 4.3◦.

The obtained RTP map (**Figure 4.3 b**) has anomalies ranging between – 355 and + 523 nT (instead of – 261 to + 302 nT), and shows light displacement of many magnetic anomalies such as the NNE-SSW, the NNW-SSE and the NE-SW lineaments. The lowest amplitude RTP anomalies occur to the northern part of the Assarag region overlaying the granitoids of the

Amassine and Ougougane suites (e.g., Imourkhssen, Imourgane and Ougougane granites; Fig. 4.1c). The highest amplitude RTP anomalies lie in the southern and eastern portions of the study area over the granodioritic Askaoun intrusion of the Assarag Suite, especially in the southwestern part where a magnetic halo occurs.

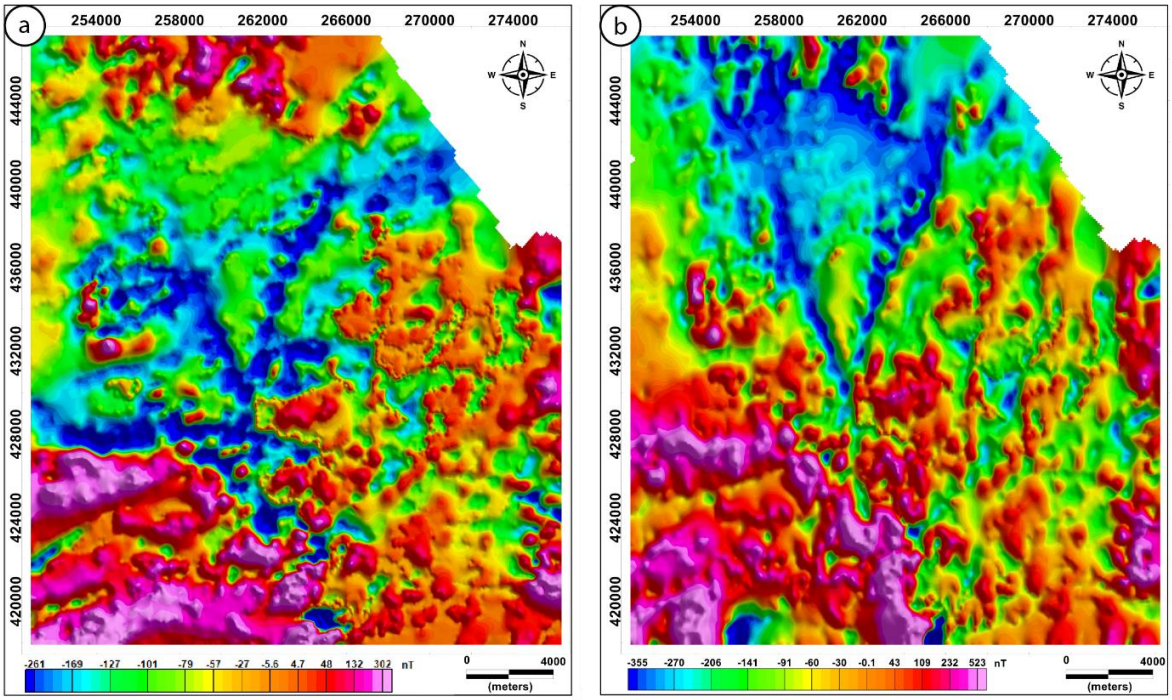

Figure 4.3
a) Residual magnetic field (RMF) and b) reduced to pole maps (RTP) of the Assarag area.

4.8.2 Upward continuation (UC)

The RTP magnetic anomaly map was extended upward at different heights (**Figure 4.4 a-d**; 250m, 500m, 1000m and 2000m respectively) to discriminate between shallow and deep magnetic sources. Moreover, the depth was limited to 2000 m, corresponding to the maximum thickness of the Ouarzazate Group (Soulimani et al., 2018), to focus on lineaments affecting this Group, and provide insights into its geodynamic and mining implications.

By increasing depths (**Figure 4.4 a-d**), the shallower anomalies disappear and deep magnetic (either positive or negative) anomalies remain. Extending to significant depths, the magnetic patterns show that: (i) the negative anomaly in the northern part of the map changes its shape and become elongated in the E-W direction: (ii) the NNE, NNW and NE trends disappear, unlike an ENE structure (**Figure 4.4 c**); (iii) the deep positive curved anomaly remains at the southern part of the Assarag map highlighting a deep magnetic halo in this area (**Figure 4.4 d**).

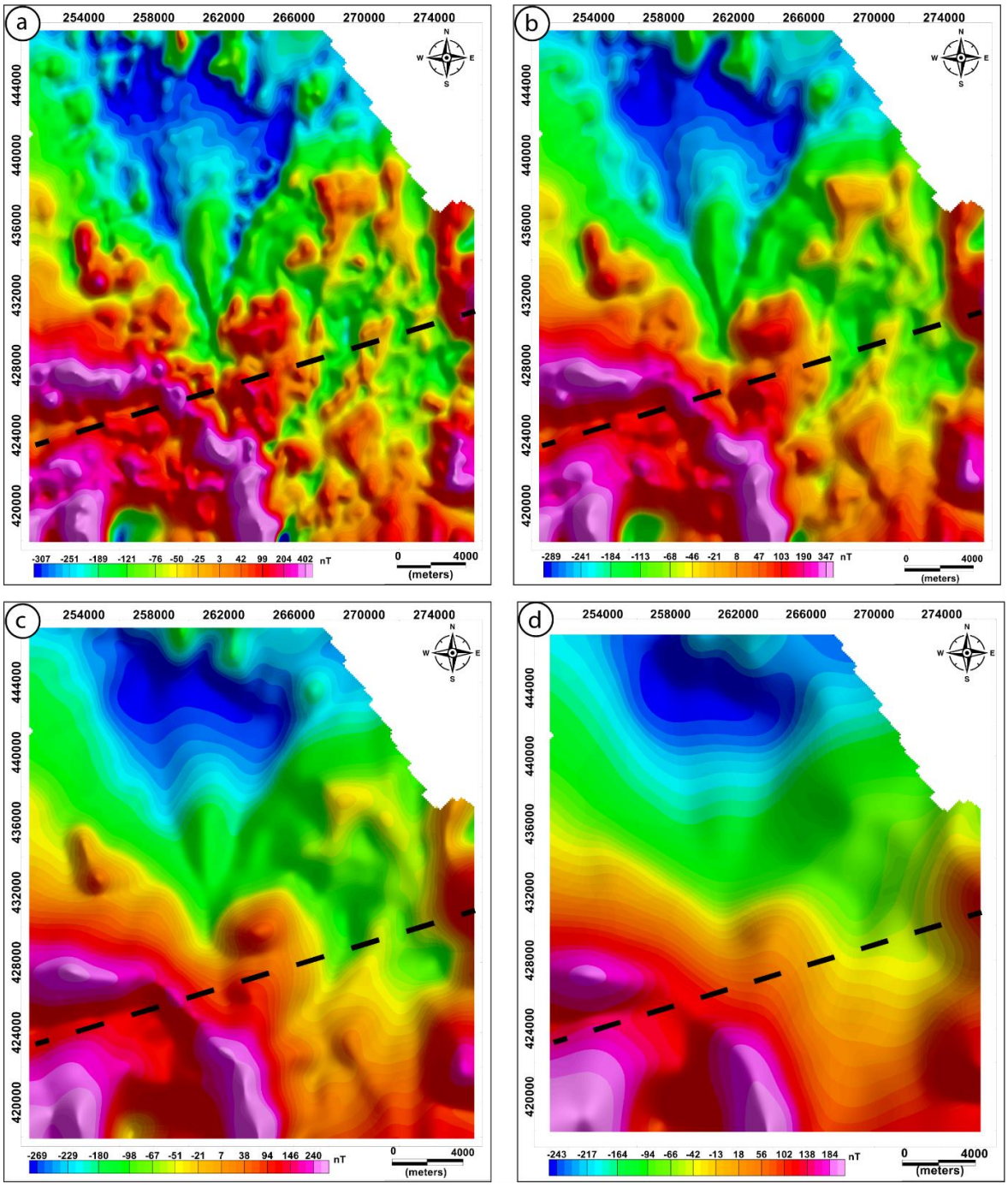

Figure 4.4
RTP maps are extended upwards to: a) 250m, b) 500m, c) 1000m and d) 2000m. The dashed lines represent the suggested ENE lineament.

Therefore, the maps continued upwards at different heights allows the subdivision of the Assarag area in two magnetic morpho-structural domains: (i) a northern region with low to negative magnetic feature overlaying the Imourkhssen, Imourgane and Ougougane granites. (ii) A southern high-magnetic region overlaying the huge magnetite-rich Askaoun batholith along with a deep positive curved magnetic halo to the southwestern part of the study area.

4.8.3 Tilt derivative (TD) and center of exploration targeting (CET)

The TD and CET filters were applied to map several lineaments trends using an additional transformation such as “shaded relief” to enhance the data visualization and to outline the small magnetic features (**Figure 4.5 a**).

The results show NE-SW, NNE-SSW and NNW-SSE orientations following the regional structures (**Figure 4.5 a** and rose diagram included). In the southern part, the curved magnetic halo is outlined in the western corner of the Assarag map, along with N to NNE trends to the east. These lineaments align perfectly with the Zaghar mafic dyke swarms cutting the entire LEMS of the studied area.

4.8.4 Euler Deconvolution (ED)

This transformation was performed to estimate the location and the depth of magnetic anomalies based on the structural index (SI), which is highly effective for mapping the subsurface structures and geological contours. The results exhibit lineaments with a range of depths varying from 150m to 2000m (**Figure 4.5 b**).

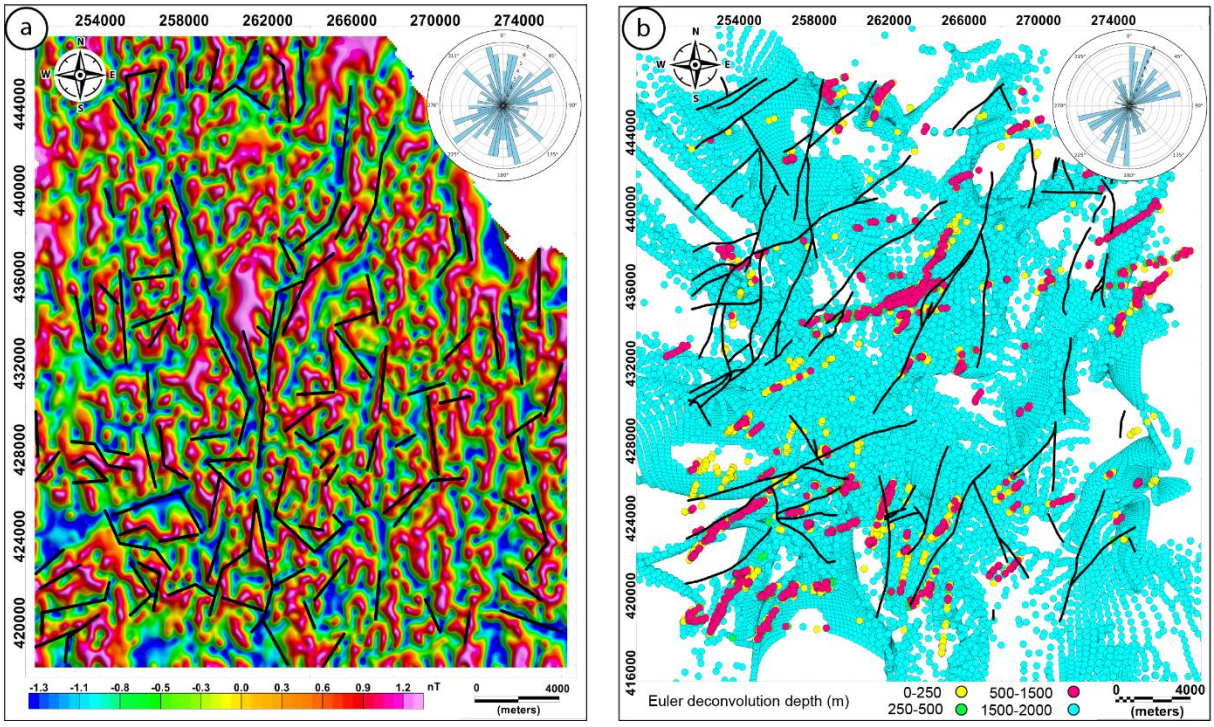

Figure 4.5
a) Tilt derivative map of the RTP data with the extracted magnetic lineaments (black lines) by the center for exploration targeting and corresponding Rose Diagram. b) Euler solution map for SI = 0 with the faults outlined by the black lines and associated rose diagram.

The highlighted trends are of NE to NNE in addition to NNW direction (see corresponding rose diagram), which match closely with the extracted lineaments by TD and CET. The slight difference between the orientation of extracted lineaments (**Figure 4.5 a**) and mapped structures (**Figure 4.5 b)** arise from comparison between the magnetic and geological–structural data. Several extracted lineaments may correspond to deep or concealed features that do not have a distinct surface expression. In the southwestern part of the map, the circular distribution of the ED solution overlay the magnetic halo already highlighted with previous filters. Consequently, The Euler deconvolution solutions support the results obtained from previous filters.

4.8.5 Two-Dimensional Continuous Wavelet transform (2D CWT)

As mentioned in the UC, the NE lineament is shallow which is not consistent with the SAF. To confirm this interpretation, the CWT (**Figure 4.6**) was carried out using the SFES2D tool (Abbassi and Cheng, 2021; Abbassi et al., 2022; Abbassi and Cheng, 2025) to further investigate the depth of many mapped lineaments. The first order derivative of the Gaussian mother wavelet was used due to its effectiveness to detect directional features including curvilinear structures across different scales and orientations (Abbassi and Cheng, 2025)

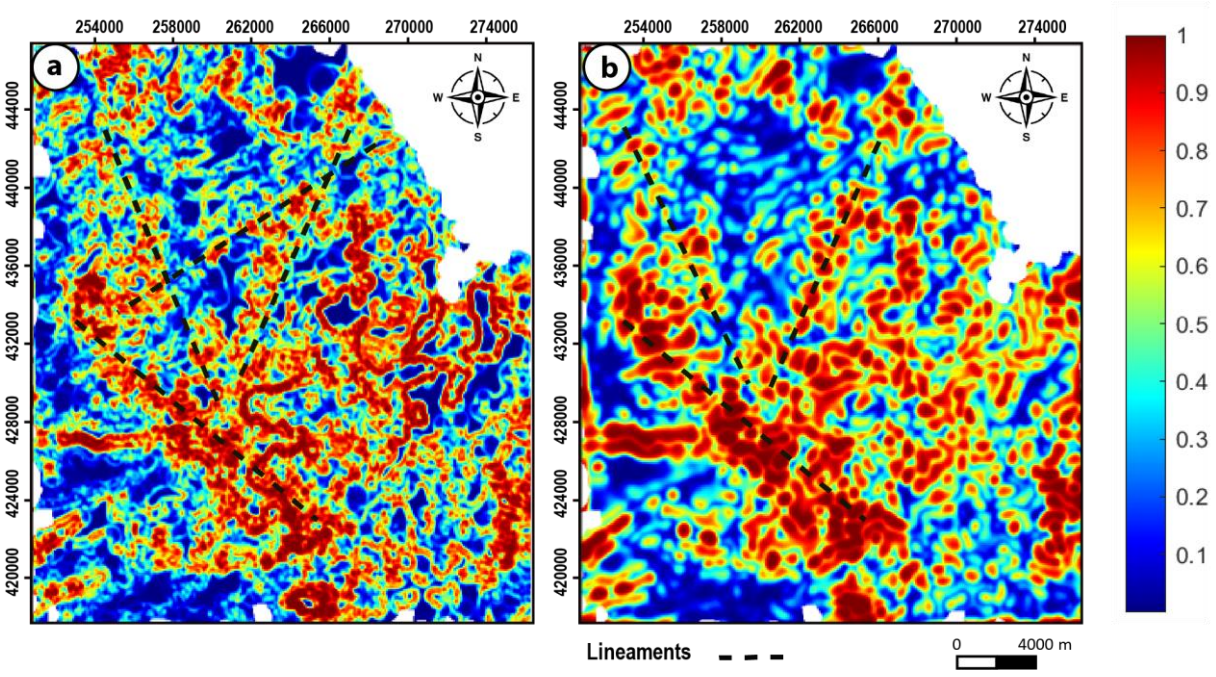

Figure 4.6
Continuous wavelet transformation (CWT) with the Gaussian mother wavelet by increasing scale map a) to map b). The black dashed lines are the extracted magnetic lineaments with a curved magnetic feature in the southwestern part of the Assarag area.

Our result shows several magnetic lineaments trends, as highlighted by the previous transformations (i.e., NNE, NNW, NE and NW) along with the curved magnetic halo (**Figure 4.6**). By increasing the scale (from map of **Figure 4.6 a** to **Figure 4.6 b**) of the CWT transformation, the NE trend disappear. From the inferred result, we deduce that the NE trend occurring in the northern part of the Assarag map are shallow structures, which support UC interpretation. Thus, the NE magnetic lineament could not correspond to the (SAF) considering that this fault is a deep-reaching structure. To the south, the curved magnetic halo is well highlighted along with a deep NW lineament. In the study area, this NW trending structure lies between the Askaoun intrusion and the volcanic rocks of the Ouarzazate Group, highlighting the deep contact between these formations.

4.8.6 Principal and independent Component Analysis by kurtosis and negentropy (PCA, kICA and nICA)

These transformations are carried out by the SFES2D tool (Abbassi and Cheng, 2021; Abbassi et al., 2022; Abbassi and Cheng, 2025) on both aeromagnetic data and RGB band of satellite image of the Assarag region. Therefore, data processing led to mapping four features (i.e., the three RGB features and the magnetic data), subsequently four resulting maps. For the following results, only maps with minimal noises are shown as referred in **Figure 4.7**.

The PCA results display the first and second component analysis maps (**Figure 4.7 a, b**) as they account for the majority of the feature variance (more than 70%). These maps show a mixture effect of the elevation inferred from the satellite image and magnetic features illustrating several geological and structural features. Negative magnetic anomalies correspond to the Imourkhssen, Imourgane and Ougougane granitoids, whereas positive ones correspond to the Askaoun intrusion and its curved magnetic contact zone (**Figure 4.7 a**). The **Figure 4.7 b** outlines the texture of the geological units, and highlights the main structural contours (e.g., NNE, NNW and NE trends), notably the ENE lineament cutting across the Assarag area. Therefore, the PCA outcomes are consistent with observations derived from the previous transformations.

The magnetic data were also processed through the ICA transform including kurtosis and negentropy maximization. The aim is to highlight different distributions of anomaly sources. From the resulting maps, the 3rd k-ICA (**Figure 4.7 c**) and 1st n-ICA (**Figure 4.7 d**) results were selected due to their minimal noises and as they highlight the most important structural feature of the Assarag area. The maps clearly highlight the ENE lineament consisting of a deep

magnetic structure that cuts across the Assarag map, which coincides with the results presented above.

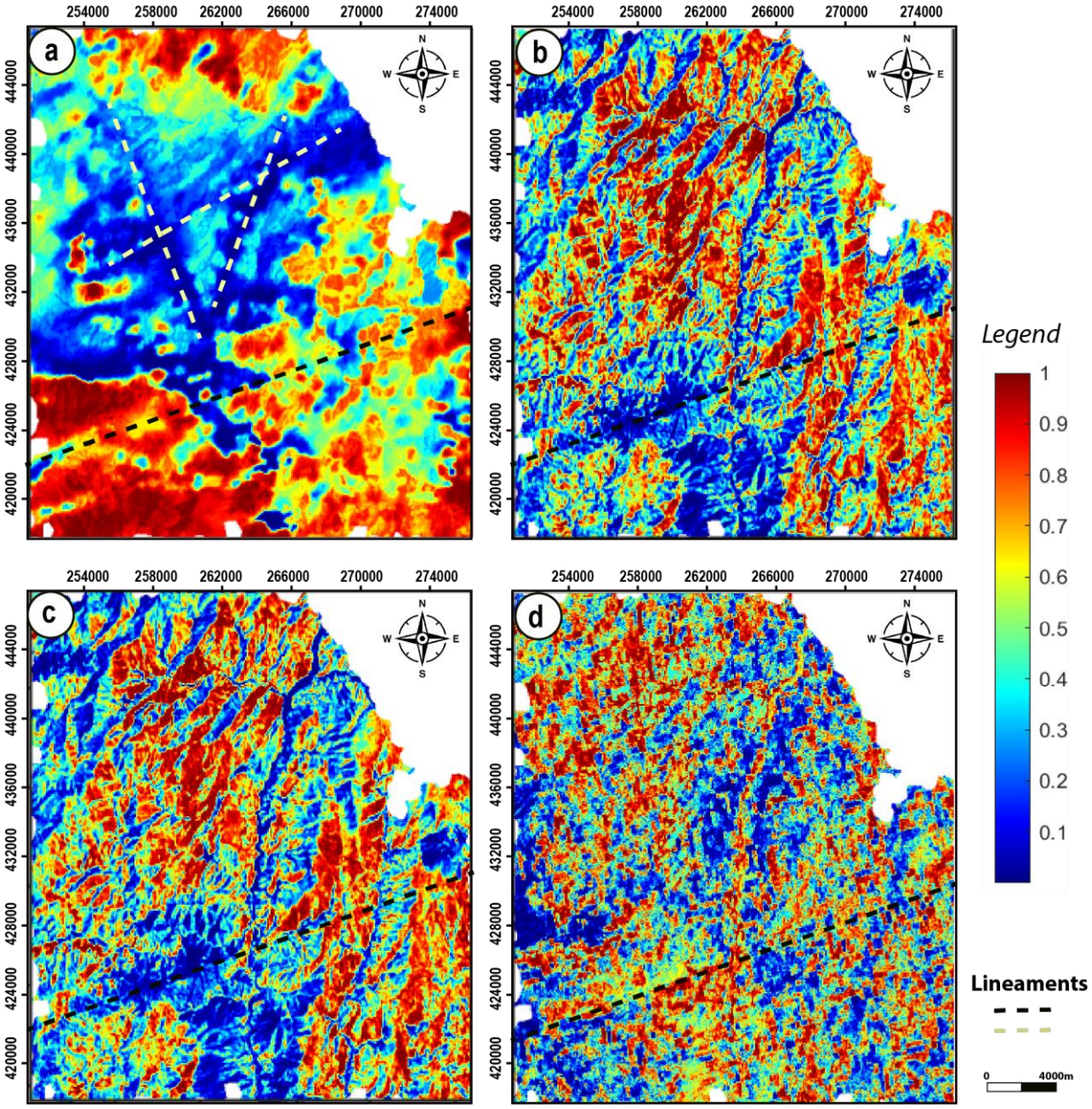

Figure 4.7
a) and b) 1st and 2nd PCA results respectively. c) 3rd k-ICA map. d) 1st n-ICA map highlighting the ENE lineament.

4.9 Discussion

4.9.1 Magnetic halo feature

RTP maps displays a very high magnetic feature in southwestern part of the Assarag region, highlighting the presence of a magnetic halo. Indeed, magnetic halos have been widely documented across the world in a variety of tectonic and magmatic contexts, highlighting their

significance as indicators of subsurface geological processes (Schwarz, 1991). This magnetic feature results either from is either of magmatic origin or results from fluid-rock interaction:

(i) Magmatic origin due to the presence of magnetic minerals (e.g., magnetite), is generally recognized as a circular magnetic response (Betts et al., 2024). As an example, an evident magnetic halo overlays the melano-syenite magnetite-rich intrusion in the region of Misery (Quebec) (Petrella et al., 2014). Such a circular magnetic pattern was as observed in the Bou Azzer inlier (Anti-Atlas, Maroc) overlaying the Jbel Boho magmatic complex (Soulimani et al., 2023).

(ii) Fluid-rock interaction can also result in the crystallization of ferromagnetic minerals during hydrothermal alteration, which is in some cases associated with ore-forming processes (Tapia et al., 2016). A magnetic halo can overprint the edges of a magmatic intrusion drawing a metasomatic aureole from fluid migration and magnetite production in high-temperature conditions, during pluton solidification, or exoskarn formation (Betts et al., 2024). n the Archean Abitibi greenstone belt of Quebec (Canada), the fluid-rock interaction has led to the formation of a distinguishable magnetic halo overprinting the Akasaba skarn during the circulation of magmatic fluids derived from the crystallization of a magnetite-rich pluton (Giroux and Lambert, 2021). Further detailed studies in the Abitibi greenstone belt explained the development of magnetic halo around the O'Brien syenitic intrusion. Fayol et al., (2016) proposed that the emplacement of this intrusion within a Fe-rich volcanic sequence triggered the circulation of oxidizing hydrothermal fluids, which subsequently promoted the mobilization of Fe from the host rocks and the generation of a magnetic halo around the intrusion.

Similarly, the magnetic halo observed in the study area is interpreted as the result of the two distinct processes (i.e., magmatic and hydrothermal). (i) The Askaoun granodiorite is a magnetite-rich magmatic intrusion (Ferraq et al., 2024). (ii) This intrusion was emplaced within the volcanic rocks (i.e., Andesite) of the Saghro Group, where the circulation of hot magmatic fluids through these host rocks could allowed the formation of ferromagnetic minerals around the intrusion, highlighting a pronounced magnetic halo. This magnetic feature underscores the fluid rock interaction at high temperature and emphasizes the late emplacement of the Askaoun intrusion in this area. Notably, the age of the Askaoun granodiorite was already debated to be considered around 575 Ma (Thomas et al., 2002; Belkacim et al., 2021) or around 558 Ma (Toummite et al., 2012). Therefore, this magnetic feature supports the multi-stage character of

the Askaoun granodiorite as suggested by Ferraq et al., (2024), and explains the different ages obtained for this granodioritic intrusion.

Alternatively, the hydrothermal alteration can be magnetite-destructive (e.g., phyllic alteration), producing low-magnetic halos (Clark, 2014), especially in porphyry copper systems, where long lived magmatic-hydrothermal processes can significantly modify the original magnetic properties of host rocks (Tapia et al., 2016).

4.9.2 Geodynamic and Mining Implications

The lineaments derived from magnetic data processing highlight the structural framework during the emplacement of the LEMS of the Ouarzazate Group, and allow to several mining implications. In fact, the main extracted lineaments in the studied area are of NE, NNE, NNW and ENE trends. The NE trend was previously documented by Gresse et al., (1997) as a dextral shear zone affecting the Late Ediacaran rocks of the Ouarzazate Group in the Assarag region, and linked to the Hercynian orogeny. Evidences of dextral sharing is also observed in the Imourkhssen area in several barite-hematite lenses (**Figure 4.8 d**), along faults affecting the LEMS of the Ouarzazate Group.

Discussing the structural framework of the emplacement of the Ouarzazate Group implies structural investigations in the neighboring inliers to be considered. This Group overlayed the whole Saghro Domain during the post Pan-African event (Belkacim et al., 2021; Shulte et al., 2022; Ferraq et al., 2024), when a transtensive regime dominated the eastern (Saghro–Ougnat) and the central (Bou Azzer) Anti-Atlas (Soulimani et al., 2014). Likewise, in the Bou Azzer inlier, Azizi Samir et al., (1990) argued for an extensional regime accompanied by synvolcanic sinistral faulting along WNW–ESE and NE–SW trends to be associated with the Ouarzazate Group emplacement. From a different perspective, the Bou Azzer inlier is very promising for base metal mineralization in Morocco. Al though its complex tectonic history, the geophysical studies in this region highlight the NNE-SSW, NW-SE, NNW-SSE, E-W, and NE-SW directions as the prospective areas for exploration (Soulimani et al., 2022).

In the Saghro inlier, the NE trend is considered a key structural control on hydrothermal fluid circulation, being associated with secondary mineralized structures in the NNE and N–S directions, that are related to the Ismlal and Tagmout deposits, respectively (Mamouch et al., 2022).

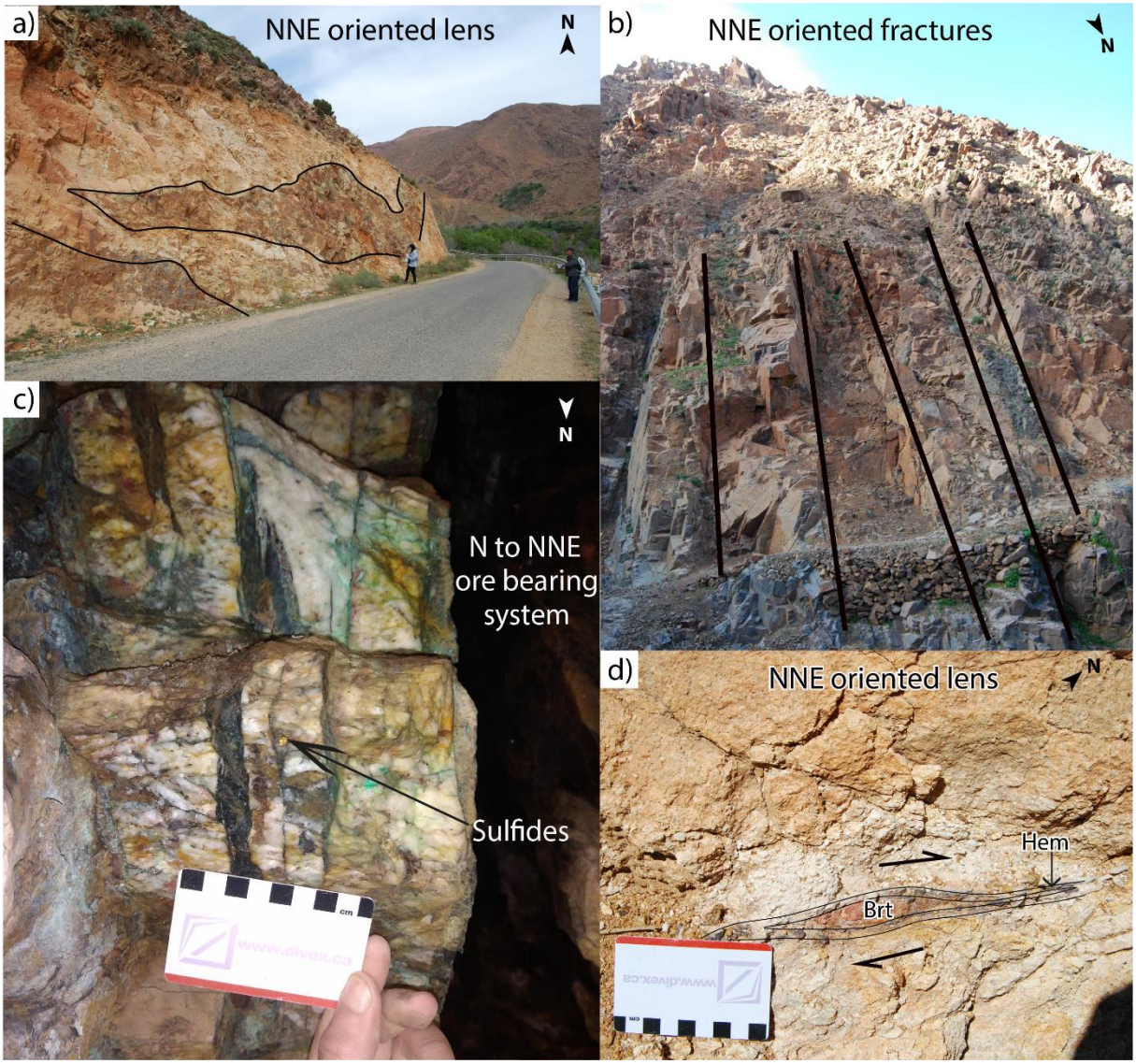

Figure 4.8
NNE-oriented fractures in the Imourkhssen area. a) Aplitic mega lens. b) Multi-scale-NNE oriented fractures. c) N to NNE ore bearing system. d) Barite-hematite lens exhibiting dextral kinematic.

In the High Atlas massif, the NE-trending structures are regarded as prospective zones for ore exploration, owing to the widespread alteration aligned with this trend, together with a structural control of the mineralization in N-S, NNE-SSW and NNW-SSE directions (Dadi et al., 2024).

In the Ouzellagh-Siroua salient, the Imourkhssen porphyry mineralization (**Figure 4.1 c**) is located closely at the juncture between the NNE and NE structures implying their potential involvement in hydrothermal circulation and mineralization trapping. In addition, several fractures show N to NNE trends, comprising: a NNE to N-S aplitic mega lens (**Figure 4.8 a**), NNE- oriented fractures (**Figure 4.8 b**), N to NNE ore bearing system (**Figure 4.8 c**) and NNE

barite-hematite lens (**Figure 4.8 d**) (Belkacim et al., 2014; Ferraq et al., 2024). Similar trends (i.e., NNE to NE) are as well observed for barite-bearing structures in the Ougnat inlier, and attributed to the Atlantic rifting event (Aabi et al., 2024)

4.9.3 South Atlas Fault (SAF) suggested trend

The results of the UC, 2D CWT, PCA, and ICA maps bring into question the previously proposed NE-oriented trend of the South Atlas Fault (SAF) reported in previous studies. While the NE trend has been widely documented and is commonly associated with ore-bearing structures (prior section), the present CWT-derived results provide additional insight into the depth distribution of the extracted lineaments. Notably, these analyses indicate that the NE-trending features are predominantly shallow, and unlikely to represent a major crustal-scale fault, delineating the two principal structural domains (Anti-Atlas; High Atlas; Fig. 1b). This evidence thus challenges the interpretation of the SAF's orientation and emphasizes the need for reassessment of structural features in the Assarag region.

Alternatively, a pronounced ENE-trending feature emerges in the upwarded maps, indicating the presence of a deep magnetic lineament. In the PCA maps, this ENE trend intersects the LEMS of the study area and is consistently manifested as a deep-seated structural feature in the ICA maps, corresponding to the proposed barrier in the UC analysis. Moreover, the SAF exhibits variable orientations and is subdivided into several fault segments across the High Atlas and Anti-Atlas Mountains. It records an ENE trend within the Oued Issen and Ouarzazate Basin fault tracts (Sébrier et al., 2006), while E–W to ENE–WSW trends are observed along the margins of the Tinghir–Errachidia–Boudenib basin (Bouzekraoui et al., 2024a).

From the observation drawn, and knowing that the structural boundary between the Anti-Atlas and High Atlas consists of anastomosed faults with major E-W to ENE-WSW directions (Bouzekraoui et al., 2024a and refrences therein), we suggest herein the ENE trend as a deep magnetic source that represents a rooted structural boundary between the two main domains, aligning with the SAF.

4.10 Conclusion:

This research introduces a novel method for extracting geological lineaments from aeromagnetic data by integrating several filters and transformations.

The different aeromagnetic transformations allowed mapping the main magnetic lineaments in the Assarag area including shallow NNE, NNW and NE trend to the north, along with deep curved magnetic halo and NW and ENE trends to the south. The extracted lineaments led to assessing the structural control for mineral exploration especially for the Imourkhssen porphyry mineralization, implying its location between the NE and NNE oriented structures and the association of the most significant sulfide veins with the NNE trend direction. Similar observations are inferred elsewhere in the Saghro domain.

The synergy between the PCA, CWT and ICA transforms allowed to extract multi-scale, multi-directional and concealed lineaments that support the previous deduced results, and led to suggest the ENE-trending as a part of the South Atlas Fault (SAF) cutting across the LEMS in the Assarag area.

Authorship: Conceptualization, M.F. and L.-Z.C and S.B; Data curation, M.F., L.-Z.C. and B.A; Investigation, M.F., S.B and L.-Z.C; Methodology, M.F. L.-Z.C. and B.A; Resources, L.-Z.C and S.B; Software, M.F., L.-Z.C. and B.A; Supervision, S.B. and L.-Z.C.; Validation, S.B., L.-Z.C. and B.A; Analysis and Visualization, M.F ; Writing—original draft, M.F., L.-Z.C., B.A and S.B ;Writing—review & editing, M.F., S.B., L.-Z.C and B.A; All authors have read, discussed and agreed to the published version of the manuscript.

Declaration of competing interests: The authors affirm that they have no known financial or personal conflicts of interest that could have influenced the content of this work

Data statement: The authors do not have permission to share data.

Acknowledgement: We gratefully acknowledge the support of the National Centre for Scientific and Technological Research (CNRST) by the PhD-Associate Scholarship – PASS program sponsoring and encouraging science researches. We further thank the University of Quebec in Abitibi-Temiscamingue (UQAT) for their assistance with data processing carried out using licensed software. Finally, I extend my acknowledgment to J.A. DeSève and the UQAT Foundations for their financial support for encouraging PhD students in their final year.

4.11 References

Aabi, A., Hejja, Y., Nait Bba, A., Boujamaoui, M., Baidder, L., El Azmi, M., Maacha, L., Hamzaoui, A., 2024. Tectonic Reactivation and Ore-Forming Fault Systems from the West African Craton Margin (Saghro, Anti Atlas, Morocco). Journal of African Earth Sciences, 211: 105182. https://doi.org/10.1016/j.jafrearsci.2024.105182.

Abbassi, B., Cheng, L-Z., 2025. Curvilinear Lineament Extraction: Bayesian Optimization of Principal Component Wavelet Analysis and Hysteresis Thresholding. Computers and Geosciences, 194: 105768. https://doi.org/10.1016/j.cageo.2024.105768.

Abbassi, B., Cheng, L-Z., Jébrak, M., Lemire, D., 2022. 3D Geophysical predictive modeling by spectral feature Subset selection in mineral exploration. Minerals, 12 (10), 1296. https://doi.org/10.3390/min12101296.

Abbassi, B., Cheng, L-Z., 2021. 3D Geophysical Post-Inversion Feature Extraction for Mineral Exploration through Fast-ICA. Minerals, 11 (9), 959. https://doi.org/10.3390/min11090959

Abbassi, B., Cheng, L-Z., Richards, J.P., Hübert, J., Legault, J.M., Rebagliati, M., Witherly, K., 2018. Geophysical Properties of an Epithermal Au-Ag Deposit in British Columbia, Canada. Interpretation, 6 (4): 907–918. https://doi.org/10.1190/INT-2017-0232.1

Abbassi, B., 2018. Integrated Imaging through 3d Geophysical Inversion, Multivariate Feature Extraction, and Spectral Feature Selection. Doctoral dissertation, University of Quebec in Abitibi-Temiscamingue, Canada, 218.

Achkouch, L., Miftah, A., Ouchchen, M., Mamouch, Y., Attou, A., Boutaleb, S., Dadi, B., 2023. Mapping and Litho-Geophysical Classification of Potential Mining Areas by Spatial Remote Sensing and Helicopter-Borne Gamma-Ray Spectrometry (Tikirt, Anti-Atlas, Morocco). Geophysical Prospecting, 71 (8): 1551–69. https://doi.org/10.1111/1365-2478.13376.

Álvaro, J. J., Bellido, F., Gasquet, D., Pereira, M. F., Quesada, C., Sánchez-García, T., 2014a. Diachronism in the Late Neoproterozoic-Cambrian Arc-Rift Transition of North Gondwana: A Comparison of Morocco and the Iberian Ossa-Morena Zone. Journal of African Earth Sciences, 98: 113–32. https://doi.org/10.1016/j.jafrearsci.2014.03.024.

Azizi Samir, M. R., Ferrandini, J., Tane, J. L., 1990. Tectonique et volcanisme tardi-Pan Africains (580-560 Ma) dans l'Anti-Atlas Central (Maroc): interprétation géodynamique à l'échelle du NW de l'Afrique. Journal of African Earth Sciences (and the Middle East), 10 (3), 549-563. https://doi.org/10.1016/0899-5362(90)90105-N

Baranov, V., 1957. A New Method for Interpretation of Aeromagnetic Maps: Psedo-Gravimetric Anomalies. Geophysics, 22 (2): 352–83. https://doi.org/10.1190/1.1438369

Belkacim, S., Perrot, M.G., Davies, J.H.F.L., Liégeois, J-P., Ikenne, M., 2021. The Ediacaran Ouarzazate Group, a Metacratonic Silicic Large Igneous Province (SLIP) : New U-Pb Zircon Ages from Ouzellarh-Siroua Salient (Tifnoute Valley, Morocco). In Geological Society of America Northeastern Section (NEGSA), 1/1. T17. Pre-Atlantic Geological Connections among Northwest Africa, Southern Europe, and Eastern North America.

Belkacim, S., Gasquet, D., Liégeois, J-P., Arai, S., Gahlan, H.A., Ahmed, H., Ishida, Y., Ikenne, M., 2017. The Ediacaran Volcanic Rocks and Associated Mafic Dykes of the Ouarzazate Group (Anti-Atlas, Morocco): Clinopyroxene Composition, Whole-Rock Geochemistry and Sr-Nd Isotopes Constraints from the Ouzellarh-Siroua Salient (Tifnoute Valley). Journal of African Earth Sciences, 127: 113–35. https://doi.org/10.1016/j.jafrearsci.2016.08.002.

Belkacim, S., Ikenne, M., Souhassou, M., Elbasbas, A., Toummite, A., 2014. The Cu-Mo ± Au Mineralizations Associated to the High-K Calc- Alkaline Type Porphyry in the Late Neoproterozoic Series. Journal of Environment and Earth Science, 4 (14): 90–106.

Betts, P. G., Moore, D., Aitken, A., Blaikie, T., Jessell, M., Ailleres, L., Armit, R., McLean, M., Munukulta, R., Chukwu, C., 2024. Geology from aeromagnetic data. Earth-Science Reviews, 258, 104958. https://doi.org/10.1016/j.earscirev.2024.104958

Blakely, R.J., 1995. Potential Theory in Gravity and Magnetic Applications. Cambridge university press, 441p.

Blakely, R.J., Connard, G.G., Curto, J.B., 2016. Tilt Derivative Made Easy. Geosoft Technical Publications, 4: 1–4.

Bouabdellah, M., Slack, J.F., 2016. Geologic and Metallogenic Framework of North Africa. In Mineral Deposits of North Africa, (pp. 3-81). https://doi.org/10.1007/978-3-319-31733-5_1.

Bouzekraoui, M., Essalhi, M., Saadi, M., Karaoui, B., Ghazali, M., Manar, A., 2024b. Foreland Evolution in the Inherited Basement Structure of the Pre-African Tinghir-Errachidia-Boudenib Basin (Moroccan Southern Atlas Margin).” Italian Journal of Geosciences, 143 (3): 391–406. https://doi.org/10.3301/IJG.2024.23

Bouzekraoui, M., Es-Sabbar, B., Karaoui, B., Essalhi, M., Saadi, M., 2024a. Structural Analysis, Tectonic Fracturing Modeling, and Kinematic Evolution along the South Atlas Fault at the Northern Border of the Tinghir-Errachidia-Boudenib Basin (Pre-African Trough, Morocco). Journal of African Earth Sciences, 212 : 105193. https://doi.org/10.1016/j.jafrearsci.2024.105193.

Choubert, G., 1963. Histoire Géologique de l’Anti-Atlas de l’Archéen à l’aurore Des Temps Primaires. Notes Mém. Serv.Géol. Maroc, 62, 350-352.

Clark, D. A., 2014. Magnetic effects of hydrothermal alteration in porphyry copper and iron-oxide copper–gold systems: A review. Tectonophysics, 624, 46-65. https://doi.org/10.1016/j.tecto.2013.12.011

Core, D., Buckingham, A., Belfield, S., 2009. Detailed Structural Analysis of Magnetic Data-Done Quickly and Objectively. SGEG Newsletter, 1 (2), 15-21.

Dadi, B., Ouchchen, M., Faik, F., Boutaleb, S., El Azzab, D., Mamouch, Y., Achkouch, L., Bajadi, L., Abia, E H., Sadeghi, B., 2024. Hydrothermal Fluid Pathways and Mineralization Potential in the High Atlas Massif (Morocco) Using Fuzzy Logic and Multifractal Modeling. Ore Geology Reviews, 175: 106401. https://doi.org/10.1016/j.oregeorev.2024.106401.

Domzalski, W., 1966. Importance of Aeromagnetics in Evaluation of Structural Control of Mineralization. Geophysical Prospecting, 14 (3), 273-291. https://doi.org/10.1111/j.1365-2478.1966.tb01761.x

Echogdali, F Z., Boutaleb, S., Abia, E H., Ouchchen, M., Dadi, B., Id-Belqas, M., Abioui, M., Pham, L T., Abu-Alam, T., Mickus, K.L., 2022. Mineral Prospectivity Mapping: A Potential Technique for Sustainable Mineral Exploration and Mining Activities–a Case Study Using the Copper Deposits of the Tagmout Basin, Morocco. Geocarto International, 37 (25): 9110–31. https://doi.org/10.1080/10106049.2021.2017006.

El Moume, W., Youbi, N., Marzoli, A., Bertrand, H., Ikenne, L., Boumehdi, M A., Ernst, R., El Hachimi, H., Bensalah, M K., Mata, J., Madeira, J., Bento dos Santos, T.M., Martins, S.,. 2020. Geochemistry of Mafic Dyke Swarms of Douar Eç-Çour (High Atlas, Morocco): The Farthest Record of the Central Iapetus Magmatic Province (CIMP) into

West African Craton. In The Farthest Record of the Central Iapetus Magmatic Province (CIMP) into West African Craton, Geólogos, 33 (1-2): 95–124.

Ennih, N., Liégeois, J P., 2001. The Moroccan Anti-Atlas: The West African Craton Passive Margin with Limited Pan-African Activity. Implications for the Northern Limit of the Craton. Precambrian Research 112 (3–4): 289–302. https://doi.org/10.1016/S0301-9268(01)00195-4.

Errami, E., Linnemann, U., Hofmann, M., G¨artner, A., Zieger, J., G¨artner, J., Mende, K., El Kabouri, J., Gasquet, D., Ennih, N., 2020. From Pan-African Transpression to Cadomian Transtension at the West African Margin: New U-PB Zircon Ages from the Eastern Saghro Inlier (Anti-Atlas, Morocco). The Geological Society of London. Spec. Publ. 503. https://doi.org/10.1144/SP503-2020-105

Errami, E., Bonin, B., Laduron, D., Lasri, L., 2009. Petrology and Geodynamic Significance of the Post-Collisional Pan-African Magmatism in the Eastern Saghro Area (Anti-Atlas, Morocco). Journal of African Earth Sciences, 55 (1–2): 105–24. https://doi.org/10.1016/j.jafrearsci.2009.02.006.

Fayol, N., Jébrak, M., Harris, L. B. , 2016. The magnetic signature of Neoarchean alkaline intrusions and their related gold deposits: Significance and exploration implications. Precambrian Research, 283, 13-23. https://doi.org/10.1016/j.precamres.2016.07.009

Ferraq, M., Belkacim, S., Cheng, L-Z., Davies, J H F L., Perrot, M.G., Ben-tami, A., Bouabdellah, M., 2024. New Geochemical and Geochronological Constraints on the Genesis of the Imourkhssen Cu±Mo±Au±Ag Porphyry Deposit (Ouzellagh-Siroua Salient, Anti-Atlas, Morocco): Geodynamic and Metallogenic Implications. Minerals, 14 (832): 38. https://doi.org/10.3390/min14080832

Gasquet, D., Ennih, N., Liégeois, J P., Soulaimani, A., Michard, A., 2008. The Pan-African Belt. Lecture Notes in Earth Sciences, 116: 33–64. https://doi.org/10.1007/978-3-540-77076-3_2.

Gasquet, D., Levresse, G., Cheilletz, Azizi-Samir, M R., Mouttaqi, A., 2005. Contribution to a Geodynamic Reconstruction of the Anti-Atlas (Morocco) during Pan-African Times with the Emphasis on Inversion Tectonics and Metallogenic Activity at the Precambrian-Cambrian Transition. Precambrian Research, 140 (3–4): 157–82. https://doi.org/10.1016/j.precamres.2005.06.009.

Giroux, M., Lambert, M ., 2021. Copper-gold (Cu-Au) skarn-type mineralization in an Archean volcanic context. Natural Resources and Forestry, Mineral Exploration Research Consortium (CONSOREM), Quebec, 40.

Gresse, P.G., De Beer, C.H., De Kock, G.S., Thomas, R.J., Chevallier, L.P., 1997. Geological map of Morocco at 1:50,000 scale, Assarag sheet. Notes and memoirs of the geological service, No. 392 bis, 84, ISSN 0374-9789.

Hassenforder, B., 1987. La Tectonique Panafricaine et Varisque de l'Anti-Atlas dans le massif du Kerdous (Maroc). Doctoral dissertation, Université Louis Pasteur, Strasbourg, (1971-2008).

Holden, E J., Wong, J C., Wedge, D., Martis, M., Lindsay, M., Gessner, K., 2016. Improving Assessment of Geological Structure Interpretation of Magnetic Data: An Advanced Data Analytics Approach. Computers and Geosciences, 87: 101–11. https://doi.org/10.1016/j.cageo.2015.11.010.

Holden, E-J., Wong, J.C., Kovesi, P., Wedge, D., Dentith, M., Bagas, L., 2012. Identifying Structural Complexity in Aeromagnetic Data: An Image Analysis Approach to Greenfields Gold Exploration. Ore Geology Reviews, 46: 47–59. https://doi.org/10.1016/j.oregeorev.2011.11.002

Holden, E.J., Kovesi, P., Dentith, M.C., Wedge, D., Wong, J.C., Fu, S.C., 2010. Detection of Regions of Structural Complexity within Aeromagnetic Data Using Image Analysis. In In Proceedings of the 25th International Conference Image and Vision Computing New Zealand, Queenstown, New Zealand, 1–8. IEEE. https://doi:10.1109/IVCNZ.2010.6148856.

Hollard, H., Suter, G., Didon, J., Guardia, P., Dresnay, R., Medioni, R., Choubert, G., Faure-Muret, A., 1985. Carte Géologique Du Maroc Au 1/1 000 000. Notes et Mémoires Du Service Géologique Du Maroc, Feuille Nord, 260 (2): 1–96.

Hyvärinen, A., 2022. Independent Component Analysis of Images. In: Jaeger, D., Jung, R. (Eds) Encyclopedia of Computational Neuroscience. Springer, New York, NY, 1665–1669.

Hyvärinen, A., Oja, E., 2000. Independent Component Analysis: Algorithms and Applications. Neural Networks, 13 (4-5): 411–30. https://doi.org/10.1016/S0893-6080(00)00026-5

Ivan, M., 1986. Upward Continuation of Unevenly Spaced Potential Field Data Using Equivalent Sources. Geophysics, 32(1), 31-42

Jacobsen, B.H., 1987. A Case for Upward Continuation as a Standard Separation Filter for Potential-Field Maps. Geophysics, 52 (8): 1138–48. https://doi.org/10.1190/1.1442378

Karaoui, B., Breitkreuz, C., Mahmoudi, A., Youbi, N., Hofmann, M., Gärtner, A., Linnemann, U., 2015. U-Pb Zircon Ages from Volcanic and Sedimentary Rocks of the Ediacaran Bas Draâ Inlier (Anti-Atlas Morocco): Chronostratigraphic and Provenance Implications. Precambrian Research, 263: 43–58. https://doi.org/10.1016/j.precamres.2015.03.003.

Kouyaté, D., Söderlund, U., Youbi, N., Ernst, R., Hafid, A., Ikenne, M., Soulaimani, A., Bertrand, H., El Janati, M., Chaham, K R., 2013. U-Pb Baddeleyite and Zircon Ages of 2040Ma, 1650Ma and 885Ma on Dolerites in the West African Craton (Anti-Atlas Inliers): Possible Links to Break-up of Precambrian Supercontinents. Lithos, 174: 71–84. https://doi.org/10.1016/j.lithos.2012.04.028.

Kovesi, P., 1997. Symmetry and Asymmetry from Local Phase. In In Tenth Australian Joint Conference on Artificial Intelligence, 190: 2–4.

Lam, L., Lee, S.W., 1992. Thinning Methodologies—A Comprehensive Survey. IEEE Trans. Pattern Anal. Mach. Intelligence, 14 (9): 61–69.

Liégeois, J P., Fekkak, A., Bruguier, O., Errami, E., Ennih, N., 2006. The Lower Ediacaran (630–610 Ma) Saghro Group: An Orogenic Transpressive Basin Development during the Early Metacratonic Evolution of the Anti-Atlas (Morocco). In In IGCP485 4th Meeting, Algiers, 57:1/1.

Linnemann, U., Ovtcharova, M., Schaltegger, U., Gärtner, A., Hautmann, M., Geyer, G., Vickers-Rich, P., Rich, T., Plessen, B., Hofmann, M., Zieger, J., Krause, R., Kriesfeld, L., Smith, J., 2019. New High-Resolution Age Data from the Ediacaran–Cambrian

Boundary Indicate Rapid, Ecologically Driven Onset of the Cambrian Explosion. Terra Nova, 31 (1): 49–58. https://doi.org/10.1111/ter.12368.

Mamouch, Y., Attou, A., Miftah, A., Ouchchen, M., Dadi, B, Moussaid, A., Et-tayea,Y., El Azmi, M., Boualoul, M., 2023. Aeromagnetic Data of the Kelâat M'Gouna Inlier (Jbel Saghro, Eastern Anti-Atlas, Morocco): Geotectonic and Mining Implications. Journal of African Earth Sciences, 197: 104744. https://doi.org/10.1016/j.jafrearsci.2022.104744.

Mamouch, Y., Attou, A., Miftah, A., Ouchchen, M., Dadi, B., Achkouch, L., Et-Tayea, Y., Allaoui, A., Boualoul, M., Randazzo, G., Lanza, S., Muzirafuti, A., 2022. Mapping of Hydrothermal Alteration Zones in the Kelâat M'Gouna Region Using Airborne Gamma-Ray Spectrometry and Remote Sensing Data: Mining Implications (Eastern Anti-Atlas, Morocco). Applied Sciences, 12 (3): 1–19. https://doi.org/10.3390/app12030957.

Marcoux, E., Wadjinny, A., 2005. Le Gisement Ag-Hg de Zgounder (Jebel Siroua, Anti-Atlas, Maroc): Un Épithermal Néoprotérozoïque de Type Imiter. Comptes Rendus - Geoscience, 337 (16): 1439–46. https://doi.org/10.1016/j.crte.2005.09.005.

Miftah, A., El Azzab, D., Attou, A., Rachid, A., Ouchchen, M., Soulaimani, A., Soulaimani, S., Manar, A., 2021b. Combined Analysis of Helicopter-Borne Magnetic and Stream Sediment Geochemical Data around an Ancient Tiouit Gold Mine (Eastern Anti-Atlas, Morocco): Geological and Mining Interpretations. Journal of African Earth Sciences, 175 : 1–12. https://doi.org/10.1016/j.jafrearsci.2020.104093.

Miller, H.G., Singh, V., 1994. Potential Field Tilt—A New Concept for Location of Potential Field Sources. J. Appl. Geophys, 32 (2-3): 213–17. https://doi.org/10.1016/0926-9851(94)90022-1

Nabighian, M.N., Grauch, V.J.S., Hansen, R.O., LaFehr, T.R., Li, Y., Peirce, J.W., and M.E Phillips, J.D., Ruder, M.E., 2005. The Historical Development of the Magnetic Method in Exploration. Geophysics, 70 (6) : 33–61. https://doi.org/10.1190/1.2133784

O'Connor, E. A., 2010. Geology of the Drâa, Kerdous, and Boumalne Districts, Anti-Atlas, Morocco. British Geological Survey, Keyworth, Nottingham, 310.

Osinowo, O.O., Alumona, K., Olayinka, A.I., 2020. Analyses of High Resolution Aeromagnetic Data for Structural and Porphyry Mineral Deposit Mapping of the Nigerian Younger Granite Ring Complexes, North-Central Nigeria.J. Afr. Earth Sci 162, 103705. https://doi.org/10.1016/j.jafrearsci.2019.103705

Ouchchen, M., Boutaleb, S., Abia, E H., El Azzab, D., Abioui, M., Mickus, K.L., Miftah, A., Echogdali, F Z., Dadi, B., 2021. Structural Interpretation of the Igherm Region (Western Anti Atlas, Morocco) from an Aeromagnetic Analysis: Implications for Copper Exploration. Journal of African Earth Sciences, 176 : 104140. https://doi.org/10.1016/j.jafrearsci.2021.104140.

Pelleter, E., Cheilletz, A., Gasquet, D., Mohammed. Mouttaqi, A., Abdellah, and H Camus, Q., Deloule, E., Ouazzani, L., Ouchtouban, L., Bounjama., 2016. U/Pb Ages of Magmatism in the Zgounder Epithermal Ag–Hg Deposit, Sirwa Window, Anti-Atlas, Morocco. In Mineral Deposits of North Africa, 143-165. Cham: Springer International Publishing.

Petrella, L., Williams-Jones, A. E., Goutier, J., Walsh, J., 2014. The nature and origin of the rare earth element mineralization in the Misery syenitic intrusion, northern Quebec, Canada. Economic Geology, 109 (6), 1643-1666.

https://doi.org/10.2113/econgeo.109.6.1643

Reid, A.B., Allsop, J.M., Granser, H., Millett, A.J., Somerton, I.W., 1990. Magnetic Interpretation in Three Dimensions Using Euler Deconvolution. Geophysics 55 (1) : 80–91. https://doi.org/10.1190/1.1442774

Sailhac, P., 1999. Analyse Multiéchelle et Inversion de Données Géophysiques En Guyane Française. Doctoral dissertation, Institut de physique du globe, Paris.

Salem, A., Williams, S., Fairhead, J.D., Ravat, D., Smith, R., 2007. Tilt-Depth Method: A Simple Depth Estimation Method Using First-Order Magnetic Derivative. Lead. Edge, 26 (12) : 1502–1505. https://doi.org/10.1190/1.2821934

Sassioui, S., Aarab, A., Benyas, K., Idrissi, A., Lakhloufi, A., Saidi, O., Courba, S., Larabi, A., 2024. Geophysical Analysis Using High-Resolution Aeromagnetic Data of Jbel Ougnat, the Moroccan Eastern Anti-Atlas: Insights into Geological Structures and Tectonic Events. Bulletin of Geophysics and Oceanography, 65 (1): 35–52. https://doi.org/10.4430/bgo00435.

Schulte, B., Boger, S.D., Benziane, F., Yazidi, A., Fanning, C.M., 2022. The Ouarzazate Supergroup and Its Plutonic Keel: The Relicts of an Ediacaran Silicic Large Igneous Province in North Africa. Journal of the Geological Society, 179 (5). jgs2021-114https://doi.org/10.1144/jgs2021-114.

Schwarz, E.J., 1991. Schwarz, E. J. (1991). Magnetic expressions of intrusions including magnetic aureoles. Tectonophysics, 192 (1-2), 191-200. https://doi.org/10.1016/0040-1951(91)90256-R.

Sébrier, M., Siame, L., Zouine, E. M., Winter, T., Missenard, Y., Leturmy, P., 2006. Active tectonics in the moroccan high atlas. Comptes Rendus Geoscience, 338 (1-2), 65-79. https://doi.org/10.1016/j.crte.2005.12.001

Soulaimani, A., Chakiri, S., Soulaimani, S., Bejjaji, Z., Miftah, A., Manar, A., 2023. Gradiometry Processing Techniques for Large-Scale of Aeromagnetic Data for Structural and Mining Implications: The Case Study of Bou Azzer Inlier, Central Anti-Atlas, Morocco. Applied Sciences, 13 (17), 9962. https://doi: 10.3390/app13179962

Soulaimani, A., Chakiri, S., Soulaimani, S., Manar, A., Bejjaji, Z., Miftah, A., Zerdeb, M A., Zidane, Y., Boualoul, M., Muzirafuti, A., 2022. Semi-Automatic Image Processing System of Aeromagnetic Data for Structural and Mining Investigations (Case of Bou Azzer Inlier, Central Anti-Atlas, Morocco). Applied Sciences, 12 (21). 11270. https://doi.org/10.3390/app122111270.

Soulaimani, A., Ouanaimi, H., Saddiqi, O., Baidder, L., Michard, A., 2018. The anti-atlas panafrican belt (Morocco): overview and pending questions. Comptes Rendus. Géoscience, 350 (6), 279-288. https://doi.org/10.1016/j.crte.2018.07.002.

Soulaimani, A., Michard, A., Ouanaimi, H., Baidder, L., Raddi, Y., Saddiqi, O., Rjimati, E.C., 2014. Late Ediacaran-Cambrian Structures and Their Reactivation during the Variscan and Alpine Cycles in the Anti-Atlas (Morocco). Journal of African Earth Sciences, 98: 94–112. https://doi.org/10.1016/j.jafrearsci.2014.04.025.

Soulaimani, A., Jaffal, M., Maacha, L., Kchikach, A., Najine, A., Saidi, A., 2006. Magnetic Modelling of the Bou Azzer-El Graara Ophiolite (Central Anti-Atlas, Morocco). Geodynamic Implications of the Panafrican Reconstruction. Comptes Rendus -

Geoscience, 338 (3): 153–60. https://doi.org/10.1016/j.crte.2005.10.001.

Tapia, J., Townley, B., Córdova, L., Poblete, F., Arriagada, C., 2016. Hydrothermal alteration and its effects on the magnetic properties of Los Pelambres, a large multistage porphyry copper deposit. Journal of Applied Geophysics, 132, 125-136. https://doi.org/10.1016/j.jappgeo.2016.07.005

Tazi, M J., El Azzab, D., Charroud, M., Jabrane, O., Ouahzizi, Y., Zahour, R., Halidou Amadou, A., 2022. Identification of Potential Mineral Exploration Targets from the Interpretation of Aeromagnetic Data Covering the Sirwa Region (Central Anti-Atlas, Morocco). Scientific African, 17: e01351. https://doi.org/10.1016/j.sciaf.2022.e01351.

Thomas, R.J., Chevallier, L.P., Gresse, P.G.., Harmer, R.E., Eglington, B.M., Armstrong, R.A., De Beer, C.H., Martini., J.E.J., de Kock, G.S., Macey, P.H., Ingram, B.A., 2002. Precambrian Evolution of the Sirwa Window, Anti-Atlas Orogen, Morocco. Precambrian Research, 118 (1–2): 1–57. https://doi.org/10.1016/S0301-9268(02)00075-X.

Tobi, A., Essalhi, M., Es-Sabbar, S., Qarqori, K., Bouzekraoui, A., Ait Baha, M., Faou, A., El Azmi, D., 2025. Application of High-Resolution Gravity and Magnetic Data for Fe-Mn-Pb Mineralization Prospecting in Jbel Skindis, Eastern High Atlas, Morocco. Economic and Environmental Geology, 58 (1): 17–31. https://doi.org/10.9719/EEG.2025.58.1.17

Toummite, A., Liegeois, J.P., Gasquet, D., Bruguier, O., Beraaouz, E.H., Ikenne, M., 2012. Field, Geochemistry and Sr-Nd Isotopes of the Pan-African Granitoids from the Tifnoute Valley (Sirwa, Anti-Atlas, Morocco): A Post-Collisional Event in a Metacratonic Setting. Mineralogy and Petrology, 107 (5): 739–63. https://doi.org/10.1007/s00710-012-0245-3.

Tuduri, J., Chauvet, A., Barbanson, L., Bourdier, J.L., Labriki, M., Ennaciri, A., Badra, L., duboit, M., Ennaciri-Leloix, C., Sizaret, S., Maacha, L., 2018. The Jbel Saghro Au(–Ag, Cu) and Ag–Hg Metallogenetic Province: Product of a Long-Lived Ediacaran Tectono-Magmatic Evolution in the Moroccan Anti-Atlas. Minerals, 8 (12). https://doi.org/10.3390/min8120592.

Verduzco, B., 2004. New Insights into Magnetic Derivatives for Structural Mapping. Lead. Edge, 23 (2): 116–19. https://doi.org/10.1190/1.1651454

Youbi, N., Ernst, R E., Mitchell, R N., Boumehdi, M A., El Moume, W., Ait Lahna, A., Bensalah, M K., Söderlund, U., Doblas, M.,. Tassinari, C. C.G., 2021. Preliminary Appraisal of a Correlation Between Glaciations and Large Igneous Provinces Over the Past 720 Million Years. Large Igneous Provinces: A Driver of Global Environmental and Biotic Changes, 169–90. https://doi.org/10.1002/9781119507444.ch8.

Youbi, N., Ernst, R E., Söderlund, U., Soulaimani, A., Bertrand, H., Marzoli, A., El Hachimi, H., Bensalah, M K., Hafid, A., Ikenne, M., Kouyaté, D., El Bahar, A., Ben Abbou, M., Madeira, J., Mata, J., Martins, L., Bellieni, G., Vérati, C., Mahmoudi, A., 2011. The Central Iapetus Magmatic Province (CIMP) Large Igneous Province. Distribution, Nature, Origin, and Environmental Impact. In American Association of Petroleum Geologists (AAPG) Search and Discovery, 2–3.

CONCLUSIONS GÉNÉRALES

Par son histoire géologique et géodynamique fini-édiacarienne, marquée par l'évolution post-collisionnelle de la chaine panafricaine de l'Anti-Atlas, le secteur d'Ouzellagh-Siroua constitue une clé de voûte pour la compréhension de la métallogénie régionale. Son architecture crustale, façonnée par les derniers épisodes tectono-magmatique de l'orogenèse panafricaine, en fait un domaine privilégié pour appréhender les processus de mise en place des systèmes magmatiques, hydrothermaux et structuraux responsables de la formation des gisements porphyriques et épithermaux néoprotérozoïques.

Ce travail de recherche mené dans la région d'Imourkhssen (Promontoire d'Ouzellagh-Siroua), s'appuie sur une approche multidisciplinaire combinant des travaux de terrain et de laboratoire spécialement axées sur des investigations géologiques, pétrographiques, géochimiques, géochronologiques, métallogéniques et géophysiques. Une démarche intégrée ayant permis de contribuer à comprendre et à décrypter l'évolution des processus magmato-hydrothermaux et structuraux à l'origine de la mise en place des minéralisations à Cu-Mo-Au-Ag d'Imourkhssen.

En effet, les travaux de terrain couplés à une analyse pétrographique détaillée, ont permis de mieux apprécier la nature pétrographique, les caractéristiques texturales ainsi que les processus d'altération ayant affectés les roches encaissantes. Ces dernières, sont notamment composées d'un emboitement de granitoïdes attachées au Group de Ouarzazate (580-539 Ma) désignés sous le terme « Suites magmatiques fini-édiacariennes » (LEMS). Leur composition géochimique marquée par un enrichissement en éléments lithophiles et en terres rares légères et par une anomalie négative Nb-Ta affichant un caractère calco-alcalin hautement potassique typique des granitoïdes de type I, et témoignant d'un context géodynamique post-orogénique.

Les datations U–Pb sur zircons réalisées sur le granite d'Imourkhssen et le porphyre granitique minéralisé ont donné des âges de 558 ± 1 et 550 ± 2 Ma, respectivement. Par conséquent, le porphyre minéralisé, précédemment considéré comme une simple apophyse du granite d'Imourkhssen, est désormais interprété comme un corps granitique distinct, dénommé granite d'Imourgane.

La minéralisation d'Imourkhssen est développée au cours d'une période magmatique-hydrothermale, qui se subdivise en deux stades (dissémination et système orienté N à NNE), suivie d'une phase supergène ultérieure. La répartition de la minéralisation et des altérations hydrothermales associées confirment l'hypothèse d'un gisement de type porphyre

cuprifère, déjà avancée par Belkacim, (2014), et mettent en évidence un type de minéralisation particulier développé durant l'Édiacarien tardif.

Le contrôle structural de la minéralisation d'Imourkhssen a été évalué à partir des traitements de données aéromagnétiques, impliquant des circulations hydrothermales le long de failles peu profondes orientées NE et NNE. De plus, La combinaison de différents filtres et traitements géophysiques met en évidence un linéament profond orienté ENE, interprété comme une structure tectonique profonde majeure traversant la région d'Assarag et s'alignant avec la faille sud-atlasique (SAF).

La genèse du gisement porphyrique d'Imourkhssen s'inscrit dans le contexte d'une activité magmatique felsique et multi phasée intense du Groupe d'Ouarzazate (SLIP), au sein de laquelle les deuxième et troisième pulses magmatiques semblent être les plus prometteuses. De plus, plusieurs d'autres gisements dans le domaine de Saghro pourraient s'intégrer dans un système porphyrique-épithermal en relation avec la mise en place de la SLIP d'Ouarzazate, durant les stages finals post-collisionnels de l'orogène panafricaine.

Les âges moyens des gisements de la province porphyrique-épithermale, conjugués à ceux de plusieurs gisements épithermaux situés dans la zone occidentale d'Avalon, mettent en évidence la possibilité d'un lien spatial durant l'Édiacarien tardif. Au cours de cette période, le domaine de Saghro et l'Avalon représentaient des terranes péri-Gondwaniens amalgamés qui témoignent des mêmes processus tectono-magmatiques et métallogéniques avant la dislocation du Gondwana.

En enregistrant les processus tectono-magmatiques qui ont façonné la bordure septentrionale du craton ouest-africain, l'Anti-Atlas, et plus particulièrement le promontoire d'Ouzellagh-Siroua, revêt une importance majeure et constitue un cadre géodynamique clé, tant à l'échelle régionale que des plaques tectoniques. Cette zone d'étude, témoin des interactions complexes entre les blocs crustaux du Gondwana, a fourni des éléments essentiels pour comprendre la dynamique des marges continentales, et la formation des corridors métallogéniques porphyriques-épithermales durant l'Édiacarien tardif.

GENERAL CONCLUSIONS

Due to its Late Ediacaran geological and geodynamic history, marked by the post-collisional evolution of the Pan-African chain of the Anti-Atlas, the Ouzellagh-Siroua area constitutes a keystone for understanding regional metallogeny. Its crustal architecture, shaped by the final tectono-magmatic episodes of the Pan-African orogeny, makes it a privileged domain for investigating the emplacement processes of magmatic, hydrothermal, and structural systems responsible for the formation of Neoproterozoic porphyry and epithermal deposits.

This research, conducted in the Imourkhssen region (Ouzellagh-Siroua promontory), is based on a multidisciplinary approach combining fieldwork and laboratory studies specifically focused on geological, petrographic, geochemical, geochronological, metallogenic, and geophysical investigations. This integrated methodology has contributed to understanding and deciphering the evolution of magmatic-hydrothermal and structural processes responsible for the emplacement of the Imourkhssen Cu-Mo-Au-Ag mineralization.

Fieldwork, coupled with detailed petrographic analysis, allowed a better appreciation of the petrographic nature, textural characteristics, and alteration processes affecting the host rocks. These are mainly composed of multi-pulsed granitoids affiliated with the Ouarzazate Group (580–539 Ma), referred to as the "Late Ediacaran Magmatic Suites" (LEMS). Their geochemical composition, characterized by enrichment in lithophile elements and light rare earth elements, along with a negative Nb-Ta anomaly, displays a high-potassium calc-alkaline character typical of I-type granitoids and indicates a post-orogenic geodynamic setting.

U–Pb zircon dating of the Imourkhssen granite and the mineralized granitic porphyry yielded ages of 558 ± 1 Ma and 550 ± 2 Ma, respectively. Consequently, the mineralized porphyry, previously considered an apophysis of the Imourkhssen granite, is now interpreted as a distinct granitic body, named the Imourgane granite.

The Imourkhssen mineralization developed during a magmatic-hydrothermal period, subdivided into two stages (dissemination and a N- to NNE-oriented system), followed by a later supergene stage. The mineralization and hydrothermal alterations patterns support the hypothesis of a porphyry copper type deposit, previously proposed by Belkacim, (2014), and highlights a particular type of mineralization developed during the Late Ediacaran period.

The structural control of the Imourkhssen mineralization was assessed using aeromagnetic data processing, involving hydrothermal circulations along shallow NE- and NNE-oriented faults. Furthermore, the combination of various geophysical filters and transformations underscores a deep ENE-oriented lineament, interpreted as a major deep tectonic structure crossing the Assarag region, and aligning with the South-Atlas Fault (SAF).

The genesis of the Imourkhssen porphyry deposit occurred in the context of an intense, multi-phase felsic magmatic activity of the Ouarzazate Group (SLIP), within which the second and third magmatic pulses appear to be the most promising. Additionally, several other deposits in the Saghro domain could be integrated into a single porphyry-epithermal system related to the emplacement of the Ouarzazate SLIP during the final post-collisional stages of the Pan-African orogeny.

The average ages of deposits in the porphyry-epithermal province, together with those of several epithermal deposits in the western Avalon zone, suggest a potential spatial link during the Late Ediacaran. At that time, the Saghro domain and Avalon represented peri-Gondwanan terranes that had amalgamated, and recorded the same tectono-magmatic and metallogenic processes prior to Gondwana's breakup.

By recording the tectono-magmatic processes that shaped the northern margin of the West African craton, the Anti-Atlas, and particularly the Ouzellagh-Siroua Salient, holds major significance and constitutes a key geodynamic framework at both regional and plate-tectonic scales. This study area, reflecting complex interactions between Gondwanan crustal blocks, provides essential insights into the dynamics of continental margins and the formation of porphyry-epithermal metallogenic corridors during the Late Ediacaran times.

APPENDIX

Appendix 1

Characteristics and localization of the samples used for different studies

ID sample	Suite	Rock	Analysis	Location	Characteristics
23IM27	Assarag	Askaoun granodiorite	Petrography Geochemistry	N30 55,13' / W007 52,05'	The Sample is collected near from Talat nl'bour galleries
J23IM13	Amassine	Imourkhssen granite	Petrography Geochronology	N30 56,72' / W007 51,57'	Fresh sample collected from the star-shaped intrusion
23IM13	Ougougane	Imourgane granite	Petrography Geochemistry	N30 55,36' / W007 52,28'	The sample exhibits molybdenite dissemination
J23IM09	Ougougane	Imourgane granite	Geochronology	N30 55,91' / W007 51,71'	The sample exhibits a molybdenite vein
23IM20		Zaghar dyke	Petrography Metallogeny	N30 57,65' / W007 52,22'	The dyke (50 cm thick) cut across the Imourgane granite. This dyke exhibit sulfide dissemination (Figure 3.15 D)
23IM07A	Ougougane	Ougougane microgranite dyke	Geochemistry	N30 56,04' / W007 51,70'	The dyke (30 cm thick) cut across the quartz-diorite
23IM09	Ougougane	Ougougane microgranite dyke	Geochemistry	N30 56,02' / W007 51,80'	N175 oriented dyke, with a thickness of about 50cm
23IM19	Ougougane	Imourgane	Geochemistry	N30 57,70' / W007 52,51'	Fresh sample
23IM22	Ougougane	Ougougane rhyolite	Geochemistry	N30 53,80' / W007 53,03'	The sample is cut by a N130 Qz-Hm vein

23IM24	Ougougane	Ougougane microgranite dyke	Geochemistry	N30 52,51’ / W007 53,62’	This dyke is cut by a Zaghar mafic dyke
23IM26B	Ougougane	Imourgane	Geochemistry	N30 55,35’ / W007 52,20’	Fresh sample
23IM26C	Ougougane	Imourgane	Geochemistry	N30 55,38’ / W007 52,11’	The intrusion is cut by a N70 hematite lens
23IM26D	Ougougane	Imourgane	Geochemistry	N30 55,52’ / W007 51,98’	Fresh sample near from molybdenite veinlets
23IM17A	Assarag	Askaoun granodiorite	Geochemistry	N30 56,15’ / W007 51,57’	This sample is near from sulfide dissemination
23IM23	Assarag	Askaoun granodiorite	Geochemistry	N30 53,81’ / W007 53,05’	Fresh sample
23IM25	Assarag	Askaoun granodiorite	Geochemistry	N30 53,95’ / W007 53,23’	The intrusion is cut by N130 doleritic dyke
23IM26A	Assarag	Askaoun granodiorite	Geochemistry	N30 52,27’ / W007 52,00’	The sample is collected near from Talat nl’bour galleries
23IM27	Assarag	Askaoun granodiorite	Geochemistry Metallogeny	N30 55,13’ / W007 52,05’	The sample displays sulfide disseminations
23IM07B	Assarag	Askaoun quartz-diorite	Geochemistry	N30 56,03’ / W007 51,71’	Fresh sample
23IM14A	Assarag	Askaoun quartz-diorite	Geochemistry	N30 55,34’/ W007 52,39’	The intrusion is cut by Ougougane dyke

23IM28	Assarag	Askaoun quartz-diorite	Geochemistry	N30 55,57’ / W007 51,92’	Fresh sample
22IM05	Ougougane	Imourgane	X-Ray Diffraction	N30 55,57’ / W007 51,92’	Altered sample collected from serecitic alteration zone
22IM02	Ougougane	Imourgane	X-Ray Diffraction	N30 55,22’ / W007 52,05’	Fresh sample from the Imourgane granite
22IM17	Assarag	Askaoun granodiorite	X-Ray Diffraction Metallogeny	N30°54,97' / W007°51,97'	The sample is collected from a quartz-chlorite sulfide veins cutting across the granodiorite. Sulfides are shown in Figure 3.15E
23IM13C	Assarag	Askaoun granodiorite	X-Ray Diffraction	N30°54,99' / W007°51,96'	The sample is collected from a quartz-chlorite sulfide veins cutting across the granodiorite
22IM20	Ougougane	Imourgane	X-Ray Diffraction	N30°55,32' / W007°51,93'	The sample is collected from silicic alteration zone
T1	Ougougane	Imourgane	X-Ray Diffraction	N30°55,21' / W007°52,20'	The sample is collected from the wall’s galleries
J23IM08	Assarag	Askaoun granodiorite	Metallogeny	N30°55,57’ / W007°51,80'	Sulfide dissemination (Figure 3.15C)
J23IM10	Ougougane	Imourgane	Metallogeny	N30°55,91' / W007°51,71'	Sulfide dissemination (Figure 3.15 F)

Appendix 2
Whole-rock major and trace elements geochemical data of the Late Ediacaran granites of the TV area (in percent "%" for major elements and part-per-million "ppm" for the trace elements).

	23IM 7A	23IM 09	23IM 19	23IM 22	23IM 24	23IM 7B	23IM 14	23IM 28	23IM 13	23IM 26	23IM 26'	23IM 26''	23IM 17	23IM 23	23IM 25	23IM 6'''	23IM 27
SiO_2	72.39	76.68	73.72	77.02	75.54	57.4	64.75	58.91	73.25	74.53	76.49	75.99	66.54	64.64	64.31	66.99	61.83
Al_2O_3	14.11	11.98	13.21	12.27	12.26	17.43	15.55	16.57	13.1	13.16	13.24	12.95	14.47	14.17	15.52	14.96	14.88
FeO	0.54	0.4	1.93	0.76	0.95	9.01	5.49	7.76	1.9	2.29	0.66	1.66	4.1	5.57	5.25	4.57	5.49
MnO	0.009	0.013	0.034	0.007	0.024	0.115	0.08	0.132	0.019	0.063	0.007	0.032	0.074	0.107	0.091	0.085	0.135
MgO	0.12	0.12	0.29	0.36	0.38	4.46	1.9	2.76	0.62	0.62	0.24	0.42	1.64	2.34	2.21	1.77	2.74
CaO	0.14	0.23	0.96	0.14	0.12	0.64	2.29	4.81	0.23	0.2	0.15	0.48	1.15	2.22	3.43	3.18	3.77
Na_2O	3.35	2.93	3.78	3.52	3.47	2.31	2.21	3.09	3.68	3.79	3.26	3.66	3.9	3.4	3.49	3.41	4.18
K_2O	6.87	5.72	3.9	4.05	5	2.9	4.11	1.77	4.44	3.88	4.81	4.32	4.04	4.08	3.58	3.66	2.9
TiO_2	0.067	0.083	0.179	0.049	0.043	0.712	0.71	0.778	0.191	0.181	0.203	0.179	0.527	0.721	0.697	0.615	0.71
P_2O_5	0.02	0.04	0.06	0.02	0.02	0.1	0.14	0.15	0.06	0.05	0.05	0.06	0.1	0.13	0.14	0.12	0.15
LOI	0.26	0.64	0.79	0.89	3.15	4.15	1.86	2.52	1.1	0.3	0.71	1.02	1.58	1.58	0.9	0.8	2.07
Total	97.86	98.84	98.85	99.07	101	99.22	99.09	99.25	98.59	99.06	99.83	100.8	97.97	98.95	99.62	100.2	98.84
Sc	1	2	3	2	2	14	13	16	3	2	3	2	9	14	13	11	14
Be	1	1	2	1	< 1	2	2	1	1	2	2	2	2	1	1	1	1
V	< 5	< 5	9	< 5	< 5	108	69	135	7	8	9	9	65	105	96	77	78
Ba	1812	1313	815	674	971	376	1946	437	674	645	500	771	844	1068	1055	1006	797
Sr	62	78	123	53	47	93	231	376	54	56	34	87	187	220	342	256	386

Y	11	14	24	12	10	18	27	18	23	20	23	17	22	25	22	22	21
Zr	75	71	136	58	52	144	261	142	147	145	141	126	274	246	242	254	258
Cr	< 20	< 20	< 20	< 20	< 20	40	30	30	< 20	< 20	20	< 20	< 20	30	30	30	30
Co	76	80	63	72	84	34	59	42	129	54	56	68	53	77	69	65	52
Ni	< 20	< 20	< 20	< 20	< 20	30	< 20	30	< 20	< 20	< 20	< 20	< 20	< 20	< 20	< 20	< 20
Cu	< 10	10	< 10	< 10	30	40	10	70	< 10	< 10	< 10	< 10	20	50	40	50	140
Zn	< 30	60	< 30	< 30	< 30	90	70	110	< 30	< 30	< 30	< 30	120	90	70	70	110
Ga	15	12	17	14	15	25	20	23	17	17	17	17	19	18	19	19	20
Ge	1	1	2	< 1	< 1	1	1	1	1	1	1	1	1	1	1	1	1
As	< 5	< 5	< 5	< 5	< 5	< 5	5	17	< 5	< 5	< 5	< 5	9	8	10	15	9
Rb	153	141	140	104	133	154	140	63	129	95	137	147	126	147	116	144	105
Nb	3	7	9	6	6	8	10	7	11	12	11	10	9	9	9	9	9
Mo	< 2	< 2	< 2	< 2	< 2	< 2	< 2	< 2	> 100	18	5	63	3	< 2	2	< 2	< 2
Ag	< 0.5	< 0.5	< 0.5	< 0.5	< 0.5	< 0.5	< 0.5	< 0.5	< 0.5	< 0.5	< 0.5	< 0.5	0.5	< 0.5	< 0.5	< 0.5	< 0.5
La	24.3	28.2	30.3	11.6	8.4	22.9	35.8	22.7	60.6	47.3	13.1	45.5	23.9	29.7	29.1	32.4	30.3
Ce	61.9	49.9	58.3	23.1	17.7	38.8	72.7	43.7	126	101	26.6	86.9	54.1	60.8	58.8	63.4	61.4
Pr	4.79	5.62	6.66	2.51	2.08	4.76	8.49	5.25	14.1	10.1	3.11	9.28	5.83	7.14	6.79	7.11	6.85
Nd	15.9	18.9	23.4	8.6	7.3	17.7	31.6	20.8	48.2	33.5	11.4	31.9	22.2	26.2	25.2	26.3	26
Sm	2.5	3.2	4.1	1.7	1.6	3.4	6.2	4.2	7.5	5.3	2.5	4.8	4.8	5.1	4.8	5	5
Eu	0.41	0.5	0.56	0.21	0.22	0.69	1.08	1.1	0.6	0.7	0.37	0.57	0.83	0.85	0.91	0.84	0.96

Gd	1.8	2.5	3.7	1.5	1.5	3.2	5.4	3.6	4.9	3.7	2.7	3.2	4.3	4.6	4	4.1	4.2
Yb	1.4	1.8	2.9	1.4	1.5	2.2	2.8	1.9	2.7	2.5	2.6	2	2.5	2.3	2.1	2.2	2.3
Lu	0.25	0.31	0.47	0.25	0.25	0.36	0.43	0.29	0.43	0.43	0.41	0.34	0.38	0.39	0.35	0.37	0.35
Hf	2.7	2.7	4.2	2.1	2	4.3	7.4	3.9	4.2	4.5	4.2	3.7	7.5	6.6	6.5	7.2	7
Ta	1.8	2.3	2.2	1.9	2	0.9	1.6	1	2.9	1.9	2.2	2.1	1.5	1.6	1.5	1.4	1.4
Tb	0.3	0.4	0.6	0.3	0.3	0.5	0.8	0.6	0.7	0.6	0.5	0.5	0.7	0.7	0.6	0.6	0.7
Dy	1.7	2.3	3.9	1.8	1.8	3.5	4.9	3.3	3.9	3.5	3.5	2.9	4.1	4.2	3.8	4.2	4
Ho	0.3	0.5	0.8	0.4	0.4	0.7	1	0.6	0.8	0.7	0.7	0.6	0.9	0.8	0.7	0.8	0.8
Er	1.1	1.5	2.4	1.2	1.2	2.1	2.8	1.9	2.3	2.3	2.4	1.8	2.4	2.5	2.2	2.4	2.3
Tm	0.19	0.25	0.38	0.21	0.2	0.31	0.42	0.27	0.37	0.35	0.37	0.29	0.36	0.37	0.32	0.33	0.34
W	616	666	548	561	620	151	457	249	1020	455	540	670	393	536	479	429	402
Tl	0.6	0.7	0.4	0.4	0.6	0.5	0.4	0.2	0.5	0.4	0.4	0.5	0.5	0.6	0.4	0.6	0.4
Bi	< 0.4	< 0.4	< 0.4	< 0.4	< 0.4	< 0.4	< 0.4	< 0.4	< 0.4	< 0.4	< 0.4	< 0.4	< 0.4	< 0.4	< 0.4	< 0.4	< 0.4
Th	18.8	18.4	19.7	8.7	8.8	8.1	16.1	6.6	15.8	15.9	17	15.9	23.1	15	15.2	18	13.2
U	4.2	5.2	6.5	4.2	5.1	3.4	8.5	4.2	4.5	8.5	12	8	14.3	4.6	8.4	5.8	8.3
In	< 0.2	< 0.2	< 0.2	< 0.2	< 0.2	< 0.2	< 0.2	< 0.2	< 0.2	< 0.2	< 0.2	< 0.2	< 0.2	< 0.2	< 0.2	< 0.2	< 0.2
Sn	< 1	< 1	< 1	< 1	1	1	1	1	2	5	2	1	2	1	1	1	1
Sb	< 0.5	< 0.5	< 0.5	< 0.5	< 0.5	0.9	1.3	2	< 0.5	< 0.5	< 0.5	< 0.5	1.7	2.1	2	3.5	3.5
Cs	0.9	0.7	0.7	0.9	0.5	2.2	2.3	0.9	1.2	1	1.2	0.8	0.8	1.8	0.9	1	0.7
Pb	< 5	14	9	< 5	6	< 5	20	7	< 5	7	< 5	7	25	24	14	24	18

Appendix 3

Quantitative results for the molybdenite dissemination (MD) and the molybdenite veinlets (MV) samples from microprobe analyses.

Element line	Net Counts	Weight %	Weight % Error	Atom %	Atom % Error	Compnd %
MD sample						
Si K	1550	0.32	+/- 0.06	0.60	+/- 0.11	0.32
Si L	0	---	---	---	---	---
S K	168319	41.59	+/- 1.59	67.77	+/- 2.59	41.59
S L	0	---	---	---	---	---
Mo L	177420	58.09	+/- 2.30	31.63	+/- 1.25	58.09
Mo M	1229	---	---	---	---	---
Total		100.00		100.00		100.00
MV sample						
Mg K	827	0.16	+/- 0.02	0.33	+/- 0.05	0.16
Al K	439	0.08	+/- 0.03	0.16	+/- 0.05	0.08
Si K	3130	0.59	+/- 0.05	1.07	+/- 0.10	0.59
Si L	0	---	---	---	---	---
S K	194626	43.51	+/- 0.65	68.85	+/- 1.03	43.51
S L	0	---	---	---	---	---
Fe K	418	0.45	+/- 0.11	0.41	+/- 0.10	0.45
Fe L	0	---	---	---	---	---

Appendix 4

LA-ICP-MS U-Pb data for the J23IM09 and the J23IM13 of the Imourgane and Imourkhssen granites respectively.

							Data for Tera-Wasserburg plot						Data for Wetherill plot					Dates						Conc -age	2s	% Conc
Sample	f206c	^{206}Pb	U_{ppm}	Th/U	^{206}Pb/^{204}Pb	1s%	^{238}U/^{206}Pb	1s%	^{207}Pb/^{206}Pb	1s%	^{208}Pb/^{206}Pb	1s%	^{207}Pb/^{235}U	1s%	^{206}Pb/^{238}U	1s%	Rho	^{207}Pb/^{235}U	2s	^{206}Pb/^{238}U	2s	^{207}Pb/^{206}Pb	2s			
J23IM09																										
IM09_42	1.82	113465.01	1856	0.22	1628.79	32.76	22.04	2.0	0.06581	2.26	0.101656532	1.542769	0.4116	2.8	0.04538	2.1	0.60	350.0	16.4	286.1	11.8	799.4	94.6	291.6	12.0	36.3
IM09_13	2.06	161550.20	2640	0.22	994.70	36.67	20.04	1.2	0.07010	1.33	0.118650273	1.143269	0.4821	1.5	0.04990	1.1	0.51	399.5	10.2	313.9	6.9	930.5	56.1	322.6	7.0	34.0
IM09_50	0.78	130894.92	1530	0.60	-10479.33	-55.20	17.08	1.7	0.06632	1.44	0.114750055	1.084423	0.5352	2.6	0.05856	1.8	0.85	435.3	18.2	366.9	12.6	815.6	59.5	336.3	12.1	45.9
IM09_8	-0.47	136017.00	1340	0.20	2367.08	44.04	13.80	1.9	0.05827	1.18	0.068617945	2.542060	0.5821	2.5	0.07249	2.1	0.86	465.8	18.3	451.1	18.7	539.0	55.0	459.2	18.3	86.6
IM09_30	-0.04	162532.62	1901	0.22	-302.55	-203.07	12.22	0.8	0.05836	0.90	0.055314891	1.154858	0.6581	1.0	0.08182	0.8	0.53	513.5	8.2	507.0	7.5	542.5	39.3	509.6	6.9	95.7
IM09_28	-0.09	115708.43	1276	0.28	3101.82	41.18	12.00	2.6	0.06029	2.27	0.063703567	1.698743	0.6923	4.2	0.08333	2.7	0.88	534.2	34.8	515.9	27.1	613.0	96.4	509.3	26.8	89.0
IM09_29	-0.28	148949.72	1918	0.43	231.34	599.99	11.81	1.6	0.05738	1.77	0.106412593	2.185354	0.6695	2.1	0.08466	1.6	0.55	520.4	17.1	523.9	16.5	505.2	80.2	522.3	14.8	107.4
IM09_36	0.09	165969.27	1000	0.31	1162.37	100.19	11.74	1.6	0.05969	1.20	0.080819076	1.358081	0.7007	1.5	0.08518	1.5	0.71	539.2	12.9	527.0	15.4	591.3	50.4	536.6	12.8	91.0
IM09_38	-0.10	97428.57	583	0.28	185.45	204.35	11.67	0.5	0.05898	1.32	0.078596684	2.589182	0.6964	1.3	0.08568	0.5	0.18	536.7	10.9	529.9	5.2	565.4	57.4	530.8	5.0	98.2
IM09_47	0.28	99263.60	937	0.33	-2107.03	-29.71	11.66	0.6	0.05814	1.34	0.083235690	1.769080	0.6874	1.3	0.08579	0.6	0.20	531.2	11.0	530.6	5.9	534.1	58.6	530.7	5.6	102.3
IM09_18	0.71	128793.30	1105	0.23	-17.07	-6060.72	11.64	0.7	0.05913	2.02	0.067701160	2.391053	0.6998	2.0	0.08588	0.7	0.22	538.7	17.1	531.1	7.3	570.8	87.6	531.8	7.2	93.2
IM09_33	-0.05	126750.48	688	0.30	4346.80	34.68	11.64	0.5	0.05920	0.96	0.076141230	1.083022	0.7009	1.0	0.08590	0.5	0.34	539.3	8.5	531.2	4.7	573.6	42.0	532.2	4.6	95.8
IM09_15	-0.32	137915.60	1182	0.26	583.68	93.37	11.59	0.8	0.06018	1.59	0.064202238	1.395470	0.7157	1.6	0.08629	0.8	0.25	548.1	13.5	533.5	8.2	609.3	68.9	536.5	7.7	89.3
IM09_27	0.35	177923.11	1987	0.21	4040.33	32.73	11.54	0.9	0.05922	0.91	0.056072724	0.776586	0.7069	1.2	0.08662	0.9	0.67	542.9	10.4	535.5	9.3	574.0	40.0	537.9	9.0	95.4
IM09_49	0.29	115149.47	956	0.34	-1373.76	-98.54	11.54	2.1	0.05892	1.84	0.092323916	2.197912	0.7038	2.4	0.08667	2.0	0.65	541.1	20.4	535.8	20.5	563.3	82.8	538.4	18.6	97.7
IM09_24	-0.54	68982.24	628	0.42	-5165.33	-322.65	11.52	0.6	0.05965	1.37	0.102088125	1.580077	0.7135	1.3	0.08680	0.6	0.14	546.8	11.1	536.6	5.9	589.8	58.9	538.4	5.5	94.4
IM09_37	0.15	145672.41	814	0.30	788.66	88.77	11.42	0.8	0.05946	0.96	0.077821272	1.931281	0.7174	1.0	0.08754	0.8	0.43	549.1	8.5	541.0	8.0	582.9	42.0	544.6	7.0	95.4
IM09_41	-0.05	147896.77	1350	0.36	273.42	198.16	11.40	0.8	0.05835	0.89	0.091891479	1.362570	0.7058	1.1	0.08776	0.9	0.64	542.2	9.4	542.3	8.9	542.1	38.3	542.2	8.3	102.5
IM09_9	-0.01	99319.66	725	0.27	1085.33	49.34	11.32	0.5	0.05841	1.18	0.068986597	1.371982	0.7113	1.2	0.08836	0.5	0.14	545.5	9.7	545.8	4.9	544.4	51.6	545.8	4.6	102.9
IM09_23	-0.55	100882.77	851	0.45	-3659.90	-38.32	11.28	0.5	0.05854	1.18	0.120289034	3.089733	0.7155	1.2	0.08868	0.5	0.26	548.0	10.4	547.7	4.9	549.1	52.2	547.8	4.8	103.6
IM09_12	0.61	37544.25	358	0.23	-81.17	-154.45	11.23	0.7	0.05857	1.93	0.059050253	1.809297	0.7188	1.9	0.08904	0.7	0.22	549.9	16.5	549.9	7.9	550.2	83.7	549.9	7.6	107.7
IM09_22	-0.28	128486.91	1012	0.27	-5413.91	-26.57	11.21	0.6	0.05893	1.03	0.068883865	2.037317	0.7246	1.0	0.08923	0.6	0.30	553.4	8.9	551.0	6.3	563.4	45.2	551.6	5.8	100.0
IM09_31	0.31	153624.47	904	0.26	-13357.62	-30.23	11.20	0.6	0.05922	1.00	0.065719123	1.417447	0.7289	1.1	0.08930	0.7	0.51	555.9	9.8	551.4	7.2	574.3	43.0	552.3	7.0	99.4
IM09_21	0.19	105753.52	790	0.36	-3438.12	-28.15	11.19	0.5	0.05820	1.19	0.088292712	1.228585	0.7170	1.1	0.08940	0.5	0.02	548.9	9.2	552.0	5.6	536.3	52.3	551.2	4.8	105.9
IM09_40	-0.40	116156.81	733	0.34	-472.08	-81.88	11.18	0.5	0.05932	1.07	0.086265604	1.564234	0.7312	1.1	0.08945	0.5	0.34	557.3	9.6	552.3	5.7	577.8	46.4	553.1	5.5	98.9
IM09_19	-0.48	123754.99	945	0.29	-530.61	-88.81	11.16	1.1	0.05791	1.14	0.072851558	1.851605	0.7153	1.5	0.08962	1.1	0.65	547.9	12.8	553.3	12.0	525.4	50.4	551.0	11.2	107.4
IM09_43	0.25	85408.40	819	0.27	-572.00	-57.53	11.15	0.7	0.05852	1.21	0.070307712	1.586753	0.7232	1.2	0.08966	0.7	0.28	552.5	10.4	553.5	7.2	548.5	53.1	553.2	6.6	104.8
IM09_25	-0.22	117840.94	1126	0.26	7043.18	41.79	11.15	0.4	0.05801	1.04	0.064470472	1.181541	0.7170	1.1	0.08969	0.4	0.32	548.9	9.3	553.7	4.4	529.1	45.5	553.3	4.3	108.0
IM09_32	0.45	137655.95	753	0.24	25790.67	30.01	11.15	0.5	0.05936	1.02	0.064902098	2.617898	0.7340	1.1	0.08972	0.5	0.37	558.9	9.4	553.9	5.4	579.4	44.7	554.5	5.3	99.0
IM09_1	0.28	76280.36	566	0.35	-633.43	-63.69	11.10	1.4	0.06049	1.70	0.096842375	1.944924	0.7508	2.0	0.09007	1.5	0.59	568.7	17.6	555.9	15.9	620.2	71.7	560.6	15.0	92.9
IM09_17	13.53	6411.62	52	2.44	-1.72	-1273.33	11.09	1.6	0.18980	2.76	0.858867869	1.438672	2.3580	2.5	0.09014	1.6	0.16	1230.0	35.7	556.4	17.4	2739.7	90.7	579.0	17.7	20.5

IM09_7	-0.07	298971.72	2201	0.27	13274.24	35.64	11.10	1.0	0.05836	1.06	0.072648344	1.134184	0.7248	1.4	0.09011	1.0	0.63	553.5	11.7	556.2	11.1	542.4	47.6	555.1	10.3	104.0
IM09_20	-0.27	92546.02	665	0.24	-71.33	-417.68	11.09	0.6	0.05787	1.42	0.061718028	1.576752	0.7189	1.4	0.09014	0.6	0.16	550.0	11.7	556.3	6.5	523.8	62.2	555.1	6.0	109.7
IM09_51	0.44	139636.21	980	0.20	1402.05	56.65	10.97	2.1	0.05699	1.54	0.059687397	2.018009	0.7159	2.1	0.09115	2.1	0.74	548.2	18.0	562.3	22.6	490.1	67.7	549.7	17.8	116.2
IM09_5	-0.97	32809.19	225	0.24	1992.02	928.31	10.79	0.6	0.05852	2.25	0.061926834	1.715075	0.7472	2.1	0.09265	0.6	-0.24	566.6	17.9	571.2	6.0	548.5	98.4	570.5	5.2	114.0
IM09_14	0.09	188290.70	1901	0.34	1501.70	61.13	10.56	1.5	0.05940	2.04	0.088092270	2.132788	0.7754	2.7	0.09472	1.6	0.63	582.9	24.3	583.4	17.8	580.8	92.7	583.3	17.7	104.7
IM09_45	0.53	130358.05	1097	0.31	-1153.73	-85.19	10.47	2.1	0.05862	1.58	0.078505954	1.819150	0.7715	2.5	0.09549	2.2	0.77	580.6	21.8	587.9	24.7	552.1	70.2	582.3	21.4	108.7
IM09_48	0.24	80335.21	696	0.33	-1348.49	-37.90	10.47	0.7	0.05958	1.42	0.086234864	2.048943	0.7840	1.5	0.09547	0.7	0.29	587.7	13.0	587.8	7.7	587.5	61.5	587.8	7.3	103.6
IM09_16	9.41	8501.25	67	2.54	-23.84	-124.06	10.35	1.1	0.18396	2.22	0.854025101	1.320554	2.4485	2.1	0.09657	1.1	0.21	1257.0	30.9	594.3	12.2	2688.2	72.3	593.2	12.4	22.3
IM09_35	0.76	102677.26	466	0.21	1088.03	58.95	10.25	2.1	0.05802	1.49	0.055250821	2.185268	0.7801	2.7	0.09755	2.3	0.82	585.5	23.6	600.0	25.9	529.6	66.1	588.9	23.0	118.7
IM09_2	17.04	5455.27	33	2.25	-102.27	-48.47	9.24	1.7	0.22251	3.64	0.912762464	1.977918	3.3177	2.9	0.10819	1.5	-0.07	1485.2	46.0	662.2	19.5	2998.2	110.3	722.8	18.9	22.4
IM09_34	25.20	2733.39	9	1.77	35.23	58.44	7.50	2.3	0.36833	3.54	1.054242935	2.695861	6.7716	4.7	0.13340	2.5	0.67	2082.0	83.4	807.2	37.5	3783.9	107.7	588.7	31.2	21.7
J23IM13																										
IM13_15	0.53	147533.31	1119	0.40	-450.29	-98.48	12.53	1.4	0.05924	1.21	0.078222216	1.249097	0.6518	1.8	0.07984	1.4	0.72	509.6	14.6	495.1	13.6	574.8	55.5	500.4	13.2	88.2
IM13_49	0.64	110748.18	935	0.23	-331.89	-119.70	12.00	0.7	0.06165	1.08	0.069503892	1.566091	0.7081	1.3	0.08334	0.7	0.54	543.6	10.8	516.0	7.2	661.1	46.4	518.8	7.2	81.2
IM13_34	0.80	139589.03	1709	0.33	-4450.49	-38.85	11.75	1.0	0.05905	1.87	0.076412682	1.368866	0.6925	2.1	0.08510	1.0	0.47	534.3	17.6	526.5	9.8	567.8	81.8	526.9	9.8	96.9
IM13_35	-0.54	105941.95	1020	0.35	-3270.66	-39.08	11.31	0.4	0.05911	1.66	0.086070256	1.822950	0.7205	1.6	0.08845	0.4	0.00	551.0	13.6	546.3	4.6	570.2	72.3	546.8	4.3	100.0
IM13_26	0.44	133027.24	1054	0.26	-1611.77	-45.20	11.23	0.5	0.05751	1.19	0.064977190	1.306250	0.7057	1.1	0.08904	0.5	0.00	542.2	8.9	549.9	4.9	510.2	50.7	548.1	4.3	109.5
IM13_41	-0.24	160436.72	1274	0.39	2326.15	56.42	11.23	0.6	0.05854	0.95	0.094449391	1.611378	0.7184	1.2	0.08905	0.6	0.60	549.7	10.1	549.9	6.2	548.9	42.3	549.9	6.2	104.3
IM13_54	-0.18	104782.17	868	0.27	888.64	60.09	11.23	0.7	0.05858	1.31	0.071699025	2.290324	0.7191	1.3	0.08908	0.7	0.27	550.2	11.2	550.1	7.3	550.5	57.2	550.1	6.8	104.8
IM13_16	0.49	127901.11	854	0.38	-379.70	-127.15	11.21	0.8	0.05860	1.28	0.096080793	1.117857	0.7207	1.4	0.08923	0.7	0.39	551.1	11.6	551.0	7.8	551.3	55.7	551.0	7.4	102.4
IM13_48	0.03	122383.66	961	0.24	731.00	103.46	11.19	0.8	0.06035	2.20	0.061771237	1.989648	0.7436	2.2	0.08940	0.8	0.16	564.5	18.7	552.0	8.2	615.3	94.3	553.4	7.9	92.7
IM13_42	-0.67	100111.59	810	0.27	774.08	70.18	11.18	0.5	0.05826	1.21	0.069183336	2.188661	0.7181	1.2	0.08942	0.6	0.27	549.5	10.4	552.1	5.9	538.7	52.5	551.7	5.7	107.7
IM13_44	-0.03	115836.08	852	0.41	1432.47	65.84	11.17	0.6	0.05882	1.40	0.094624155	1.457772	0.7254	1.3	0.08949	0.6	0.08	553.9	11.3	552.5	6.1	559.5	61.0	552.8	5.5	102.8
IM13_23	0.22	132400.68	1237	0.35	-779.71	-77.94	11.17	2.0	0.05792	1.77	0.078672272	2.986619	0.7148	2.8	0.08954	2.1	0.78	547.6	23.9	552.8	22.1	525.8	78.3	551.0	21.4	107.9
IM13_6	0.42	89477.78	947	0.31	1395.99	62.19	11.17	0.7	0.06017	1.78	0.063985802	2.649602	0.7423	1.8	0.08951	0.7	0.24	563.7	15.6	552.6	7.4	608.9	76.4	553.8	7.2	94.4
IM13_9	0.40	65994.37	621	0.24	-1965.39	-42.32	11.15	0.6	0.05919	1.83	0.064447794	4.362465	0.7319	2.0	0.08972	0.6	0.43	557.7	17.5	553.9	6.6	573.1	80.8	553.8	6.6	100.4
IM13_53	-0.26	49261.05	418	0.32	834.03	44.95	11.14	0.7	0.05958	2.27	0.082380675	2.488174	0.7370	2.3	0.08975	0.7	0.17	560.6	19.6	554.0	7.6	587.5	98.2	554.6	7.4	104.1
IM13_17	1.38	87767.81	578	0.38	240.40	131.51	11.14	0.9	0.05911	1.33	0.101777241	2.334647	0.7311	1.5	0.08976	0.9	0.48	557.2	13.0	554.1	9.2	570.0	58.0	554.7	8.9	99.7
IM13_36	-0.06	54280.28	538	0.48	-731.14	-53.58	11.13	1.6	0.05801	1.84	0.120337029	2.034620	0.7182	2.2	0.08983	1.8	0.60	549.6	18.9	554.5	18.9	529.3	80.5	552.0	16.9	111.0
IM13_11	-0.23	163860.51	1282	0.35	-3922.11	-28.20	11.14	0.7	0.06043	1.17	0.090428852	1.170878	0.7477	1.3	0.08977	0.8	0.47	566.9	11.4	554.2	8.0	618.2	50.5	556.6	7.8	90.6
IM13_20	0.41	112039.04	723	0.40	-1102.63	-50.89	11.13	0.5	0.05873	1.18	0.103191626	1.141426	0.7273	1.2	0.08985	0.5	0.18	555.0	10.1	554.7	5.0	556.2	51.9	554.7	4.8	101.8
IM13_12	0.34	93512.91	681	0.26	59.05	577.72	11.13	0.4	0.05798	1.23	0.065409197	1.451185	0.7183	1.2	0.08988	0.4	0.07	549.6	10.0	554.9	4.6	528.1	53.8	554.0	4.3	107.0
IM13_3	-0.13	148766.49	1500	0.34	1503.88	64.08	11.12	0.6	0.05923	1.48	0.081113927	1.368830	0.7338	1.5	0.08990	0.6	0.19	558.8	12.6	554.9	6.6	574.5	64.1	555.6	6.2	97.3
IM13_43	-0.20	89308.87	740	0.42	817.54	72.34	11.12	0.7	0.05818	1.37	0.107712452	1.852263	0.7211	1.4	0.08994	0.8	0.34	551.3	12.2	555.2	8.1	535.4	60.6	554.4	7.6	110.1
IM13_25	0.33	96562.84	782	0.44	-451.12	-90.23	11.09	0.6	0.05746	1.17	0.106879351	1.328882	0.7142	1.3	0.09019	0.6	0.44	547.2	11.1	556.6	6.4	508.3	51.9	555.7	6.3	113.3
IM13_55	-0.23	90481.69	734	0.46	526.49	67.63	11.08	0.7	0.05884	1.30	0.107549014	1.279030	0.7317	1.2	0.09023	0.6	0.09	557.6	10.4	556.9	6.8	560.2	57.4	557.1	5.9	103.9
IM13_50	0.59	113672.47	846	0.39	-337.24	-143.96	11.07	1.8	0.06161	1.78	0.108557100	1.498952	0.7672	3.1	0.09036	2.2	0.82	578.2	27.3	557.6	23.4	659.6	76.7	558.6	23.9	90.6

IM13_7	0.11	102662.94	983	0.29	8291.72	222.96	11.04	0.4	0.05999	1.23	0.073550934	1.271346	0.7487	1.1	0.09055	0.5	0.01	567.4	9.9	558.8	4.8	602.4	53.0	560.4	4.4	94.6
IM13_24	-0.08	160638.02	1383	0.33	745.50	119.38	11.03	1.4	0.05910	1.58	0.084129965	1.708132	0.7382	2.0	0.09064	1.3	0.60	561.4	17.0	559.3	14.2	569.7	68.8	559.9	13.7	99.2
IM13_27	1.15	99831.71	714	0.43	-2017.12	-79.95	11.03	0.7	0.05834	2.74	0.108375047	2.255178	0.7292	2.9	0.09069	0.7	0.39	556.1	24.9	559.6	7.7	541.6	118.7	559.7	7.6	106.5
IM13_8	0.46	120910.30	1211	0.38	-6090.48	-44.82	11.03	0.7	0.05860	1.41	0.091002477	1.054368	0.7325	1.4	0.09070	0.7	0.20	558.0	12.0	559.7	7.4	551.2	62.3	559.3	6.8	104.3
IM13_10	0.08	128480.70	1209	0.38	-1535.32	-77.61	11.01	0.6	0.06091	1.59	0.093252216	1.419036	0.7625	1.5	0.09083	0.6	0.02	575.4	13.2	560.5	6.2	635.0	68.9	563.0	5.6	89.1
IM13_5	0.14	119308.67	1225	0.35	2271.39	49.07	10.99	0.6	0.06008	1.44	0.087078501	0.902088	0.7536	1.5	0.09102	0.6	0.21	570.3	12.7	561.6	6.0	605.4	62.7	562.6	5.8	94.8
IM13_29	0.21	111713.12	889	0.34	-383.84	-118.77	10.97	0.5	0.05901	1.08	0.079388664	0.988541	0.7411	1.1	0.09113	0.5	0.23	563.0	9.1	562.2	5.8	566.4	46.6	562.4	5.4	101.7
IM13_21	-0.40	161314.06	1256	0.38	-2162.87	-32.48	10.96	0.8	0.05862	1.15	0.088702902	1.317675	0.7371	1.4	0.09124	0.8	0.62	560.7	12.3	562.9	8.7	552.0	49.1	562.6	8.7	103.8
IM13_1	0.57	86884.00	776	0.30	82.95	338.19	10.95	0.6	0.06001	1.27	0.083938084	3.599114	0.7550	1.5	0.09129	0.6	0.48	571.1	12.9	563.2	6.6	602.9	56.0	563.3	6.6	97.4
IM13_31	0.26	144575.99	1668	0.40	106.18	477.09	10.95	1.1	0.05757	2.21	0.093619397	2.073641	0.7247	2.5	0.09133	1.1	0.41	553.4	21.4	563.4	11.3	512.5	100.9	562.6	11.2	116.7
IM13_39	0.03	100297.21	849	0.27	-7731.54	-27.24	10.94	0.6	0.05741	1.17	0.070715278	1.263577	0.7234	1.1	0.09142	0.6	0.17	552.7	9.7	563.9	6.1	506.5	52.2	561.2	5.5	116.2
IM13_58	-0.20	147215.03	1215	0.32	596.25	92.72	10.92	0.5	0.05850	0.96	0.083069719	1.540365	0.7383	1.1	0.09157	0.5	0.50	561.4	9.5	564.8	5.4	547.7	41.8	564.6	5.4	107.0
IM13_52	-0.29	69707.24	531	0.41	1468.18	46.09	10.90	0.5	0.05805	1.55	0.107016081	2.603264	0.7339	1.5	0.09173	0.5	0.00	558.8	12.6	565.7	5.3	530.8	67.9	564.7	4.9	113.1
IM13_56	1.10	87406.21	740	0.30	886.20	44.52	10.90	0.9	0.05745	1.58	0.078624198	1.475047	0.7266	1.5	0.09177	0.9	0.24	554.5	13.1	566.0	9.8	507.9	69.7	562.3	8.7	117.6
IM13_22	0.31	156323.77	1311	0.41	-1604.66	-58.22	10.90	1.1	0.06023	1.11	0.103068820	2.003954	0.7617	1.4	0.09176	1.1	0.62	575.0	11.9	565.9	11.6	610.9	47.1	570.1	10.7	91.7
IM13_37	-0.52	80362.95	763	0.46	-1991.26	-44.33	10.89	0.6	0.05757	1.56	0.099873606	1.355422	0.7285	1.6	0.09183	0.6	0.20	555.7	13.3	566.3	7.0	512.4	68.4	564.6	6.7	118.3
IM13_51	-0.20	118399.91	932	0.38	6100.86	33.01	10.86	1.3	0.05812	1.02	0.090155355	1.802596	0.7377	1.7	0.09209	1.4	0.78	561.0	14.6	567.9	15.1	533.4	46.5	563.9	13.9	111.4
IM13_18	-0.20	117878.12	783	0.34	-126.24	-349.95	10.81	0.7	0.05846	1.61	0.084755922	1.805144	0.7451	1.4	0.09248	0.8	0.08	565.4	12.5	570.2	8.2	546.1	68.4	568.8	7.1	105.8
IM13_45	1.74	44565.77	325	0.35	246.15	96.17	10.80	0.7	0.06105	2.31	0.097219699	1.756498	0.7787	2.2	0.09255	0.7	-0.03	584.8	19.4	570.6	7.6	640.1	99.6	572.6	7.0	96.1
IM13_19	0.33	130761.47	814	0.40	-339.65	-124.23	10.80	0.5	0.05964	1.09	0.098772336	0.997957	0.7612	1.3	0.09261	0.6	0.54	574.7	11.4	571.0	6.3	589.6	47.8	571.0	6.3	98.8
IM13_38	-0.18	110061.75	956	0.20	-2590.83	-56.77	10.77	1.7	0.05788	1.68	0.049271998	1.427632	0.7410	2.4	0.09289	1.7	0.72	563.0	20.5	572.6	18.4	524.3	72.6	569.5	17.7	114.9
IM13_47	-0.51	68121.92	528	0.21	201.43	139.60	10.75	0.5	0.05971	1.39	0.057103024	2.027474	0.7652	1.5	0.09299	0.5	0.31	577.0	13.0	573.2	5.7	592.2	61.0	573.4	5.6	102.8
IM13_14	-0.31	124210.46	765	0.37	-969.96	-57.81	10.72	1.8	0.05818	1.59	0.091099598	2.533829	0.7483	2.3	0.09333	2.0	0.73	567.2	20.2	575.2	21.9	535.5	70.1	569.9	19.3	109.6
IM13_46	-0.51	89226.11	686	0.34	-49.52	-460.24	10.72	0.5	0.05770	1.27	0.086775141	1.888714	0.7421	1.3	0.09332	0.5	0.23	563.7	11.2	575.2	5.4	517.5	56.0	573.7	5.2	118.2
IM13_33	-0.06	89593.37	978	0.36	-353.36	-115.38	10.71	0.7	0.05815	1.20	0.088873497	2.804020	0.7479	1.3	0.09333	0.7	0.39	567.0	11.5	575.2	7.4	534.3	53.8	573.7	7.1	113.1
IM13_30	0.41	52307.02	376	0.20	-620.39	-73.43	10.71	0.7	0.05944	2.62	0.048122591	2.385948	0.7647	2.4	0.09334	0.7	-0.17	576.7	21.4	575.3	8.0	582.4	114.9	575.5	7.0	105.2
IM13_4	0.59	72465.89	741	0.26	565.16	54.49	10.71	1.0	0.05886	2.21	0.066866732	1.775229	0.7576	2.1	0.09339	1.1	0.18	572.6	18.6	575.6	12.0	561.0	96.0	574.8	10.8	106.5
IM13_57	0.25	89756.77	743	0.21	511.45	64.57	10.67	1.9	0.05861	1.17	0.052707283	1.772673	0.7568	2.0	0.09369	1.8	0.83	572.2	17.4	577.4	19.9	551.6	48.9	572.8	17.3	108.8
IM13_32	-0.34	104143.31	1131	0.43	-2354.77	-27.97	10.67	1.4	0.05846	1.14	0.103238028	1.054163	0.7553	1.9	0.09375	1.4	0.79	571.3	17.0	577.7	15.7	546.0	52.1	575.6	15.2	110.2
IM13_59	-0.11	87044.51	683	0.20	213.33	162.94	10.65	0.5	0.05838	1.38	0.050685443	1.866758	0.7554	1.5	0.09389	0.5	0.33	571.3	12.9	578.5	5.3	542.9	61.0	578.2	5.3	112.2
IM13_13	0.28	110912.19	770	0.43	-699.05	-61.21	10.61	1.2	0.05924	1.32	0.105976791	1.501405	0.7693	1.8	0.09423	1.3	0.71	579.4	16.2	580.5	14.0	574.9	56.2	580.2	13.7	104.4
IM13_2	0.97	44639.49	419	0.23	346.72	54.14	10.58	0.6	0.05952	1.89	0.056390584	2.796483	0.7751	2.0	0.09450	0.6	0.23	582.7	17.6	582.1	7.1	585.1	84.1	582.1	6.9	107.4
IM13_28	0.14	108327.20	804	0.48	-1388.23	-42.88	10.45	1.4	0.05779	1.33	0.110251321	1.149506	0.7622	1.9	0.09570	1.4	0.70	575.3	16.3	589.2	15.3	520.9	57.8	583.4	14.4	116.3
IM13_40	0.34	25969.57	191	0.29	-2437.47	-32.93	10.16	0.7	0.05847	2.39	0.078128186	2.595515	0.7934	2.4	0.09846	0.7	0.06	593.1	21.2	605.4	7.9	546.5	105.8	604.0	7.5	129.4
IM13_60	-0.21	41358.80	287	0.57	-189.01	-101.40	10.12	1.0	0.06110	2.67	0.145046360	1.762176	0.8324	2.9	0.09886	1.0	0.36	615.0	26.7	607.7	11.5	641.6	116.4	608.0	11.5	103.2

Appendix 5

LA-ICP-MS U-Pb data for the Plešovice as a secondary reference material.

						Data for Wetherill plot					Data for Tera-Wasserburg plot						Dates						U_{ppm}	%Conc
Identifier	**f206c**	**^{206}Pb**	**Th/U**	**^{206}Pb/^{204}Pb**	**1s%**	**^{207}Pb/^{235}U**	**1s%**	**^{206}Pb/^{238}U**	**1s%**	**Rho**	**^{238}U/^{206}Pb**	**1s%**	**^{207}Pb/^{206}Pb**	**1s%**	**^{208}Pb/^{206}Pb**	**1s%**	**^{207}Pb/^{206}Pb**	**2s**	**^{206}Pb/^{238}U**	**2s**	**^{207}Pb/^{235}U**	**2s**		
Ples_23	0.75	53639.15	0.10	-475.66	-55.12	0.3910	1.9	0.05333	0.7	0.14	18.75	0.7	0.05320	1.91	0.026077042	2.334217	336.1	86.3	335	4.4	335.1	10.7	755	113.2
Ples_24	0.65	51582.22	0.10	-333.03	-59.50	0.3930	1.6	0.05398	0.5	0.15	18.53	0.6	0.05283	1.58	0.026185734	2.417102	320.5	71.5	338.9	3.6	336.6	9	753	117.0
Ples_21	-0.16	54056.98	0.10	-710.06	-44.95	0.3849	1.9	0.05355	0.6	0.18	18.68	0.6	0.05215	1.85	0.026301091	2.096167	291.1	84.6	336.3	3.9	330.6	10.5	756	132.3
Ples_22	0.50	56947.94	0.10	-481.16	-58.94	0.4003	1.5	0.05406	0.6	0.35	18.50	0.6	0.05372	1.42	0.026484392	2.432624	358.4	63.7	339.4	3.9	341.8	8.7	756	100.5
Ples_19	0.34	64492.82	0.10	-717.73	-42.90	0.3862	1.4	0.05306	0.5	-0.07	18.85	0.5	0.05282	1.54	0.026989844	2.255749	320	70.4	333.3	3.4	331.6	8.1	759	110.7
Ples_20	-0.68	60841.23	0.10	-128.01	-151.71	0.3967	1.6	0.05380	0.5	0.15	18.59	0.5	0.05351	1.57	0.027760912	2.252616	349.3	71.1	337.8	3.1	339.2	9.1	749	103.6
Ples_17	-0.13	50483.61	0.10	-538.81	-38.77	0.4027	1.7	0.05417	0.6	0.04	18.46	0.6	0.05394	1.76	0.024589258	2.786096	367.6	78.8	340.1	4.1	343.6	9.7	761	102.4
Ples_18	0.94	45108.48	0.10	-145.53	-91.66	0.3929	1.9	0.05352	0.6	0.16	18.68	0.6	0.05326	1.90	0.025098741	2.681902	339	85.8	336.1	4	336.5	10.9	746	113.5
Ples_15	0.22	57762.89	0.10	3293.35	38.95	0.3978	1.8	0.05339	0.7	0.16	18.73	0.7	0.05406	1.79	0.026339451	2.085549	372.7	81.5	335.3	4.6	340.1	10.3	759	102.5
Ples_16	-0.10	56786.00	0.10	3399.06	30.13	0.4058	1.5	0.05379	0.6	0.08	18.59	0.6	0.05473	1.60	0.026293593	2.371205	400.3	72	337.8	3.9	345.8	9	751	92.9
Ples_13	0.38	58465.39	0.10	-3269.51	-25.66	0.3986	1.6	0.05351	0.5	0.03	18.69	0.5	0.05406	1.65	0.025898016	2.310606	372.5	74.2	336	3.2	340.7	9.2	755	100.9
Ples_14	0.87	58262.30	0.10	-7853.69	-40.70	0.3842	1.5	0.05413	0.5	0.05	18.48	0.5	0.05150	1.58	0.030559173	3.721279	262.2	72.9	339.8	3.6	330.1	8.6	754	152.0
Ples_12	-0.53	58000.28	0.10	-412.24	-50.33	0.3962	1.5	0.05373	0.5	0.04	18.61	0.5	0.05350	1.62	0.027386150	2.289054	349.2	73	337.4	3.6	338.9	8.9	755	106.2
Ples_9	-0.87	55100.71	0.10	-229.31	-86.58	0.3907	1.7	0.05361	0.6	-0.03	18.65	0.6	0.05288	1.84	0.026982504	2.353171	322.6	82.5	336.6	3.8	334.9	9.7	758	114.0
Ples_10	0.35	50624.57	0.10	181.71	103.68	0.3932	1.6	0.05346	0.6	0.00	18.70	0.6	0.05337	1.66	0.026793920	2.393834	343.4	75.9	335.7	3.8	336.7	9	750	105.5
Ples_7	-0.54	65704.87	0.10	-1017.31	-33.47	0.3838	2.0	0.05366	0.5	0.06	18.64	0.5	0.05190	2.03	0.027179428	2.478643	280	92.8	336.9	3.6	329.8	11.2	756	140.8
Ples_8	-0.08	64016.75	0.10	-881.40	-36.59	0.3945	1.5	0.05359	0.4	0.21	18.66	0.4	0.05342	1.48	0.026915904	2.317759	345.5	66.6	336.5	2.8	337.7	8.6	755	104.6
Ples_5	1.06	57925.43	0.10	-378.49	-78.35	0.3958	1.9	0.05341	0.7	0.10	18.72	0.7	0.05377	1.92	0.031027944	4.375674	360.2	88.7	335.4	4.5	338.6	11	746	104.3
Ples_6	-0.21	70445.41	0.10	-2120.34	-32.08	0.3977	1.3	0.05407	0.4	-0.05	18.50	0.4	0.05337	1.43	0.026248336	2.105787	343.4	64.8	339.5	2.9	340	7.7	764	107.5
Ples_4	0.52	53505.12	0.10	-311.05	-66.13	0.3899	1.7	0.05365	0.5	-0.08	18.64	0.5	0.05273	1.85	0.026213515	2.597983	316.1	84.4	336.9	3.5	334.3	9.9	753	121.1
Ples_2	0.55	61258.80	0.10	344.80	81.34	0.3948	1.5	0.05357	0.5	0.15	18.67	0.5	0.05347	1.50	0.026234842	2.470396	347.9	67.7	336.4	3.6	337.9	8.5	756	102.4

Appendix 6

Mineral abbreviations from Evan and Whitney (2010).

Mineral	Symbol	Mineral	Symbol	Mineral	Symbol	Mineral	Symbol	Mineral	Symbol	Mineral	Symbol	Mineral	Symbol	Mineral	Symbol
acmite	aq	böhmite	Bhm	crossite	Crt	ferroglaucophane	Fgl	hibonite	Hbn	magnesioferrite	Mfr	orthoclase	Or	sadanagaite	Sdg	tridymite	Trd
actinolite	Act	bornite	Bn	cryolite	Crl	ferrokaersutite	Fkrs	hibschite	Hbs	Magnesio-hastingsite	Mhs	orthoenstatite	Oen	sanidine	Sa	troilite	Tro
adularia	Adl	brookite	Brk	cubanite	Cbn	ferronyboite	Fny	hogbomite	Hgb	Magnesio-hornblende	Mhb	orthopyroxene	Opx	saponite	Sap	tschermakite	Ts
aegirine	Aeg	brucite	Brc	cummingtonite	Cum	ferropargasite	Fprg	hollandite	Hol	Magnesio-katophorite	Mkt	osumilite	Osm	sapphirine	Spr	ulvospinel	Usp
akermanite	Ak	bustamite	Bst	cuprite	Cpr	ferrorichterite	Frct	holmquistite	Hlm	Magnesio-riebeckite	Mrbk	palygorskite	Plg	scapolite	Scp	uraninite	Urn
albite	Ab	calcite	Cal	cuspidine	Csp	ferrosilite	Fs	hornblende	Hbl	Magnesio-sadanagite	Msdg	paragonite	Pg	scheelite	Sch	uvarovite	Uv
alkali	Afs	cancrinite	Ccn	daphnite	Dph	ferrotschermakite	Fts	howieite	Hw	Magnesio-staurolite	Mst	pargasite	Prg	schorl	Srl	vaterite	Vtr
allanite	Aln	cannilloite	Cnl	datolite	Dat	ferrowinchite	Fwn	humite	Hu	Magnesio-taramite	Mtm	pectolite	Pct	schreibersite	Scb	vermiculite	Vrm
almandine	Alm	carbonate	Cb	daubreelite	Dbr	fibrolite	Fi	Hydro-grossular	Hgr	magnesiowustite	Mws	pentlandite	Pn	sepiolite	Sep	vesuvianite	Ves
Alumino-silicate	Als	carpholite	Car	deerite	Dee	fluorite	Fl	hypersthene	Hyp	magnesite	Mgs	periclase	Per	sericite	Ser	wadsleyite	Wds
alunite	Alu	cassiterite	Cst	diamond	Dia	forsterite	Fo	illite	Ilt	magnetite	Mag	perovskite	Prv	serpentine	Srp	wagnerite	Wag

amakinite	Amk	celadonite	Cel	diaspore	Dsp	foshagite	Fos	ilmenite	Ilm	majorite	Maj	petalite	Ptl	siderite	Sd	wairakite	Wrk
amesite	Ame	celestine	Clt	dickite	Dck	franklinite	Frk	ilvaite	Ilv	malachite	Mlc	phase	PhA	sillimanite	Sil	wavellite	Wav
amphibole	Amp	celsian	Cls	digenite	Dg	fullerite	Ful	jadeite	Jd	manganosite	Mng	phengite	Ph	smectite	Sme	whitlockite	Wht
analcime	Anl	cerussite	Cer	diopside	Di	gahnite	Ghn	jarosite	Jrs	marcasite	Mrc	phillipsite	Php	sodalite	Sdl	willmenite	Wlm
anatase	Ant	chabazite	Cbz	dioptase	Dpt	galaxite	Glx	Jimthom-psonite	Jim	margarite	Mrg	phlogopite	Phl	spessartine	Sps	winchite	Wnc
andalusite	And	chalcocite	Cct	dolomite	Dol	galena	Gn	johannsenite	Jhn	marialite	Mar	piemontite	Pmt	sphalerite	Sp	witherite	Wth
andradite	Adr	chalcopyrite	Ccp	dravite	Drv	garnet	Grt	kaersutite	Krs	meionite	Mei	pigeonite	Pgt	sphene	Spn	wollastonite	Wo
anglesite	Ang	chamosite	Chm	dumortierite	Dum	gedrite	Ged	kalsilite	Kls	melilite	Mll	plagioclase	Pl	spinel	Spl	wurtzite	Wur
anhydrite	Anh	chesterite	Chs	eastonite	Eas	gehlenite	Gh	kamacite	Kam	merwinite	Mw	prehnite	Prh	spodumene	Spd	wustite	Wus
ankerite	Ank	chlorite	Chl	ecandrewsite	Ec	geikielite	Gk	kaolinite	Kln	mesolite	Mes	prismatine	Prm	spurrite	Spu	xenotime	Xtm
annite	Ann	chloritoid	Cld	eckermannite	Eck	gibbsite	Gbs	katophorite	Ktp	microcline	Mc	pseudobrookite	Psb	staurolite	St	xonotlite	Xon
anorthite	An	chondrodite	Chn	edenite	Ed	gismondine	Gis	K-feldspar	Kfs	millerite	Mlr	pumpellyite-(Al)	Pmp	stevensite	Stv	yugawaralite	Yug
anorthoclase	Ano	chromite	Chr	elbaite	Elb	glauconite	Glt	K-hollandite	Khl	minnesotaite	Mns	pyrite	Py	stilbite	Stb	zeolite	Zeo
anthophyllite	Ath	chrysocolla	Ccl	ellenbergerite	Ell	glaucophane	Gln	kirschsteinite	Kir	moganite	Mog	pyrochlore	Pcl	stilpnomelane	Stp	zinnwaldite	Znw
antigorite	Atg	chrysotile	Ctl	enargite	Eng	gmelinite	Gme	kornerupine	Krn	molybdenite	Mol	pyrope	Prp	stishovite	Sti	zircon	Zrn
apatite	Ap	cinnabar	Cin	enstatite	En	goethite	Gth	kosmochlor	Kos	monazite	Mnz	pyrophanite	Pph	strontianite	Str	zoisite	Zo

apophyllite	Apo	Clino-amphibole	Cam	epidote	Ep	grandidierite	Gdd	kutnohorite	Kut	monticellite	Mtc	pyrophyllite	Prl	sudoite	Sud	
aragonite	Arg	clinochlore	Clc	erionite	Eri	graphite	Gr	kyanite	Ky	montmorillonite	Mnt	pyroxferroite	Pxf	sylvite	Syl	
arfvedsonite	Arf	Clino-enstatite	Cen	eskolaite	Esk	greenalite	Gre	larnite	Lrn	mordenite	Mor	pyroxmangite	Pxm	taenite	Tae	
armalcolite	Arm	Clino-ferrosilite	Cfs	esseneite	Ess	grossular	Grs	laumontite	Lmt	mullite	Mul	pyrrhotite	Po	talc	Tlc	
arsenopyrite	Apy	clinohumite	Chu	eudialite	Eud	grunerite	Gru	lawsonite	Lws	muscovite	Ms	qandilite	Qnd	taramite	Trm	
augite	Aug	Clino-ptilolite	Cpt	fassaite	Fas	gypsum	Gp	lazulite	Lzl	natrolite	Ntr	quartz	Qz	tennantite	Tnt	
awaruite	Awr	Clino-pyroxene	Cpx	fayalite	Fa	halite	Hl	lazurite	Lzr	nepheline	Nph	rankinite	Rnk	tenorite	Tnr	
axinite	Ax	clinozoisite	Czo	feldspar	Fsp	harmotome	Hrm	lepidolite	Lpd	norbergite	Nrb	realgar	Rlg	tephroite	Tep	
babingtonite	Bab	clintonite	Cln	ferro-actinolite	Fac	hastingsite	Hst	leucite	Lct	nosean	Nsn	rhodochrosite	Rds	Tetra-hedrite	Ttr	
baddeleyite	Bdy	coesite	Coe	ferro-anthophyllite	Fath	hausmannite	Hsm	limonite	Lm	nyböite	Nyb	rhodonite	Rdn	thomsonite	Thm	
barite	Brt	cohenite	Coh	ferrobarroisite	Fbrs	hauyne	Hyn	liquid	Liq	olivine	Ol	richterite	Rct	thorite	Thr	
barroisite	Brs	cordierite	Crd	ferrocarpholite	Fcar	heazlewoodite	Hzl	lizardite	Lz	omphacite	Omp	riebeckite	Rbk	tilleyite	Tly	
beidellite	Bei	corrensite	Crr	ferroceladonite	Fcel	hedenbergite	Hd	lollingite	Lo	opal	Opl	ringwoodite	Rwd	titanite	Ttn	
beryl	Brl	corundum	Crn	ferro-eckermannite	Fec	hematite	Hem	maghemite	Mgh	opaque	Opq	roedderite	Rdr	topaz	Tpz	

biotite	Bt	covellite	Cv	ferro-edenite	Fed	hercynite	Hc	magnesio-arfvedsonite	Marf	orpiment	Orp	rossmanite	Rsm	tourmaline	Tur				
bixbyite	Bxb	cristobalite	Crs	ferrogedrite	Fgd	heulandite	Hul	magnesiocarpholite	Mcar	orthoamphibole	Oam	rutile	Rt	tremolite	Tr				

GENERAL REFERENCES

Aabi, A., Hejja, Y., Nait Bba, A., Boujamaoui, M., Baidder, L., El Azmi, M., Maacha, L., Hamzaoui, A., 2024. Tectonic Reactivation and Ore-Forming Fault Systems from the West African Craton Margin (Saghro, Anti Atlas, Morocco). Journal of African Earth Sciences, 211: 105182. https://doi.org/10.1016/j.jafrearsci.2024.105182.

Abbassi, B., Cheng, L-Z., 2025. Curvilinear Lineament Extraction: Bayesian Optimization of Principal Component Wavelet Analysis and Hysteresis Thresholding. Computers and Geosciences, 194: 105768. https://doi.org/10.1016/j.cageo.2024.105768.

Abbassi, B., Cheng, L-Z., Jébrak, M., Lemire, D., 2022. 3D Geophysical predictive modeling by spectral feature Subset selection in mineral exploration. Minerals, 12 (10), 1296. https://doi.org/10.3390/min12101296.

Abbassi, B., Cheng, L-Z., 2021. 3D Geophysical Post-Inversion Feature Extraction for Mineral Exploration through Fast-ICA. Minerals, 11 (9), 959. https://doi.org/10.3390/min11090959

Abbassi, B., Cheng, L-Z., Richards, J.P., Hübert, J., Legault, J.M., Rebagliati, M., Witherly, K., 2018. Geophysical Properties of an Epithermal Au-Ag Deposit in British Columbia, Canada. Interpretation, 6 (4): 907–918. https://doi.org/10.1190/INT-2017-0232.1

Abbassi, B., 2018. Integrated Imaging through 3d Geophysical Inversion, Multivariate Feature Extraction, and Spectral Feature Selection. Doctoral dissertation, University of Quebec in Abitibi-Temiscamingue, Canada, 218.

Abia, E.H., Nachit, H., Marignac, C., Ibhi, A., Ait Saadi, S., 2003. The Polymetallic Au-Ag-Bearing Veins of Bou Madine (Jbel Ougnat, Eastern Anti-Atlas, Morocco): Tectonic Control and Evolution of a Neoproterozoic Epithermal Deposit. Journal of African Earth Sciences, 36 (4): 251–71. https://doi.org/10.1016/S0899-5362(03)00051-4.

Achkouch, L., Miftah, A., Ouchchen, M., Mamouch, Y., Attou, A., Boutaleb, S., Dadi, B., 2023. Mapping and Litho-Geophysical Classification of Potential Mining Areas by Spatial Remote Sensing and Helicopter-Borne Gamma-Ray Spectrometry (Tikirt, Anti-Atlas, Morocco). Geophysical Prospecting, 71 (8): 1551–69. https://doi.org/10.1111/1365-2478.13376.

Ait Lahna, A., Youbi, N., Admou, H., Bouougri, E. H., Chaib, L., Boumehdi, M. A., Bensalah, MK., Aarab, E.M., Tassinari, C.C.G., Mata, J., Ernst, R.E., Söderlund, U., 2016. Refining the Stratigraphy of the Taghdout Group by Using the U-Pb Geochronology of the Taghdout Sill (Zenaga inlier, Anti-Atlas, Morocco). *Acta Geologica Sinica (English edition)*, *90*.

Aït Malek, H., Gasquet, D., Bertrand, J.M., Leterrier, J., 1998. Géochronologie U–Pb Sur Zircon de Granitoïdes Éburnéens et Panafricains Dans Les Boutonnières pro-Térozoïques d'Igherm, Du Kerdous et Du Bas Drâa (Anti-Atlas Occidental, Maroc). R.C Sciences.

Alimohammadi, M., Alirezaei, S., Kontak, D.J., 2015. Application of ASTER Data for Exploration of Porphyry Copper Deposits: A Case Study of Daraloo–Sarmeshk Area, Southern Part of the Kerman Copper Belt, Iran. Ore Geology Reviews, 70: 290–304.

Álvaro, J. J., Bellido, F., Gasquet, D., Pereira, M. F., Quesada, C., Sánchez-García, T., 2014a. Diachronism in the Late Neoproterozoic-Cambrian Arc-Rift Transition of North

Gondwana: A Comparison of Morocco and the Iberian Ossa-Morena Zone. Journal of African Earth Sciences, 98: 113–32. https://doi.org/10.1016/j.jafrearsci.2014.03.024.

Álvaro, J. J., Benziane, F., Thomas, R., Walsh, G. J., Yazidi, A., 2014b. Neoproterozoic–Cambrian stratigraphic framework of the Anti-Atlas and Ouzellagh promontory (High Atlas), Morocco. Journal of African Earth Sciences, 98, 19-33.

Arbiol, C., Layne, G., Zanoni, G., Šegvić, B., 2021. Characteristics and Genesis of Phyllosilicate Hydrothermal Assemblages from Neoproterozoic Epithermal Au-Ag Mineralization of the Avalon Zone of Newfoundland, Canada. Applied Clay Science, 202 . https://doi.org/10.1016/j.clay.2020.105960.

Arribas, A., 1995. Characteristics of High-Sulfidation Epithermal Deposits, and Their Relation to Magmatic Fluid. Mineralogical Association of Canada Short Course Series, 23: 419–54.

Azizi Samir, M. R., Ferrandini, J., Tane, J. L., 1990. Tectonique et volcanisme tardi-Pan Africains (580-560 Ma) dans l'Anti-Atlas Central (Maroc): interprétation géodynamique à l'échelle du NW de l'Afrique. Journal of African Earth Sciences (and the Middle East), 10 (3), 549-563. https://doi.org/10.1016/0899-5362(90)90105-N

Baidada, B., Ikenne, M., Barbey, P., Soulaimani, A., Cousens, B., Haissen, F., Ilmen, S., Alansari., A., 2019. SHRIMP U–Pb Zircon Geochronology of the Granitoids of the Imiter Inlier: Constraints on the Pan-African Events in the Saghro Massif, Anti-Atlas (Morocco). Journal of African Earth Sciences, 150 : 799–810. https://doi.org/10.1016/j.jafrearsci.2018.10.008.

Baranov, V., 1957. A New Method for Interpretation of Aeromagnetic Maps: Psedo-Gravimetric Anomalies. Geophysics, 22 (2): 352–83. https://doi.org/10.1190/1.1438369

Bard, J.P., 1980. Microtexture Des Roches Magmatique et Métamorphiques.

Belkacim, S., Perrot, M.G., Davies, J.H.F.L., Liégeois, J-P., Ikenne, M., 2021. The Ediacaran Ouarzazate Group, a Metacratonic Silicic Large Igneous Province (SLIP) : New U-Pb Zircon Ages from Ouzellarh-Siroua Salient (Tifnoute Valley, Morocco). In Geological Society of America Northeastern Section (NEGSA), 1/1. T17. Pre-Atlantic Geological Connections among Northwest Africa, Southern Europe, and Eastern North America

Belkacim, S., Gasquet, D., Liégeois, J.P., Arai, S., Gahlan, H.A., Ahmed, H., Ishida, Y., Ikenne, M., 2017. The Ediacaran Volcanic Rocks and Associated Mafic Dykes of the Ouarzazate Group (Anti-Atlas, Morocco): Clinopyroxene Composition, Whole-Rock Geochemistry and Sr-Nd Isotopes Constraints from the Ouzellarh-Siroua Salient (Tifnoute Valley). Journal of African Earth Sciences, 127: 113–35. https://doi.org/10.1016/j.jafrearsci.2016.08.002.

Belkacim, S., Ikenne, M., Souhassou, M., Elbasbas, A., Toummite, A., 2014. The Cu-Mo±Au Mineralizations Associated to the High-K Calc- Alkaline Granitoids from Tifnoute Valley (Siroua Massif, Anti- Atlas, Morocco): An Arc-Type Porphyry in the Late Neoproterozoic Series. Journal of Environment and Earth Science, 4 (14): 90–106.

Belkacim, S., 2014. Pétrographie, Géochimie et Isotopes (Sr-Nd) Du Volcanisme Édiacarien et Des Dykes Doléritiques de La Vallée de Tifnoute et Caractérisation Des Indices de Cu-Mo±Au d'Imourkhssan (Siroua, Anti-Atlas Central, Maroc). Doctoral dissertation, Ibn Zohr University, 237p.

Betts, P. G., Moore, D., Aitken, A., Blaikie, T., Jessell, M., Ailleres, L., Armit, R., McLean, M., Munukulta, R., Chukwu, C., 2024. Geology from aeromagnetic data. Earth-Science Reviews, 258, 104958. https://doi.org/10.1016/j.earscirev.2024.104958

Benziane, F., 2007. Lithostratigraphie et évolution géodynamique de l'Anti-Atlas (Maroc) du Paléoprotérozoïque au Néoprotérozoïque: exemples de la boutonnière de Tagragra de Tata et du Jbel Saghro. PhD thesis, Université de Savoie CISM, Chambéry, France, 320p.

Blakely, R.J., 1995. Potential Theory in Gravity and Magnetic Applications. Cambridge university press, 441p.

Blakely, R.J., Connard, G.G., Curto, J.B., 2016. Tilt Derivative Made Easy. Geosoft Technical Publications, 4: 1–4

Blein, O., Baudin, T., Soulaimani, A., Cocherie, A., Chevremont, P., Admou, H., Roger, J., 2014. New geochemical, geochronological and structural constraints on the Ediacaran evolution of the south Sirwa, Agadir-Melloul and Iguerda inliers, Anti-Atlas, Morocco. Journal of African Earth Sciences, 98, 47-71.

Bodnar, R. J., Lecumberri-Sanchez, P., Moncada, D., Steele-MacInnis, M., 2014. 13.5–Fluid inclusions in hydrothermal ore deposits. Treatise on geochemistry, 13, 119-142.

Bouabdellah, M., Chekroun, F., Alansari, A., Margoum, D., 2016. The Granitoid-Related Tiouit Gold Deposit, Saghro Inlier, Eastern Anti-Atlas (Morocco): Neoproterozoic Mineralization by a Polyphase Late-Magmatic to Hydrothermal System, 405–14. https://doi.org/10.1007/978-3-319-31733-5_16.

Bouabdellah, M., and Slack, J.F., 2016. Geologic and Metallogenic Framework of North Africa. https://doi.org/10.1007/978-3-319-31733-5_1.

Bouougri, E. H., Ait Lahna, A., Tassinari, C. C., Basei, M. A., Youbi, N., Admou, H., Saquaque, A., Boumehdi, M.H., Maacha, L. (2020). Time constraints on Early Tonian Rifting and Cryogenian Arc terrane-continent convergence along the northern margin of the West African craton: Insights from SHRIMP and LA-ICP-MS zircon geochronology in the Pan-African Anti-Atlas belt (Morocco). Gondwana Research, 85, 169-188.

Bouzekraoui, M., Essalhi, M., Saadi, M., Karaoui, B., Ghazali, M., Manar, A., 2024b. Foreland Evolution in the Inherited Basement Structure of the Pre-African Tinghir-Errachidia-Boudenib Basin (Moroccan Southern Atlas Margin). Italian Journal of Geosciences, 143 (3): 391–406. https://doi.org/10.3301/IJG.2024.23

Bouzekraoui, M., Es-Sabbar, B., Karaoui, B., Essalhi, M., Saadi, M., 2024a. Structural Analysis, Tectonic Fracturing Modeling, and Kinematic Evolution along the South Atlas Fault at the Northern Border of the Tinghir-Errachidia-Boudenib Basin (Pre-African Trough, Morocco). Journal of African Earth Sciences, 212 : 105193. https://doi.org/10.1016/j.jafrearsci.2024.105193.

Bowman, J. R., Parry, W. T., Kropp, W. P., & Kruer, S. A., 1987. Chemical and isotopic evolution of hydrothermal solutions at Bingham, Utah. Economic Geology, 82(2), 395-428.

Boynton, W. V., 1983. Cosmochemistry of the Rare Earth Elements: Meteorite Studies. Rare Earth Element Geochemistry, 63–114. https://doi.org/10.1016/b978-0-444-42148-7.50008-3.

Brimhall, G.H., 1977. Early Fracture-Controlled Disseminated Mineralization at Butte, Montana. Economic Geology, 72 (1): 37–59. https://doi.org/10.2113/gsecongeo.72.1.37.

Bryan, S.E., and Ferrari, L., 2013. Large Igneous Provinces and Silicic Large Igneous Provinces: Progress in Our Understanding over the Last 25 Years. Bulletin of the Geological Society of America, 125 (7–8): 1053–78. https://doi.org/10.1130/B30820.1.

Bryan, S., Ferrari, E., Reiners, P.W., Allen, C.M., Petrone, C.M., Ramos-rosique, A., H. Campbell, I., 2008. New Insights into Crustal Contributions to Large-Volume Rhyolite Generation in the Mid-Tertiary Sierra Madre Occidental Province, Mexico, Revealed by U-Pb Geochronology. Journal of Petrology, 49 (1): 47–77. https://doi.org/10.1093/petrology/egm070.

Burisch, M., Walter, B.F., Markl, G., 2017. Silicification of Hydrothermal Gangue Minerals in Pb-Zn-Cu-Fluoritequartz-Baryte Veins. Canadian Mineralogist, 55 (3): 501–14. https://doi.org/10.3749/canmin.1700005.

Byrne, K., Lesage, G., Gleeson, S.A., Lee, R.G., 2016. Large-Scale Sodic-Calcic Alteration around Porphyry Cu Systems: Examples from the Highland Valley Copper District, Guichon Batholith, South-Central British Columbia.

Camprubí, A., Chomiak, B. A., Villanueva-Estrada, R. E., Canals, À., Norman, D. I., Cardellach, E., Stute, M., 2006. Fluid sources for the La Guitarra epithermal deposit (Temascaltepec district, Mexico): Volatile and helium isotope analyses in fluid inclusions. Chemical Geology, *231*(3), 252-284.

Candela, P. A., and H. D. Holland., 1986. A Mass Transfer Model for Copper and Molybdenum in Magmatic Hydrothermal Systems: The Origin of Porphyry-Type Ore Deposits. Economic Geology, 81 (1): 1–19. https://doi.org/10.2113/gsecongeo.81.1.1.

Cao, M.Y., Jiang, S.Y., Su, H.M., Liu, T., 2021. Indosinian Magmatic–Hydrothermal Metallogenic Event in the North Wuyi Area, Southeastern China: An Example from the Chenfang Skarn Deposit in Jiangxi Province. Ore Geology Reviews, 138 : 104386. https://doi.org/10.1016/j.oregeorev.2021.104386.

Cardon, O., André-Mayer, A.S., Sausse, J., Milu, V., Chauvet, A., Leroy, J.L., Lespinasse, M., Udubasa, S., 2004. The Link between Porphyry Copper and Low-Sulfidation Epithermal Deposit: Structural Study and 3D Representation of the Sector of Bolcana, Apuseni Mountains, Romania. Comptes Rendus - Geoscience, 337 (9): 824–31. https://doi.org/10.1016/j.crte.2005.03.014.

Carten, R.B., White, W.H., Stein., H.J., 1993. High-Grade-Granite Related Molybdenium Systems: Classification and Origin. Geological Association of Canada, no. Special paper: 521–44.

Champion, D.C., Heinemann, M.A., 1994. Igneous Rocks of Northern Queensland. 1:500,000 Map and GIS Explanatory Notes. AGSO, Record 11.

Chappell, B. W., 1999. Aluminium Saturation in I- and S-Type Granites and the Characterization of Fractionated Haplogranites. Lithos, 46 (3): 535–51. https://doi.org/10.1016/S0024-4937(98)00086-3.

Chappell, B. W., and White, A. J.R.., 2001. Two Contrasting Granite Types: 25 Years Later. Australian Journal of Earth Sciences, 48 (4): 489–99. https://doi.org/10.1046/j.1440-0952.2001.00882.x.

Choubert, G., 1963. Histoire Géologique de l'Anti-Atlas de l'Archéen à l'aurore Des Temps Primaires. Notes Mém. Serv.Géol. Maroc, 62, 350-352.

Cheilletz, A., Levresse, G., Gasquet, G., Azizi-Samir, M., Zyadi, R., Archibald, D.A., Farrar, E., 2002. The Giant Imiter Silver Deposit: Neoproterozoic Epithermal Mineralization in the Anti-Atlas, Morocco. Mineralium Deposita, 37 (8): 772–81. https://doi.org/10.1007/s00126-002-0317-0.

Chen, Y.J., Zhang, C., Wang, P., Pirajno, F., Li, N., 2017. The Mo Deposits of Northeast China: A Powerful Indicator of Tectonic Settings and Associated Evolutionary Trends. Ore Geology Reviews, 81: 602–40. https://doi.org/10.1016/j.oregeorev.2016.04.017.

Claiborne, L. L., Miller, C. F., Walker, B. A., Wooden, J. L., Mazdab, F. K., Bea, F. Tracking Magmatic Processes through Zr/Hf Ratios in Rocks and Hf and Ti Zoning in Zircons: An Example from the Spirit Mountain Batholith, Nevada. Mineralogical Magazine, 70 (5): 517–43. https://doi.org/10.1180/0026461067050348.

Choubert, G., 1963. Histoire Géologique de l'Anti-Atlas de l'Archéen à l'aurore Des Temps Primaires. Notes Mém. Serv.Géol. Maroc, 62, 350-352.

Clark, D. A., 2014. Magnetic effects of hydrothermal alteration in porphyry copper and iron-oxide copper–gold systems: A review. Tectonophysics, 624, 46-65. https://doi.org/10.1016/j.tecto.2013.12.011

Cooke, D.R., Hollings, P.,.Walshe, J.L., 2005. Giant Porphyry Deposits: Characteristics, Distribution, and Tectonic Controls. Turkish Journal of Fisheries and Aquatic Sciences, 18: 539–46.

Cooke, D. R., P. Hollings, J. J. Wilkinson, and R. M. Tosdal., 2014. Geochemistry of Porphyry Deposits. Treatise on Geochemistry: Second Edition. 2nd ed. Vol. 13. Elsevier Ltd. https://doi.org/10.1016/B978-0-08-095975-7.01116-5.

Core, D., Buckingham, A., Belfield, S., 2009. Detailed Structural Analysis of Magnetic Data-Done Quickly and Objectively.SGEG News,

Crusius, J., Calve, S., Pedersen, T., Sage, D., 1996. Rhenium and Molybdenum Enrichments in Sediments as Indicators of Oxic, Suboxic and Sulfidic Conditions of Deposition. Earth and Planetary Science, Letters, no. 96: 65–78.

Dadi, B., Ouchchen, M., Faik, F., Boutaleb, S., El Azzab, D., Mamouch, Y., Achkouch, L., Bajadi, L., Abia, E H., Sadeghi, B., 2024. Hydrothermal Fluid Pathways and Mineralization Potential in the High Atlas Massif (Morocco) Using Fuzzy Logic and Multifractal Modeling. Ore Geology Reviews, 175: 106401. https://doi.org/10.1016/j.oregeorev.2024.106401.

D'Lemos, R.S., Inglis, J.D., Samson, S.D., 2006. Newly Discovered Orogenic Event in Morocco: Neoproterozic Ages for Supposed Eburnean Basement of the Bou Azzer Inlier, Anti-Atlas Mountains. Precambrian Research, 147: 65–78.

Dabiri, R., Akbari-Mogaddam, M., Ghaffari, M., 2018. Geochemical Evolution and Petrogenesis of the Eocene Kashmar Granitoid Rocks, NE Iran: Implications for Fractional Crystallization and Crustal Contamination Processes. Iranian Journal of Earth Sciences, 10 (1): 68–77.

Dadi, B., Ouchchen, M., Faik, F., Boutaleb, S., El Azzab, D., Mamouch, Y., Achkouch, L., Bajadi, L., Abia, E H., Sadeghi, B., 2024. Hydrothermal Fluid Pathways and

Mineralization Potential in the High Atlas Massif (Morocco) Using Fuzzy Logic and Multifractal Modeling. Ore Geology Reviews, 175: 106401. https://doi.org/10.1016/j.oregeorev.2024.106401.

Delibaş, O., Moritz, R., Chiaradia, M., Selby, D., Ulianov, A., Revan, M.K., 2017. Post-Collisional Magmatism and Ore-Forming Systems in the Menderes Massif: New Constraints from the Miocene Porphyry Mo–Cu Pınarbaşı System, Gediz–Kütahya, Western Turkey. Mineralium Deposita, 52 (8): 1157–78. https://doi.org/10.1007/s00126-016-0711-7.

Di Tommaso, I and Rubinstein, N., 2007. Hydrothermal alteration mapping using ASTER data in the Infiernillo porphyry deposit, Argentina. Ore Geology Reviews, 32(1-2), 275-290.

Dilles, J.H., and John., D.A., 2020. Porphyry and Epithermal Mineral Deposits. Encyclopedia of Geology, (1-6), Second Edition 5: 847–66. https://doi.org/10.1016/B978-0-08-102908-4.00005-9.

Domzalski, W., 1966. Importance of Aeromagnetics in Evaluation of Structural Control of Mineralization. Geophysical Prospecting, 14 (3), 273-291. https://doi.org/10.1111/j.1365-2478.1966.tb01761.x

Dubé, B., Dunning, G., Lauzière, K., 1998. Geology of the Hope Brook Mine, Newfoundland, Canada: A Preserved Late Proterozoic High-Sulfidation Epithermal Gold Deposit and Its Implications for Exploration. Economic Geology, 93 (4): 405–36. https://doi.org/10.2113/gsecongeo.93.4.405.

Echogdali, F Z., Boutaleb, S., Abia, E H., Ouchchen, M., Dadi, B., Id-Belqas, M., Abioui, M., Pham, L T., Abu-Alam, T., Mickus, K.L., 2022. Mineral Prospectivity Mapping: A Potential Technique for Sustainable Mineral Exploration and Mining Activities–a Case Study Using the Copper Deposits of the Tagmout Basin, Morocco. Geocarto International, 37 (25): 9110–31. https://doi.org/10.1080/10106049.2021.2017006.

El Azmi, D., Aissa, M., Ouguir, H., Mahdoudi, M. L., El Azmi, M., Ouadjo, A., Zouhair, M., 2014. Magmatic Context of Bou Skour Copper Deposit (Eastern Anti-Atlas, Morocco): Petrogrography, Geochemistry and Alterations. Journal of African Earth Sciences, 97: 40–55. https://doi.org/10.1016/j.jafrearsci.2014.04.020.

El Bahat, A., Ikenne, M., Söderlund, U., Cousens, B., Youbi, N., Ernst, R.E., Soulaimani, A., Hafid, A., 2013. U–Pb baddeleyite ages and geochemistry of dolerite dykes in the Bas Drâa Inlier of the Anti-Atlas of Morocco: newly identified 1380 Ma event in the West African Craton. Lithos, 174, 85-98.

El Kabouri, J., 2023. Geobiology and Lithostratigraphy of the Ediacaran Successions of the Eastern Anti-Atlas (Morocco): Implications for the Geobiological and Geodynamic Evolution of the Northern Margin of the West African Craton (Doctoral dissertation, Departement of Geology, University of Chouaib Doukkali)

Elkhateeb, O.M., Abdellatif, M.A.G., 2018. Delineation Potential Gold Mineralization Zones in a Part of Central Eastern Desert, Egypt Using Airborne Magnetic and Radiometric Data. NRIAG Journal of Astronomy and Geophysics, 7: 361–376.

El Moume, W., Youbi, N., Marzoli, A., Bertrand, H., Ikenne, L., Boumehdi, M A., Ernst,

R.E., El Hachimi, H., Bensalah, M K., Mata, J., Madeira, J., Bento dos Santos, T.M., Martins, S.,. 2020. Geochemistry of Mafic Dyke Swarms of Douar Eç-Çour (High Atlas, Morocco): The Farthest Record of the Central Iapetus Magmatic Province (CIMP) into West African Craton. In The Farthest Record of the Central Iapetus Magmatic Province (CIMP) into West African Craton, Geólogos, 33 (1-2): 95–124.

Ennih, N., Liégeois, J P., 2001. The Moroccan Anti-Atlas: The West African Craton Passive Margin with Limited Pan-African Activity. Implications for the Northern Limit of the Craton. Precambrian Research, 112 (3–4): 289–302. https://doi.org/10.1016/S0301-9268(01)00195-4.

Ennih, N., Liégeois, J P., 2008. The Boundaries of the West African Craton, with Special Reference to the Basement of the Moroccan Metacratonic Anti-Atlas Belt. Geological Society Special Publication, 297: 1–17. https://doi.org/10.1144/SP297.1.

Errami, E., Linnemann, U., Hofmann, M., Gärtner, A., Zieger, J., Gärtner, J., Mende, K., El Kabouri, J., Gasquet, D., Ennih, N., 2021. From Pan-African transpression to Cadomian transtension at the West African margin: new U–Pb zircon ages from the Eastern Saghro inlier (Anti-Atlas, Morocco).

Errami, E., Linnemann, U., Hofmann, M., G¨artner, A., Zieger, J., G¨artner, J., Mende, K., El Kabouri, J., Gasquet, D., Ennih, N., 2020. From Pan-African Transpression to Cadomian Transtension at the West African Margin: New U-PB Zircon Ages from the Eastern Saghro Inlier (Anti-Atlas, Morocco). The Geological Society of London. Spec. Publ. 503. https://doi.org/10.1144/SP503-2020-105

Errami, E., Bonin, B., Laduron, D., Lasri, L., 2009. Petrology and Geodynamic Significance of the Post-Collisional Pan-African Magmatism in the Eastern Saghro Area (Anti-Atlas, Morocco). Journal of African Earth Sciences, 55: 105–124.

Ernst, R. E., Bond, D. P., Zhang, S. H., Buchan, K. L., Grasby, S. E., Youbi, N., El Bilali, H., Bekker, A., Doucet, L. S., 2021. Large igneous province record through time and implications for secular environmental changes and geological time-scale boundaries. Large igneous provinces: A driver of global environmental and biotic changes, American Geophysical Union, 1–26. https://doi.org/10.1002/9781119507444.ch1.

Ernst, R.E., Jowitt, M., Thompson, J. F. H., 2013. Large Igneous Provinces (LIPs) and Metallogeny. Tectonics, Metallogeny, and Discovery, no. C: 17–51. https://doi.org/10.5382/sp.17.02.

Fayol, N., Jébrak, M., Harris, L. B. , 2016. The magnetic signature of Neoarchean alkaline intrusions and their related gold deposits: Significance and exploration implications. Precambrian Research, 283, 13-23. https://doi.org/10.1016/j.precamres.2016.07.009

Fekkak, A., Pouclet, A., Ouguir, H., Badra, L., Gasquet, D., 1999. Le groupe du Neoproterozoique inferieur de Kelaat Mgouna (Saghro, Anti-Atlas, Maroc); temoin d'un stade precoce de l'extension pre-panafricaine. Bulletin de la Societe Geologique de France, 170(6), 789-797.

Ferdous, S, and J Podder. 1970. Growth and Characterization of Epsomite Single Crystals Doped with KCl from Low Temperature Aqueous Solutions. Journal of Bangladesh Academy of Sciences, 33 (1): 47–54. https://doi.org/10.3329/jbas.v33i1.2949.

Ferguson, S A., 2017. Late Neoproterozoic Epithermal-Style Au Mineralization of the Burin Peninsula, Newfoundland: U-Pb Geochronology and Deposit Characteristics. Memorial

University of Newfoundland October.

Ferraq, M., Belkacim, S., Cheng, L-Z., Davies, J H F L., Perrot, M.G., Ben-tami, A., Bouabdellah, M., 2024. New Geochemical and Geochronological Constraints on the Genesis of the Imourkhssen Cu±Mo±Au±Ag Porphyry Deposit (Ouzellagh-Siroua Salient, Anti-Atlas, Morocco): Geodynamic and Metallogenic Implications. Minerals, 14 (832): 38. https://doi.org/10.3390/min14080832

Ferraq, M., Belkacim, S., Cheng, L.Z., Alansari, A., 2023. Le Porphyre-Épithermal à Cu-Mo-Au-Ag d'Imourkhssen, Anti-Atlas Central, Maroc : Aperçu Des Données Métallogéniques, Géochimiques et Aéromagnétiques et Implications Pour l'exploration Minière." Québec Mines et Energie. Québec.

Feteha, B.F., Lentz, D.R., El Bouseily, A.M., Khalil, K.I., Khamis, H.A., Moghazi, A.K., 2022. Petrogenesis of Neoproterozoic Mo-Bearing A-Type Granites in the Gattar Area, Northern Eastern Desert, Egypt: Implications for Magmatic Evolution and Mineralization Processes. Ore Geology Reviews ,148 . https://doi.org/10.1016/j.oregeorev.2022.105007.

Figueroa, A. J. T., Gabo-Ratio, J. A. S., Manalo, P. C., Takahashi, R., Sato, H., Ramos, A. Bs., 2022. Breccia and Vein Mineralization of the Balatoc Diatreme, Acupan Gold Deposit, Baguio Mineral District: An Example of a Diatreme-Hosted Epithermal Deposit in the Philippines. Ore Geology Reviews, 144: 104826. https://doi.org/10.1016/j.oregeorev.2022.104826.

Frizon de Lamotte, D., Zizi, M., Missenard, Y., Hafid, M., Azzouzi, M. E., Maury, R. C., Charrière, A., Taki, Z., Benammi, M., Michard, A., 2008. The Atlas System. In A. Michard et al. (Eds.), Continental Evolution: The Geology of Morocco (pp. 133–202). Springer.in Earth Sciences 116, Springer-Verlag Berlin Heidelberg 2008

Gasquet, D., Ennih, N., Liégeois, J P., Soulaimani, A., Michard, A., 2008. The Pan-African Belt. Lecture Notes in Earth Sciences, 116: 33–64. https://doi.org/10.1007/978-3-540-77076-3_2.

Gasquet, D., Levresse, G., Cheilletz, Azizi-Samir, M R., Mouttaqi, A., 2005. Contribution to a Geodynamic Reconstruction of the Anti-Atlas (Morocco) during Pan-African Times with the Emphasis on Inversion Tectonics and Metallogenic Activity at the Precambrian-Cambrian Transition. Precambrian Research, 140 (3–4): 157–82. https://doi.org/10.1016/j.precamres.2005.06.009.

Giroux, M., Lambert, M ., 2021. Copper-gold (Cu-Au) skarn-type mineralization in an Archean volcanic context. Natural Resources and Forestry, Mineral Exploration Research Consortium (CONSOREM), Quebec, 40.

Green, T.H., 1995. Significance of Nb/Ta as an Indicator of Geochemical Processes in the Crust-Mantle System. Chemical Geology, 120 (3–4): 347–59. https://doi.org/10.1016/0009-2541(94)00145-X.

Gresse, P.G., De Beer, C.H., De Kock, G.S., Thomas, R.J., Chevallier, L.P., 1997. Geological map of Morocco at 1:50,000 scale, Assarag sheet. Notes and memoirs of the geological service, No. 392 bis, 84, ISSN 0374-9789.

Haibi, H. E., Hadi, H. E., Tahiri, A., Poyatos, D. M., Gasquet, D., Pérez-Cáceres, I., Lodeiro, F.G., Mehdioui, S., 2020. Geochronology and Isotopic Geochemistry of Ediacaran High-K Calc-Alkaline Felsic Volcanism: An Example of a Moroccan Perigondwanan

(Avalonian?) Remnant in the El Jadida Horst (Mazagonia). Journal of African Earth Sciences, 163. https://doi.org/10.1016/j.jafrearsci.2019.103669.

Hassenforder, B., 1987. La Tectonique Panafricaine et Varisque de l'Anti-Atlas dans le massif du Kerdous (Maroc). Doctoral dissertation, Université Louis Pasteur, Strasbourg, (1971-2008).

Heald, P., Foley, N.K., Hayba, D.O., 1987. Comparative Anatomy of Volcanic-Hosted Epithermal Deposits: Acid-Sulfate and Adularia-Sericite Types. Economic Geology and the Bulti of the society of economic Geologists, 82, page 1-26

Hedenquist, J., and Arribas, A., 2022. Exploration Implications of Multiple Formation Environments of Advanced Argillic Minerals. Economic Geology, 117 (3): 609–43. https://doi.org/10.5382/econgeo.4880.

Hedenquist, J, Arribas, A., Eliseo, G.U., 2000. Exploration for Epithermal Gold Deposits. Reviews in Economic Geology, 13: 245–77.

Hedenquist, J., and Arribas, A., 1998. Evolution of an Intrusion-Centered Hydrothermal System: Far Southeast-Lepanto Porphyry and Epithermal Cu-Au Deposits, Philippine. Economic Geology, 93: 373–404.

Hedenquist, J., Lowenstern, J.B., 1994. The Role of Magma in the Formation of Hydrothermal Deposits. Nature, 370: 519–27

Hefferan, K., Soulaimani, A., Samson, S. D., Admou, H., Inglis, J., Saquaque, A., Chaib, L., Heywood, N. (2014). A reconsideration of Pan African orogenic cycle in the Anti-Atlas Mountains, Morocco. Journal of African Earth Sciences, 98, 34-46.

Hefferan, K. P., Admou, H., Karson, J. A., Saquaque, A., 2000. Anti-atlas (Morocco) role in Neoproterozoic western Gondwana reconstruction. Precambrian Research, 103 (1-2), 89-96.

Herbosch, A., Liégeois, J. P., Pin, C., 2016. Coticules of the Belgian type area (Stavelot-Venn Massif): Limy turbidites within the nascent Rheic oceanic basin. Earth-Science Reviews, 159, 186-214.

Holden, E.J., Wong, J C., Wedge, D., Martis, M., Lindsay, M., Gessner, K., 2016. Improving Assessment of Geological Structure Interpretation of Magnetic Data: An Advanced Data Analytics Approach. Computers and Geosciences, 87: 101–11. https://doi.org/10.1016/j.cageo.2015.11.010.

Holden, E.J., Wong, J.C., Kovesi, P., Wedge, D., Dentith, M., Bagas, L. 2012. Identifying Structural Complexity in Aeromagnetic Data: An Image Analysis Approach to Greenfields Gold Exploration. Ore Geology Reviews, 46: 47–59.

Holden, E. J., Fu, S. C., Kovesi, P., Dentith, M., Bourne, B., Hope, M., 2011. Automatic identification of responses from porphyry intrusive systems within magnetic data using image analysis. Journal of Applied Geophysics, 74(4), 255-262.

Holden, E.J., Kovesi, P., Dentith, M.C., Wedge, D., Wong, J.C., Fu, S.C., 2010. Detection of Regions of Structural Complexity within Aeromagnetic Data Using Image Analysis. In In Proceedings of the 25th International Conference Image and Vision Computing New Zealand, Queenstown, New Zealand, 1–8. IEEE. https://doi:10.1109/IVCNZ.2010.6148856.

Hollard, H., Suter, G., Didon, J., Guardia, P., Dresnay, R., Medioni, R., Choubert, G., Faure-Muret, A., 1985. Carte Géologique Du Maroc Au 1/1 000 000. Notes et Mémoires Du Service Géologique Du Maroc, Feuille Nord, 260 (2): 1–96.

Hoschke, T., 2011. Geophysical signatures of copper-gold porphyry and epithermal gold deposits, and implications for exploration (p. 47). ARC Centre of Excellence in Ore Deposits, University of Tasmania.

Hyvärinen, A., 2022. Independent Component Analysis of Images. In: Jaeger, D., Jung, R. (Eds) Encyclopedia of Computational Neuroscience. Springer, New York, NY, 1665–1669.

Hyvärinen, A., Yutaka, K., 2001. Independent Component Analysis for Non-Normal Factor Analysis. In New Developments in Psychometrics, 469–656. In New Developments in Psychometrics: Proceedings of the International Meeting of the Psychometric Society IMPS2001. Osaka, Japan, (pp. 649-656). Tokyo: Springer Japan.

Hyvärinen, A., Oja, E., 2000. Independent Component Analysis: Algorithms and Applications. Neural Networks, 13 (4-5): 411–30. https://doi.org/10.1016/S0893-6080(00)00026-5

Ikenne, M., Söderlund, U., Ernst, R. E., Pin, C., Youbi, N., El Aouli, E. H., Hafid, A., 2017. A c. 1710 Ma mafic sill emplaced into a quartzite and calcareous series from Ighrem, Anti-Atlas–Morocco: evidence that the Taghdout passive margin sedimentary group is nearly 1 Ga older than previously thought. Journal of African Earth Sciences, 127, 62-76.

Ivan, M., 1986. Upward Continuation of Unevenly Spaced Potential Field Data Using Equivalent Sources. Geophysics, 32(1), 31-42

Jacobsen, B.H., 1987. A Case for Upward Continuation as a Standard Separation Filter for Potential-Field Maps. Geophysics, 52 (8): 1138–48. https://doi.org/10.1190/1.1442378

Jébrak, M., Marcoux, É., 2008. Géologie des ressources minérales (p. 667).

Jébrak, M., É Marcoux, M. Nasloubi, and M. Zaharaoui. 1998. From Sandstone- to Carbonate-Hosted Strata Bound Deposits: An Isotope Study of Galena in the Upper-Moulouya District (Morocco). Mineralium Deposita, 33 (4): 406–15. https://doi.org/10.1007/s001260050158.

Karaoui, B., Breitkreuz, C., Mahmoudi, A., Youbi, N., Hofmann, M., Gärtner, A., Linnemann, U., 2015. U-Pb Zircon Ages from Volcanic and Sedimentary Rocks of the Ediacaran Bas Draâ Inlier (Anti-Atlas Morocco): Chronostratigraphic and Provenance Implications. Precambrian Research, 263: 43–58. https://doi.org/10.1016/j.precamres.2015.03.003.

Keppie, J. D., Nance, R. D., Murphy, J. B., Dostal, J., 2003. Tethyan, Mediterranean, and Pacific analogues for the Neoproterozoic–Paleozoic birth and development of peri-Gondwanan terranes and their transfer to Laurentia and Laurussia. Tectonophysics, 365 (1-4), 195-219

Kirkwood, T.B.L., 1979. Geometric Means and Measures of Dispersion. Biometrics, 35 (4): 908–909.

Kósaka, H., and Wakita, K., 1978. Some Geologic Features of the Mmnut Porphyry Copper Deposit, Sabah, Malaysia. Economic Geology, 73: 618–27.

Kouyaté, D., Söderlund, U., Youbi, N., Ernst, R.E., Hafid, A., Ikenne, M., Soulaimani, A., Bertrand, H., El Janati, M., Chaham, K R., 2013. U-Pb Baddeleyite and Zircon Ages of 2040Ma, 1650Ma and 885Ma on Dolerites in the West African Craton (Anti-Atlas Inliers): Possible Links to Break-up of Precambrian Supercontinents. Lithos, 174: 71–84. https://doi.org/10.1016/j.lithos.2012.04.028.

Kovesi, P., 1997. Symmetry and Asymmetry from Local Phase. In In Tenth Australian Joint Conference on Artificial Intelligence, 190: 2–4.

Lam, L., Lee, S.W., 1992. Thinning Methodologies—A Comprehensive Survey. IEEE Trans. Pattern Anal. Mach. Intelligence, 14 (9): 61–69.

Leblanc, M., and Lancelot, J. R., 1980. Interprétation géodynamique du domaine pan-africain (Précambrien terminal) de l'Anti-Atlas (Maroc) à partir de données géologiques et géochronologiques. Canadian Journal of Earth Sciences, 17(1), 142-155.

Leblanc, M., 1975. Ophiolites précambriennes et gites arseniés de cobalt: Bou Azzer (Maroc). These Doctorat d'Etat, Faculte des Science Paris VI, Memoires Centre Geologique et Geophysique.

Lee, C.T.A., and Tang., M., 2020. How to Make Porphyry Copper Deposits. Earth and Planetary Science, Letters, 529 (115868).

Le Heron, D. P., 2007. Late Ordovician glacial record of the Anti-Atlas, Morocco. Sedimentary Geology, 201 (1-2), 93-110.

Letsch, D., Large, S., Buechi, M.W., Winkler, W., Quadt., A.V., 2018. Ediacaran Glaciations of the West African Craton – Evidence from Morocco. Precambrian Research, 310: 17–18.

Levresse, G., 2001. Contribution to the Establishment of a Genetic Model of the Imiter (Ag-Hg), Bou Madine (Pb-Zn-Cu-Ag-Au), Bou Azzer (Co-Ni-As-Au-Ag) Deposits in the Moroccan Anti-Atlas. Doctoral dissertation, PhD Thesis.

Levresse, G., Cheilletz, A., Gasquet, D., Reisberg, L., Deloule, E., Marty, B., Kyser, K., 2004. Osmium, Sulphur, and Helium Isotopic Results from the Giant Neoproterozoic Epithermal Imiter Silver Deposit, Morocco: Evidence for a Mantle Source. Chemical Geology, 207 (1–2): 59–79. https://doi.org/10.1016/j.chemgeo.2004.02.004.

Liégeois, J P., Fekkak, A., Bruguier, O., Errami, E., Ennih, N., 2006. The Lower Ediacaran (630–610 Ma) Saghro Group: An Orogenic Transpressive Basin Development during the Early Metacratonic Evolution of the Anti-Atlas (Morocco). In In IGCP485 4th Meeting, Algiers, 57:1/1.

Liégeois, J. P., Navez, J., Hertogen, J., Black, R., 1998. Contrasting Origin of Post-Collisional High-K Calc-Alkaline and Shoshonitic versus Alkaline and Peralkaline Granitoids. The Use of Sliding Normalization. Lithos, 45 (1–4): 1–28. https://doi.org/10.1016/S0024-4937(98)00023-1.

Lindgren, W., 1922. A Suggestion for the Terminology of Certain Mineral Deposits. Economic Geology, 17: 292–94.

Linnemann, U., Ovtcharova, M., Schaltegger, U., Gärtner, A., Hautmann, M., Geyer, G., Vickers-Rich, P., Rich, T., Plessen, B., Hofmann, M., Zieger, J., Krause, R., Kriesfeld, L., and Smith, J., 2019, New high-resolution age data from the Ediacaran-Cambrian boundary indicate rapid, ecologically driven onset of the Cambrian explosion: Terra

Nova, v. 31, no. 1, p. 49–58, https://doi.org/10.1111/ter.12368.

Linnemann, U., Gerdes, A., Hofmann, M., Marko, L., 2014. The Cadomian Orogen: Neoproterozoic to Early Cambrian Crustal Growth and Orogenic Zoning along the Periphery of the West African Craton-Constraints from U-Pb Zircon Ages and Hf Isotopes (Schwarzburg Antiform, Germany). Precambrian Research, 244 (1): 236–78. https://doi.org/10.1016/j.precamres.2013.08.007.

Lonergan, L., White, N., 1997. Origin of the Betic-Rif Mountain belt. Tectonics, 16(3), 504-522

Lowell, J.D., Guilbert, J.M. 1970. Lateral and Vertical Alteration-Mineralization Zoning in Porphyry Ore Deposit. Economic geology, 65(4), 373-408.

Macnae, J., 1995. Applications of geophysics for the detection and exploration of kimberlites and lamproites. Journal of Geochemical Exploration, 53(1-3), 213-243.

Maloof, A.C., Schrag, D.P., Crowley, J.L., Bowring, S.A. 2005. An Expanded Record of Early Cambrian Carbon Cycling from the Anti-Atlas Margin, Morocco. Journal of Earth Sciences, 42: 2195–2216.

Mamouch, Y., Attou, A., Miftah, A., Ouchchen, M., Dadi, B, Moussaid, A., Et-tayea,Y., El Azmi, M., Boualoul, M., 2023. Aeromagnetic Data of the Kelâat M'Gouna Inlier (Jbel Saghro, Eastern Anti-Atlas, Morocco): Geotectonic and Mining Implications. Journal of African Earth Sciences, 197: 104744. https://doi.org/10.1016/j.jafrearsci.2022.104744.

Mamouch, Y., Attou, A., Miftah, A., Ouchchen, M., Dadi, B., Achkouch, L., Et-Tayea, Y., Allaoui, A., Boualoul, M., Randazzo, G., Lanza, S., Muzirafuti, A., 2022. Mapping of Hydrothermal Alteration Zones in the Kelâat M'Gouna Region Using Airborne Gamma-Ray Spectrometry and Remote Sensing Data: Mining Implications (Eastern Anti-Atlas,

Maniar, P.D., and Piccoli, P.M., 1989. Tectonic Discrimination of Granitoids. Geological Society of America Bulletin, 101 (5): 635–43.

Marcoux, E., Wadjinny, A., 2005. Le Gisement Ag-Hg de Zgounder (Jebel Siroua, Anti-Atlas, Maroc): Un Épithermal Néoprotérozoïque de Type Imiter. Comptes Rendus - Geoscience, 337 (16): 1439–46. https://doi.org/10.1016/j.crte.2005.09.005.

Mao, J., Zhang, J., Pirajno, F., Ishiyama, D., Su, H., Guo, C., Chen, Y., 2011. Porphyry Cu-Au-Mo-Epithermal Ag-Pb-Zn-Distal Hydrothermal Au Deposits in the Dexing Area, Jiangxi Province, East China-A Linked Ore System. Ore Geology Reviews, 43 (1): 203–16. https://doi.org/10.1016/j.oregeorev.2011.08.005.

Menezes, P-T.L., Barbosa, V-C. F., Pereira, R.M., Salomão, M., 2022. The Multiscale Edge Detection Filter Applied to Airborne Electromagnetic Data Interpretation: A Case Study at the Rio Das Velhas Greenstone Belt, Quadrilátero Ferrífero, Brazil. Journal of South American Earth Sciences, 11 (103966).

Meng, X., Kleinsasser, J. M., Richards, J. P., Tapster, S. R., Jugo, P. J., Simon, A.C., Kontac, D.J., Robb, L., Bybee, G.M., Marsh, J.H., Stern, R. A., 2021. Oxidized sulfur-rich arc magmas formed porphyry Cu deposits by 1.88 Ga. Nature Communications, 12(1), 2189.

Meyer, C., and Hemley, J.J., 1967. Wall Rock Alteration. In Geochemistry of Hydrothermal Ore Deposits, 166–235.

Michard, A., Driouch, Y., Kuiper, Y. D., Caby, R., Farah, A., Ouanaimi, H., Soulimani, A.,

Chanou, M.C., Saddiqi, O., 2023. The Variscan belts of north-west Africa: An African legacy to the Wilson Cycle concept. Journal of African Earth Sciences, 208, 105042.

Michard, A., Soulaimani, A., Hoepffner, C., Ouanaimi, H., Baidder, L., Rjimati, E. C., Saddiqi, O., 2010. The south-western branch of the Variscan Belt: evidence from Morocco. Tectonophysics, 492(1-4), 1-24.

Michard, A. C. A. L. A., Hœpffner, C., Soulaimani, A., Baidder, L., 2008. The Variscan belt. In Continental evolution: The geology of Morocco: Structure, stratigraphy, and tectonics of the Africa-Atlantic-Mediterranean triple junction (pp. 65-132). Berlin, Heidelberg: Springer Berlin Heidelberg.

Middlemost, E.A.K., 1994. Naming Materials in the Magma/Igneous Rock System. Earth Science Reviews, 37 (3–4): 215–24. https://doi.org/10.1016/0012-8252(94)90029-9.

Mifdal, A., and Peucat, J.J., 1985. Datation U/Pb et Rb/Sr Du Volcanisme Acide de l'Anti-Atlas Marocain et Du Socle Sous-Jacent Dans La Région de Ouarzazate; Apport Au Problème de La Limite Précambrien-Cambrien. Sci. Géol, no. Strasbourg 38,: 185–200.

Miftah, A., El Azzab, D., Attou, A., Rachid, A., Ouchchen, M., Soulaimani, A., Soulaimani, S., Manar, A., 2021b. Combined Analysis of Helicopter-Borne Magnetic and Stream Sediment Geochemical Data around an Ancient Tiouit Gold Mine (Eastern Anti-Atlas, Morocco): Geological and Mining Interpretations. Journal of African Earth Sciences, 175 : 1–12. https://doi.org/10.1016/j.jafrearsci.2020.104093.

Miller, H.G, and V Singh., 1994. Potential Field Tilt—A New Concept for Location of Potential Field Sources. Journal of Applied Geophysics, 32: 213–17.

Mining Research and Participation Office., 1976.

Montsion, R. M., Perrouty, S., Lindsay, M. D., Jessell, M. W., Frieman, B. M., 2021. Mapping structural complexity using geophysics: A new geostatistical approach applied to greenstone belts of the southern Superior Province, Canada. Tectonophysics, 812, 228889.

Morris, G. A., Larson, P. B., Hooper, P. R., 2000. Subduction Style Magmatism in a Non-Subduction Setting: The Colville Igneous Complex, NE Washington State, USA. Journal of Petrology, 41 (1): 43–67. https://doi.org/10.1093/petrology/41.1.43.

Mouttaqi, A, Rjimati, E.C., Maacha, L., Michard, A., Soulaimani, A., Ibouh, H., 2011. Main Mines of Morocco. New Geological and Mining Guidebooks of Morocco 9: 3–376.

Murphy, J. B., and Nance, R. D.,1989. Model for the evolution of the Avalonian-Cadomian belt. Geology, 17 (8), 735-738.

Nabighian, M.N., Grauch, V.J.S., Hansen, R.O., LaFehr, T.R., Li, Y., Peirce, J.W., and M.E Phillips, J.D., Ruder, M.E., 2005. The Historical Development of the Magnetic Method in Exploration. Geophysics, 70 (6) : 33–61. https://doi.org/10.1190/1.2133784

Nance , R.D., Guti errez-Alonso, G., Keppie, J. D., R., Linnemann, U., Murphy, J. B., Quesada, C., Strachan, A., Woodcock, N H., 2012. A Brief History of the Rheic Ocean. Geoscience Frontiers, 3 (2): 125–35.

O'Connor, E. A., 2010. Geology of the Drâa, Kerdous, and Boumalne Districts, Anti-Atlas, Morocco. British Geological Survey, Keyworth, Nottingham, 310.

Osinowo, O.O., Alumona, K., Olayinka, A.I., 2020. Analyses of High Resolution

Aeromagnetic Data for Structural and Porphyry Mineral Deposit Mapping of the Nigerian Younger Granite Ring Complexes, North-Central Nigeria.J. Afr. Earth Sci 162, 103705. https://doi.org/10.1016/j.jafrearsci.2019.103705

Ouabid, M., and Garrido, J.C., 2023. Widespread Cadomian–Pan-African Ediacaran Magmatism across the Moroccan Meseta: Implication for the Geodynamic Evolution of the NW Gondwana Margin. Precambrian Research, 387 , 106992. https://doi.org/10.1016/j.precamres.2023.106992.

Ouchchen, M., Boutaleb, S., Abia, E H., El Azzab, D., Abioui, M., Mickus, K.L., Miftah, A., Echogdali, F Z., Dadi, B., 2021. Structural Interpretation of the Igherm Region (Western Anti Atlas, Morocco) from an Aeromagnetic Analysis: Implications for Copper Exploration. Journal of African Earth Sciences, 176 : 104140. https://doi.org/10.1016/j.jafrearsci.2021.104140.

Pearce, J.A., 1996. Petrogenetic Implications of Ti, Zr, Y, and Nb Variations in Volcanic Rocks. Contributions to Mineralogy and Petrology, 69: 33–47.

Pearce, J. A., Harris, N. B., Tindle, A. G., 1984. Trace Element Discrimination Diagrams for the Tectonic Interpretation of Granitic Rocks. Journal of Petrology, 25 (4): 956–83. https://doi.org/10.1093/petrology/25.4.956.

Pearce, J.A., 1983. Role of the Sub-Continental Lithosphere in Magma Genesis at Active Continental Margins. In Continental Basalts and Mantle Xenoliths, 230-249.

Pearson, M.F., Clark, K.F., and Porter, E.W., 1988. Mineralogy, Fluid Characteristics, and Silver Distribution at Real de Angeles, Zacatecas, Mexico. Economic Geology, 83: 1737–59.

Pei, N. I., Zhe, C. H. I., Junyi, P. A. N., 2020. An integrated investigation of ore-forming fluid evolution in porphyry and epithermal deposits and their implication on exploration. Earth Science Frontiers, 27(2), 60.

Pelleter, E., Cheilletz, A., Gasquet, D., Mouttaqi, A., Annich, M., Camus, Q., Deloule, E., Ouazzani, L., Bounjama, H., Ouchtouban, L., 2016. U/Pb Ages of Magmatism in the Zgounder Epithermal Ag–Hg Deposit, Sirwa Window, Anti-Atlas, Morocco. In Mineral Deposits of North Africa (pp. 143-165). Cham: Springer International Publishing.

Pereira, M. F., El Houicha, M., Chichorro, M., Armstrong, R., Jouhari, A., El Attari, A., Ennih, N., Silva, J. B., 2015. Evidence of a Paleoproterozoic basement in the Moroccan Variscan belt (Rehamna massif, western Meseta). Precambrian Research, 268, 61-73

Perrot, M., Tremblay, A., David, J., 2017. Detrital Zircon U-Pb Geochronology of the Magog Group, Southern Quebec - Stratigraphic and Tectonic Implications for the Quebec Appalachians. American Journal of Science, 317 (10): 1049–94. https://doi.org/10.2475/10.2017.01.

Petrella, L., Williams-Jones, A. E., Goutier, J., Walsh, J., 2014. The nature and origin of the rare earth element mineralization in the Misery syenitic intrusion, northern Quebec, Canada. Economic Geology, 109 (6), 1643-1666. https://doi.org/10.2113/econgeo.109.6.1643

Piqué, A., 2003. Evidence for an important extensional event during the Latest Proterozoic and Earliest Paleozoic in Morocco. Comptes rendus. Géoscience, 335 (12), 865-868.

Piqué, A., Soumaimani, 1., Hoepffner, C., Bouabdeli, M., Laville, Edgard, M., Chalouan, A.,

2001. Géologie du Maroc. Earth and Patrimony collection, Ediotion GEODS, 287p.

Platt, J. P., Behr, W. M., Johanesen, K., Williams, J. R., 2013. The Betic-Rif arc and its orogenic hinterland: a review. Annual Review of Earth and Planetary Sciences, 41(1), 313-357.

Pouclet, A., El Hadi, H., Álvaro, J. J., Bardintzeff, J. M., Benharref, M., Fekkak, A., 2018. Review of the Cambrian volcanic activity in Morocco: geochemical fingerprints and geotectonic implications for the rifting of West Gondwana. International Journal of Earth Sciences, 107 (6), 2101-2123.

Pour, A.B., and Hashim, L., 2012. The Application of ASTER Remote Sensing Data to Porphyry Copper and Epithermal Gold Deposits. Ore Geology Reviews, 44 (1–9).

Raeisi, D., Babazadeh, S., Long, L. E., Zhao, M., Cottle, J. M., Nayebi, N., Modabberi, S., 2024. Geochemical and Isotopic Signatures, and Zircon U-Pb Ages of the Oldest Known Intrusive Rocks Associated with Porphyry Cu Deposits in the Central Urumieh–Dokhtar Magmatic Arc, Iran. Journal of Geochemical Exploration, 256: 107366. https://doi.org/10.1016/j.gexplo.2023.107366.

Ransome, F.L., 1907. The Association of Alunite with Gold in the Goldfield Ditrict, Nevada. Economic Geology, 2: 667–92.

Reid, A.B., Allsop, J.M., Granser, H., Millett, A.J., Somerton, I.W., 1990. Magnetic Interpretation in Three Dimensions Using Euler Deconvolution. Geophysics 55 (1) : 80–91. https://doi.org/10.1190/1.1442774

Richards, J.P., 2003. Tectono-Magmatic Precursors for Porphyry Cu-(Mo-Au) Deposit Formation. Economic Geology, 98: 1515−1533.

Richards, J.P., 2009. Post Subduction Porphyry Cu-Au and Epithermal Au Deposits: Products of Remelting of Subduction-Modified Lithosphere. Geology, 37: 247−250.

Robert, B., Besse, J., Blein, O., Greff-Lefftz, M., Baudin, T., Lopes, F., Meslouh, S., Belbadaoui, M., 2017. Constraints on the Ediacaran Inertial Interchange True Polar Wander Hypothesis: A New Paleomagnetic Study in Morocco (West African Craton). Precambrian Research, 295: 90–116. https://doi.org/10.1016/j.precamres.2017.04.010.

Sailhac, P., 1999. Analyse Multiéchelle et Inversion de Données Géophysiques En Guyane Française. Doctoral dissertation, Institut de physique du globe, Paris.

Salem, A., Williams, S., Fairhead, J.D., Ravat, D., Smith, R., 2007. Tilt-Depth Method: A Simple Depth Estimation Method Using First-Order Magnetic Derivative. Lead. Edge, 26 (12) : 1502–1505. https://doi.org/10.1190/1.2821934

Samson, S. D., Inglis, J. D., D'lemos, R. S., Admou, H., Blichert-Toft, J., Hefferan, K., 2004. Geochronological, geochemical, and Nd–Hf isotopic constraints on the origin of Neoproterozoic plagiogranites in the Tasriwine ophiolite, Anti-Atlas orogen, Morocco. Precambrian Research, 135(1-2), 133-147

Saquaque, A., Admou, H., Cisse, A., Benyousef, A., Reuber, I., 1989. Les intrusions calco-alcalines de la boutonnière de Bou Azzer-El Graara (Anti-Atlas, Maroc): marqueurs de la déformation panafricaine majeure dans un contexte de collision d'arc. CR Acad. Sci. Paris, 308 (14), 1279-1283.

Sassioui, S., Aarab, A., Benyas, K., Idrissi, A., Lakhloufi, A., Saidi, O., Courba, S., Larabi,

A., 2024. Geophysical Analysis Using High-Resolution Aeromagnetic Data of Jbel Ougnat, the Moroccan Eastern Anti-Atlas: Insights into Geological Structures and Tectonic Events. Bulletin of Geophysics and Oceanography, 65 (1): 35–52. https://doi.org/10.4430/bgo00435.

Schulte, B., Boger, S.D., Benziane, F., Yazidi, A., Fanning, C. M., 2022. The Ouarzazate Supergroup and Its Plutonic Keel: The Relicts of an Ediacaran Silicic Large Igneous Province in North Africa.Journal of the Geological Society, 179 (5). https://doi.org/10.1144/jgs2021-114.

Schwarz, E.J., 1991. Schwarz, E. J. (1991). Magnetic expressions of intrusions including magnetic aureoles. Tectonophysics, 192 (1-2), 191-200. https://doi.org/10.1016/0040-1951(91)90256-R.

Sébrier, M., Siame, L., Zouine, E. M., Winter, T., Missenard, Y., Leturmy, P., 2006. Active tectonics in the moroccan high atlas. Comptes Rendus Geoscience, 338 (1-2), 65-79. https://doi.org/10.1016/j.crte.2005.12.001

Seedorf, E., Dilles, J.D., Proffett, J.M., Einaudi, Jr., Zurcher, M.T., Stavast, M.D., Johnson, W.J.A., Barton, D.A., 2005. Porphyry Deposits: Characteristics and Origin of Hypogene Features. In Economic Geology, 251–98.

Seequent., 2019. Oasis Montaj, Software to Visualize, Analyze, and Integrate Geophysical and Geoscientific Data.

Shives, R.B.K., Charbonneau, B.W., Ford, K.L., 1997. The Detection of Potassic Alteration by Gamma-Ray Spectrometry—Recognition of Alteration Related to Mineralization. In Proceedings of Exploration 97: Fourth Decennial International Conference on Mineral Exploration" Edited by A.G. Gubins, 741–752

Shives, R.B.K., Ford, K.L., Charbonneau, B.W., 1995. Applications of Gamma- Ray Spectrometric/Magnetic/VLF-EM Surveys—Workshop Manual; Geological Survey of Canada, Open File 3061.

Sillitoe, R. H., 2025. Precambrian subduction onset: a porphyry copper perspective. Journal of the Geological Society, 182 (4), jgs2025-046.

Sillitoe, R.H., 2010. Porphyry Copper Systems. Economic Geology ,105 (1): 3–41. https://doi.org/10.2113/gsecongeo.105.1.3.

Sillitoe, R.H., 2008. Major Gold Deposits and Belts of the North and South American Cordillera: Distribution, Tectonomagmatic Settings, and Metallogenic Considerations. Economic Geology, 103 (4): 663–87. https://doi.org/10.2113/gsecongeo.103.4.663.

Sillitoe, R.H., and Perelló, J., 2005. Andean Copper Province: Tectono-Magmatic Settings, Deposit Types, Metallogeny, Exploration, and Discovery. Economic Geology, 100th anni: 845−890.

Sillitoe, R.H Hedenquist, J., 2003. Linkages between Volcanotectonic Settings, Ore-Fluid Compositions, and Epithermal Precious Metal Deposits. Volcanic, Geothermal, and Ore-Forming Fluids, 315–43. https://doi.org/10.5382/sp.10.16.

Sillitoe, R.H., 1980. Cauldron Subsidence as a Possible Inhibitor of Porphyry Copper Formation: Mining Geology, Special Issue 8: 85−93.

Sillitoe, R.H., Halls, C., and Grant, J.N. 1975. "Porphyry Tin Deposits in Bolivia." Economic

Geology 70: 913–27.

Sillitoe, Richard H. 1972. “A Plate Tectonic Model for the Origin of Porphyry Copper Deposits.” Economic Geology 67 (2): 184–97. https://doi.org/10.2113/gsecongeo.67.2.184.

Simancas, J. F., Azor, A., Martínez-Poyatos, D., Tahiri, A., El Hadi, H., González-Lodeiro, F., Pérez-Estaún, A., Carbonell, R., 2009. Tectonic relationships of Southwest Iberia with the allochthons of Northwest Iberia and the Moroccan Variscides. Comptes Rendus Geoscience, 341(2-3), 103-113.

Simmonds, V., Mathur, R., Selby., D., 2019. Rhenium Abundance in Molybdenites: A Case Study on Vein-Type Cu-Mo-Au Mineralization in the Qarachilar Area, Sungun Porphyry Cu and Siah Kamar Porphyry Mo de Pos Its, NW Iran. Geological Quarterly, 63 (3): 478–492. http://dx.doi.org/10.7306/gq.1488.

Simmons, S. F., White, N. C., John, D. A., 2005. Geological Characteristics of Epithermal Precious and Base Metal Deposits. Economic Geology, no. 1: 485–522. https://doi.org/10.5382/av100.16.

Sinclair, W.D., 2007. Porphyry Deposits. In Understanding Mineral Deposits, 353–413. https://doi.org/10.1007/978-94-011-3925-0_8.

Sláma, J., Košler, J., Condon, D. J., Crowley, J. L., Gerdes, A., Hanchar, J. M., Horstwood, MS.A., Morris, G.A., Nasdala, L., Norberg, N., Schaltegger, U., Schoene, B., Tubrett, N.M., Whitehouse, M. J., 2008. Plešovice Zircon - A New Natural Reference Material for U-Pb and Hf Isotopic Microanalysis. Chemical Geology, 249 (1–2): 1–35. https://doi.org/10.1016/j.chemgeo.2007.11.005.

Söderlund, U., Ibanez-Mejia, M., El Bahat, A., Ernst, R. E., Ikenne, M., Soulaimani, A., Youbi, N., Hafid, A., 2013. Reply to Comment on “U–Pb baddeleyite ages and geochemistry of dolerite dykes in the Bas-Drâa inlier of the Anti-Atlas of Morocco: Newly identified 1380 Ma event in the West African Craton” by André Michard and Dominique Gasquet. Lithos, 174, 101-108.

Soulaimani, A., Chakiri, S., Soulaimani, S., Bejjaji, Z., Miftah, A., Manar, A., 2023. Gradiometry Processing Techniques for Large-Scale of Aeromagnetic Data for Structural and Mining Implications: The Case Study of Bou Azzer Inlier, Central Anti-Atlas, Morocco. Applied Sciences, 13 (17), 9962. https://doi: 10.3390/app13179962

Soulaimani, A., Chakiri, S., Soulaimani, S., Manar, A., Bejjaji, Z., Miftah, A., Zerdeb, M A., Zidane, Y., Boualoul, M., Muzirafuti, A., 2022. Semi-Automatic Image Processing System of Aeromagnetic Data for Structural and Mining Investigations (Case of Bou Azzer Inlier, Central Anti-Atlas, Morocco). Applied Sciences, 12 (21). 11270. https://doi.org/10.3390/app122111270.

Soulaimani, A., Ouanaimi, H., Saddiqi, O., Baidder, L., Michard, A., 2018. The anti-atlas panafrican belt (Morocco): overview and pending questions. Comptes Rendus. Géoscience, 350 (6), 279-288. https://doi.org/10.1016/j.crte.2018.07.002.

Soulaimani, A., Michard, A., Ouanaimi, H., Baidder, L., Raddi, Y., Saddiqi, O., Rjimati, E.C., 2014. Late Ediacaran-Cambrian Structures and Their Reactivation during the Variscan and Alpine Cycles in the Anti-Atlas (Morocco). Journal of African Earth Sciences, 98: 94–112. https://doi.org/10.1016/j.jafrearsci.2014.04.025.

Soulaimani, A., Jaffal, M., Maacha, L., Kchikach, A., Najine, A., Saidi, A., 2006. Magnetic Modelling of the Bou Azzer-El Graara Ophiolite (Central Anti-Atlas, Morocco). Geodynamic Implications of the Panafrican Reconstruction. Comptes Rendus - Geoscience, 338 (3): 153–60. https://doi.org/10.1016/j.crte.2005.10.001.

Sparkes, G. W., Ferguson, S. A., Layne, G. D., Dunning, G. R., O'Brien, S. J., Langille, A., 2016. The Nature and Timing of Neoproterozoic High-Sulphidation Gold Mineralization from the Newfoundland Avalon Zone : Insights from New u – Pb Ages , Ore Petrography and Spectral Data from the Hickey's Pond Prospect. Newfoundland and Labrador Department of Natural Resources Geological Report 16- 1(Geological Survey): 91–116.

Sparkes, G W., and G R Dunning., 2014. Late Neoproterozoic Epithermal Alteration and Mineralization in the Western Avalon Zone: A Summary of Mineralogical Investigations and New U/Pb Geochronological Results. Current Research, 99–128.

Steven, T.A., and Ratte, J .C., 1960. Geology and ore deposit of the Summitville district, San Juan Mountains, Colorado: U.S. Geol. Survey, Prof. Paper 343, 70 p

Stoffregen, R., 1987. Genesis of Acid-Sulfate Alteration and Au-Cu-Ag Mineralization at Summitville, Colorado. Economic Geology, 82: 1575−1591.

Sun, W., Huang, R. F., Li, H., Hu, Y. B., Zhang, C. C., Sun, S. J., Zhang, L.P., Ding, X., Li, C-Y., Zartman, R.E., Ling, M.X., 2015. Porphyry Deposits and Oxidized Magmas. Ore Geology Reviews, 65 (P1): 97–131. https://doi.org/10.1016/j.oregeorev.2014.09.004.

Sylvester, P.J. 1994. Archean Granite Plutons. Developments in Precambrian Geology, 11 (C): 261–314. https://doi.org/10.1016/S0166-2635(08)70225-1.

Tapia, J., Townley, B., Córdova, L., Poblete, F., Arriagada, C., 2016. Hydrothermal alteration and its effects on the magnetic properties of Los Pelambres, a large multistage porphyry copper deposit. Journal of Applied Geophysics, 132, 125-136. https://doi.org/10.1016/j.jappgeo.2016.07.005

Tazi, M J., El Azzab, D., Charroud, M., Jabrane, O., Ouahzizi, Y., Zahour, R., Halidou Amadou, A., 2022. Identification of Potential Mineral Exploration Targets from the Interpretation of Aeromagnetic Data Covering the Sirwa Region (Central Anti-Atlas, Morocco). Scientific African, 17: e01351. https://doi.org/10.1016/j.sciaf.2022.e01351.

Thomas, R. J., Fekkak, A., Ennih, N., Errami, E., Loughlin, S. C., Gresse, P. G., Chevallier, L. P., Liégeois, J. P., 2004. A New Lithostratigraphic Framework for the Anti-Atlas Orogen, Morocco. Journal of African Earth Sciences, 39 (3–5): 217–26. https://doi.org/10.1016/j.jafrearsci.2004.07.046.

Thomas, R.J., Chevallier, L.P., Gresse, P.G.., Harmer, R.E., Eglington, B.M., Armstrong, R.A., De Beer, C.H., Martini., J.E.J., de Kock, G.S., Macey, P.H., Ingram, B.A., 2002. Precambrian Evolution of the Sirwa Window, Anti-Atlas Orogen, Morocco. Precambrian Research, 118 (1–2): 1–57. https://doi.org/10.1016/S0301-9268(02)00075-X

Tobi, A., Essalhi, M., Es-Sabbar, S., Qarqori, K., Bouzekraoui, A., Ait Baha, M., Faou, A., El Azmi, D., 2025. Application of High-Resolution Gravity and Magnetic Data for Fe-Mn-Pb Mineralization Prospecting in Jbel Skindis, Eastern High Atlas, Morocco. Economic and Environmental Geology, 58 (1): 17–31. https://doi.org/10.9719/EEG.2025.58.1.17

Toummite, A., Liegeois, J.P., Gasquet, D., Bruguier, O., Beraaouz, E.H., Ikenne, M., 2012.

Field, Geochemistry and Sr-Nd Isotopes of the Pan-African Granitoids from the Tifnoute Valley (Sirwa, Anti-Atlas, Morocco): A Post-Collisional Event in a Metacratonic Setting. Mineralogy and Petrology, 107 (5): 739–63. https://doi.org/10.1007/s00710-012-0245-3.

Triantafyllou, A., Berger, J., Baele, J.M., Mattielli, N., Ducea, M.N., Sterckx, S., Samson, S., Hodel, F., Ennih, N., 2020. Episodic Magmatism during the Growth of a Neoproterozoic Oceanic Arc (Anti-Atlas, Morocco). Precambrian Research, 339, 105610.

Triantafyllou, A., Berger, J., Baele, J. M., Diot, H., Ennih, N., Plissart, G., Monnier, C., Watlet, A., Bruguier, O., Spagna, P., Vandycke, S., 2016. The Tachakoucht-Iriri-Tourtit Arc Complex (Moroccan Anti-Atlas): Neoproterozoic Records of Polyphased Subduction-Accretion Dynamics during the Pan-African Orogeny. Journal of Geodynamics, 96: 81–103. https://doi.org/10.1016/j.jog.2015.07.004.

Tuduri, J., Chauvet, A., Barbanson, L., Bourdier, J.L., Labriki, M., Ennaciri, A., Badra, L., duboit, M., Ennaciri-Leloix, C., Sizaret, S., Maacha, L., 2018b. The Jbel Saghro Au(–Ag, Cu) and Ag–Hg Metallogenetic Province: Product of a Long-Lived Ediacaran Tectono-Magmatic Evolution in the Moroccan Anti-Atlas. Minerals, 8 (12). https://doi.org/10.3390/min8120592

Tuduri, J., Chauvet, A., Barbanson, L., Labriki, M., Dubois, M., Trapy, P.-H., Lahfid, A., Poujol, M. Melleton, J., Badra, L., 2018a. Structural Control, Magmatic-Hydrothermal Evolution and Formation of Hornfels-Hosted, Intrusion-Related Gold Deposits: Insight from the Thaghassa Deposit in Eastern Anti-Atlas, Morocco." Ore Geol 97: 171–198.

Vallée, M.A., Morris, W.A., Perrouty, S., Lee, R.G., Wasyliuk, K., King, J.J., Ansdell, K., Mir, R., Shamsipour, P., Farquharson, C.G., Chouteau, M., Enkin, R.J., Smith, R.S., 2019. Geophysical Inversion Contributions to Mineral Exploration: Lessons from the Footprints. Journal of Earth Sciences, 56: 525–543.

Van Staal, C. R., Barr, S. M., Waldron, J. W., Schofield, D. I., Zagorevski, A., White, C. E., 2021. Provenance and Paleozoic tectonic evolution of Ganderia and its relationships with Avalonia and Megumia in the Appalachian-Caledonide orogen. Gondwana Research, 98, 212-243

Verduzco, B., 2004. New Insights into Magnetic Derivatives for Structural Mapping. Lead. Edge, 23 (2): 116–19. https://doi.org/10.1190/1.1651454

Vermeesch, P., 2018. IsoplotR: A Free and Open Toolbox for Geochronology. Geoscience Frontiers, 9 (5): 1479–93. https://doi.org/10.1016/j.gsf.2018.04.001.

Villeneuve, M., and Cornée, J. J., 1994. Structure, evolution and paleogeography of the West African craton and bordering belts during the Neoproterozoic. Precambrian Research, 69 (1-4), 307-326.

Voudouris, P., Mavrogonatos, C., Spry, P. G., Baker, T., Melfos, V., Klemd, R., Haase, K., Repstock, A, Djiba, A., Bismayer, U., Trantola, A., Scheffer, C., Moritz, R., Kouzmanov, K., Alfiferis, A., Papvasiliou, K., Schaarschmidt, A., Glanopoulos, E., Galanos, E., Kolodziejczyk, J., 2019. Porphyry and Epithermal Deposits in Greece: An Overview, New Discoveries, and Mineralogical Constraints on Their Genesis. Ore Geology Reviews, 107: 654–91. https://doi.org/10.1016/j.oregeorev.2019.03.019.

Walsh, G. J., Benziane, F., Aleinikoff, J. N., Harrison, R. W., Yazidi, A., Burton, W. C., Quick, J.E., Saadane, A., 2012. Neoproterozoic Tectonic Evolution of the Jebel Saghro

and Bou Azzer-El Graara Inliers, Eastern and Central Anti-Atlas, Morocco. Precambrian Research, 216–219: 23–62. https://doi.org/10.1016/j.precamres.2012.06.010.

Walsh, G.J., Aleiniko, J.N., Benziane, F., Yazidi, A., Armstrong, T.R., 2002. U–Pb Zircon Geochronology of the Palaeoproterozoic Tagragra de Tata Inlier and Its Neoproterzoic Cover, Western Anti-Atlas, Morocco. Precambrian Research, 117: 11–20.

Wang, X. Q., and Ji, F. B., 2024. Petrogenesis and Metallogenic Implications of Eocene–Oligocene Magmatism in the Yulong Porphyry Copper Belt, Eastern Tibet: A Review and Analysis of Geochronological, Geochemical, and Sr–Nd–Pb–Hf Isotopic Data. Canadian Journal of Earth Sciences, 61 (3): 270–85. https://doi.org/10.1139/cjes-2023-0087.

Warr, L.N., 2021. IMA–CNMNC Approved Mineral Symbols. Mineralogical Magazine, *85* (3), 291-320

White, N.C., Hedenquist., J., 1995. Epithermal Gold Deposits: Styles, Characteristics and Exploration. Society of Economic Geology, 23: 9–13.

Whitney, D. L., and Evans, B. W., 2010., Abbreviations for Names of Rock-Forming Minerals. American Mineralogist, 95 (1): 185–87. https://doi.org/10.2138/am.2010.3371.

Wiedenbeck, M., Allé, P., Corfu, F., Griffin, W.L., Meier, M., Oberli, F., Von quadt, A., Roddick, J.C., Spiegel, W., 1995. Three Natural Zircon Standards for U-Th-Pb, LU-HF, Trace Element and REE Analyses."Geostandards Geostandards newsletter, 19(1), 1-23

Williams, N., 2010.Integrated Interpretation of Geology and Geophysics, Using Inversions, to Predict Geology under Cover. In SEG Extended Abstracts: (ASEG2010-21st Geophysical Conference), 1-4.

Yang, H-H., Wang, Q., Li, Y-B., Lin, B., Song, Y., Wang, Y-Y., He, W., Li, H-W., Li, J-W., Liu, C-C., Feng, C-B., Xin, T., Fu, W-L., Liang, X-J., Zhang, Q., Wang, B-Q., Li, Y., 2022. Geology and Mineralization of the Tiegelongnan Supergiant Porphyry-Epithermal Cu (Au, Ag) Deposit (10 Mt) in Western Tibet, China: A Review. China Geology, 5: 136−159.

Yang, Z., and Cooke, D., R., 2019. Chapter 5 Porphyry Copper Deposits in China. In Mineral Deposits of China . Society of Economic Geologists, (pp. 133-187).

Youbi, N., Ernst, R E., Mitchell, R N., Boumehdi, M A., El Moume, W., Ait Lahna, A., Bensalah, M K., Söderlund, U., Doblas, M.,. Tassinari, C. C.G., 2021. Preliminary Appraisal of a Correlation Between Glaciations and Large Igneous Provinces Over the Past 720 Million Years. Large Igneous Provinces: A Driver of Global Environmental and Biotic Changes, 169–90. https://doi.org/10.1002/9781119507444.ch8.

Youbi, N., Ernst, R. E., Söderlund, U., Boumehdi, M. A., Ait Lahna, A., Tassinari, C. C. G., El Moume, W., Bensalah, M. K., 2020. The Central Iapetus magmatic province: An updated review and link with the ca. 580 Ma Gaskiers glaciation.

Youbi, N., Soderlund, U., Ernst, R. E., Ait Malek, M., Barzouk, A., Ait Lahna, A., Palassia, M., Gong, Z., Evans, D., Wen, B., Jing, X.Q., Boumehdi, M.A., Ikenne, M., Bensalah, M.K., Admou, H., Bajddi, A., Maacha, L., 2019. Ca. 1.65 Ga mafic sills emplaced into the quartzite of jbel Lkest from Kerdous Inlier, Anti-Atlas, West African craton, Morocco: additional evidence that the basal part of Taghdout group is nearly 1 Ga older than previously thought. In Large igneous provinces through earth history: mantle

plumes, supercontinents, climate change, metallogeny and oil-gas, planetary analogues (LIP-2019) (pp. 165-166).

Youbi, N., Kouyaté, D., Söderlund, U., Ernst, R. E., Soulaimani, A., Hafid, A., Ikenne, M., El Bahat, A., Bertrand, H., Rkha Chaham, K., Ben Abbou, M., Mortaji, A., El Ghorfi, M., Zouhair, M., El Janati., 2013. The 1750 Ma magmatic event of the west African craton (Anti-Atlas, Morocco). Precambrian Research, 236, 106-123.

Youbi, N., Ernst, R E., Söderlund, U., Soulaimani, A., Bertrand, H., Marzoli, A., El Hachimi, H., Bensalah, M K., Hafid, A., Ikenne, M., Kouyaté, D., El Bahar, A., Ben Abbou, M., Madeira, J., Mata, J., Martins, L., Bellieni, G., Vérati, C., Mahmoudi, A., 2011. The Central Iapetus Magmatic Province (CIMP) Large Igneous Province. Distribution, Nature, Origin, and Environmental Impact. In American Association of Petroleum Geologists (AAPG) Search and Discovery, 2–3

Yousefi, M., Tabatabaei, S.H., Rikhtehgaran, R., Pour, A.B., Pradhan, B., 2021. Application of Dirichlet Process and Support Vector Machine Techniques for Mapping Alteration Zones Associated with Porphyry Copper Deposit Using ASTER Remote Sensing Imagery. Minerals, 11 (11): 1235.

Zahour, R., Zahour, G., Hadi, H. E., Zerhouni, Y., Baroudi, Z., Khoukhouchi, M., 2022. Petrology, Geochemistry, and Geodynamic Implications of the Ediacaran Volcanism of the Southwestern Edge of the Saghro Massif (Eastern Anti-Atlas, Morocco). Turkish Journal of Earth Science, 339–58.